



HAL
open science

prediction of proximal femur fracture: finite element modeling based on mechanical damage and experimental validation

Awad Bettamer

► **To cite this version:**

Awad Bettamer. prediction of proximal femur fracture: finite element modeling based on mechanical damage and experimental validation. Other. Université d'Orléans, 2013. English. NNT : 2013ORLE2045 . tel-00994604

HAL Id: tel-00994604

<https://theses.hal.science/tel-00994604>

Submitted on 21 May 2014

HAL is a multi-disciplinary open access archive for the deposit and dissemination of scientific research documents, whether they are published or not. The documents may come from teaching and research institutions in France or abroad, or from public or private research centers.

L'archive ouverte pluridisciplinaire **HAL**, est destinée au dépôt et à la diffusion de documents scientifiques de niveau recherche, publiés ou non, émanant des établissements d'enseignement et de recherche français ou étrangers, des laboratoires publics ou privés.

ÉCOLE DOCTORALE SCIENCES ET TECHNOLOGIES

LABORATOIRE PRISME

THÈSE présentée par :
Awad BETTAMER

soutenue le : **22 Novembre 2013**

pour obtenir le grade de : **Docteur de l'Université d'Orléans**

Discipline : Génie Mécanique

**Prédiction de la fracture osseuse du col du
fémur : Modélisation par éléments finis
basée sur la mécanique d'endommagement
et validation expérimentale**

THÈSE dirigée par :

Ridha HAMBLI
Samir ALLAOUI

Professeur, Université d'Orléans
Maître de conférences, Université d'Orléans

RAPPORTEURS :

Pierre VACHER
Sébastien LAPORTE

Professeur, Université de Savoie, Annecy
Professeur, ENSAM Paris

JURY :

Ali MKADDEM
Eric LESPESSAILLES
Pascal SWIDER
Pierre VACHER
Ridha HAMBLI
Samir ALLAOUI
Sébastien LAPORTE

Maître de conférences, ENSAM Chalons
HDR, praticien hospitalier, CHR Orléans
Professeur, Université Toulouse III – Paul Sabatier
Professeur, Université de Savoie, Annecy
Professeur, Université d'Orléans
Maître de conférences, Université d'Orléans
Professeur, ENSAM Paris



UNIVERSITY OF ORLEANS



DOCTORALE SCHOOL FOR SCIENCES AND TECHNOLOGY

PRISME LABORATORY

THESIS presented by :
Awad BETTAMER

Date of thesis defense: **22 November 2013**

In partial fulfillment of the requirement for the degree:
Doctor of Philosophy from the University of Orleans

Discipline : Mechanical Engineering

**PREDICTION OF PROXIMAL FEMUR FRACTURE:
FINITE ELEMENT MODELING BASED ON
MECHANICAL DAMAGE AND EXPERIMENTAL
VALIDATION**

THESIS directed by :

Ridha HAMBLI

Samir ALLAOUI

Professeur, University of Orleans

Lecturer, University of Orleans

RAPPORTEURS :

Pierre VACHER

Sébastien LAPORTE

Professeur, University of Savoie, Annecy

Professeur, ENSAM Paris

JURY :

Ali MKADDEM

Eric LESPESSAILLES

Pascal SWIDER

Pierre VACHER

Ridha HAMBLI

Samir ALLAOUI

Sébastien LAPORTE

Lecturer, ENSAM Chalons

HDR, hospital practitioner , CHR Orléans

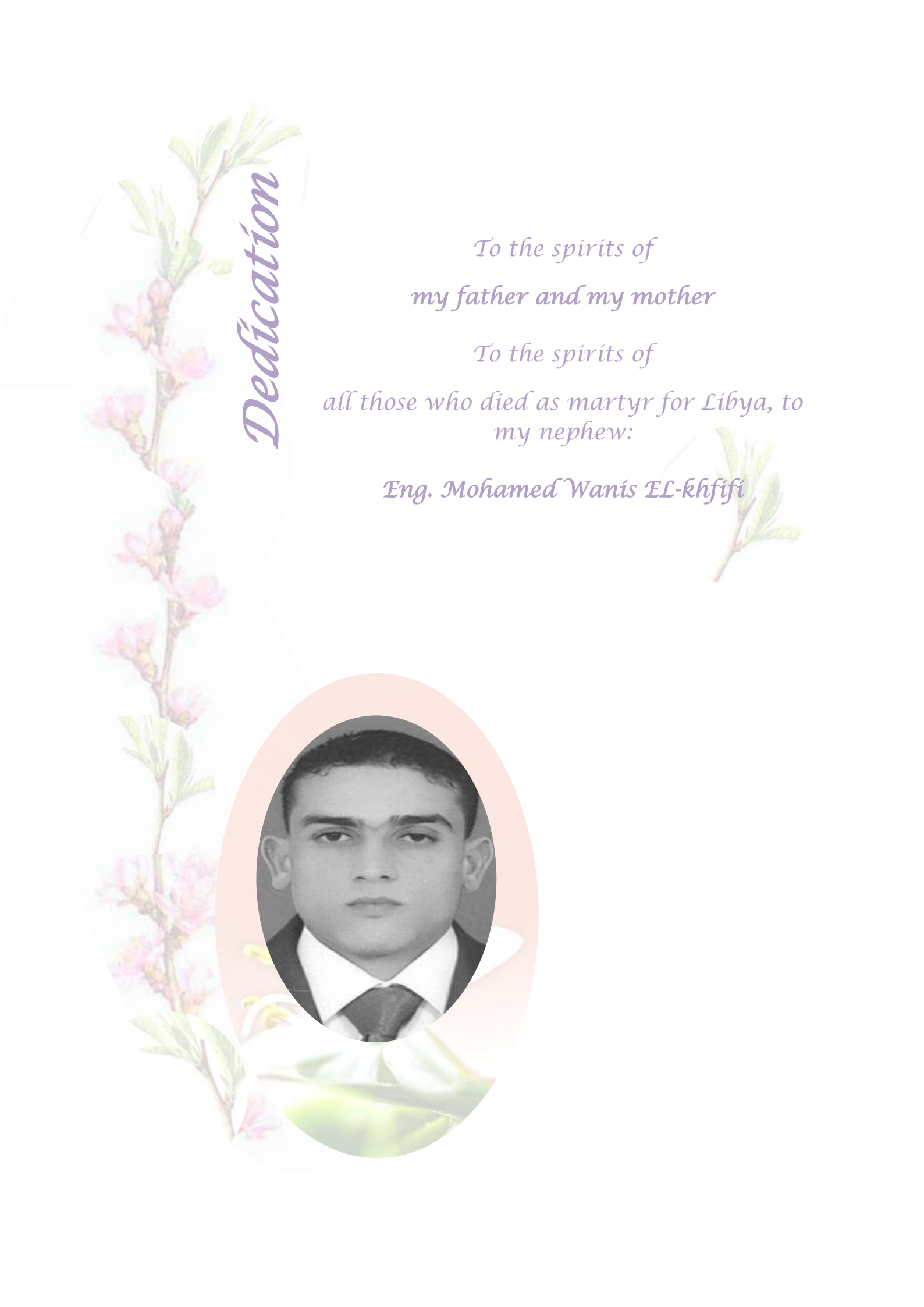
Professeur, University of Toulouse III–Paul Sabatier

Professeur, University of Savoie, Annecy

Professeur, University of Orleans

Lecturer, University of Orleans

Professeur, ENSAM Paris



Dedication

*To the spirits of
my father and my mother*

*To the spirits of
all those who died as martyr for Libya, to
my nephew:*

Eng. Mohamed Wanis EL-khfifi



Acknowledgement

First of all, I wish to express my sincere thanks and gratitude to God, the Almighty **ALLAH**, for helping me during the course of my studies.

I also would like to gratefully acknowledge the **Libyan government** for financing this work.

I would like to express my gratitude and indebtedness to **Prof. Ridha HAMBLI** and **Dr. Samir ALLAOUI** for their valuable guidance at each step of the work and for their efforts in providing useful suggestions.

I thank **Prof. Pierre VACHER** and **Prof. Sébastien LAPORTE** for agreeing to critically review this thesis and for their pertinent remarks which helped me a lot to improve the quality of this work.

My sincere thanks and gratitude also go to **Prof. Pascal SWIDER** for assessing this work and presiding over the jury.

I would also like to thank the examiners, **Dr. Eric LESPESSAILLES** and **Dr. Ali MKADDEM**, to whom I extend my most respectful sentiments.

My appreciations and thanks also go to **Dr. Ahmad ALMHDEI** and **Dr. Amine ALHARAICHE** for their co-operation and generous help.

It's with pleasure that I thank all the academic, technical and administrative staff in the **Polytech Orléans**, particularly those associated with the **MMH** department (Mécanique des Matériaux Hétérogènes) of the **PRISME** laboratory (laboratoire Pluridisciplinaire de Recherche en Ingénierie des Systèmes, Mécanique et Energétique) for welcoming me and providing help and support.

I would like to extend my thanks to all MMH students, (**Doudou, Aristide, Nicolas, Jean-Emile, Nga, Camille, Amal, Julien, Audrey, Aurélie, Christophe, Emilie**) for giving me friendship and encouragement throughout the course of this work.

I am eternally grateful to my officemate **Dr. Abdulwahed BARKOUI** and to **Dr. Frank RICHTER** for their scientific discussions, valuable suggestions and encouragement at each step of this work during their stay in Orleans city and from the distance until the last moment of work. Thanks for the help and support which came when I really needed it most.

Thanks to all my friends in France and Libya (**Ahmad, Abakar, Mustafa, Marwen, Murad, Mohamed, Khaled, Kaled, Salah, Hafed, Yassin**) for their honest support.

Last but not least, I am very grateful to my family, brothers (**Mr. Fathi BETTAMER and Mr. Faraj BETTAMER**), sisters, wife and my daughters for their great support and their sincere concerns about my study.

TABLE OF CONTENTS

GENERAL INTRODUCTION	1
INTRODUCTION GENERALE	5
Chapter 1	
Bone and damage: background	9
1.1. Introduction	10
1.2. Bone structure	10
1.3. Hierarchical structure of bone	11
1.4. Mechanical behavior of bone	13
1.4.1. Mechanical behavior of cortical bone.....	15
1.4.2. Mechanical behavior of trabecular bone	18
1.5. Bone damage	21
1.5.1. Damage and crack formation.....	22
1.5.1.1. Damage and crack formation in cortical bone	23
1.5.1.2. Damage and crack formation in trabecular bone.....	24
1.5.2. Influence of damage on mechanical bone properties	26
1.5.3. Visualization of bone damage	26
1.5.4. Damage measurement.....	28
1.5.5. Influence of loading mode on bone damage	30
1.5.6. Influence of loading mode on bone fracture	33
1.5.7. Conclusion	34
1.6. Femur bone fracture.....	35
1.6.1. Classification of femur neck fractures.....	36
1.7. Femur testing	38
1.7.1. Human femur geometry.....	38
1.7.2. Loading modes	41
1.8. Conclusion.....	43
Chapter 2	
Review on finite element models to predict damage and fracture of bone	45
2.1. Introduction	46
2.2. Finite element simulation of femur bone fracture	46
2.2.1. Finite element simulation of femur fracture using uncoupled fracture criteria.....	52
2.2.2. Finite element simulation using fracture mechanics	54
2.2.2.1. Finite element simulation using the continuum damage mechanics	55
2.3. Finite element mesh generation.....	56
2.4. Conclusion.....	57
Chapter 3	
Finite element simulation of human femur fracture using continuum damage mechanics	59
3.1. Introduction	60
3.2. Concept of continuum damage mechanics	60

3.3. Anisotropic and orthotropic quasi brittle damage behavior law.....	63
3.4. Isotropic quasi-brittle behavior law.....	66
3.5. Material properties assignment	67
3.5.1. Anisotropic /orthotropic material properties assignment.....	67
3.5.2. Isotropic material properties assignment.....	68
3.5.3. Orthotropic direction assignment.....	70
3.6. Loading and boundary conditions	74
3.6.1. Loading and boundary conditions of single limb stance simulation in 3D.....	74
3.6.2. Loading and boundary conditions of single limb stance configuration in 2D.....	75
3.6.3. Loading and boundary conditions of sideway falls simulation in 2D.....	75
3.7. Validation of the developed quasi brittle damage models.....	76
3.7.1. Preliminary validation of the femur fracture model.....	76
3.7.2. Evaluation of mesh sensitivity.....	77
3.7.3. Effect of material assignment on femur fracture pattern	80
3.8. Conclusion.....	81

Chapter 4

Experimental Work	83
4.1. Introduction	84
4.2. Femur specimens.....	84
4.2.1. Femur specimens preparation	84
4.3. Image acquisition.....	87
4.3.1. Image Segmentation	87
4.3.1.1. Data from DXA.....	87
4.3.1.2. Data Extraction from XCT Images	88
4.4. Femur specimen mesh generation	90
4.4.1. Relation between grey level and mechanical properties.....	91
4.5. Femur specimen testing.....	92
4.5.1. Single limb stance test	92
4.5.2. Measuring methods used to measure bone deformation.....	93
4.5.3. Single limb stance fixture assembly	96
4.5.4. Mechanical compression test of single limb stance loading configuration of human femur specimens.....	97
4.5.4.1. Deformation and displacement measurement under compression conditions using DIC method	99
4.5.4.2. Validation of the designed single limb stance assembly and measuring protocol	103
4.6. Conclusion.....	106

Chapter 5

Results and Validation	107
5.1. Introduction	107
5.2. Results and validation of the three dimensional finite element simulation	108
5.2.1. Results and validation of Force-Displacement curve.....	108
5.2.2. Results and validation of three dimensional fracture pattern.....	112

5.2.3. Results and validation of three dimensional model using image correlation technique.....	115
5.3. Results and validation of the two dimensional finite element model.....	119
5.3.1. Results and validation of single limb stance model	119
5.3.1.1. Results and validation of two dimensional fracture pattern.....	123
5.3.1.2. Comparison between the predicted two dimensional model and experimental force displacement curves for single limb stance	128
5.3.1.3. Effect of force direction on femoral fracture load in single limb stance..	129
5.3.2. Sideways fall configuration results.....	133
5.3.2.1. Resulted two dimensional fracture patterns under sideways fall configuration.	133
5.3.2.2. Effect of load direction angle on the damage of human neck femoral under sideways fall configuration.....	135
5.3.2.3. Effect of geometric parameters and density on the fracture force of human proximal femur under sideways fall configuration.....	139
5.4. Anisotropic finite element modeling results for single limb stance and sideways fall configurations.....	141
5.5. Conclusion.....	143
GENERAL CONCLUSION	145
CONCLUSION GENERALE.....	149
References.....	151

LIST OF TABLES

Table 1. 1: Elastic properties of human cortical bone.....	17
Table 1. 2: Elastic moduli of trabecular bone at structure level.	20
Table 1. 3: Microcrack density measurements in vivo	29
Table 1. 4: Subcapital femoral neck fractures following Garden’s classification.....	37
Table 1. 5: Illustrative diagrams showing the human femur Anthropometry	39
Table 1. 6: Measurements of the femoral anthropometrics-dimensions.....	40
Table 2. 1: FE modeling of human proximal femur under single limb stance configuration.....	48
Table 3. 1: Estimated anisotropic Material properties.....	68
Table 3. 2: Material properties for femur and acetabulum used for the isotropic simulation.....	69
Table 3. 3: Damage law parameters used for femur in the isotropic simulation	69
Table 3. 4: Different mesh sizes used for the evaluation of mesh sensitivity.....	77
Table 3. 5: Resulted maximum facture force at 10 different mesh sizes	80
Table 4. 1: Measured total and neck femoral densities for human femur specim.....	86
Table 4. 2: Physical dimensions measured for human femurs	87
Table 4. 3: Human femur resolution and dimensions used in the current simulations.	91
Table 4. 4: Summary of experimental force at fracture values and different force angles under single limb stance configurations.	93
Table 5. 1 Post processing treatments on a representative sample (B).....	115

LIST OF FIGURES

Figure 1. 1: Human Skeltal body	7
Figure 1. 2: Hierarchical structure of bone.	12
Figure 1. 3: Bone section of proximal end of femur	13
Figure 1. 4: A typical stress-strain curve of cortical bone	14
Figure 1. 5: Mechanical compression test of cortical bone.	15
Figure 1. 6: Bone behavior under different strain rates	16
Figure 1. 7: Different orthotropic directions within the specimens.	17
Figure 1. 8: Internal vertical and horizontal trabeculae bone.....	18
Figure 1. 9: Sketch of stress–strain curve behavior under uniaxial compression for cancellous bone	19
Figure 1. 10: Trabecular bone specimen before and after the mechanical test	20
Figure 1. 11: Damage morphology in vivo	22
Figure 1. 12: Images of damage and cracks (arrows) from the anterior sector of femurs of males ...	23
Figure 1. 13: Microcracking in human cortical bone under transverse compression.....	23
Figure 1. 14: Microcracking in human cortical bone under longitudinal compression	24
Figure 1. 15: Trabecular bone sample under compression.....	25
Figure 1. 16: Fuchsin-stained microcracks in cortical bone	27
Figure 1. 17: Microdamage description and classification in trabecular bone	28
Figure 1. 18: Qualitative assessment of damage evaluation.	29
Figure 1. 19: Stress–strain curves of trabecular vertebral bone	30
Figure 1. 20: Experimental averaged damage accumulation in human vertabrae trabecular specimens.	31
Figure 1. 21: Influence of loading mode on bone damage type	32
Figure 1. 22: The shear diffuse damage area	32
Figure 1. 23: Crack pattern and microdamage morphologies	33
Figure 1. 24: Basic femur fracture types	36
Figure 1. 25: Pauwels femoral neck fracture classification.....	38
Figure 1. 26: Typical mechanical tests of the femoral neck.....	41
Figure 1. 27: Force introduction at the proximal femur	42
Figure 2. 1: Correlation coefficients for measured fracture load versus FE computed fracture load.....	53
Figure 2. 2: Schematic diagram of the simulation and validation approaches of the current thesis. .	58
Figure 3. 1: Definition of damage.....	61
Figure 3. 2: Breakdown of number of damaged trabeculae	65
Figure 3. 3: Schematic diagram of the proposed simulated crack propagation implemented in UMAT user subroutine	70
Figure 3. 4: Assignment of orthotropic directions and corresponding material properties	71
Figure 3. 5: The developed models of the current study.....	73
Figure 3. 6: An example of 3D FE loading and boundary conditions applied for human femur.....	74
Figure 3. 7: FE model: (a) applied boundary conditions in single limb stance configuration.	75
Figure 3. 8: Applied boundary conditions in sideway fall configuration.....	76

Figure 3. 9: FE mesh for the femur and the acetabulum.13150 four-nodes quadratic elements.....	77
Figure 3. 10: Reaction force versus vertical displacement, using ten different FEM meshes	78
Figure 3. 11: Crack propagation (crack profile) in the course of the simulation at different instants for three different mesh sizes.	78
Figure 3. 12: Damage accumulations at different instants for three different mesh sizes.	79
Figure 3. 13: Crack propagation in a homogenous human femur.	81
Figure 4. 1: Some samples before testing.....	85
Figure 4. 2: Degreasing process of human femur specimens.	85
Figure 4. 3: Definition of the parameters measured for femur specimens	86
Figure 4. 4: DXA of a proximal femur specimen.....	88
Figure 4. 5: Image segmentation: correction step.	89
Figure 4. 6: Steps of meshing a FE model from DXA data.....	90
Figure 4. 7: Assembly for the single limb test designed in the current research.....	96
Figure 4. 8: Universal testing machine.....	98
Figure 4. 9: The steps of calculation of displacement distribution and local strain by using Digital Image Correlation.	99
Figure 4. 10: Region of interest area on a reference image and a distorted picture.....	100
Figure 4. 11: Binocular stereovision.....	101
Figure 4. 12: Applying speckle pattern.....	102
Figure 4. 13: Geometrical reconstruction of the 3D external Shape of the region of interest (ROI)	102
Figure 4. 14: Mechanical test validation on bovine femur in single limb configuration.....	103
Figure 4. 15: Force-displacement curve of bovine femur under single limb stance configuration. ...	104
Figure 4. 16: Examination of fixture device assembly under compression loading.....	105
Figure 5. 1: Measured force displacement curves of human femur specimens.....	109
Figure 5. 2: Some examples of the comparison between experimental and 3D FE simulations.....	110
Figure 5. 3: Current predicted and experimental failure load correlation.....	111
Figure 5. 4: Predicted and experimental failure load correlation.....	112
Figure 5. 5: Weak areas in femur bone.	112
Figure 5. 6: Fracture sites and 3D damage pattern for sample (G).....	113
Figure 5. 7: Different obtained fracture patterns of proximal femurs under single limb stance configuration.	113
Figure 5. 8: Simulated 3D damage contour and fracture sites for a tested specimen (I).	114
Figure 5. 9: Measured displacement fields in the temporal matching of the compression experiment of a representative specimen (B).....	116
Figure 5. 10: Comparison between the predicted displacements	118
Figure 5. 11: Shear and principal strain distribution for the two dimensional measurement areas of a proximal femur (specimen B).....	121
Figure 5. 12: Axial strains measured in vitro using strain gauges along the femoral shaft.	122
Figure 5. 13: Axial strains measured <i>in vitro</i> using DIC technique along the femoral shaft	123
Figure 5. 14: Prediction of failure location.....	125
Figure 5. 15: FE and experimental Fracture patterns under single limb stance configuration.....	126
Figure 5. 16: Displacement fields just before failure for specimen (B).....	127

Figure 5. 17: Correlation between experimental and predicted proximal femur fracture under single limb stance configuration.	128
Figure 5. 18: Experimental and equivalent 2D force displacement curves.....	129
Figure 5. 19: Contact force vector F (Frontal plan) during nine activities.....	130
Figure 5. 20: Force directions for single limb stance loading condition (Frontal plane).....	131
Figure 5. 21: Force displacement curves at different load angles: 5°,10°,15°, 20°, 25° (specimen I).131	
Figure 5. 22: Contact force F during nine activities.....	132
Figure 5. 23: Fracture pattern during different applied load directions under single limb stance configuration (specimen A).	133
Figure 5. 24: Fracture location and fracture pattern for side way fall configuration.....	134
Figure 5. 25: Force directions for the sideways fall configuration.....	135
Figure 5. 26: Predicted different damage patterns at different load directions	136
Figure 5. 27: Effect of loading direction on predicted fracture load under sideways fall conditions.137	
Figure 5. 28: A Qualitative comparison of damaged areas in sideways fall configuration	139
Figure 5. 29: Effect of femur geometry and density on the femur fracture load under sideways fall configuration.....	140
Figure 5. 30: Correlations under single limb stance configuration.	141
Figure 5. 31: Correlation between stiffness and failure loads under sideways fall configuration.....	142
Figure 5. 32: Correlation between femur neck density and femur stiffness under sideways fall configuration.....	143

GENERAL INTRODUCTION

The annually increasing number of hip fractures due to osteoporosis and other bone diseases has been declared a major public health problem [Mirzaei et al., 2012]. A total of 1.5 million fractures occur every year in the world, including 280,000 hip fractures [Bouxsein and Karasik, 2006]. Owing to ageing of the world population, osteoporosis will become not only an increasing social, but also an increasing economic problem. For example, european medical care costs associated with osteoporosis were estimated at 31.7 billion Euros in 2000 and are expected to rise to 76.7 billion Euros in 2050 [Kanis and Johnell, 2005]. The annual cost of osteoporotic fractures is estimated at 1.2 billion Euros in France alone. This prognosis points out the importance of preventing and reducing such fractures. It is therefore important to detect the disease in time and before the occurrence of the first fracture leading to postoperative complications.

Understanding femoral fractures caused by osteoporosis is, for this reason, becoming an increasingly significant goal for both clinicians and biomedical researchers alike in order to evaluate and to prevent the risk of neck femur fracture with suggestions concerning the required necessary treatments. The effect of these treatment strategies for osteoporosis on bone quality should, however, ideally be evaluated in terms of bone strength [Lenaerts and Lenthe, 2010]. At present, Bone Mineral Density (BMD) measurements with Dual-Energy X-ray Absorptiometry (DXA) are being used as a surrogate measure of bone strength. Although DXA measurement of BMD may provide an indication of the changes in femoral strength induced by osteoporosis treatments, the predictive capacity of bone density is of limited value for individual patients. Computer tomography (CT) is a methodology used to measure both density and structure in a single measurement. The combination with Finite Element (FE) analysis, the most widely used computational technique for structural analysis in engineering, seems especially promising. CT-based FE models can provide insight into load transfer through a study of bone architecture, thereby enhancing our understanding how differences in bone microarchitecture affect bone strength.

In clinical practice, bone mineral density is assessed by imaging techniques such as dual X-ray absorptiometry (DXA). Even though, DXA is the clinical standard for assessing osteoporotic fracture risk, it is not a perfect predictor of fracture [Aspray et al., 2009]. Furthermore, other factors such as bone geometry, density and mineralization play an important role in predicting fracture. Bone mineral density was selected by the World Health Organization (WHO) to establish criteria for the diagnosis of osteoporosis. Bone mineral

density measurements are specified in terms of T-score and Z-score [Johnell et al., 2005]. Both scores are calculated by taking the relative standard deviation of BMD from the average or normalized patients' BMDs. Despite the general acceptance of the T-score and Z-score, there have been a number of problems in its use as a clinical assessment. However, one of the most significant problems of using such scores is the different correlation coefficient between different skeletal sites. Furthermore, the population variances are differing as do apparent rates of bone loss. This makes the decision is so far to be used for the predictive purposes [Kanis, 2001].

Therefore, the FE method has been employed as a verification tool. Over the past decades, a number of different 2D and 3D FE models based on DXA and CT were developed in order to predict the human proximal failure under different conditions [Lotz et al., 1991, Ford et al., 1996, Ota et al., 1999, Pietruszczak et al., 1999, Testi et al., 1999, Keyak and Falkinstein, 2003, Schileo et al., 2008, Taddei et al., 2006, Dragomir-Daescu et al., 2011].

The clinical implementation of 3D CT/FE methods is still limited due to the requirement of expensive computer hardware to achieve solutions of 3D FE models within a clinically acceptable time, as well as the need for robust 3D segmentation and meshing techniques [Aspray et al., 2009]. Segmentation, meshing and FE analysis of a 2D geometry can be accomplished fast and is potentially more robust than 3D CT/FE [Langton et al., 2009]. This practical and rapid tool was employed in femur fracture prediction [Testi et al., 1999, Viceconti et al., 1998, Taddei et al., 2007].

After reviewing the literature on 2D and 3D FE models, the following aspects and deficiencies were identified:

- Progressive fracture initiation and fracture propagation of the neck femur was not modeled.
- The experimental validation phase was performed only by comparing the fracture force. Neither fracture pattern nor full strain contours were compared.
- Surface strains were measured using traditional techniques such as strain gauges.
- Most of the proposed models were focusing on the prediction of the maximum force at fracture by using different mechanical approaches based on uncoupled fracture criteria.

Although these models succeeded to predict the fracture type, they failed to give sufficient information on the fracture profile type or crack propagation behavior [Hamblin et al., 2012].

To overcome these limitations, the objective of this research is to develop a validated FE model in order to simulate human proximal femur fracture considering the progressive cracks initiation and propagation. In order to validate the model, eight human proximal femurs are tested *ex vivo* up to complete fracture under quasi-static load in a setting equivalent to one-legged stance. Both 2D and 3D CT/FE models are generated and FE simulations are performed on these femurs with the same loads and boundary conditions during the stance experiments.

The retained validation metrics are (i) the force-displacement curve, (ii) the fracture pattern and (iii) the distribution of the full-strain contour during the fracturing tests based on a powerful optical resolution techniques. This validation procedure of femur deformation is developed based on 2D and 3D Digital Image Correlation (DIC) method. In addition to the advantage of a noncontact process, the DIC method measures and quantifies the full-strain contour at all recorded instants using visual strain gradients and is able to catch details absent in single point measurement such as strain gauges.

From a FE perspective, two behavioral models were implemented, isotropic and anisotropic. Both models were coupled to specific damage law using the concept of continuum damage mechanics.

In order to demonstrate the capability of the 2D model in predicting results, a correlation analysis between the validated 2D and 3D models is undertaken with 2D DXA models being applied to investigate the influence of some selected factors on the ultimate force and the fracture patterns. The proposed 2D FE models lead to an excellent conformity between predicted and measured results both in the shape of the force-displacement curve (yielding and fracturing) and the profile of the fractured edge.

The incentive behind this study is to propose a FE model for possible clinical use with a high-quality compromise between the complexity and capability of the simulation. The results obtained suggest that 2D models can be applied with high accuracy to simulate the fracture pattern.

The present work is composed of two main parts:

Part I: Finite element modeling

Development and implementation of 2D (plane-strain) and 3D FE models into ABAQUS/Standard code based on continuum damage mechanics in order to simulate the complete force–displacement curve and the profile of the fractured area of proximal femur under given applied boundary conditions such as single limb stance and sideways fall configurations. The UMAT Subroutine of ABAQUS code was used for the numerical implementation.

This part is structured into three chapters: The first chapter presents a general overview of bone and its histological structure, introducing the mechanical damage and its effects on the mechanical properties of bone. The second chapter discusses the literature review of the FE models of proximal femur fracture. The third chapter describes the proposed novel 2D and 3D FE models simulating femur fracture based on the continuum damage mechanics concept. The 2D FE models will be preliminary validated with a previously validated model of the right adult human femur investigated by Keyak and Falkinstein (male, age61) [[Keyak and Falkinstein, 2003](#)].

Part II: Experimental validation

The second part of this work deals with the validation procedure. This part is composed of two chapters. Chapter (4) compiles the experimental approach: (i) the cadaveric femur specimens preparation, (ii) the specimens imaging, (iii) the specimens meshing and (iv) the testing procedure including the single stance set up and the novel developed 3D full-strain in situ measurement during the load application using the digital image correlation technique.

The fifth chapter contrasts experimental and numerical data, thus featuring the validation of the models. Simulations employing these models will model one-legged stance load until complete fracture. The 2D and 3D FE models were applied reproducing the experiments on the eight femurs for validation. Finally, the influence of some selected factors on the ultimate force and the fracture patterns is investigated. For simplicity, the 2D DXA model is applied for this purpose as its potential will be demonstrated prior to this study.

The current work is a new attempt to better understand the mechanisms of fracture of the femoral neck through coupling the constitutive equation with quasi brittle damage law and the novel use of digital image correlation technique to measure the 3D response of human proximal femur.

INTRODUCTION GÉNÉRALE

Le nombre annuel croissant de fracture de la hanche dues à l'ostéoporose et d'autres maladies osseuses a été déclaré un problème de santé publique majeur [Mirzaei et al., 2012]. Un total de 1,5 million de fractures se produisent chaque année dans le monde, dont 500,000 fractures vertébrales et 280,000 fractures de la hanche [Bouxsin et Karasik, 2006]. En raison du vieillissement de la population mondiale, l'ostéoporose va devenir non seulement un problème social croissant, mais aussi un problème économique croissant. Par exemple, les coûts des soins médicaux européens associés à l'ostéoporose ont été estimés à 31,7 milliards d'euros en 2000 et devrait augmenter à 76,7 milliards d'euros en 2050 [Kanis et Johnell 2005]. Le coût annuel des fractures ostéoporotiques est estimé à 1,2 milliards d'euros rien qu'en France. Ce pronostic souligne l'importance de la prévention et de la réduction des fractures ostéoporotiques.

Comprendre les fractures du fémur dues à l'ostéoporose est, pour cette raison, un objectif de plus en plus important pour les cliniciens et les chercheurs biomédicaux afin d'évaluer et de prévenir le risque de telles fractures avec des suggestions concernant les traitements nécessaires. Cependant, l'effet des stratégies de traitements contre l'ostéoporose sur la qualité de l'os devrait idéalement être évalué en termes de résistance osseuse [Lenaerts et Lenthe, 2010]. L'ostéodensitométrie DEXA est aujourd'hui la norme pour mesurer la densité minérale osseuse (DMO). Bien que le procédé DEXA puisse fournir une indication des changements dans la résistance fémorale induite par les traitements contre l'ostéoporose, la capacité prédictive de la densité osseuse est de valeur limitée pour les patients individuels. La tomодensitométrie (CT) est une méthodologie pour mesurer la densité et de la structure en une seule mesure. En particulier, la combinaison avec les analyses par éléments finis (EF), la technique de calcul la plus largement utilisée pour l'analyse structurelle dans l'ingénierie, semble prometteuse peut fournir des indications sur le transfert de charge à travers l'architecture osseuse, ce qui améliore notre compréhension des effets de la microarchitecture osseuse sur la résistance des os.

Dans la pratique clinique, la densité minérale osseuse est évaluée par imagerie DEXA. Cependant, la DEXA n'est pas un indicateur fiable et robuste de la fracture [Aspray et al. , 2009]. En outre, d'autres facteurs tels que la géométrie de l'os, la densité et la minéralisation jouent un rôle important dans la prédiction de la fracture. La densité minérale osseuse a été choisie par l'Organisation Mondiale de la Santé (OMS) pour établir des critères pour le diagnostic de l'ostéoporose. Ces mesures sont spécifiées en termes de T-score et Z-score [Johnell et al. , 2005]. Les deux scores sont calculés en prenant l'écart type relatif de la DMO à partir des DMO des patients ou des moyennes normalisées. Cependant, un certain nombre de problèmes existent dans l'utilisation des T-score et Z-score en évaluation clinique. En effet, Toutefois, un des problèmes les plus importants de l'utilisation de ces scores est la dépendance des résultats mesures par rapport aux sites osseux

mesurés, à la variation des patients et aux âges. Cela rend la décision est loin d'être utilisée à des fins prédictives [Kanis, 2001].

Par conséquent, la méthode EF a été utilisée comme un outil de prédiction. Au cours des dernières décennies, un certain nombre de modèles EF en 2D et 3D basé sur DEXA et CT ont été développés afin de prédire la fracture proximal du fémur humain dans des conditions différentes [Lotz et al., 1991, Keyak et Falkinstein 2003, Ota et al. 1999, Ford et al.1996, Pietruszczak et al., 1999, Schileo et al., 2008, Taddei et al., 2006, Dragomir-Daescu et al, 2011].

La mise en œuvre clinique de la méthode EF 3D (CT/EF) est encore limitée en raison du temps de calcul très long et le manque de techniques de segmentation 3D et de maillage robustes et automatiques [Aspray et al. 2009]. L'analyse par EF 2D (DEXA) peut être effectuée rapidement et potentiellement plus robustes que le 3D [Langton et al., 2009, Testi et al., 1999, Viceconti et al., 1998, Taddei et al., 2007].

L'étude bibliographique effectué sur ce thème a montré que:

- L'amorce de la rupture et sa propagation progressive dans le col du fémur n'ont pas été modélisés physiquement.
- La phase de validation expérimentale des modèles EF proposés a été réalisée uniquement en comparant les forces de fracture prédites et mesurées. Ni le type de fractures ni les contours de déformations entiers n'ont été comparés.
- Les déformations de surface ont été mesurées en utilisant des techniques traditionnelles, telles que des jauges de déformations.
- La plupart des modèles proposés se concentraient sur la prédiction de la force maximale à la rupture en utilisant différentes approches mécaniques basées sur des critères de fracture non couplés.

Pour pallier à ces insuffisances, l'objectif de cette recherche est de développer un modèle EF validé pour simuler la fracture du col du fémur avec la prise en compte de l'initiation et la propagation des fissures. Afin de valider le modèle, huit fémurs proximaux humains sont testés ex vivo jusqu'à la fracture sous chargement quasi-statique en position appui monopodal. Deux modèles EF 2D et 3D sont générés et les simulations EF sont effectuées sur ces fémurs reproduisant les mêmes conditions aux limites des expériences. Du point de vue EF, deux modèles de comportement ont été mises en œuvre, isotrope et anisotrope. Les deux modèles ont été couplés à l'endommagement mécanique des milieux continus (CDM).

Afin de démontrer la capacité prédictive du modèle EF 2D, une analyse de corrélation entre les modèles 2D et 3D est effectuée pour étudier l'influence de certains facteurs sélectionnés sur la force ultime et les faciès de la rupture.

Les métriques de validation retenus sont: la courbe force déplacement obtenu par les essais mécaniques, les profils des fractures et les champs de déformations et des déplacements obtenus à l'aide de mesures optiques par corrélation d'images (DIC).

L'objectif issu de cette étude est de proposer un modèle EF simple, rapide et fiable pour une utilisation clinique. Les résultats obtenus suggèrent que les modèles 2D peuvent être appliquées avec une grande précision pour simuler le type de fracture.

Les travaux effectués dans le cadre de cette thèse se composent de deux parties principales:

Partie I: Modélisation par EF

Le développement et la mise en œuvre de modèles EF de prédiction de la fracture 2D (déformation plane) et 3D à l'aide du code ABAQUS/Standard (sous-programme UMAT). La mécanique d'endommagement a été mise en œuvre afin de simuler la fissuration de l'os et de prédire la courbe complète force-déplacement et le profil de la zone de fracture.

Cette partie est structurée en trois chapitres: le premier chapitre présente une vue d'ensemble de l'os humain et sa structure histologique, l'introduction de l'endommagement mécanique et ses effets sur les propriétés mécaniques de l'os. Le deuxième chapitre traite de la revue de la littérature des modèles EF de fracture proximale du fémur. Le troisième chapitre décrit les modèles 2D et 3D proposés.

Partie II: Validation

La deuxième partie de ce travail traite de la procédure de validation. Cette partie comprend deux chapitres. Le chapitre (4) commence par une brève étude bibliographique sur les essais biomécaniques sur le fémur humains et les bancs d'essais associés en configuration d'appui monopodal. Dans une deuxième étape, les expérimentations développées dans le cadre de cette thèse pour la validation sont présentées considérant (i) les échantillons des fémurs cadavériques et la préparation des échantillons, (ii) l'imagerie des échantillons, (iii) les maillages des spécimens et (iv) les procédures des essais.

Le cinquième chapitre compare les résultats d'essais à ceux obtenus par simulations. Ensuite, l'influence de certains facteurs sélectionnés sur la force à la fracture et les profils de la rupture a été étudiée. Pour plus de simplicité, le modèle 2D DEXA est appliqué à cet effet.

Chapter 1

Bone and damage: background

Abstract

The human skeleton consists of 206 bones. Bones have several functions. They support the body, produce the blood cells and store the needed minerals for the body. Bone quality is not only defined by bone mineral density (BMD) but also by the mechanical properties. During normal daily activities, bone structure is subjected to a complex cyclic loading exerted by the gravity forces as well as by external forces. Under excessive loading, the risk of fractures increases progressively and continuously as BMD declines. One of the most common orthopedic problems caused by the decline of BMD is femur fracture. Being aware of the hierarchical level of bone enables understanding the mechanical properties of bone as an entity; we will start in this chapter with a brief description of the hierarchical structure of bone. The mechanical properties of the main components of bone will be reviewed. From other side, bone damage process is considered to be a mechanism that increases the likelihood of such fractures. A review of bone damage and its influence on femur bone failure will be presented in order to apprehend the different mechanisms involved. Finally, crack formation in bone, femur geometry and types of neck femur fractures will be presented.

Résumé

Le squelette humain est composé de 206 os. Ces os assurent plusieurs fonctions. Ils soutiennent le corps, produisent des cellules sanguines et stockent les minéraux nécessaires à l'organisme. La qualité osseuse n'est pas seulement définie par la densité minérale osseuse (DMO) mais aussi par les propriétés mécaniques. Au cours des activités quotidiennes, la structure osseuse est soumise à des chargements cycliques complexes exercés par les forces de gravité, ainsi que par des forces extérieures. Sous chargement, le risque de fractures augmente progressivement lorsque la DMO diminue. La prise en compte de la structure hiérarchique de l'os permet de mieux analyser les propriétés mécaniques de l'os entier. Nous allons donc commencer dans ce chapitre avec une brève description de la structure hiérarchique de l'os. Les propriétés mécaniques des composants principaux de l'os seront examinées.

En outre, un des problèmes orthopédiques le plus courant causé par la diminution de la DMO est la fracture du fémur. De l'autre côté, le processus de l'endommagement osseux est considérée comme étant un mécanisme qui augmente la probabilité de telles fractures. Un état de l'art sur l'endommagement osseux et son influence sur la fracture de l'os du fémur sera présenté afin d'appréhender les différents mécanismes mis en jeu. Enfin, la formation de fissures dans les os, la géométrie du fémur et les types de fractures du col du fémur seront présentés.

1.1. Introduction

The emphasis of this chapter will be on the structure and mechanical properties of bone as a composite material. This chapter has two main sections. Firstly, the structure of bone at different scales including the two different types of bone, cortical and trabecular will be described. Secondly, failure under general loading conditions will be discussed related to damage accumulation processes.

1.2. Bone structure

Bone is a complex stiff tissue able to resist deformation in response to both internal (primarily muscular) and external forces [Currey, 2002]. Bones can be classified based on their location, shape, size, and structure.

Based on location, bones can be divided into two components, the axial skeleton and the appendicular skeleton. The axial skeleton forms the central axis of the body. It consists of the bones of the skull, the vertebral column and the ribs cage. The appendicular skeleton consists of the upper hinged bones (arms, forearms and hands supported by the pelvic girdles) and lower limb bones (Figures 1.1a and 1.1b). The pelvic girdle articulates with the femur at the acetabulum hip joint. The skeletal body has a variety of important functions, including the support of soft tissues, producing blood cells for the body and storing minerals that the physical structure needs.

Based on shape, skeletal bones can be classified as flat bone such as bones of the skull, pelvis and ribs, tubular bone such as bones of limbs and irregular bone such as bones of vertebral column.

Based on size, bones can be classified as long bone and short bone. Long bones are tubular in shape, with a hollow shaft and two ends, including bones of the limbs such as femurs. Short bones are roughly cubical in shape, located only in the foot (tarsal bones) and wrist (carpal bones).

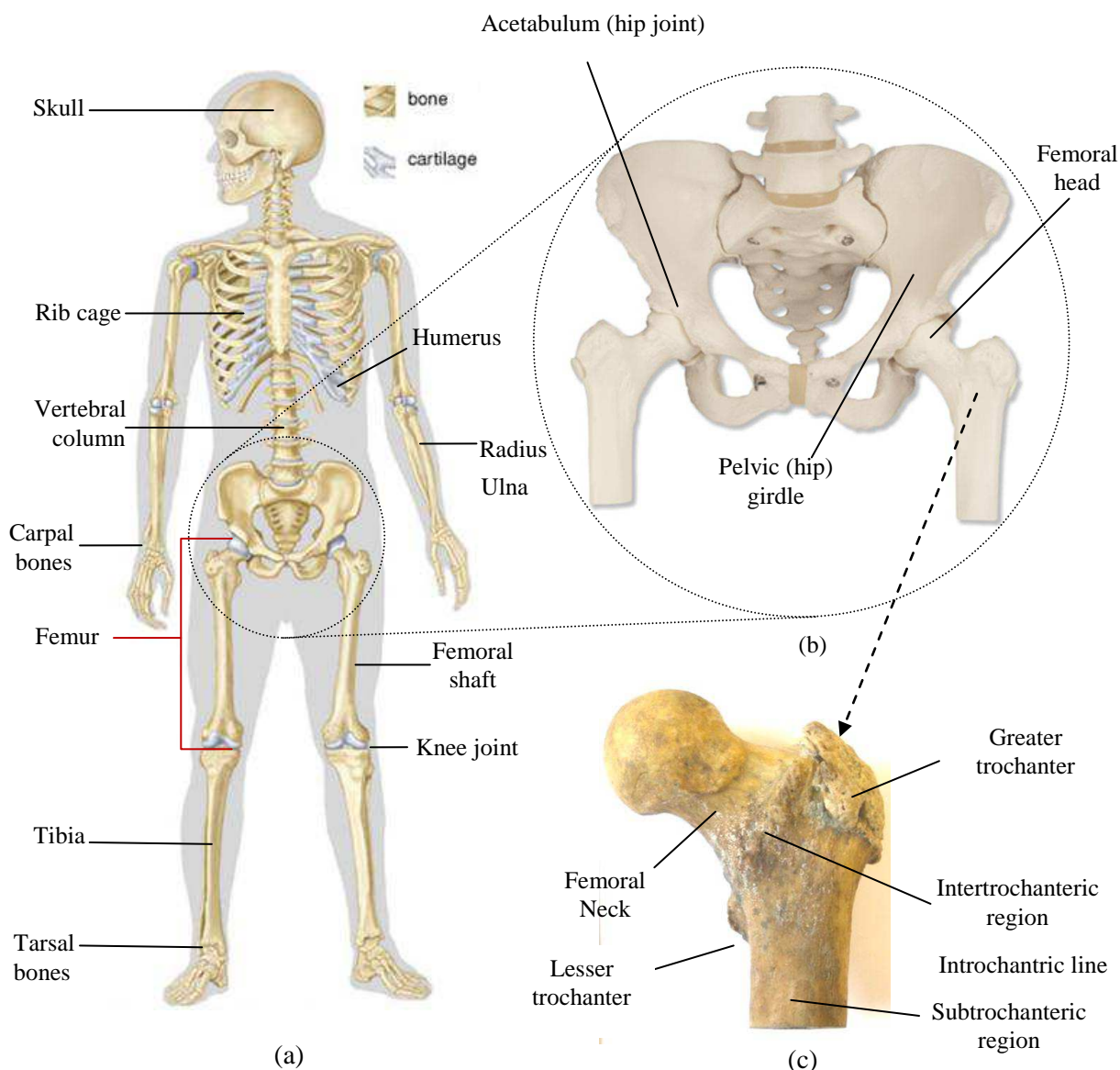


Figure 1. 1 Human Skeltal body: (a) Human skeletal system, (b) bones of the hip and pelvis (c) anatomy of human proximal femur.

The femur is the longest and heaviest bone in the body that extends from the pelvis to the knee, Figure 1.1c. Its proximal head articulates with the acetabulum of the hip bone, and distally, the femur along with the tibia forms the knee joint. The structure of the proximal femur will be detailed in the following section.

1.3. Hierarchical structure of bone

Bone can be considered as an assembly of different levels of hierarchical structural units designed on various scales from macro to nano (Figure 1.2).

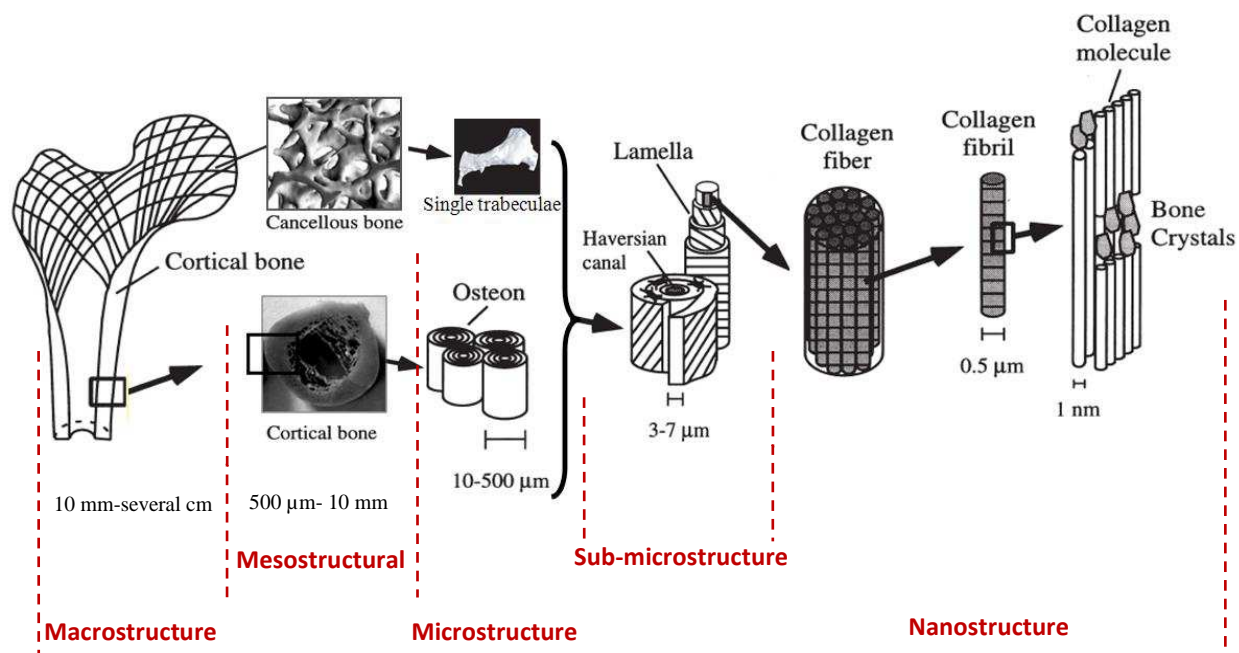


Figure 1. 2 Hierarchical structure of bone.

The structure of bone can be described as follows [Rho et al., 1998, Rubin and Jasiuk, 2005]:

- **The macrostructure level:** this level is defined as the range from 10 mm to several centimetres, or the whole bone level. It is comprised of cortical and trabecular bone.
- **The mesostructural level:** ranged from 0.5 to 10 mm, taking a femur as an example of a long bone, at the mesostructural level, bone is consisted of two subtypes: cortical (compact) bone (80% volume of the total skeleton) and trabecular (cancellous or spongy) bone (20% volume) type (Figure 1.3). The dense nature of cortical bone determines its strength and stiff mechanical properties compared with trabecular bone. The trabecular bone is classified as a porous cellular solid, consisting of an irregular three dimensional array of bony rods and plates called trabeculae.
- **The microstructure level:** this level is ranged from 10 to 500 μm. It consists of haversian systems, randomly arranged osteons, single trabeculae.
- **The sub-microstructure level:** it is called also single lamellae and it is ranged from 3 to 7 μm. This level consists of several structures of oriented fibrils, depending on the location in the bone (parallel, circumferential, twisted) with respect to the longitudinal axis of the diaphysis.

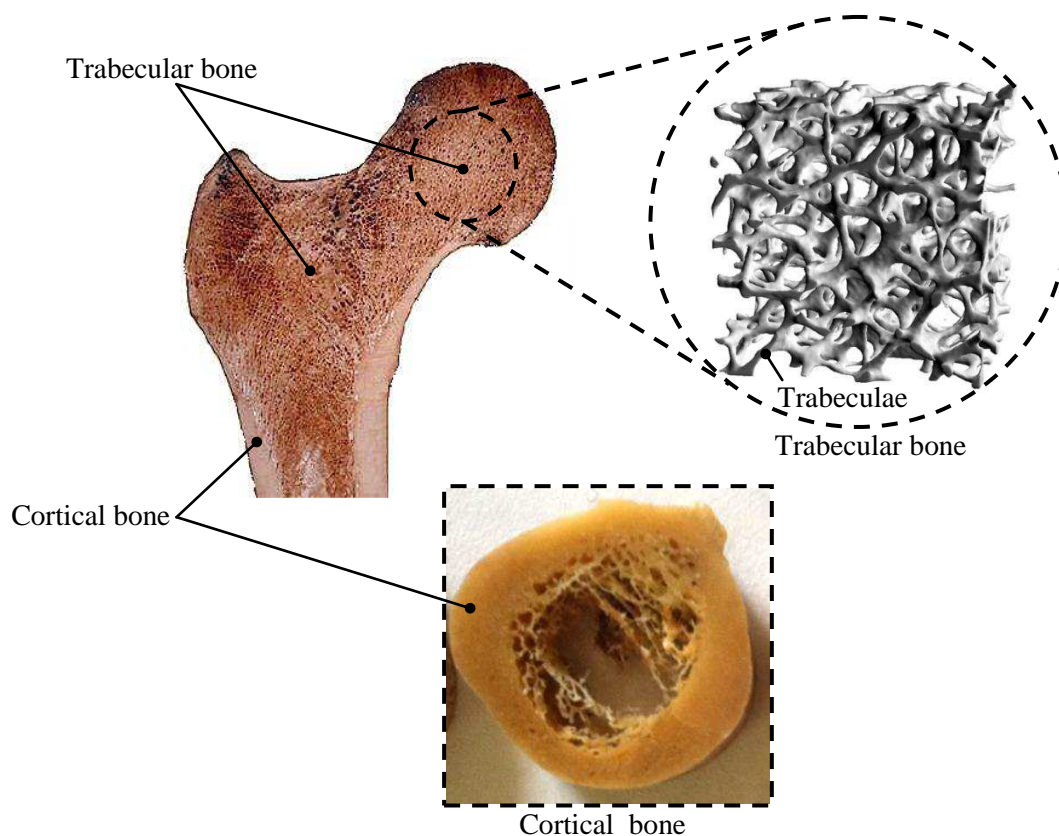


Figure 1. 3 Bone section of proximal end of femur [Cowin, 2001].

- **The nanostructure level:** this level, with size less than $1\ \mu\text{m}$, consists of fibrillar collagen. At this level, we found also mineralized collagen fibrils which are the basic unit of bone. It is composed of elementary molecular structure such as mineral, collagen, and non-collagenous organic proteins. These elements assembled as a composite material (material matrix) which is dispersed in the gap regions and around the collagen.

Being aware of the hierarchical level of bone enables understanding the mechanical properties of bone as an entity, and the structural relationship between them and the various hierarchical levels of bone [Rho et al., 1998]. This work studies the bone at the macroscopic level i.e. whole bone such as femur. The term ‘bone material’ denotes bone at mesostructural level i.e. cortical and/or trabecular bone. Below this level, bone was not the focus of the current research.

1.4. Mechanical behavior of bone

The hierarchically organized structure, as shown in the previous subsection, has an irregular arrangement and orientation of the components, making the material of bone heterogeneous and anisotropic. Nowadays, a considerable amount of work is in progress

around the world to analyze its mechanical properties. A concise summary of the common mechanical concepts and terminology used in the field of bone biomechanics, mechanical testing and measurements will be discussed in this subsection.

Imposing Force (load), which is applied to a bone material either from a muscle attached to it or from external forces or by falling, the bone material will deform according to its constitutive behavior. The initial response is elastic. The slope of the linear region of the force-displacement curve represents the stiffness or rigidity of the structure. Besides stiffness, other mechanical properties can be determined, such as ultimate load and displacement, work to failure which can be defined by the area under the load-displacement curve (Figure 1.4a). Each of these measured parameters represents a different property of the bone:

- **Ultimate load:** represents the general integrity of the bone structure.
- **Work to failure:** is the amount of energy necessary to break the bone; ultimate displacement is inversely related to the brittleness of the bone.
- **Stiffness:** is the ability of a material to resist being deformed when a force is applied to it. It is divided by its corresponding deformation within the elastic range of the load–displacement curve. Stiffness is closely related to the mineralization of the bone.
- **Strength:** can be defined as the internal resistance of a material to deformation and ultimate fracture (failure).

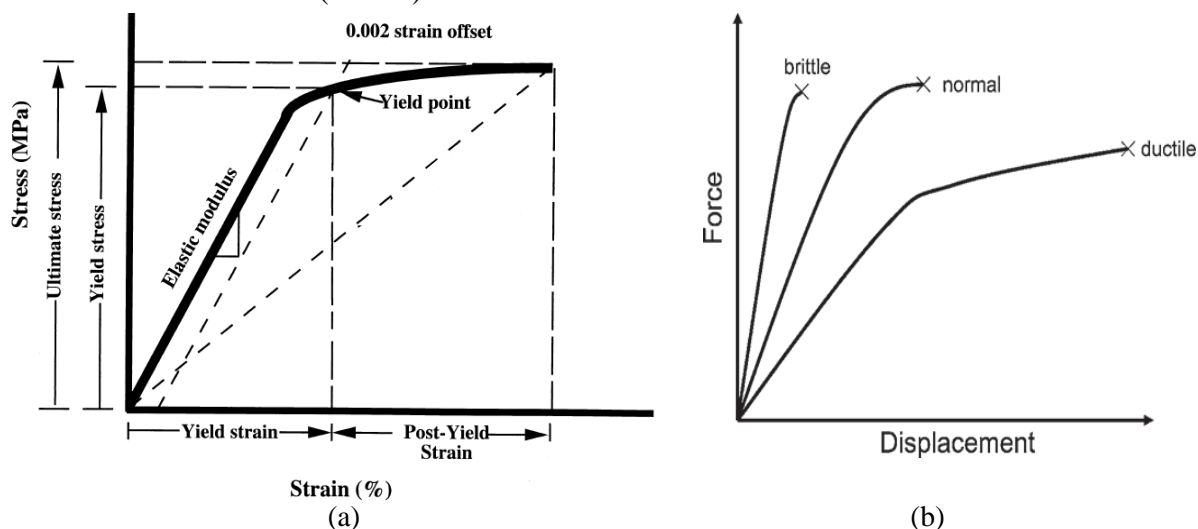


Figure 1.4 (a) A typical stress-strain curve of cortical bone [Vashishth et al., 2001] (b) Load-displacement curves for different bone conditions [Turner et al., 2006].

Force- displacement curves are particularly useful for measuring the strength and stiffness of bone at both microstructural and mesostructural levels. However, the biomechanical status of bone structure cannot be described by just one of these properties. For example, a bone from an osteoporotic patient will tend to be very stiff, but also very brittle, resulting in reduced

work to failure and increased risk of fracture (Figure 1.4b). In other words, if that energy exceeds what the bone can absorb, the bone will break. Highly mineralized bone is also stiff and brittle and will require much less energy to fracture than a bone that is more compliant [Turner, 2006].

The slope of the stress versus strain curve within the linear region defines the Young's modulus of the bone (Figure 1.4a). Mechanical testing also provides information concerning the yield point, load and work to failure and ultimate strain. At macrostructure level, bone varies in its behavior depending on its nature i.e. cortical or trabecular. The following subsections describe briefly the behavior of cortical and trabecular bone.

1.4.1. Mechanical behavior of cortical bone

Parallel to the long axis, cortical bone responds differently in compression and tension. In uniaxial compression test, cortical bone yields at higher stress than in tension. It strain hardens rapidly to a peak then fails at strains of about 1.5% (Figures 1.5a and 1.5b).

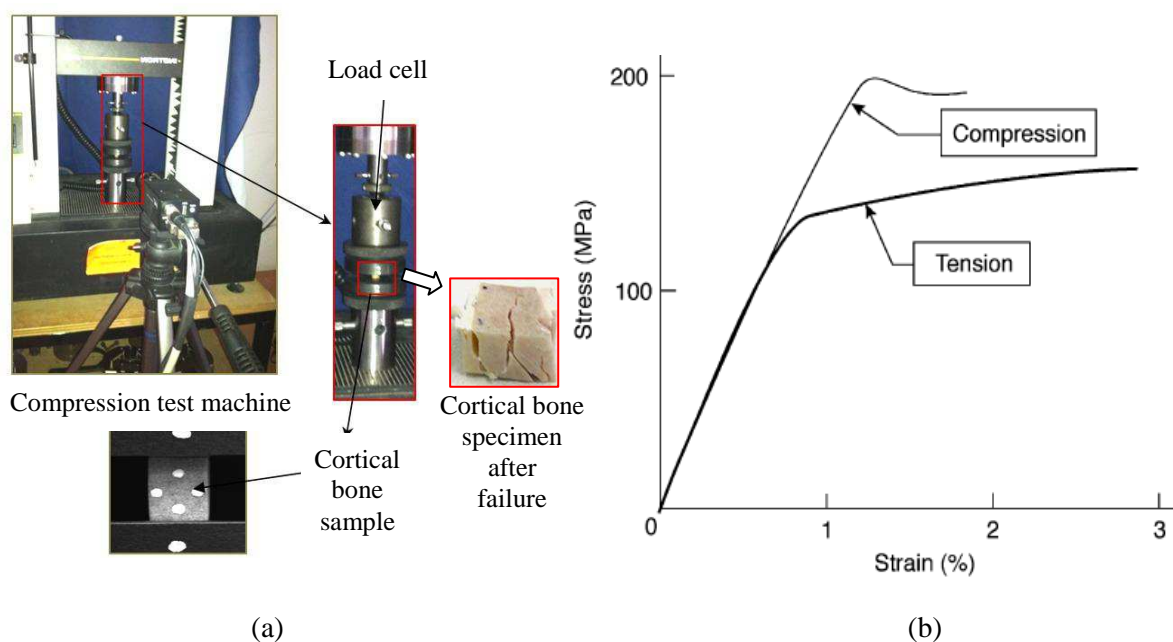


Figure 1. 5 (a) Mechanical compression test of cortical bone. (b) Schematic of the compressive and tensile stress/strain curves for cortical bone along the axis of a long bone [Mercer et al., 2006].

Factors causing these differences are the size of specimens, the equations used for calculations of the mechanical properties of cortical bone depending on the type of mechanical testing [An and Draughn, 2000] or the simple fact that the specimens are already partly damaged [Fondrk et al., 1999]. The mechanical properties of bone are also highly dependent on the mineral content [Currey, 2010], age [Kulin et al., 2011], the amount of

hydration [Nalla et al., 2005] and the amount of porosity [Carter and Hayes, 1977, Bonfield and Clark, 1973].

Bone is described as elastic/brittle. Bone develops internal damage when the elasticity limit for stress or strain are reached [An and Draughn, 2000]. The viscoelasticity property is another property of the bone behavior. Viscoelasticity has been reported with an initial modulus increasing by more than a factor of 2 as the applied strain rate is increased from 0.001 to 1500 s⁻¹ [Johnson et al., 2010]. Generally, for both tension and compression, Young's modulus increases with increasing strain rates. As shown in Figures 1.6a,b for low strain rates (beyond 1 s⁻¹), both strength and strain at maximum load decreased to some extent in tension and increased in compression with increasing strain rate. On the other side, stress and strain at yield decreased for both tension and compression suggesting a simple linear relationship between bone yield properties and strain rate.

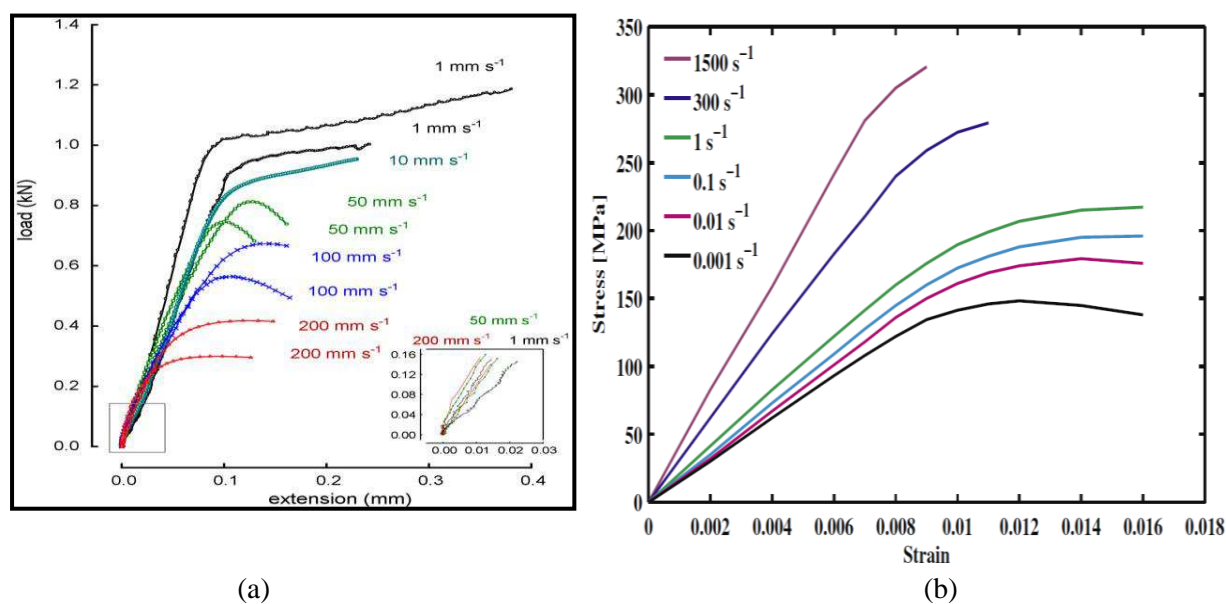


Figure 1. 6 Bone behavior under different strain rates (a) Force-displacement curves under tensile loads (b) compressive stress–strain curves for human femoral cortical bone as a function of strain rate [Johnson et al., 2010].

From a qualitative point of view, the human cortical bone can be considered as a linear elastic material with low elongation at break. Most reported mechanical properties were measured under quasi static loading (low rates). In the current thesis, low strain rate was adopted.

Cortical bone has been identified to behave transversely isotropic and significantly different in the longitudinal directions corresponding to axial bone direction [Reilly and

[Burstein, 1975, Dong and Guo, 2004], Figure 1.7. The elastic modulus and strength of bone, in the longitudinal direction exceed those in the transverse direction by a factor greater than 2 [Reilly and Burstein, 1975]. Peng et al. [Peng et al., 2006] recognized bone material as an orthotropic material rather than isotropic. In general, it is evident that the highest value of Young's modulus occurs in the longitudinal direction E_3 as shown in Table 1.1.

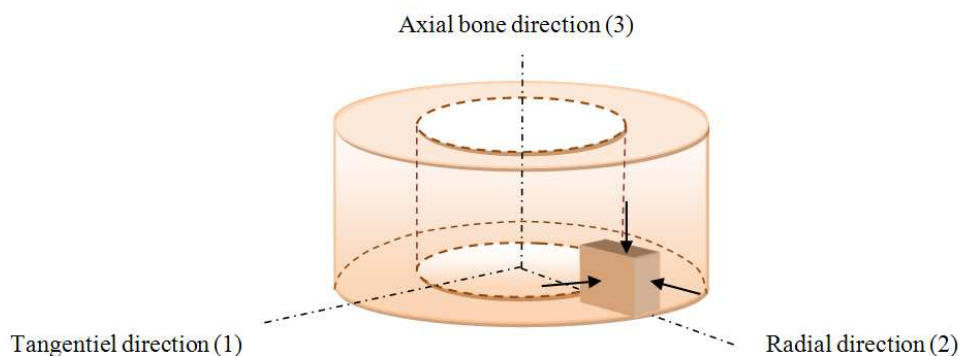


Figure 1. 7 Different orthotropic directions within the specimens.

This indicates that the mechanical properties depend strongly on the orientation of osteons [Baïotto, 2004]. A less pronounced anisotropy was observed in the plane perpendicular to the long axis of the human cortical bone (tangential and radial directions) [Hoffmeister et al., 2000]. This is why Peng et al. [Peng et al., 2006] recognized bone material as an orthotropic material.

Table 1. 1 Elastic properties of human cortical bone.

	Mechanical test (Compression)	Mechanical test (Tension)	Ultrasound measurement		
	[Reilly et al., 1975]	[Reilly et al., 1975]	[Yoon et al., 1976]	[Van Buskirk and Ashman, 1981]	[Taylor et al., 2002]
E_1	11.7 (GPa)	12.8 (GPa)	18.8 (GPa)	13.0 (GPa)	17.9 GPa
E_2	11.7 (GPa)	12.8 (GPa)	-	14.4 (GPa)	18.8 GPa
E_3	18.2 (GPa)	17.7 (GPa)	27.4 (GPa)	21.5 (GPa)	22.8 GPa
G_{12}	-	-	-	4.74 (GPa)	5.71 GPa
G_{13}	-	3.3 (GPa)	8.7(GPa)	5.85 (GPa)	6.58 GPa
G_{23}	-	3.3 (GPa)	-	6.56 (GPa)	7.11(GPa)
ν_{12}	0.63	0.53	0.31	0.37	0.37
ν_{13}	-	-	-	0.24	0.30
ν_{23}	-	-	-	0.22	0.31
ν_{21}	0.63	0.53	-	0.42	0.28
ν_{31}	0.38	0.41	0.28	0.40	0.38
ν_{32}	0.38	0.41	-	0.33	0.26

As evident from Table 1.1, Young's modulus of human cortical bone varies from 11.7 to 18.2 GPa in the compression test. In the tension test, these values range from 12.8 to 17.7 GPa. Besides the mentioned reasons of this discrepancy, other factors like the testing method or the influence of microstructure [Rho et al., 1998], may also contribute when the properties are measured experimentally. However, 70–80% of the variability in bone mechanical properties (in the stiffest direction) can be explained in terms of true density variations alone.

1.4.2 Mechanical behavior of trabecular bone

The human neck femur has an internal structure consisting of two trabecular groups (Figure 1.8). The first is in the vertical direction parallel to femur axis called trabeculae of compression. The resistance to axial loads is maximum in the vertical axis of trabeculae. It absorbs the compressive forces during standing and walking.

The second group deals with tension forces which resist the compression loads transmitted through the vertical trabeculae during limb stance and walking [Hammer, 2010].

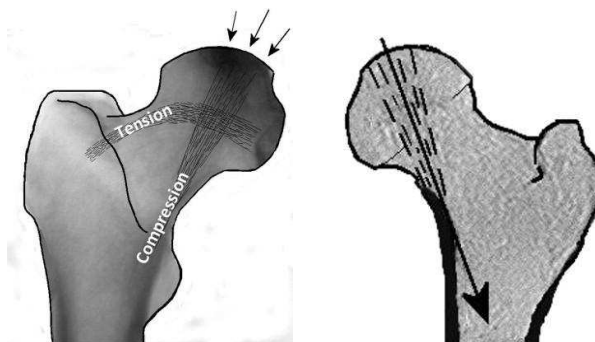


Figure 1.8 (a) Internal vertical and horizontal trabeculae of bone (b) direction of resultant force through the upper femur during single limb stance [Hammer, 2010].

Each of these two trajectory groups of trabecular plays a specific role in the solicitation of the femur and both are important. During frequent daily activities such as walking and standing, the femoral head is subjected to a large component of compressive stress on the inferior surface of the femoral neck and bending stresses on superior left side. The compressive forces as a whole are supported by the vertical trabeculae (first group). The second horizontal group deal with the tension stresses which oppose the bending of the compression forces.

Both groups are essential for the strength and integrity of the femur. So the knowledge of their characteristics and mechanical behavior in these two loads is required.

Mechanical properties of trabecular bone are usually measured experimentally by performing mechanical tests such as uniaxial compression. During this test, trabecular bone behavior can be described in three stages as shown in Figure 1.9. The first stage (stage I) reflects hardening of the stress–strain curve. The second stage is characterized by slight changes in stress (Stage II), advancing well into the large and inelastic strain regime.

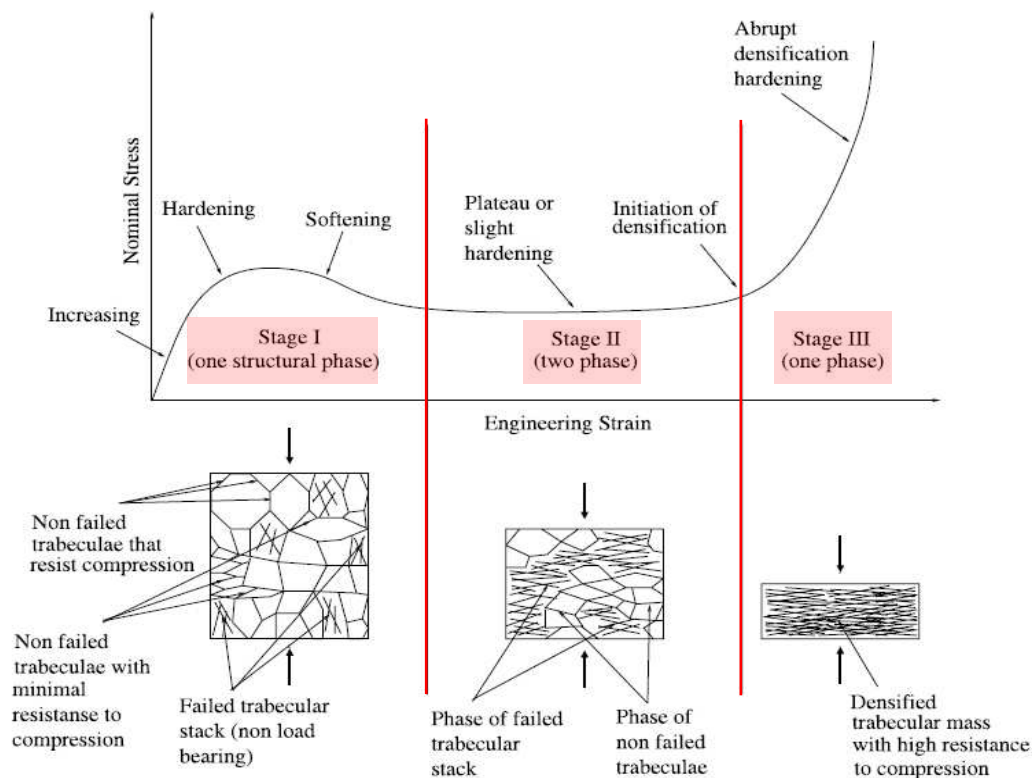


Figure 1.9 Sketch of stress–strain curve behavior under uniaxial compression for cancellous bone [Kefalas and Eftaxiopoulos, 2012].

Further compression causes compaction of the porous structure (Stage III) depending on the nature as well as on the density of the trabecular bone. Ultimately all trabeculae have collapsed and constitute a densified trabecular structure (Figures 1.9 and 1.10). The strain at which this transformation from trabecular to compacted bone mass starts is defined as the initiation of densification. This process leads to a sharply rising of the stress with high tangent modulus [Kefalas and Eftaxiopoulos, 2012].

Mechanical properties of trabecular bone depend on the position in the organ as well as on anatomic location [Goldestein, 1987]. Trabecular bone displays anisotropic behavior (Table 1.2) which is usually described as orthotropic [Van Rietbergen et al., 1996].

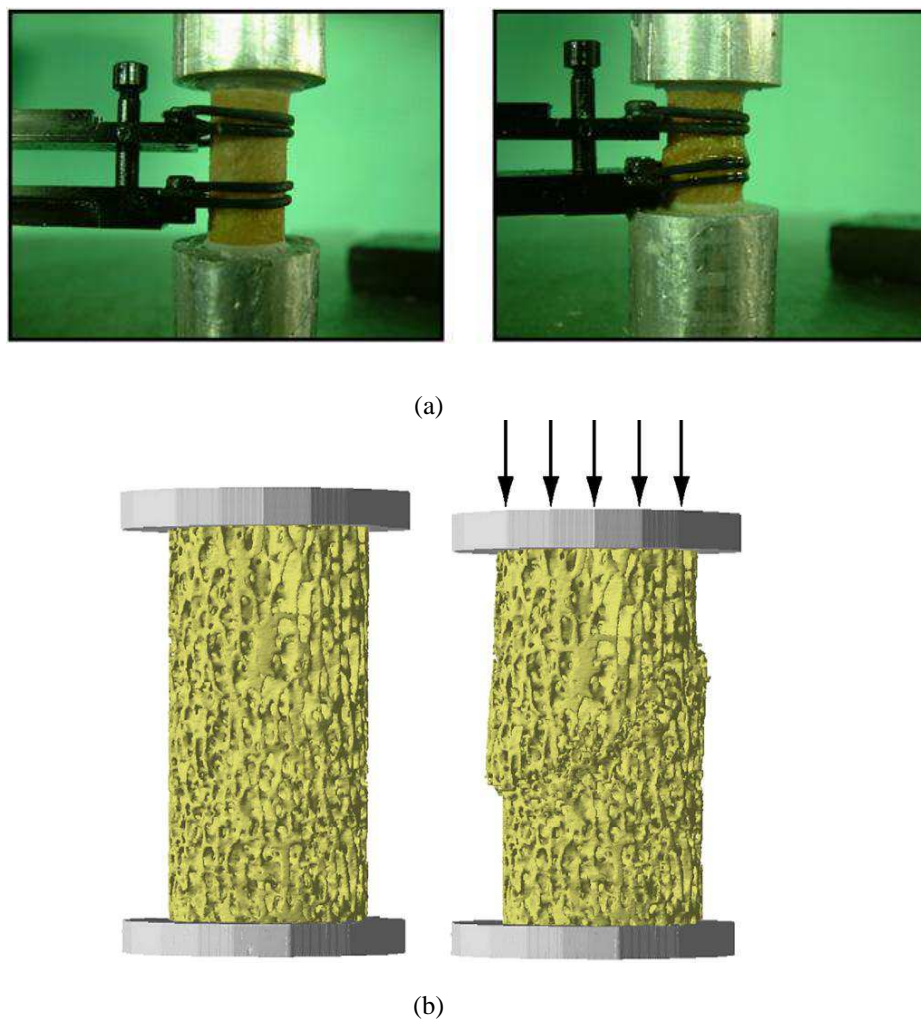


Figure 1. 10 Trabecular bone specimen before and after the mechanical test (a) tested specimen (b) micro CT-image of a trabecular bone specimen before and after failure, [Perilli et al., 2008].

According to the selected references from the literature, Table 1.2, the normal and shear moduli of trabecular bone are 346 to 1107 MPa and 98 to 165 MPa respectively. The structural properties of cancellous bone are much smaller than those of cortical bone. It was reported that the average values of elastic modulus are several hundred mega Pascal for cancellous bone, compared with 5 to 21 GPa for cortical bone [An and Draughn, 2000].

Table 1. 2 Elastic moduli of trabecular bone at structure level.

Elastic Property (MPa)	References	
	[Ashman and Rho, 1988] Proximal tibia	[Turner et al., 1999] Femur
E_1	346	292
E_2	457	359
E_3	1107	784
G_{23}	98	81
G_{31}	132	67
G_{12}	165	144

Additionally, the mechanical properties of bone can be modified by diseases such as osteoporosis. Indeed, osteoporosis causes a decrease in bone density and thus the bone brittleness that reduce the work to failure and ultimately increase the risk of fracture particularly those which concerns hip fractures. It is therefore important to consider the mechanical properties of bone taking into account such diseased. On the other side, femur fracture injuries may not lead to an immediate fracture, but may introduce microdamage in the proximal femur. Skeletal fragility and traumatic fracture may result from the accumulation of microdamage [Nagaraja et al., 2005]. This ultimately leads to undesirable effects on the mechanical properties of bone, decreasing both the elastic modulus and the work to failure in whole bones [Keaveny et al., 1994, Hoshaw et al., 1997].

As the bone damage process is a mechanism that increases the likelihood of fracture, it is very important to assess the damage level when bone fracture is subjected to study. A review of bone damage and its influence on bone failure will be presented in the following subsections.

1.5. Bone damage

In vivo, bone supports daily cyclic loading associated with physical activities such as walking, running or climbing stairs. During these activities, the femur cortical bone is predominantly exposed to compressive stresses that induce the accumulation of damage [Burr et al., 1998, Pattin et al., 1996]. Though macroscopic damage is hardly visible before a large crack and subsequent global failure occurs, a substantial alteration in mechanical properties may occur at early stages [Zysset and Curnier, 1996].

Bone fails as a result of damage accumulation in the form of microcracks [Zioupou and Currey, 1994]. Bone fracture normally initiates in an area of stress concentration. When the crack is not repaired, damage will start. At the submicroscopic level (microdamage), it grows to microscopic cracks (crack propagation). The crack then extends as microdamage accumulation during normal activities or sudden trauma causing a macroscopic bone fracture.

Damage description of bone as a material requires understanding the physical mechanisms of microcracking and investigating the influence of damage on overall mechanical properties.

1.5.1. Damage and crack formation

Damage forms regularly by the accumulation of microdamage in bone as a result of daily loading activities during walking as well as during overloading situations such as sideways injury.

Damage occurs at several hierarchical scales beginning at the organic matrix fibrils, lamellar and osteonal levels which is collectively called microdamage. At submicrostructure levels, this damage occurs in the form of linear microcracks. At this level, damage is hypothesized to be associated with debonding of the collagen-hydroxyapatite composite [Mammone and Hudson, 1993]. At the microstructural level, damage is associated with slipping of lamellae along cement lines, shear cracking in cross-hatched patterns [Choi et al., 1994] and progressive failure of the weakest bonds [Guo, 1994].

Linear microcracks are formed under compressive loading from the accumulation of microdamage in vivo, Figure 1.11a. An additional type of damage, so-called diffuse damage, has been identified and occurs typically in the form of a large number of short submicroscopic cracks [Vashishth et al., 2000], Figure 1.11b.

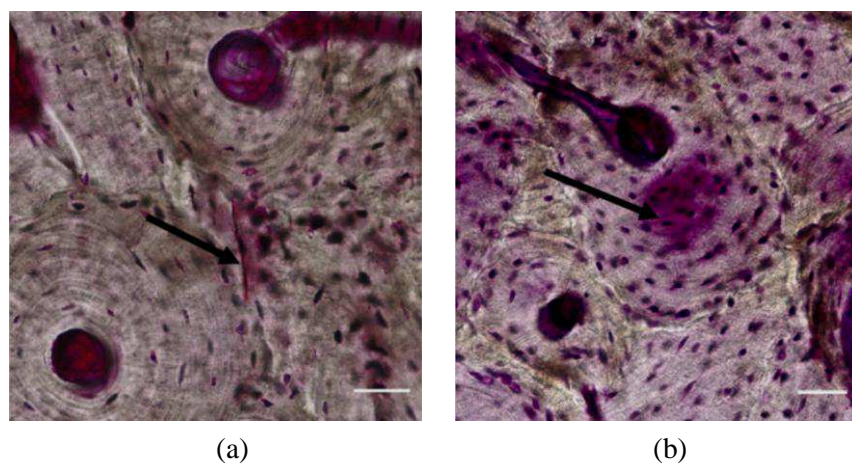


Figure 1.11 Damage morphology in vivo (a) linear microcracks, (b) diffuse damage.

Damage and crack formation in cortical bone has been a lively area of research. In addition to being the precursor to the growth of crack to failure (i.e., a stress fracture), microcracking damage is also believed to adversely affect the mechanical properties of bone and induce in long-term effects on mechanical properties. With age, crack density (cracks/mm² of cross-section) increases in both cortical and trabecular bone, see Figure 1.12, [Fazzalari et al., 1998, Mori et al., 1997, Norman and Wang, 1997, Schaffler et al., 1995] suggesting that microcracks contribute to bone weakness and fractures in the elderly [Sobelman et al., 2004].

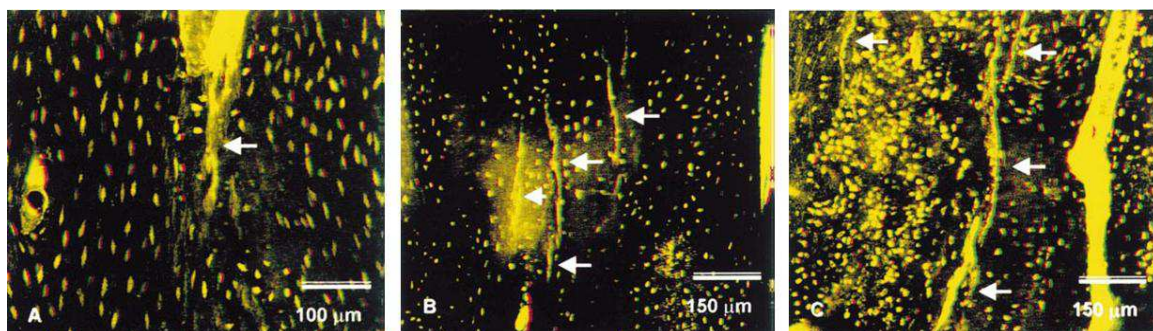


Figure 1.12 Images of damage and cracks (arrows) from the anterior sector of femurs of males aged: (a) 35 years; (b) 56 years; (c) 92 years. Cracks in the bone of the 35-year-old are accompanied by some collateral damage seen here as a hint of diffuse staining in the area of the crack [Zioupou, 2001].

Damage accumulation and crack formation in both cortical and trabecular bone will be presented in the following subsections.

1.5.1.1. Damage and crack formation in cortical bone

In vivo, the majority of microcracks formed from normal human activity are located in the interstitial human femur and tibia extending to the cement lines of cortical bone [Kruzic and Ritchie, 2008]. This phenomenon can be highlighted experimentally by conducting compression tests on cortical bone. In fact, transverse compressive loading of human femur cortical bone results in a fracture at plane oblique to the loading direction and along the length of the osteons, (Figures 1.13a, 1.13b)). Extensive crosshatched damage ($80 \pm 5\%$ of osteons were damaged after failure) was homogeneously distributed within the bulk (Figure 1.13c). Longitudinally, the fracture follows an oblique path to the osteons, Figures (1.14a, 1.14b).

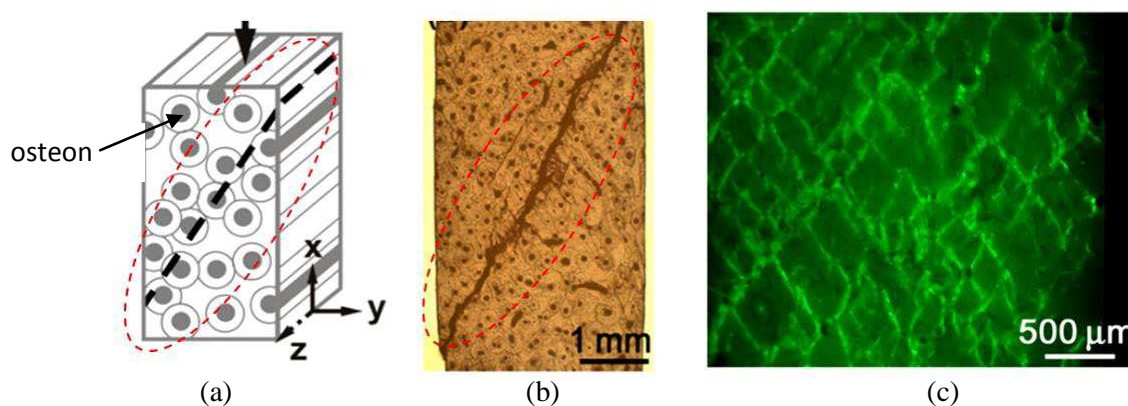


Figure 1.13 Microcracking in human cortical bone under transverse compression: (a) schematics of the transverse (90°) loading orientation with respect to the osteons; (b) stained image of the macroscopic oblique fracture pattern; (c) fluorescence microscope image of distributed cross-hatched damage at the osteonal–interstitial level [Ebacher et al., 2012].

At the osteonal–interstitial level, extensive homogeneously distributed cross hatched damage ($69 \pm 5\%$) of the osteons is observable, Figure 1.14c.

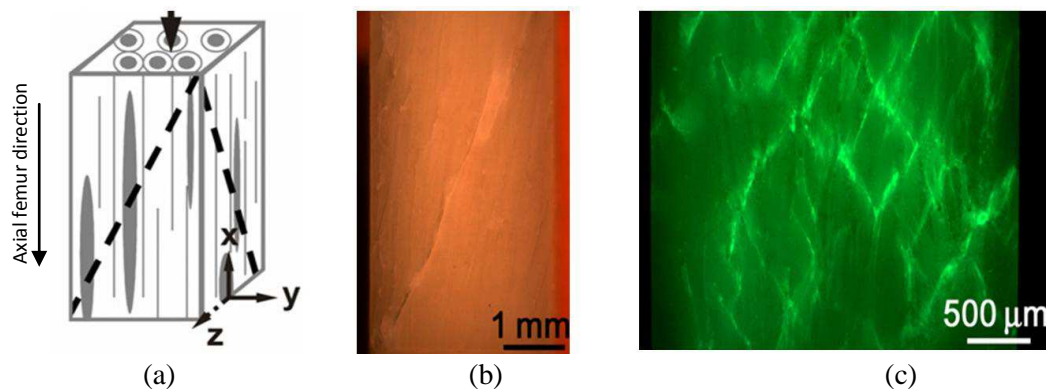


Figure 1.14 Microcracking in human cortical bone under longitudinal compression (a) schematics of the longitudinal (0°) loading orientation with respect to the osteons; (b) stereomicroscope image of the macroscopic oblique fracture pattern; (c) fluorescence microscope image of distributed cross-hatched damage at the osteonal–interstitial level [Ebacher et al., 2012].

In both longitudinal and transverse loading orientations, bone lamellae was found influenced the microcrack paths. The microcracking process involved high densities of sub-lamellar cracks forming cross-hatched patterns. Those cracks consisted of fine cracks (few microns in length) and less than $1 \mu\text{m}$ apart. It was suggested that their regularity and size could result from crack control at the nanostructure level of the mineralized collagen fibrils. Therefore, these findings suggest that fracture resistance in bone is achieved by controlling microcrack development at multiple hierarchical levels [Ebacher et al., 2012].

1.5.1.2. Damage and crack formation in trabecular bone

Damage of trabecular bone is a mixture of microcracking, diffuse damage and fractured trabeculae [Wolfram et al., 2011]. Using high-speed photography technique, it was shown that when trabecular bone is loaded under compression to the yield region shows whitening, Figure 1.15a. Whitening was previously correlated significantly to microdamage in trabecular bone samples using scanning electron microscopy [Turner et al., 2007] and more recently also in single trabeculae [Jungmann et al., 2011]. The whitening technique was also used to detect microdamage. It was proved that whitening of bone is caused by microdamage [Turner et al., 2007, Jungmann et al., 2011]. This technique is a texture correlation method performed by using high speed photography. Briefly, the whitening is quantified by using texture correlation algorithms. These algorithms define the highest pixel value (laying between 0 and 255) in five consecutive frames prior loading. After load is applied, based on the found brightest pixel, all pixels above the threshold were counted as whitened pixels in each of the subsequent frames. The whitening appears only when the bone has yielded and is

accentuated around large stress concentrators, such as holes and notches (Figures 1.15b and 1.15c).

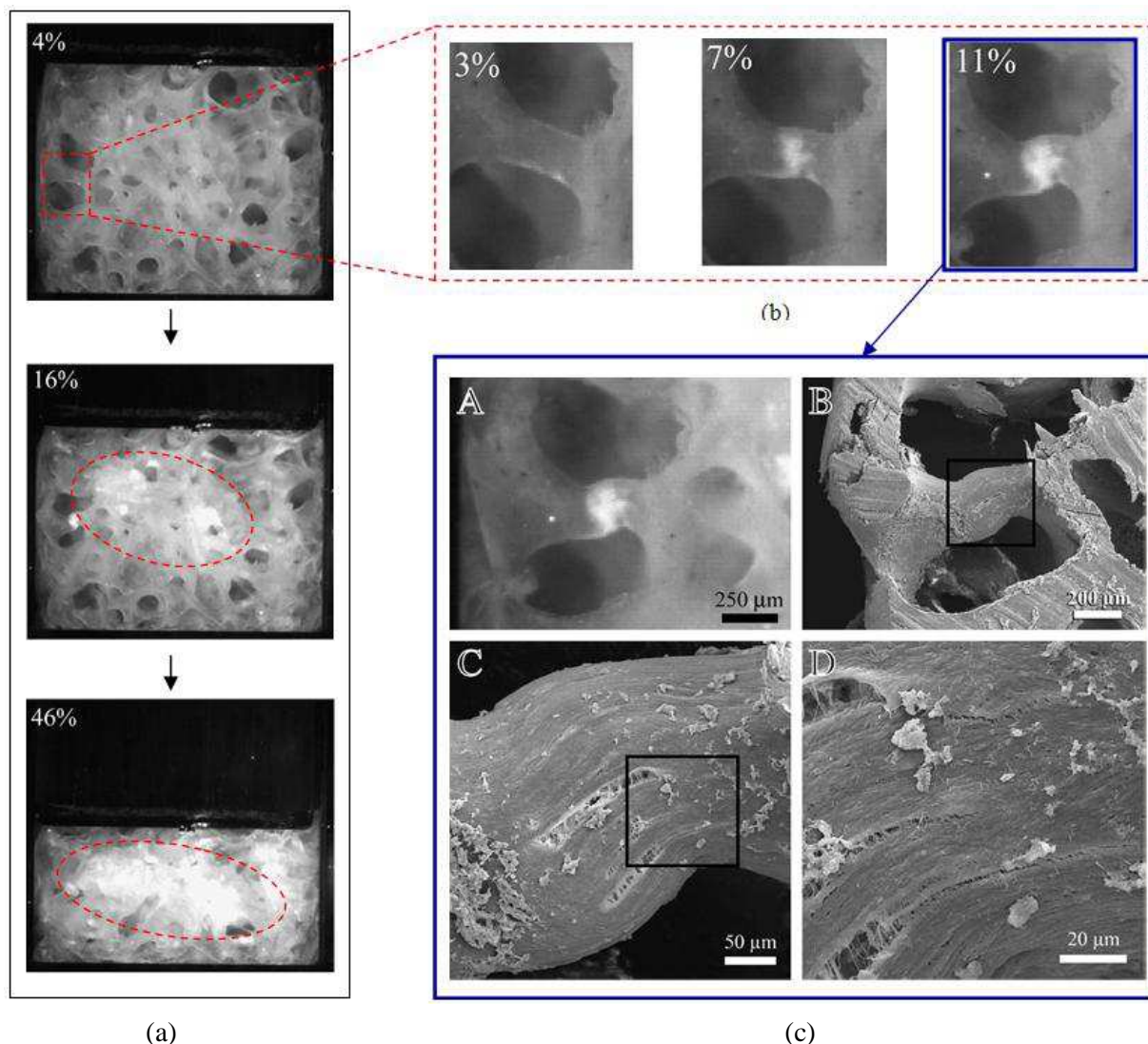


Figure 1.15 Trabecular bone sample under compression: (a) damaged trabeculae corresponding to the whitened region at 4%,16% and 46% strain (b) whitening progression: from the plastic region to failure (c) magnification of microcracks taken by scan electron microscopy corresponds to whitened region [Thurner et al., 2007].

Trabecular damage leads then to the formation of fracture bands or greater regions of fractured trabeculae [Thurner et al., 2006] until overall failure. Physically, bone when loaded emits cracking sounds each corresponding to the release of some energy beyond the yield region. These sounds vanish in the post yield region before appearing again as the final crack spreads through the specimen [Currey, 2002].

1.5.2. Influence of damage on mechanical bone properties

Damage is defined as a permanent change in structure that results in property degradation [Jepsen and Davy, 1997]. Degradation of bone elastic modulus, energy dissipation and strength reduction can be considered as reliable indicators to monitor the damage process in cortical bone. Damage accumulation is a critical component of the fracture process in bone under monotonic [Ziopoulos and Currey, 1994], creep [Fondrk et al., 1988], and fatigue [Carter and Hayes, 1977] load conditions.

Bone can undergo significant modulus degradation before microcracks appear. The implication of this is that the mechanical properties of bone can be significantly compromised even before substantial crack accumulation is observed at the microscopic level. Therefore, the absence of visible damage is not an indication of the mechanical integrity of bone. Inversely, the presence of significant amounts of observable damage when observed in a light microscope is certainly a valid indicator that the strength and stiffness of the bone have been compromised [Burr et al., 1998].

It has been reported that different damage morphologies (diffuse damage or linear microcracks) affect the mechanical properties of bone differently [Diab et al., 2006]. Diffuse damage formation plays a significant role in prolonging the fatigue life of bone and resisting a catastrophic fracture. In contrast, linear microcracks can reduce bone strength and bone stiffness and will gradually lead to failure by accumulation of fatigue damage [Burr et al., 1998].

In a study conducted by Garrison et al. [Garrison et al., 2011] damage was first induced in bovine trabecular bone specimens by either low or high amounts of compressive overloading (2.5 or 4.5% strain, respectively).

Overloading trabecular bone leads to severe loss of stiffness and accumulation of residual strain [Zysset and Curnier, 1996]. Cracks and diffuse damage that accumulate within trabeculae cause reductions in apparent modulus prior to failure of whole trabeculae [Wachtel and Keaveny, 1997]. Trabecular damage ultimately leads to the formation of fracture bands or greater regions of fractured trabeculae [Turner et al., 2006] until overall failure.

1.5.3. Visualization of bone damage

In engineering terms, damage is the result of a process that impairs the mechanical properties of the material. In bone, microdamage has been described referring to microscopic

cracks or microcracks, ultrastructural matrix failure and bone damage at macroscale level.

The presence of damage in vivo may be highlighted by staining techniques using fuchsin. This technique using transmitted light microscopy to represent microcracks by variations in light intensity and depth of focus. Microdamage formation in bone using the staining technique was firstly studied by Frost [Frost, 1960]. The application of fuchsin is a means to differentiate between in vivo formed microcracks from ex vivo sample preparation. This has been the dominant technique over the years for detecting microdamage in bone [Burr et al., 1985, Burr and Stafford, 1990, Norman and Wang, 1997]. Figure 1.16 shows a typical fuchsin stained micrograph from Lee et al. [Lee et al., 2003].

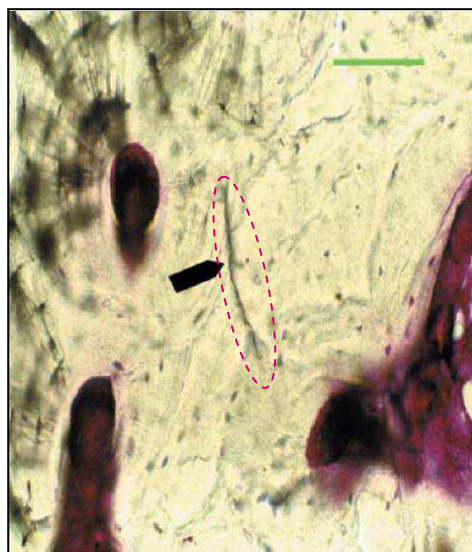


Figure 1.16 Fuchsin-stained microcracks in cortical bone, scale bar = 50 μm [Lee et al., 2003].

Another staining technique using heavy metals (lead-uranyl acetate) has been developed by Schaffler et al. [Schaffler et al., 1994] and permits to visualize bone microdamage by either light microscopy or scanning electron microscopy. Variants of the staining technique have been introduced such as epifluorescence microscopy [Lee et al., 1998] or laser scanning confocal microscopy (LSCM) [Ziopoulos, 2001]. This allows easier crack identification [Lee et al., 1998], sequential labeling with various chelating agents to monitor crack propagation [Lee et al., 2000].

The visualization of bone microdamage permits to classify it into three morphological categories: (a) Linear damage including: single crack and parallel cracks, (b) diffuse (crosshatch) damage including: equal crosshatching and large area distribution, (c) severe

damage including: one primary crack with minor secondary cracks and through-thickness cracks [O'Neal et al., 2010]. Figure 1.17 shows these three categories.

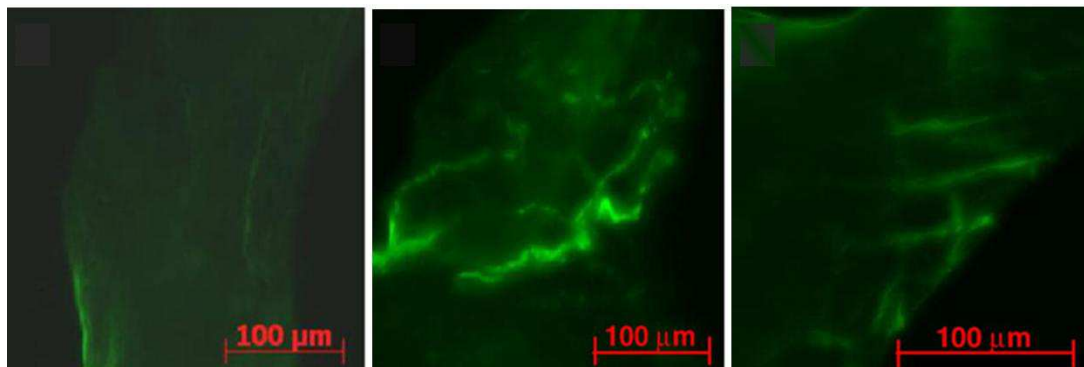


Figure 1.17 Microdamage description and classification in trabecular bone: (a) Linear damage (b) diffuse damage (c) Severe damage [O'Neal et al., 2010].

The linear microcracks are identified as individual, sharply defined cracks, while diffuse damage is an array of cracks [O'Neal et al., 2010].

1.5.4. Damage measurement

Damage is the formation of small cracks in the bony material which, for some reason, do not join to form large fatal cracks [Zioupou and Currey, 1994]. The damaged area in bone is quantifiable by one or several of the following parameters: the number of microcracks, mean crack length and calculating the percentage of damaged area [Burr et al., 1998].

Areas of damage can likewise be observed microscopically. Diffuse damage appears as stained regions with irregular borders under ultraviolet epifluorescence microscopy [Fyhrie and Schaffler, 1994]. Experimentally, diffuse damage is assessed by dehydrating the tested specimens in ethanol and subsequent embedding in transparent methacrylate (MMA) under vacuum. Thick sections of approximately 200 μm are cut. The surfaces are subjected to a polishing process using progressively finer abrasive papers. Finally, each section is mounted on glass slides using Eukitt's mounting medium [Wang and Nieber, 2006].

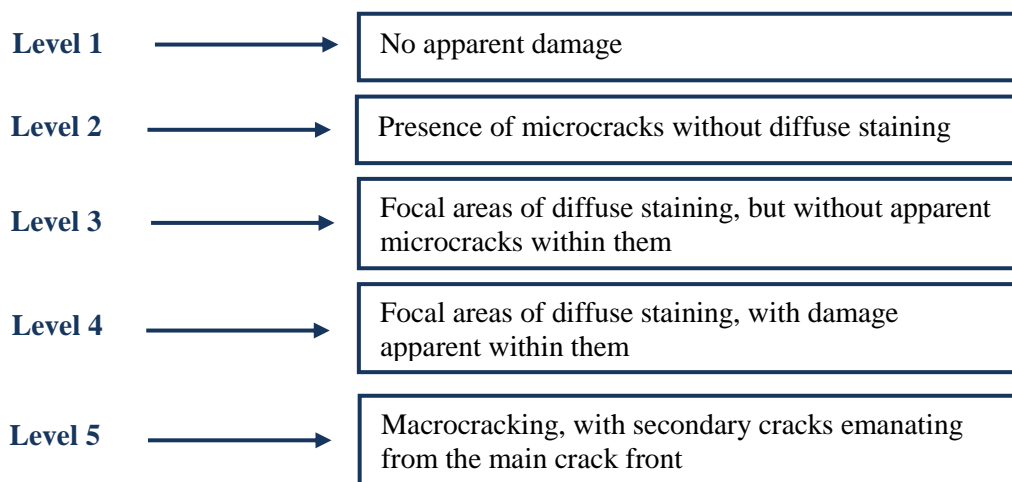
Conventionally, the individual cracks in the damaged zone are counted or the percentage area of the damaged zone is measured in all loaded or nonloaded specimens. This can be achieved by point counting using a (1cm \times 1cm) intraocular grid [Burr et al., 1998]. It can be measured also by a montage of images of thin sections captured using CCD (Charge-Coupled Device) camera [Wang and Nieber, 2006]. In vivo microcracks are distributed throughout the local microstructure, but a preference can be discerned within the bone tissue. They tend to exhibit similar crack lengths regardless of the tissue under examination, see Table 1.3.

Table 1. 3 Microcrack density measurements in vivo [Cowing, 2001].

Source	Section	Crack density (Number/cm ²)	Crack length (μ m)	Reference
Female femur	Transverse	0–500	-	[Schaffler et al.,1995]
Male femur	Transverse	0–300	-	[Schaffler et al.,1995]
Female tibia/femur	Transverse	22.7	2–50	[Norman and Wang al., 1997]
Male tibia/femur	Transverse	15.2	2–50	[Norman and Wang., 1997]
Femoral trabecular	Longitudinal	50–250	-	[Fazzalari et al., 1998]

Whereas the magnitudes of crack density as well as crack length vary greatly between investigators, it is undisputed that one half to two thirds of the total in vivo cracks can be observed in the interstitial bone tissue [Cowin, 2001].

Another qualitative assessment is feasible by classifying damage on a scale ranging from 1 to 5 (Figure 1.18), differentiating the microscopic visible cracks [Schaffler et al., 1994].

**Figure 1. 18** Qualitative assessment of damage evaluation [Schaffler et al., 1994].

Damage accumulation is qualitatively similar between axial and transverse loading directions under compression and tension loads. Generally, damage accumulation for both load cases was higher in the axial direction, including anisotropic damage [Wolfram et al., 2011].

Recently, in vitro, damage accumulation were measured by Wolfram et al., [Wolfram et al., 2011] in order to determine elastic modulus degradation and to investigate whether damage accumulation depends on loading mode and direction. Vertebral trabecular bone specimens were mechanically tested under compression, tension and torsion loading modes. Under compression load, five load steps at a strain rate of 0.2%/s were applied. Ultimate strain steps were ranged from 0.4 % to 4.0 %. Damage was determined as modulus degradation during the load steps (Figure 1.19).

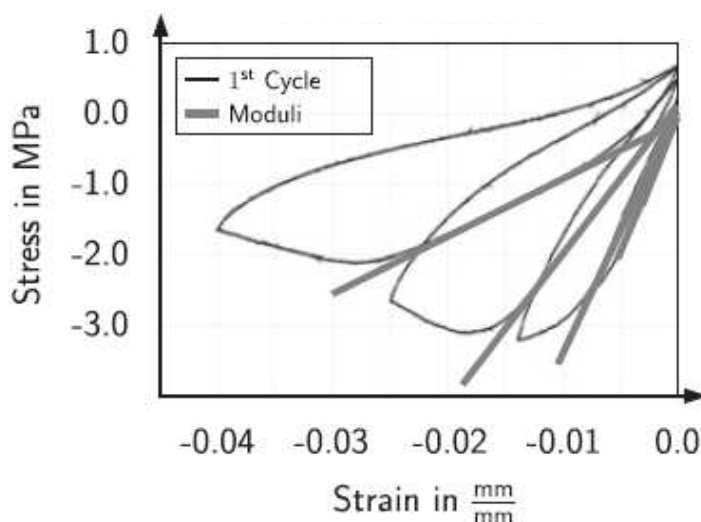


Figure 1.19 Stress–strain curves of trabecular vertebral bone : Moduli devolution in compression [Wolfram et al., 2011].

Apparent moduli were obtained from the stiffest section of the loading part. It was found from this investigation that in both compression and tension, damage in axial direction was higher than in transverse direction indicating an anisotropic damage process.

1.5.5. Influence of loading mode on bone damage

The type of damage formed depends on the imposed loading mode (e.g., tensile, compressive, torsional, bending) and is influenced by the underlying bone microarchitecture. Depending on the mode of loading, damage manifests itself differently. Under tensile load, damage is generated at submicroscales predominantly as a diffuse damage which can be observed, after staining of the bone, by fluorescence. This damage can also occur around microcracks. Under compression loads, damage occurs in the form of rather cracks and microcracks, with a length varying between 10 and 300 μm observable under an optical microscope. Microcracks in the compression zone during bending have generally an elliptical shape, with preferential growth occurring along the longitudinal axis of the bone [O'Brien et al., 2000]. This is not surprising considering the anisotropy of the bone microstructure; indeed, the longitudinal direction has long been known to be the easiest direction for fracture under monotonic loading [Nalla et al., 2003]. Thus, the ease of cracking in this direction appears to be pivotal in fracture and fatigue.

Damage accumulation and residual strains (ε^{RES}) and their dependence on loading mode were investigated in the study of [Wolfram et al., 2011]. Specimens were mechanically loaded in uniaxial compression, tension and torsion in five load steps at a strain rate of 0.2%/s. It was found that damage accumulation seems to be more linear in uniaxial tension (D_{UC}) compared

to uniaxial compression (D_T) and torsion, Figure 1.20. However, under compressive loads, the greatest potential risk of microdamage accumulation in bone is that cracks can begin to coalesce at some threshold, rapidly weakening the tissue and leading to mechanical failure. Although compact bone develops microcracks quite readily within normal ranges of loading, the nature of lamellar organization is limiting microcracks propagation by creating boundaries (primarily cement lines between lamellae) able to arrest cracks [Currey, 2002]. In addition, microcrack damage decreases bone stiffness, in contradiction making the bone less susceptible to further fracturing [Currey, 2002].

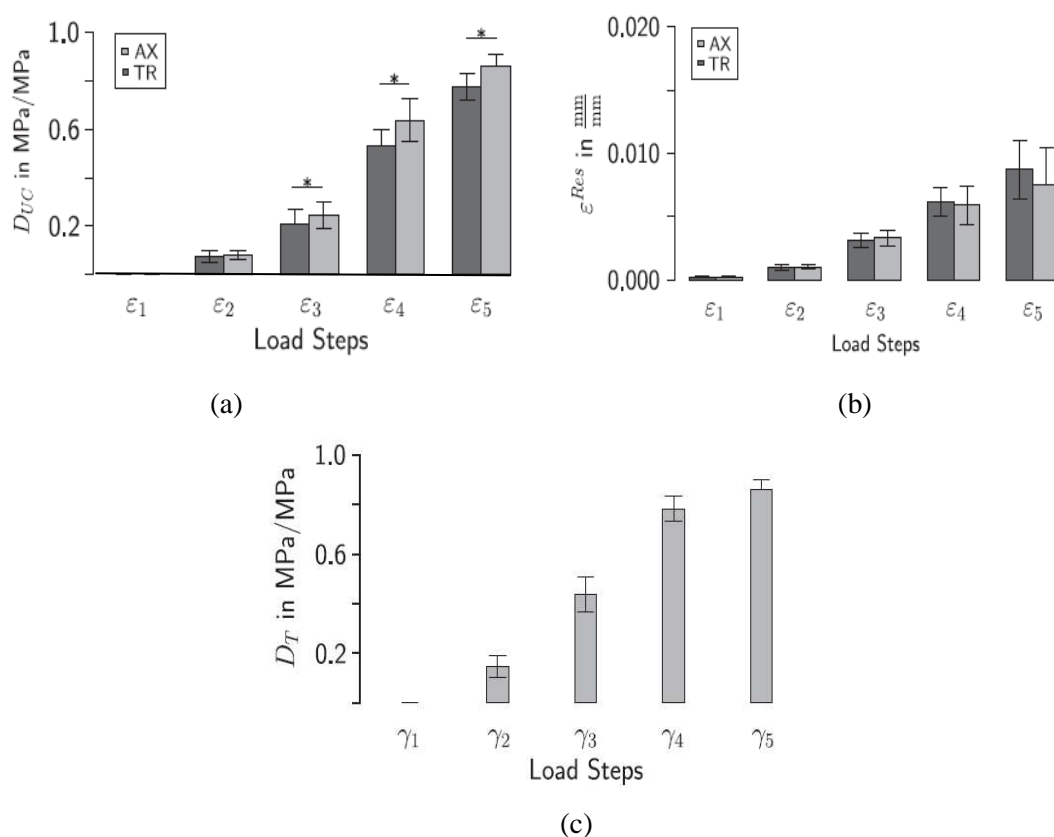


Figure 1. 20 Experimental averaged damage accumulation in human vertebrae trabecular specimens in axial (AX) and transverse (TR) load direction in (a) average damage in tension, (b) residual strains in compression and (c) average damage in torsion [Wolfram et al., 2011].

The formation of microdamage due to compressive and shear loads was studied by Wang and Niebur [Wang and Niebur, 2006] in 14 trabecular bovine tibial bone specimens. The undamaged elastic properties (Young's and shear) moduli of each specimen were measured by loading in compression three times to 0.4% strain, followed by three torsional loads to 0.7% shear strain without any damage. The initial damage was induced by torsional overloading, followed by further damage by an axial compressive overload in order to

simulate subsequent normal loading. Fluorescent agents were used to differentiate specimen damage due to these two loading modes, Figure 1.21.

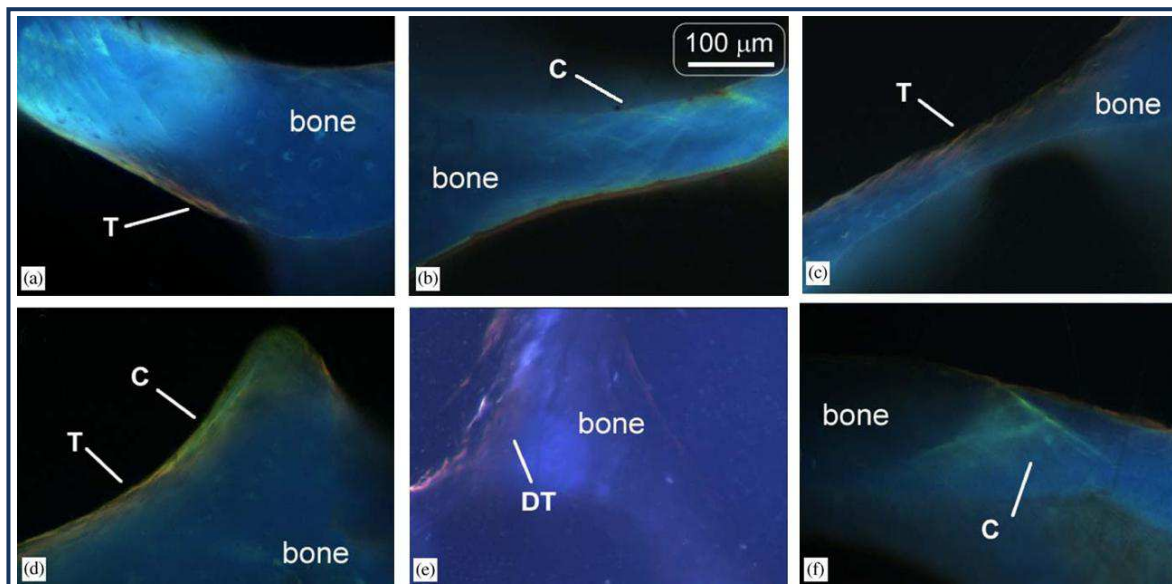


Figure 1. 21 Influence of loading mode on bone damage type (a) single microcrack due to torsion, (b) cross-hatch microcracks due to compression, (c) parallel microcracks due to torsion, (d) propagating microcrack, (e) diffuse damage due to torsion, (f) cross-hatch microcracks due to compression. ‘DT’: Diffuse damage, ‘T’: microcrack due to torsion, and ‘C’: microcrack due to compression [Wang and Niebur, 2006].

It was found that, under compressive loads, the average microcrack density was slightly higher near the center than in the outer region of the tested specimens, while under torsion loads, the diffuse damage area was uniform across the cross-section, Figure 1.22. This may be a result of stress relief in the outer region due to the higher density of pre-existing torsional microcracks and diffuse damage.

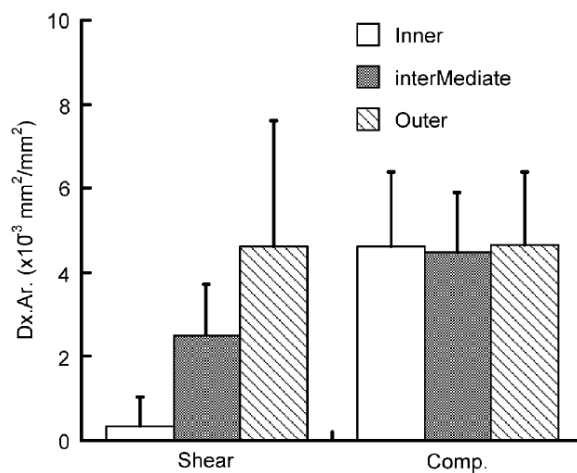


Figure 1. 22 The shear diffuse damage area inside and at the surface due to shear and compressive loads [Wang and Niebur, 2006].

Changes in loading mode can cause propagation of microcracks beyond the microstructural barriers that normally limit the length. In vivo, damage induced under fall loads may propagate during subsequent normal loading, which could affect fracture susceptibility [Wang and Niebur, 2006].

1.5.6. Influence of loading mode on bone fracture

Fracture in quasi brittle materials such as bone occurs as a result of formation of microcracks. Consistent with fracture mechanics theory, it is suggested that bone fails by extensive propagation of a few cracks [Sobelman et al., 2004]. Bone microcracking occurs naturally in vivo [Burr et al., 1985]. Ebacher et al. [Ebacher et al., 2007] studied the crack behavior of human bone during bending of the tibia bone. They contrasted the behavior of human long bones to the ones of standard cortical bone specimens. The macro-scale fracture patterns were compared. It was found that the fracture patterns feature a straight fracture path and run in an oblique direction towards the compressive surface, Figure 1.23.

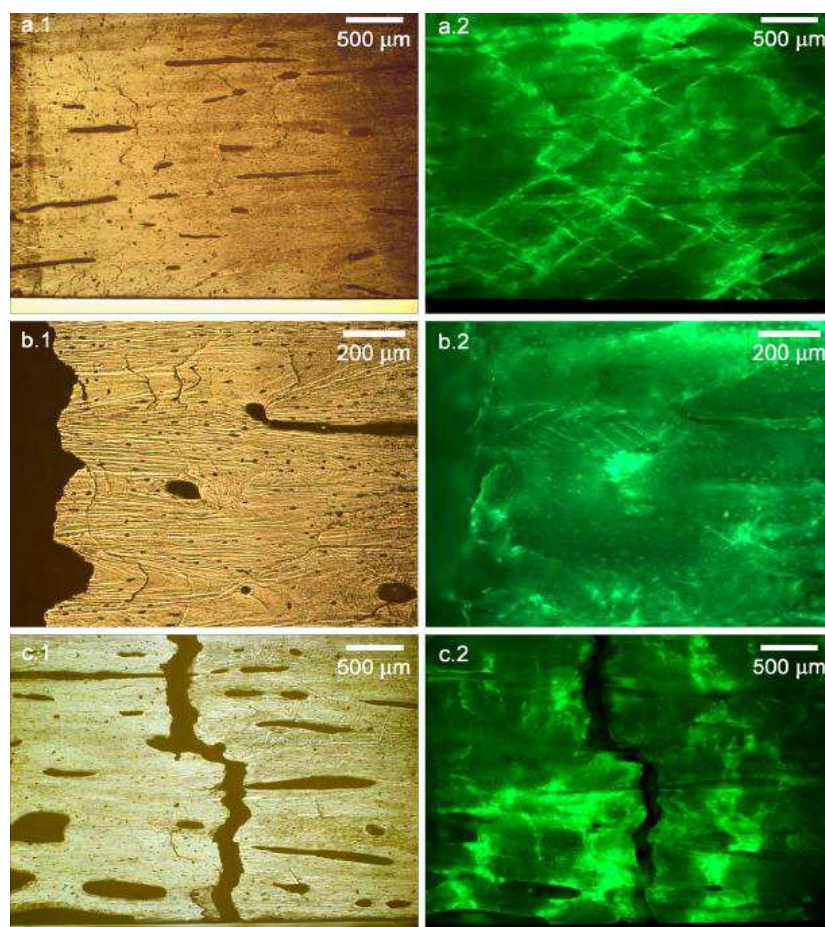


Figure 1. 23 Crack pattern and microdamage morphologies under bright field (left) and epifluorescence (right): (a) compression surface showing cross-hatching microdamage, (b) compression surface showing scale-type microdamage and (c) tensile surface showing diffuse microdamage [Ebacher et al., 2007].

It can be seen from Figure (1.23) that microdamage occurs in the form of either linear microcracks or diffuse damage on the face subjected to tensile loads. At the same time the compression surface shows cross-hatched microdamage. This implies that the type of damage formed depends on the imposed loading mode.

1.5.7. Conclusion

The accumulation of bone microdamage has been proposed as one factor that contributes to increased skeletal fragility with age and that may increase the risk for fracture associated with aging [Burr et al.,1997]. Qualitatively, damage accumulation in bone is independent on site and bone density [Keaveny et al., 1994, Zysset and Curnier, 1996]. Cortical bone shows qualitatively similar damaging behaviour as trabecular bone [Fondrk et al., 1988, Garcia et al., 2009]. The accumulation of bone damage has been absolutely influence the increasing of risk of fracture [Burr et al., 1997, Fyhrie and Schaffler, 1994] and may finally lead to bone failure. In addition, the ability of bone to repair itself leads to damage decreases with age even as bone microdamage increases with age [Burr et al., 1997, Waldorff et al., 2007].

Even though microdamage has unfavorable effects on bone's mechanical properties, under certain conditions, it may also have advantage. For example, microdamage may toughen bone, making it harder to fracture from repetitive loading. A complex net of microcracks has energy absorbing ability which can dissipate stress and slow crack propagation. It is not well clear whether this capability of a microcrack to toughen or embrittle bone may depend on whether toughening is caused by the existing properties like microdamage or by extrinsic means.

However, it is possible that the relatively small increment of damage that may accumulate in bone only becomes significant when added to the bone-weakening effects of reduced bone mass [Burr et al., 1997]. Excessive levels of bone microdamage may play a significant role in maintaining bone structural integrity.

Understanding and finding a relationship between damage properties and bone behaviour is important to understand hip fractures.

Gaining insight into the underlying mechanisms of femur fractures and how these mechanisms are modulated by intrinsic (i.e. damage) as well as extrinsic (e.g. mechanical loading) factors may improve the ability to define fracture risk and develop and assess preventative therapies for femur fractures. The following subsection will review briefly the subject of the fracture of bone with particular emphasis on the femur (the subject of the

current work) with a focus on the neck femoral fracture types. The in vitro modes likely to produce such fractures will be then introduced.

1.6. Femur bone fracture

Femur fracture is the most common orthopedic problem caused by osteoporosis in the elderly [Reginster et al., 1999]. About one fifth of all available orthopaedic beds are occupied by patients with hip fracture. Thus, owing to the progressive aging of populations an estimated 1.7 million hip fractures occurred in the elderly throughout the world in 1990. This problem is expected to double or triple by the year 2040 [Cummings et al., 1990, Kelsey and Hofman, 1987]. A large fraction of these fractures lead to permanent disability and/or death [Cummings et al., 1985, Graves, 1992] and in about 50% of all cases, recovery is not achieved within one year. In France, osteoporosis was recorded by the High Committee on Public Health (HCPH) as one of the fourteen priority public health problems [Vellas et al., 2000]. The World Health Organization also ranked osteoporosis as a major public health concern. The financial burden of osteoporosis is growing rapidly as the population ages. In the USA, an estimated 13.8 billion dollars are spent annually to treat osteoporotic fracture. For acute and long-term treatment of osteoporotic fractures of the proximal femur alone, the cost was estimated to exceed 10 billion dollars annually in the United States.

Understanding the underlying mechanisms of such fractures may help to generate strategies for prevention and treatment. As a result, it has been generally accepted that osteoporosis manifests itself not only in reduced bone mass but also in altered bone quality.

Proximal femur fractures involve the uppermost portion of the femur, just adjacent to the hip joint. From the clinical point of view, risk factors include osteoporosis, a family history of hip fractures, excessive consumption of alcohol, large doses of caffeine, physical inactivity, low body weight, previous hip fracture, the use of certain psychotropic medications, and smoking. Fractures can lead to substantial mortality.

Proximal femoral fracture types are classified as either femoral neck, intertrochanteric, subtrochanteric or diaphyseal fracture [Shane et al., 2010], Figure (1.24 (a)). Femoral neck fractures are divided according to the level of the fracture line in the neck as: subcapital, transcervical and intertrochanteric (basal) fractures, Figure (1.24, (b,c)). Femoral neck fractures account for 60% of the annual worldwide incidence of hip fractures [Basso et al., 2012]. Representative to assess this serious injury in the elderly, this study investigates femoral neck fractures. As a trial to assess this serious injury in the elderly patient, this work takes femoral neck fractures into consideration.

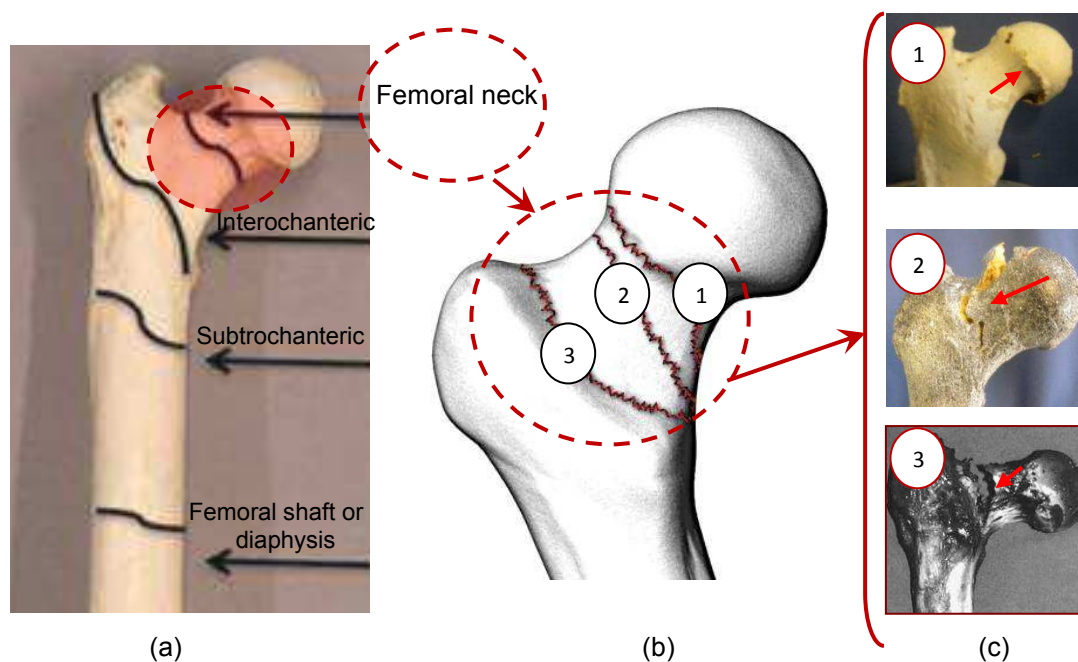


Figure 1.24 Basic femur fracture types: (a) locations of common femur fractures [Shane et al., 2010] (b) neck fracture types: (1) subcapital, (2) transcervical and (3) basicervical fracture [Basso et al., 2012] (c) experimental femur neck fracture types.

Several classification systems have been proposed for fractures of the femoral neck. The Garden classification is the most widely currently used in clinical practice.

1.6.1. Classification of femur neck fractures

As seen previously there are three types of femur neck fractures. The subcapital one is the most recurrent fracture for with several classification systems have been proposed. The Garden classification is the most widely currently used in clinical practice. Garden classification system is categorized into four stages: Garden fracture stage I, Garden fracture stage II, Garden fracture stage III and Garden fracture stage IV. The descriptions of these four types are shown in Table 1.4. These four stages are based on the degree of displacement of the fracture as seen on depicted images.

Table 1. 4 Subcapital femoral neck fractures following Garden's classification.

Fracture type	Description		Radiographic images
Garden fracture stage I	An incomplete subcapital fracture. This type can be explained by the fact that femoral shaft is twisted externally. The trabecular markings in the femoral neck are displaced away from the midline relative to those in the femoral head.		
Garden fracture stage II	A complete, but non displaced, fracture. The femoral neck has moved in such a way as to maintain normal alignment with the femoral head.		
Garden fracture stage III	A complete, partially displaced subcapital fracture. The femoral shaft is externally rotated.		
Garden fracture stage IV	A complete and fully displaced fracture. The femur is externally rotated and superiorly displaced relative to the femoral head. The head is completely detached from the neck.		

Another common classification is the one by Pauwels originating from 1951. The Pauwels classification is related to the shearing angle of the fracture surface [Parker and Dynan, 2011]. Type I describes a valgus¹ impaction of the head of femur, an in itself stable fracture. A Type II fracture by Pauwels describes an oblique fracture line in the anterior posterior plane with angulation of the plane of the fracture between 30° to 50°, Figure 1.25.

¹ A valgus deformity is a term for outward angulations of distal segment of a bone.

These fractures are unstable, at the same time the oblique fracture line provides more stability with osteosynthesis than Pauwels III fractures. Pauwels III or Type III fractures show an inclination of the fractured planes up to 70° to the horizontal [Lein et al., 2011].

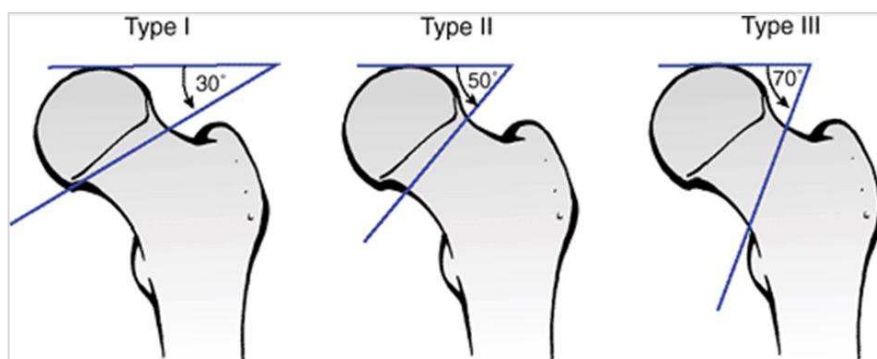


Figure 1.25 Pauwels femoral neck fracture classification [Bucholz et al., 2006].

In these fractures, the cranial fracture line always ends in the transition zone between the cartilage part of the femoral head and the cranial onset of the femoral neck.

1.7. Femur testing

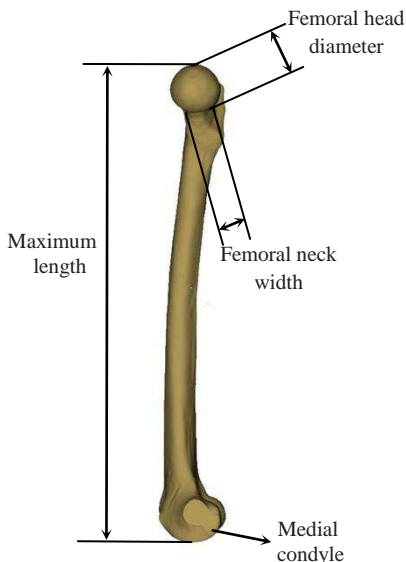
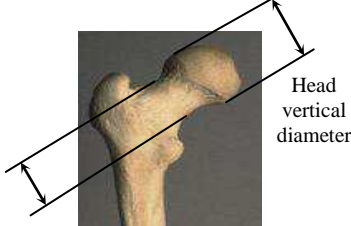
Mechanical testing of femur is a basic method in bone-related research. During normal daily activities, femur structure is subjected to a complex system of loading exerted by the forces of gravity. Depending upon the conditions of application, a force applied can be axial compressive, tensile, torsional or bending. Strain distribution found in biomechanical experiments is dependent on the choice of biomechanical setup [Basso et al., 2012].

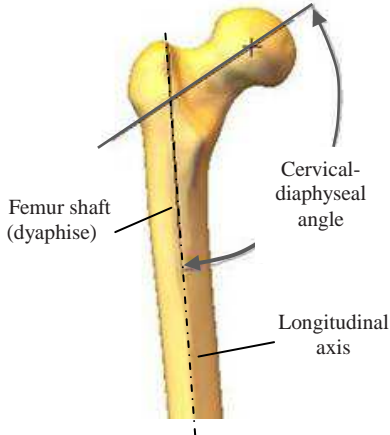
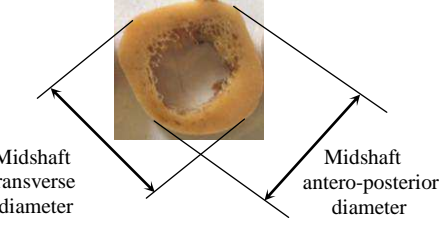
In vitro, in order to reproduce femur neck fractures, jig fixtures are most often employed. The simplest setup consists of a fixed distal diaphysis with a head-enclosing device to mimic the acetabulum. To design a jig fixture to reproduce bone fracture i.e. femur neck fracture, femur geometry, dimensions and femur fracture types should be identified. In the following subsection, a brief description of the femur geometry and dimensions will be presented.

1.7.1. Human femur geometry

Knowledge of bone shape is important as it has been established that mechanical loading may cause changes in bone strength through geometric adaptations, with little change in BMD. Several studies have suggested that factors other than bone mineral density (BMD) may also be important in hip fracture occurrence. One of these factors is the structural geometry of the proximal femur. Table 1.5 defines the different geometrical parameters of the femur. All these geometrical characteristics have an impact on the mechanical strength of the proximal femur [Alonso et al., 2000].

Table 1. 5 Illustrative diagrams showing the human femur Anthropometry.

Human femur anthropometry	Definition	Illustrative diagram
Maximum length	Maximum length from the head of the femur to the medial condyle	 <p>The diagram shows a lateral view of a human femur. A vertical double-headed arrow on the left indicates the 'Maximum length' from the top of the femoral head to the bottom of the medial condyle. A horizontal double-headed arrow at the top indicates the 'Femoral head diameter'. A horizontal double-headed arrow at the neck indicates the 'Femoral neck width'. An arrow points to the 'Medial condyle' at the bottom.</p>
Femoral head diameter	Maximum anteroposterior diameter of the head of the femur	
Femoral neck width	Minimum diameter of the neck of the femur at the anteroposterior direction	
Trochanter length	Maximum length from the tip of the greater trochanter of the femur to the lateral condyle	
Femoral neck axis length	Maximum width between the head of the femur and the greater trochanter	
Midshaft circumference	A tape followed the contour of the midshaft point of the body of the femur	
Distal breadth	Maximum width between the epicondyles of the femur	
Femoral head diameter	Maximum vertical diameter of the femoral head	 <p>The diagram shows a lateral view of a human femur. A vertical double-headed arrow indicates the 'Head vertical diameter'. A vertical double-headed arrow at the neck indicates the 'Neck vertical diameter'.</p>
Neck vertical diameter	Minimum diameter of the neck of the femur	

Cervical-diaphyseal angle	The angle between the longitudinal axis of the neck and the longitudinal axis of the femur shaft (diaphyse)	
Midshaft antero-posterior diameter	minimum antero-posterior diameter at the middle of the shaft of the femur	
Midshaft transverse diameter	Minimum transverse diameter at the middle of the shaft (perimeter at the middle)	

Ziylan and Murshid [Ziylan and Murshid, 2002] compiled measured data from 72 human adult femora (36 right and 36 left) in order to obtain osteometric data to estimate the bilateral differences between the right and left bones. Their results are tabulated in Table 1.6.

Table 1. 6 Measurements of the femoral anthropometrics-dimensions [Ziylan and Murshid, 2002].

Geometric parameter	Left femur (mm)	Right femur (mm)
Maximum length	428.4 ± 24.9	416.8 ± 68.6
Trochanter length	405.4 ± 22.9	402.6 ± 28.1
Collo-diaphyseal angle	128.7 ± 4.7	127.6 ± 3.3
Proximal breadth	90.1 ± 7.0	90.2 ± 7.6
Head vertical diameter	43.4 ± 3.2	45.2 ± 4.0
Head transverse diameter	44.3 ± 3.3	44.7 ± 4.1
Neck vertical diameter	30.6 ± 3.0	30.7 ± 3.6
Neck transverse diameter	25.5 ± 2.7	26.3 ± 3.1
Midshaft circumference	87.2 ± 7.6	86.2 ± 6.5
Midshaft antero-posterior diameter	26.8 ± 3.0	27.1 ± 3.0
Midshaft transverse diameter	26.8 ± 2.4	26.4 ± 2.4
Distal breadth	77.3 ± 5.2	76.8 ± 5.9

The statistical analysis of all measured parameters showed no significant differences between the right and left femora except for the maximum length where the standard deviation of the right femurs is about 2.5 times the maximum length of the left femurs. The

slight difference between other geometric parameters between left and right femurs will be disregarded in the current work.

1.7.2. Loading modes

Testing methods such as compression, tensile, bending and torsion tests can be applied in order to establish the mechanical behavior of bone. In order to assess the tolerance limits of bones, it is important to determine their failure behavior under these loading conditions. In vitro, mechanical testing of bone is often used on cadaveric human as well as on animal one. It leads to destruction of the bone to reach the failure point. If we consider the case of stance phase, the femur is loaded predominately in compression [Taylor et al., 1995]. Therefore, the compression test can be considered one of the most common tests to represent such configuration.

Using the concept of compression test conditions, several methods have been developed to measure the mechanical behavior of bone at a variety of different sites. Such tests help to assess hip fractures associated with osteoporosis [Cowan, 2001].

In order to measure femoral neck strength, the proximal end of the femur is mounted in a loading assembly by fixing its distal part. The Force (F) is then applied to the head until the femoral neck fractures.

Two common loading configurations are applied, axial compression load to simulate the single limb stance configuration (Figure 1.26a) or the femur is positioned to simulate fall configuration position (Figure 1.26b).

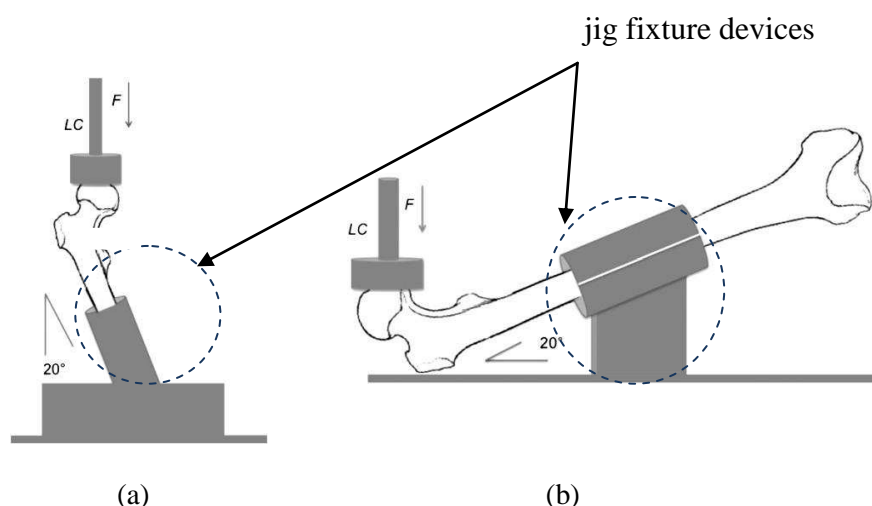


Figure 1. 26 Typical mechanical tests of the femoral neck (a) Single limb stance loading configuration (b) Sideway fall configuration [Van der Steenhoven et al., 2012].

The main objectives were taken into consideration in the current work is to assess the femoral neck fracture under one-legged stance loads: this evaluation is necessary to study the

incidence of spontaneous fractures [Cristofolini et al., 2007], the behavior of the hip during daily activities [Juszczak et al., 2011].

In the single limb stance configuration (Figure 1.27a), the inclination of the Force (F) is varied depending on the test conditions. During walking and stand positions, the resultant joint load vector (F) makes a femoral neck angle of 16° to the vertical [Delaere et al., 1989] plus 3° offset of the femoral shaft axis from the sagittal plane [Hollister et al., 1993, Sermon et al., 2012], (Figures 1.27a and 1.27b).

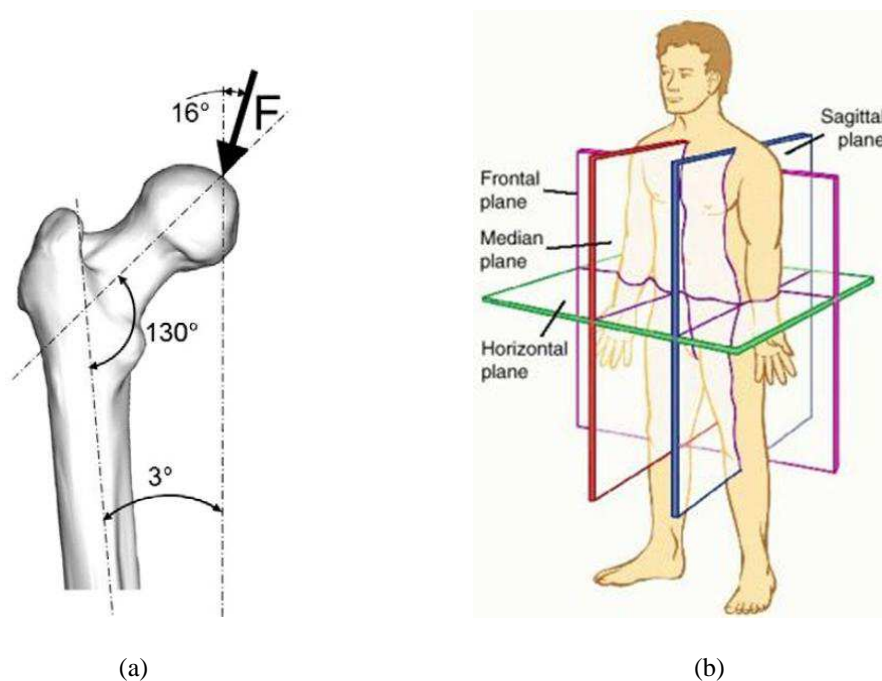


Figure 1.27 Force introduction at the proximal femur: (a) illustration of the force at the proximal femur according to sagittal planes [Sermon et al., 2012] (b) vertical planes passing through the body parallel to the median plane (or to the sagittal plane), dividing the body into left and right portions. Source: <http://medical-dictionary.tfd.com/plane>

The orientation of this loading angle is another important factor which can affect the structural capacity of the proximal femur and consequently can help to determine an accurate factor of risk [Pinilla et al., 1996]. Several numerical and in vitro investigation have been attempted to simulate femur fractures under single limb stance configuration. The direction of the applied load on the proximal femoral head ranges between 0° [Lochmüller et al., 1998], 11° [Link et al., 2003], 20° [Keyak et al., 1998, Hambli et al., 2012], 24° [Smith et al., 1992], and 25° [Cody et al., 1999] with vertical axis in the frontal plane.

In the current study, as will be presented later in chapter (4), an angle of 20° will be taken into consideration.

1.8. Conclusion

This introductory chapter has reiterated general knowledge about human bone structure and its mechanical behavior at macroscopic scale. Structural and microstructural bone damage is reviewed. This chapter highlights the richness and complexity of human bone as well as the difficulty to predict its failure mechanisms due to the different factors which influence significantly its ultimate failure values. We focused on the femur bone principally the neck femoral due to its frequent fractures related to osteoporosis. Damage accumulation process under a general loading history was presented.

Understanding hip fractures becomes increasingly important goal for both clinicians and biomedical researchers trying to evaluate the risk of neck femur fracture. Modeling the fracture behavior of bone will help researchers find proper treatments to strengthen the bone in order to prevent such fractures.

Finite element analysis has been proven to be a useful method for studying the mechanical characteristics of hip fracture. Nonlinear FE analysis that incorporates two-dimensional and three-dimensional geometry has been shown to be a useful method to predict hip fracture under given boundary conditions (single limb stance, side fall) with reasonable accuracy. A review on the simulation of femur damage and fracture will be the subject of our next chapter.

Chapter 2

Review on finite element models to predict damage and fracture of bone

Abstract

Finite element analysis has been shown to be a useful method, with reasonable accuracy, to predict hip fracture under given boundary conditions of the single limb stance configuration. The literature review on 2D and 3D FE models show that there are three different approaches to predict femur bone fracture: uncoupled fracture criteria, fracture mechanics based models and finite element simulation using the continuum damage mechanics (CDM). This review of the literature shows that despite the progress in the field of bone fracture simulation under monotonic load, there is still a lack of models that permit to give an accurate prediction of the fracture profile and the propagation path of the fracture from the beginning till the total separation of bone. In the current chapter a review on each approach will be presented.

Résumé

La simulation par éléments finis (EF) s'est révélée être une méthode utile pour prédire la fracture de la tête fémorale, avec une précision raisonnable, en configuration monopodal sous des conditions aux limites données. L'état de l'art, sur les modèles EF en 2D et 3D, montre l'existence de trois approches différentes pour la prédiction de la fracture: Modèles basés sur des critères de rupture non couplés, modèles basés sur la mécanique de la rupture et modèles basées sur l'utilisation de la mécanique de l'endommagement des milieux continus (CDM). Cette revue de la littérature montre que, malgré les progrès réalisés dans le domaine de la simulation de la fracture osseuse sous charge monotone, il existe encore un manque de modèles qui permettent de prédire le profil de fracture et la propagation de fissure du début jusqu'à la séparation totale de l'os. Dans le chapitre en cours un examen de chaque approche sera présenté.

2.1. Introduction

This chapter concentrates on a review of the relevant literature concerning the Finite Element (FE) simulation of human femur. Firstly, a review of FE simulation of femur bone fracture will be introduced. Secondly, the different approaches used to predict femur bone fracture will be presented. Finally, FE used Continuum Damage Mechanics (CDM) will be reviewed and discussed. Limitations and drawbacks will be introduced.

2.2. Finite element simulation of femur bone fracture

Over the last years, a large number of 2D and 3D FE models have been developed to predict proximal femur fracture. In the recent past, in order to develop more sophisticated prediction of femoral fracture load, investigators proposed 2D mesh-based Geometry FE models using DXA or CT scans [Bettamer et al., 2011, Buijs and Dragomir-Daescu, 2011, Hambli et al., 2012, Testi et al., 1999, Testi et al., 2004] or from stereoradiographic reconstruction technique which allow obtaining 3D femur geometry from 2D contours identified on biplanar radiographs [Laporte et al., 2003, Le Bras et al., 2003] or by using 3D mesh-based Voxel FE models [Cody et al., 1999, Keyak et al., 1999, Keyak et al., 2001, Keyak et al., 2005, Orwoll et al., 2009, Viceconti et al., 1998] or 3D mesh-based Geometry from CT scans [Bessho et al., 2007, Ford et al., 1996, Hambli, 2012, Lotz et al., 1991a, Lotz et al., 1991b, Merz et al., 1996, Ota et al., 1999, Trabelsi and Yosibash, 2011] or (see Table 2.1). In these investigations, the load applied an equal and opposite force to femoral head in single limb stance to represent daily spontaneous fracture and on the lateral greater trochanter, to represent the posterolateral and sideways (lateral) falls on the ground.

Based on DXA, 2D mesh-based geometry, FE models were developed to predict the femoral neck fracture under fall configuration with respect to bone mineral density using homogenous [Hambli et al., 2012, Testi et al., 1999] or heterogeneous [Testi et al., 2004] mechanical properties of cortical and trabecular femur bone. However, the effect of the impact conditions i.e. impact loading velocity, impact loading directions and mean energy absorbed on the modulus of elasticity has to be experimentally verified.

Based on CT scans, a validated 2D mesh-based geometry FE model of human proximal femur was developed in order to estimate patient bone stiffness and strength [Buijs and Dragomir-Daescu, 2011]. The model succeeded to predict 70% of hip fracture pattern

under the assumption that the stresses during a fall lie principally in the coronal plane of the hip. Using the same mesh-base geometry, 3D FE modeling was proposed to predict stress distributions for one-legged stance (see Table 2.1) and for a fall to the lateral greater trochanter using linear and nonlinear bone material properties [Lotz et al., 1991a, Lotz et al., 1991b]. It was reported that the load at fracture was rather accurately predicted for the two tested specimens.

In order to predict fracture load in both single limb stance and sideway fall configuration, linear FE models were applied under quasi-static force on femoral head [Keyak et al., 1998]. Their models can predict femoral fracture load to within a precision of (-40% to +60%) compared to that of densitometry (with 95% confidence). The location of the fracture was correct in 13 cases out of 18 in the single limb stance simulation, and in 10 cases out of 15 in sideways fall. They modified these models to predict that the femoral fracture location by using nonlinear behavior of bone [Keyak et al., 2001]. They found that the location of 15 out of 18 fractures was correctly predicted and localized. However, the numerical value of the fracture force in these models deviates from the experimentally obtained one (F_{exp} , (N) = $0.77 F_{\text{Numerical}} + 1150$ (N)). Table 2.1 resumed some of the recent developed works of femur fracture simulation under single limb stance configuration.

Table 2. 1 FE modeling of human proximal femur under single limb stance configuration.

Reference	The assumption of bone behavior	Number of specimens	Mesh		Orthotropic direction assignment	fracture criteria	Fracture pattern validation	Assigned mechanical properties	Empirical equations	Validated experimentally
			Mesh type	Imaging modality						
Taylor, 2002	Heterogeneous Orthotropic Elastic	1	3D geometry based	CT scan	Methods using anatomical directions corresponding to the bone shape.	Elastic region	No	Empirical relation between density and material properties	$E_{1,i} = E_{1,max} \frac{\rho_{app,i}^2}{\rho_{app,max}^2}^*$ $E_{2,i} = E_{2,max} \frac{\rho_{app,i}^2}{\rho_{app,max}^2}$ $E_{3,i} = E_{3,max} \frac{\rho_{app,i}^2}{\rho_{app,max}^2}$ $G_{12,i} = G_{12,max} \frac{\rho_{app,i}^2}{\rho_{app,max}^2}$ $G_{13,i} = G_{13,max} \frac{\rho_{app,i}^2}{\rho_{app,max}^2}$ $G_{23,i} = G_{23,max} \frac{\rho_{app,i}^2}{\rho_{app,max}^2}$	No
Keyak and Falkinstein, 2003	Heterogeneous Isotropic Elastic plastic	2	3D voxel	CT scan	Isotropic	Uncoupled fracture criteria : Distortion energy failure theory	No	Empirical relation between density and material properties	$E_{Cort} = 10200 \rho_{ash}^{2.01*}$ $E_{Trab} = 33900 \rho_{ash}^{2.20}$ $E_{Trab/Cort} = 5307 \rho_{ash} + 469$	Yes
Keyak et al., 2005	Heterogeneous Isotropic Elastic plastic	26	3D voxel	CT scan	Isotropic	Uncoupled fracture criteria	No	Empirical relation between density and material properties	$E_{Cort} = 10200 \rho_{ash}^{2.01*}$ $E_{Trab} = 33900 \rho_{ash}^{2.20}$ $E_{Trab/Cort} = 5307 \rho_{ash} + 469$	Yes
Bessho et al., 2007	Heterogeneous Isotropic Elastic plastic	42	3D geometry based	CT scan	Isotropic	Uncoupled fracture criteria: maximum principal stress	No	Empirical relation between density and material properties	$E_{Cort} = 10200 \rho_{ash}^{2.01*}$ $E_{Trab} = 33900 \rho_{ash}^{2.20}$ $E_{Trab/Cort} = 5307 \rho_{ash} + 469$	yes

Schileo et al., 2007	Heterogeneous Isotropic Elastic plastic	8	3D geometry based	DXA	Isotropic	Uncoupled fracture criteria	No	Empirical relation between density and material properties	Three different laws were implemented : $E = 3.790 \rho_{app}^3$ * $E = 10.500 \rho_{ash}^{2.29}$ $E = 6.950 \rho_{app}^{1.49}$ $\frac{\rho_{ash}}{\rho_{app}} = 0.6$	yes
Yosibash et al., 2007	Heterogeneous Isotropic Elastic	1	3D geometry based	CT scan	Isotropic	Elastic region	No	Empirical relation between density and material properties	$E_{Cort} = 10200 \rho_{ash}^{2.01}$ * $E_{Trab} = 33900 \rho_{ash}^{2.20}$ $E_{Trab/Cort} = 5307 \rho_{ash} + 469$	Yes
Schileo et al., 2008	Heterogeneous Isotropic Quasi-brittle	3	3D geometry based	CT scan	Isotropic	Uncoupled fracture criteria: maximum principal strain theory		Empirical relation between density and material properties	$E = 6.950 \rho_{app}^{1.49}$	No
Baca et al., 2008	Homogenous Isotropic, Elastic Heterogeneous Isotropic, Elastic Heterogeneous Orthotropic, Elastic	1	3D geometry based	CT scan	Variation of the CT Hounsfield unit values	Uncoupled fracture criteria	No	Empirical relation between density and material properties	<u>For isotropic simulation:</u> $E_{Cort} = 2065 \rho^{3.09}$, $\nu_{Cort} = 0.3$, $E_{Trab} = 1904 \rho^{1.64}$, $\nu_{Trab} = 0.3$ <u>For orthotropic simulation:</u> $E_{1(Cort)} = 2314 \rho^{1.57}$, $E_{2(Cort)} = 2314 \rho^{1.57}$, $E_{3(Cort)} = 2065 \rho^{3.09}$ $E_{1(Trab)} = 1157 \rho^{1.78}$, $E_{2(Trab)} = 1157 \rho^{1.78}$, $E_{3(Trab)} = 1904 \rho^{1.64}$ $G_{12} = G_{12,max} \frac{\rho^2}{\rho_{max}^2}$, $G_{23} = G_{23,max} \frac{\rho^2}{\rho_{max}^2}$ $G_{31} = G_{31,max} \frac{\rho^2}{\rho_{max}^2}$ $\nu_{12} = 0.4$, $\nu_{23} = 0.25$, $\nu_{31} = 0.25$	No

Keyak et al., 2009	Heterogeneous isotropic Elastic plastic	13	3D voxel	CT scan	Isotropic	Uncoupled fracture criteria	No	Empirical relation between density and material properties	$E = 14900 \rho_{ash}^{1.86}$, $S = 102 \rho_{ash}^{1.80}$ $\rho_{ash} = 0.0633 + 0.887 \rho_{QCT}$	No
Orwall et al., 2009	Heterogeneous Isotropic Elastic- plastic	51	3D voxel	CT scan	Isotropic	Uncoupled fracture criteria	No	Empirical relation between density and material properties	NA	No
Tanck et al., 2009	Heterogeneous Isotropic Elastic plastic	10	3D voxel	CT scan	Isotropic	Uncoupled fracture criteria	yes	Empirical relation between density and material properties	$E = 14900 \rho_{ash}^{1.86}$, $S = 102 \rho_{ash}^{1.80}$ $\rho_{ash} = 0.0633 + 0.887 \rho_{QCT}$	yes
Yang et al., 2010	Heterogeneous Isotropic Elastic Heterogeneous Orthotropic Elastic	1	3D voxel	CT scan	Methods using anatomical directions corresponding to the bone shape	Elastic region	No	Empirical relation between density and material properties	$E_{Cort} = 2065 \rho^{3.09}$, $\nu = 0.3$, $G = \frac{E}{2(1 + \nu)}$ $E_{Trab} = 1904 \rho^{1.64}$, $\nu = 0.3$, $G = \frac{E}{2(1 + \nu)}$	No
Trabelsi and Yosibash, 2011	Heterogeneous Orthotropic Elastic	4	3D geometry based	CT scan	Methods using anatomical directions corresponding to the bone shape	Elastic region	No	Empirical relation between density and material properties	$E_{Cort} = 10200 \rho_{ash}^{2.01*}$ $E_{Trab} = 33900 \rho_{ash}^{2.20}$ $E_{Trab/Cort} = 5307 \rho_{ash} + 469$	yes

Testi et al., 1999	homogenous Isotropic	1	2D geometry based	DXA	Isotropic	Uncoupled fracture criteria	No	Isotropic properties were assigned from the literature	$E = 14200 \text{ MPa}$ $\nu = 0.3$	Yes
Rudman et al., 2006	homogenous trabecular and homogenous cortical Isotropic	1	2D geometry based	DXA	Isotropic	Elastic region	No	Isotropic properties were assigned from the literature	$E_{Cort} = 17 \text{ GPa}$ $E_{Trab} = 40 \text{ MPa}$	No
Khanoki and Pasini, 2013	heterogeneous Isotropic	1	2D geometry based	CT scan	Isotropic	Uncoupled fracture criteria	No	Empirical relation between density and material properties	$E_{Cort} = 2065 \rho^{3.09}$, $\nu = 0.3$, $G = \frac{E}{2(1 + \nu)}$ $E_{Trab} = 1904 \rho^{1.64}$, $\nu = 0.3$, $G = \frac{E}{2(1 + \nu)}$	No

i: refers to the principal three directions, E_{Cort} : Young modulus of cortical bone, E_{Trab} : Young modulus of trabecular bone, heterogeneous: elements of cortical or trabecular bones are defined each by its density, homogenous: the lattice work structure of the trabecular and cortical bone are assumed to be identical material. NA: the empirical equations were not available in the corresponding reference. ρ_{ash} : ash density. ρ_{app} : apparent density.

As shown in Table 2.1 femur bone was considered in the recent investigations as heterogeneous structure consisting of two types of material: cortical and trabecular bone [Bessho et al., 2007, Yang et al., 2010, Trabelsi and Yosibash, 2011]. These differences between the properties of the trabecular and cortical bone contribute to the anisotropy, orthotropy or the isotropy of bone material assignment [Reilly and Burstein, 1975]. Even though, some investigations were based on only one specimen [Baca et al., 2008, Rudman et al., 2006, Taylor, 2002, Yosibash et al., 2007,] or several specimens [Bessho et al., 2007, Keyak et al., 2005]. This review of studies on the FE method of the proximal femur confirms its capability to arrive more or less relevant results.

However, three different approaches exist to predict femur bone fracture:

- At macrostructure level (as an organ): uncoupled fracture criteria for example [keyak et al., 2005, Schileo et al., 2008, Orwall et al., 2009, Baca et al., 2008] and fracture mechanics based models approaches, for example [Malik et al., 2003, Nalla et al., 2005, Ural et al., 2006, Ural et al., 2007].
- At mesostructure level: CDM approach models, for example [Zysset and Curnier, 1996, Garcia et al., 2009, Keaveny et al., 1999].

In the next section we will try to details these three different approaches.

2.2.1. Finite element simulation of femur fracture using uncoupled fracture criteria

Different mechanical approaches based on uncoupled (i.e. not coupled with damage) fracture criteria were proposed when the fracture of proximal femur is simulated. Keyak and Rossi [Keyak and Rossi, 2000] tried to assess the performance of nine fracture stress- and strain-based non coupled failure theories. The following fracture criteria were evaluated: von Mises distortion energy, Hoffman (H_σ) and a strain-based Hoffman analog (H_ϵ), maximum normal stress (σ_{max}), maximum normal strain (ϵ_{max}), maximum shear strain (γ_{max}), maximum shear stress, Coulomb-Mohr (CM), and modified Mohr (MM). Their investigation was based on the CT scan-based FE models of the proximal femur. The applicability was assessed by correlating the FE load at fracture for each failure theories and loading conditions with the femoral fracture load obtained experimentally. It was found in their investigation that the performance of the maximum shear stress and the distortion energy failure theories were superior and could interpret the femur failure due to shearing or distortion of the material. Experimental and simulated fracture loads were significantly correlated for both

used, the von Mises criterion is considered as one of the most accurate criteria for predicting the fracture location of proximal femur [Keyak and Rossi, 1983]. This theory provides the best agreement between experiment and numerics. In addition this theory gives the same results as the octahedral shear stress theory.

Tsai and Wu [Tsai and Wu, 1971] developed a quadratic failure criterion for anisotropic materials which was equally applicable for transversely isotropic materials in its reduced form. This theory could be applied to bone but with some modifications. In fact, Keaveny et al. [Keaveny et al., 1999] used this criterion as a function of apparent density and they applied it to 139 bovine tibial trabecular bone. However, this criterion requires to determine twelve constants to describe the failure behavior of an orthotropic material, and the values of the majority of these are unknown [Keyak and Rossi, 2000].

2.2.2. Finite element simulation using fracture mechanics

Fracture mechanics combines applied stress, fracture toughness, and the fracture process zone response to determine the crack initiation and crack propagation in a material [Vashisth et al., 1997]. Recently, several authors investigated the fracture of cortical bone based on fracture mechanics concepts [Malik et al., 2003, Nalla et al., 2005, Ural et al., 2006, Ural et al., 2007, Vashisth et al., 1997, 2003, Yang et al., 2006]. The simulations were based on cohesive FE modeling which is a phenomenological representation of the physical processes occurring in the vicinity of a propagating crack. Generally, the cohesive zone relationship are defined by a traction–displacement relationship based on the critical normal, shear stress and the energy needed for opening the crack in normal and shear mode (to define the cohesive zone non linear behavior). In the FE approach, cohesive models can be implemented as interface elements that are compatible with regular solid finite elements. Each cohesive element follows the traction-crack opening profile to form a crack. The cohesive elements represent the nonlinear behavior of the process zone which cannot be captured by linear elastic fracture mechanics analysis. However, the major restrictions of the cohesive element methods to realistically simulate an entire bone fracture can be summarized as follow:

- The fracture description based on cohesive element methods is restricted to the problem of a single dominant idealized planar crack with a cohesive zone [Yang et al., 2006].

- The cohesive interface elements must be placed in the direction of the expected crack growth and the fracture processes in the vicinity of a propagating crack is described by a traction–crack opening displacement relationship.
- During monotonic femur loading, tensile and compressive stresses are observed suggesting that cracks can be initiated and propagated in different modes.
- High-resolution imaging of cracks in human cortical bone shows that the crack advances as a complex system. Microcracks are spawned ahead of and around the primary crack [Yang et al., 2006].

However, the authors focused their attention on the failure initiation stage only without considering the crack propagation stage. The fracture load was determined as the load at which at least one solid element had exceeded the threshold value of the fracture criteria. Such 3D representations enhance the proximal femurs geometries.

An alternative method to simulate in a simple, accurate and realistic way the crack initiation and propagation under an applied excessive load is the CDM [Lemaitre, 1985, Hambli et al., 2012]. With the application of CDM, one can simulate cracks initiation and their progressive growth based on specific experimental brittle to quasi-brittle damage laws [Currey, 2002, Kaneko et al., 2003, Bayraktar et al., 2004]. This approach will more detailed in the next section.

2.2.2.1. Finite element simulation using the continuum damage mechanics (CDM)

Numerous investigations have been performed, seeking to characterize damage in bone. In these works, CDM was incorporated in order to simulate the realistic behavior of the failure of the bone organ. The CDM was applied only to bone specimens at mesoscale level i.e. trabecular and cortical bone specimens [Zysset and Curnier, 1996, Garcia et al., 2009, Keaveny et al., 1999, Bettamer et al., 2012a].

For bone specimens, a theoretical 3D damage model for bovine trabecular bone based on fabric tensor (a quantitative measure of the degree of structural anisotropy of bone) was developed by Zysset and Curnier [Zysset and Curnier, 1996]. The investigation considered the bone behavior in general at continuum level. In the investigation of Garcia et al. [Garcia et al., 2009], the authors developed a model to describe the apparent behavior of trabecular bone at continuum level as a porous, heterogeneous and anisotropic material. The model combines anisotropic elasticity and anisotropic plasticity with isotropic damage. The authors considered a plastic flow with hardening. Damage is described by a scalar damage depending on the

plastic strain. To avoid mesh-dependence problems, the non-local regularization method for the damage growth was implemented. Such behavior is valid in general for ductile materials. Also, Garcia's model needs a large number of parameters which are not easily available for bone. Further, the authors did not carry out any simulation on proximal femur fracture to compare to experimental.

For cortical bone, the damaged behavior corresponds to the generation of microcracks was evaluated [Keaveny et al., 1999]. Damage was found to lead to stiffness reduction, energy dissipation and permanent strains that ultimately lead to failure. The damage threshold stress was defined to be coincides with the elastic limit quantifies the onset of damage behavior. After evaluating the damage, the behavior of cortical bone was described as follows: after having reached the ultimate stress at fracture, the stress decreases gradually for increasing strain which corresponds to a softening stage till complete fracture. This phase corresponds by generation and coalescence of microcracks which leads to the stiffness reduction.

Similarly, excessive loading on trabecular bone may lead to severe loss of stiffness and accumulation of residual strain [Zysset, 1994; Keaveny et al., 1994, 1999]. It is obvious that cortical bone shows qualitatively identical damaging behaviour as trabecular bone [Fondrk et al., 1988; Garcia et al., 2009]. This damage occurs at the nanometer level [Keaveny et al., 2001]. Cracks and diffuse damage that accumulate within trabeculae cause reductions in apparent modulus prior to failure of whole trabeculae [Wachtel and Keaveny, 1997].

These investigations have revealed the relevance of diffuse damage and damage accumulation in the failure process of the main constitutions of human femur, namely cortical and trabecular bone. Besides, they highlight the significance of damage at macrostructure level (the femur). To the best to our knowledge, CDM has not yet been employed at macrostructure level (organ level) in either 2D or 3D FE simulations. Therefore, this aspect constitutes a prime task in studying the failure of the proximal femur in the current thesis (Chapter 3).

2.3. Finite element mesh generation

The complex structure of femur is revealed in medical images. Mesh generation utilizing these data constitutes the first step before applying FE method to a particular biomechanics problem. The mesh generation method deals with the decomposition of a specified geometry into finite elements with the purpose of facilitate the numerical solution to partial differential equations.

Over the past decades, various FE methods to transfer CT/MRI (Computer Tomography scan/ Magnetic Resonance Imaging) data have been proposed for the 3D modeling of femur [Keyak and Falkinstein, 2003, Viceconti et al., 2004, Lee et al., 2005; Wang et al., 2005, Canton and Gilchrist, 2010]. Particularly, two methods are in widespread use. The first method, bone voxels of 3D femur image are directly converted into equally shaped brick-element meshes [Pothuaud et al., 2004]. The second method is based on preliminary acquisition geometry, most often obtained by segmentation techniques and contouring data.

The voxel-based FE model is considered as an accuracy reference [Ulrich et al., 1998, Bayraktar, 2004], since it allows a precise description of the full geometry of the bone [Ladd et al., 1998, Van der Linden et al., 2001]. Its drawback, however, resides in the high time consumption and huge memory requirements. To overcome this inconvenience, each group of voxels that has a rod-like geometry is converted into a simple beam element [Pothuaud et al., 2004]. In this method, a beam element is described by a 1D segment of equally-sized circular cross section. Despite the huge gain in computation time, the beam-based FE models suffer from a significant lack of accuracy. Therefore, the voxel-based model has been chosen for the work of this thesis.

2.4. Conclusion

The ability to better predict incident proximal femur fractures could lead to interventions that would prevent or delay the occurrence of such fractures and their significant associated mortality. The current chapter reviewed several investigations of FE models of bone femur fracture as well as damage simulations. Some of previously published models employed simple uncoupled failure criteria to linear and non-linear with isotropic and anisotropic material behavior was presented. The authors focused their attention on the failure initiation stage only without considering the crack propagation stage. Nevertheless they are not able to predict the progressive cracks initiation and propagation. Until now, direct comparisons of predicted and measured force-displacement curves and complete fracture profile of the proximal femur have not been performed.

This can lead us to the main objective of the current thesis work which aims to develop 2D and 3D FE models based on continuum damage mechanics to simulate the profile of the fractured area of proximal femur and the complete force–displacement. The previous models based on the CDM have been made on the bone at mesostructure level. This approach is applied for the first time on the femur as an organ. These models will be validated by

Chapter 3

Finite element simulation of human femur fracture using continuum damage mechanics

Abstract

The analysis of the literature reviews has shown that previous studies focused their attention only on the failure initiation stage of the femoral neck without considering the crack propagation stage. Nevertheless, these studies were not able to predict the progressive cracks initiation and propagation. Direct comparison of predicted and measured force-displacement curves and complete fracture profile of the proximal femur have not been performed. In the current chapter, we will start firstly with a brief review of the basic fundamentals of the concept of Continuum Damage Mechanics (CDM). Then, we will present the developed models, loading and boundary conditions. These models are the following: An isotropic 3D FE model, referred by Model A. In two dimensions (2D), two models referred by Models B and C are developed. These two models are based on orthotropic and isotropic behavior laws respectively. All these models are coupled to isotropic quasi brittle damage law using heterogenous material assignment. Finally, 2D models, homogenous material, are developed for preliminary validation referred by model test-I and model test-II.

Résumé

L'étude bibliographique a montré que les travaux antérieures se sont essentiellement intéressés à la prédiction de la phase d'initiation de la fracture du col du fémur sans tenir compte de la phase de propagation des fissures. Par ailleurs, la charge à la rupture est déterminée comme étant la charge à laquelle au moins un élément solide a dépassé la valeur seuil des critères de rupture. Les comparaisons directes des courbes force-déplacement prédites et expérimentales associée au profil d'une fracture complète de la partie proximale du fémur n'ont pas été réalisées. Dans ce chapitre, nous allons commencer par un bref rappel des principes fondamentaux du concept de la mécanique de l'endommagement des milieux continus. Ensuite, nous allons présenter les modèles EF développés en 2D et 3D ainsi que les conditions aux limites utilisées. Ces modèles sont les suivants : Un modèle EF 3D isotrope, nommé modèle A. Deux modèles EF 2D, nommés modèles B et C, qui sont basés respectivement sur des lois de comportement orthotrope et isotrope. Tous ces modèles sont couplés à une loi d'endommagement isotrope quasi fragile en utilisant un matériau hétérogène. Enfin, deux modèles en 2D, matériau homogène, sont développés pour une validation préliminaire (modèle test-I et modèle test-II).

3.1. Introduction

A review of the literature shows that despite the progress in the field of bone fracture simulation under monotonic load, there is still a lack of models that permit to give an accurate prediction of the fracture profile and the propagation path of the fracture from the beginning till the total separation of bone. Such prediction can be used by clinicians as a helping tool to assess the recent augmentation of femoral fracture.

The current chapter portrays the developed 2D and 3D finite element (FE) models of proximal femur fracture. An isotropic 3D FE model, referred by Model A, is developed based on voxel element type C3D8. In 2D, two models based on pixel quadratic C2D4 element type and referred by Models B and C are developed. These two models are based on orthotropic and isotropic behavior laws respectively. All these models are coupled to isotropic quasi brittle damage law using heterogenous (each element in cortical bone as well as in trabecular bone is defined by its density) material assignment. Finally, 2D models are developed for preliminary validation. As their purpose is for preliminary validation, the lattice work structure of the trabecular and cortical bone was ignored, allowing the material to be modeled as a homogeneous. These two homogenous models (model test-I and model test-II) are based on isotropic and orthotropic behavior laws coupled to quasi brittle damage laws.

Ever since, our proposed models were based on the concept of Continuum Damage Mechanics (CDM), we will start with a brief review of the basic fundamentals of this concept.

3.2. Concept of continuum damage mechanics

Continuum damage mechanics (CDM) has a wide range of applicability for different materials as steel, composite, ceramics, and concrete [Krajcinovic and Fonseka, 1981, La Borderie et al., 1990, Mazars and Pijaudier-Cabot, 1989, Zhang et al., 2010].

In bone, the presence of bone damage in the form of microcracks is a well-known fact [Ziopoulos and Currey, 1994].

Damage causes a progressive degradation of material continuity, which distinguishes it from other types of inelastic material behavior [Lemaitre and Chaboche, 1990]. The loss of integrity can have an adverse effect on mechanical properties, and can be attributed to microscopic cracks and/or voids. Hence, fracture behavior and crack propagation corresponding to damage accumulation should be all put in consideration for realistic and accurate simulation.

Nowadays, extensive studies have been made to characterize and to simulate the damage in bone. The presence of damage has direct effects on mechanical properties such as degradation of stiffness, strength and most other properties which culminate in bone failure.

In CDM models, damage can be considered as a macroscopic state variable that affects the mechanical properties entailing stiffness degradation of the material. In physical terms, the loss of stiffness can be considered as a result of distributed microcracks and microvoids. Continuum mechanics deals with mathematical quantities that represent averages of a specific volume [Lemaitre, 1990] called “representative volume element” (RVE).

This concept can be demonstrated by taking into consideration the RVE at a point M presented in Figure 3.1.

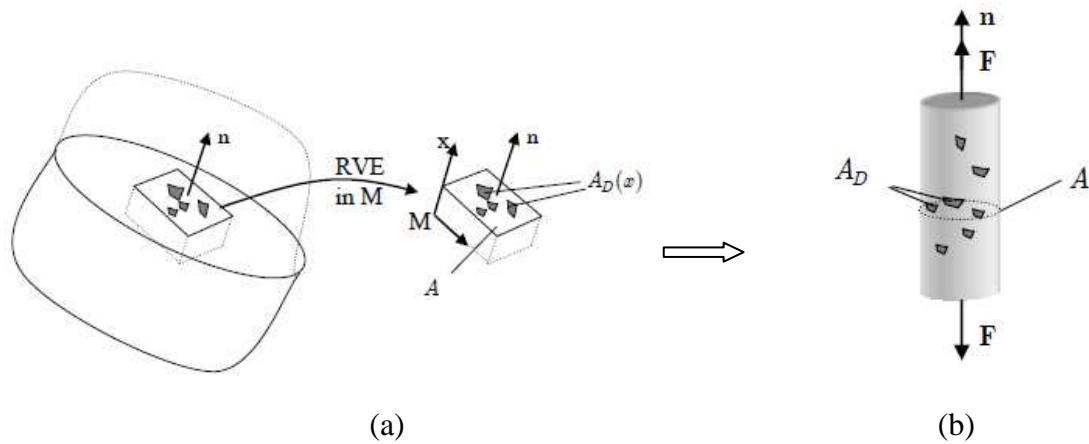


Figure 3. 1 (a) Definition of damage (b) damaged element [Lemaitre, 1990].

The value of the damage variable D associated with the point M defined by the normal \vec{n} to the area A can be expressed as:

$$D_n = \frac{A_D}{A^0} \quad (3.1)$$

where A^0 is the surface area, and A_D is the area of all microcracks and microcavities that lie on the intersection A^0 , the value of the scalar damage variable is in the range:

$$0 \leq D_n < 1 \quad (3.2)$$

where the value of 0 corresponds to undamaged RVE material and the value of 1 to fully damaged material.

In the current thesis, it is assumed that D_n is approximately the same in any direction. Thus, the state of damage can be represented by a scalar quantity ($D_n \cong D$).

When the RVE in Figure 3.1 is loaded by a force F , the uniaxial (σ) and the effective (σ_{eff}) stresses can be expressed respectively as:

$$\sigma = F/A^0 \quad (3.3)$$

$$\sigma_{eff} = F / (A^0 - A_D) \quad (3.4)$$

where $(A^0 - A_D)$ is the area perpendicular effectively resists the load. Using the definition of damage given in equations 3.1, 3.3 and 3.4, the effective stress can be expressed as:

$$\sigma_{eff} = \sigma (1 - D)^{-1} \quad (3.5)$$

The parameter (D) has the meaning of a physical reduction in section resistant due to the presence of microcracks. The damage variable(D) used in equation 3.5 can be expressed in the terms of the Young's modulus of bone material (E) and of undamaged bone material (E^0) as mentioned in equation 3.6 [Baste et al., 1989]:

$$D = 1 - (E/E^0) \quad (3.6)$$

The undamaged bone material is referred by the exposant (0)

In the case of anisotropic damage, the damage variable can be expressed in a tonsorial form. This allows expressing the anisotropic behavior law of elasticity based on damage mechanics by the following relation:

$$\sigma_{ij} = C_{ijkl}(D)\varepsilon_{kl} \quad (3.7)$$

where σ_{ij} the Cauchy stress components , ε_{kl} linear strains, $C_{ijkl}(D)$ the components of a symmetric fourth-order tensor of damaged material, D the damage diagonal tensor.

The nonzero elements in the tensor equation 3.7 can be expressed using a symmetric matrix and the relation of between the engineering elastic constants of undamaged and damaged bone material. These nonzero elements are:

$$E_1 = E_1^0 (1 - D_1)^2$$

$$E_2 = E_2^0 (1 - D_2)^2$$

$$E_3 = E_3^0 (1 - D_3)^2$$

$$\begin{aligned}
G_{23} &= G_{23}^0(1-D_4)^2 \\
G_{13} &= G_{13}^0(1-D_5)^2 \\
G_{12} &= G_{12}^0(1-D_6)^2
\end{aligned} \tag{3.8}$$

$$\begin{aligned}
\nu_{12} &= \nu_{12}^0(1-D_1)(1-D_2)^{-1} \\
\nu_{13} &= \nu_{13}^0(1-D_1)(1-D_3)^{-1} \\
\nu_{23} &= \nu_{23}^0(1-D_2)(1-D_3)^{-1}
\end{aligned}$$

where D_1, D_2 and D_3 are the damage variables at their principal axes. The conventions used for subscripts indicating coordinate direction (x,y,z) can be generally represented by the values 1, 2, or 3.

When $D_1 = D_2 = D_3 = D$, the case will be called as isotropic damage case. In the current thesis, anisotropic damage was developed and not applied for the reason of simplicity and data availability. Hence, a homogenized measure of the isotropic damage expressed by the variable (D) was retained coupled with the general isotropic bone. This assumption is adopted for all developed models in 3D and 2D.

3.3. Anisotropic and orthotropic quasi brittle damage behavior law

In order to complete the formulation of the anisotropic behaviour in three dimension coupled to isotropic scalar damage, the behaviour law can be expressed by:

$$\sigma_{ij} = (1 - D)C_{ij \ kl} \varepsilon_{kl} \tag{3.9}$$

$$\begin{Bmatrix} \sigma_{11} \\ \sigma_{22} \\ \sigma_{33} \\ \sigma_{12} \\ \sigma_{13} \\ \sigma_{23} \end{Bmatrix} = (1 - D) \begin{pmatrix} C_{1111} & C_{1122} & C_{1133} & 0 & 0 & 0 \\ & C_{2222} & C_{2233} & 0 & 0 & 0 \\ & & C_{3333} & 0 & 0 & 0 \\ & sym & & C_{1212} & 0 & 0 \\ & & & & C_{1313} & 0 \\ & & & & & C_{2323} \end{pmatrix} \begin{Bmatrix} \varepsilon_{11} \\ \varepsilon_{22} \\ \varepsilon_{33} \\ \varepsilon_{12} \\ \varepsilon_{13} \\ \varepsilon_{23} \end{Bmatrix} \tag{3.10}$$

where:

$$\left\{ \begin{array}{l} C_{1111} = E_1 (1 - \nu_{23} \nu_{32}) \Upsilon \\ C_{2222} = E_2 (1 - \nu_{13} \nu_{31}) \Upsilon \\ C_{3333} = E_3 (1 - \nu_{12} \nu_{21}) \Upsilon \\ C_{1122} = E_1 (\nu_{21} - \nu_{31} \nu_{23}) \Upsilon = E_2 (\nu_{12} - \nu_{32} \nu_{13}) \Upsilon \\ C_{1133} = E_1 (\nu_{31} - \nu_{21} \nu_{32}) \Upsilon = E_3 (\nu_{13} - \nu_{12} \nu_{23}) \Upsilon \\ C_{2233} = E_2 (\nu_{32} - \nu_{12} \nu_{31}) \Upsilon = E_3 (\nu_{23} - \nu_{21} \nu_{13}) \Upsilon \\ C_{1212} = G_{12} \\ C_{1313} = G_{13} \\ C_{2323} = G_{23} \end{array} \right. \quad (3.11)$$

And Υ is defined as :

$$\Upsilon = \left(\frac{1}{1 - \nu_{12} \nu_{21} - \nu_{23} \nu_{32} - \nu_{31} \nu_{13} - 2 \nu_{21} \nu_{32} \nu_{13}} \right) \quad (3.12)$$

the restrictions on the elastic constants due to material stability are:

$$\left\{ \begin{array}{l} C_{1111}, C_{2222}, C_{3333}, C_{1212}, C_{1313}, C_{2323} > 0, \\ |C_{1112}| < (C_{1111} C_{2222})^{1/2}, \\ |C_{1133}| < (C_{1111} C_{3333})^{1/2}, \\ |C_{2233}| < (C_{2222} C_{3333})^{1/2}, \\ \det(C) > 0 \end{array} \right. \quad (3.13)$$

In the current work, the elasticity matrix coefficients were expressed in terms of engineer's constants defined in simple uniaxial stress conditions. This leads to a formulation of Hooke's law for the orthotropic plane-stress case assigned for model B and model test-II:

$$\left\{ \begin{array}{l} \sigma_1 \\ \sigma_2 \\ \sigma_{12} \end{array} \right\} = (\mathbf{1} - \mathbf{D}) \left[\begin{array}{ccc} \frac{E_1}{1 - \nu_{12} \nu_{21}} & \frac{\nu_{12} E_2}{1 - \nu_{12} \nu_{21}} & \mathbf{0} \\ & \frac{E_2}{1 - \nu_{12} \nu_{21}} & \mathbf{0} \\ \mathbf{sym} & & \mathbf{2}G_{12} \end{array} \right] \left\{ \begin{array}{l} \varepsilon_1 \\ \varepsilon_2 \\ \varepsilon_{12} \end{array} \right\} \quad (3.14)$$

Young's modulus, shear modulus and Poisson's ratio are totally independent in the orthotropic case and have to be measured separately.

Quasi-brittle damage growth depends on a damage loading function in terms of the strain components. The growth of the damage variable is controlled by the damage threshold parameter (k), which is defined as the maximum of the equivalent strain measure (ε_{eq}) reached during the load history [Mazars and Pijaudier-Cabot, 1996]:

$$k = \max (\varepsilon_{eq}) \quad (3.15)$$

The loading function of damage is expressed by Mazars and Pijaudier-Cabot [Mazars and Pijaudier-Cabot, 1996]:

$$f(\varepsilon_{eq}, \varepsilon_0) = \varepsilon_{eq} - \max(k, \varepsilon_0) \quad (3.16)$$

where ε_0 is the initial value of k when damage starts. If the loading function (f) is negative, damage does not develop. During monotonic loading, the parameter k grows (it coincides with ε_{eq}) and during unloading and reloading it remains constant:

$f < 0$: No damage growth and the material behavior is elastic.

$f \geq 0$: Damage growth and reduction of the stiffness.

Numerous studies have shown that the damage threshold strains of compact bone tissue are different in tension and compression [Keaveny et al., 1999, 2001, Currey, 2002, Kotha and Guzelsu, 2003]. All microdamage parameters showed an increase with increasing strain (Figure 3.2). Regions of cross-hatching and bone fracture are seen more frequently in highly strained specimens. The extent of damage across the trabecular thickness also increased with increasing strain [Arthur Moore and Gibson, 2002].

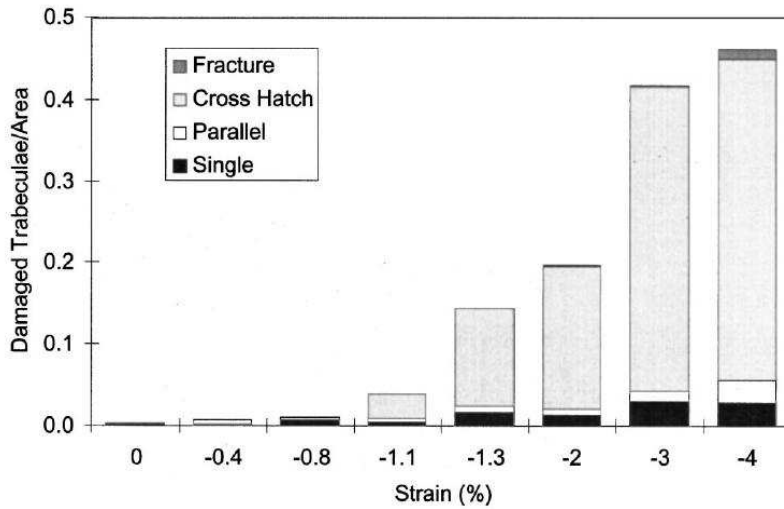


Figure 3.2 Breakdown of number of damaged trabeculae, normalized by section area, by damage pattern for each strain level [Arthur Moore and Gibson, 2002].

With referring to the relation observed experimentally by [Arthur Moore and Gibson, 2002] for both the experimental law and the dependence of damage growth on the hydrostatic pressure, a quasi-brittle damage law can be expressed in principal directions by:

$$\left\{ \begin{array}{ll} D_{i=1,2,3} = 0 & , \varepsilon_{eq} \leq \varepsilon_0 \\ D_{i=1,2,3} = D_c \varepsilon_{eq}^n & , \varepsilon_0 < \varepsilon_{eq} < \varepsilon_{f_i} \\ D_{i=1,2,3} = 1 & , \varepsilon_{eq} \geq \varepsilon_{f_i} \end{array} \right. \quad (3.17)$$

Where ε_{f_i} denotes the strain at fracture in the three anisotropic directions ($i = 1, 2 \text{ and } 3$), D_c critical value of damage and n the damage exponent.

In general, the tensile longitudinal strain at fracture (ε_f^T) of femoral human bone is in the range of 0.4–0.7% and the compressive longitudinal values (ε_f^C) is the range of 0.9–1.2% [Bayraktar et al., 2004, Kaneko et al., 2003]. Subsequently, to perform a personalized prediction of a given patient, yield strain (ε_f) can be assessed using the power law fitted based on experimental data on human femur proposed by Dragomir-Daescu et al. [Dragomir-Daescu et al., 2011]:

$$\varepsilon_f = 0.008 \rho_{ash}^{-1.42} \quad (3.18)$$

where ρ_{ash} (g/cm³) denotes the ash density of bone.

3.4. Isotropic quasi-brittle damage behavior law

Within the assumption of homogenous isotropic damage the isotropic formulation of Hook's law can be expressed as:

$$\begin{Bmatrix} \sigma_{11} \\ \sigma_{22} \\ \sigma_{33} \\ \sigma_{23} \\ \sigma_{31} \\ \sigma_{12} \end{Bmatrix} = \frac{(1-D)E}{(1+\nu)(1-2\nu)} \begin{pmatrix} 1-\nu & \nu & \nu & 0 & 0 & 0 \\ \nu & 1-\nu & \nu & 0 & 0 & 0 \\ \nu & \nu & 1-\nu & 0 & 0 & 0 \\ 0 & 0 & 0 & \frac{(1-2\nu)}{2} & 0 & 0 \\ 0 & 0 & 0 & 0 & \frac{(1-2\nu)}{2} & 0 \\ 0 & 0 & 0 & 0 & 0 & \frac{(1-2\nu)}{2} \end{pmatrix} \begin{Bmatrix} \varepsilon_{11} \\ \varepsilon_{22} \\ \varepsilon_{33} \\ 2\varepsilon_{23} \\ 2\varepsilon_{31} \\ 2\varepsilon_{12} \end{Bmatrix} \quad (3.19)$$

In the current work, the isotropic properties materials were assigned for each heterogeneous element in model A. The properties are assigned for each element depending on the grey level value (will be detailed in chapter 4).

In plane case (2D), the isotropic Hooks law, equation 3.19 becomes in the following form:

$$\begin{Bmatrix} \sigma_1 \\ \sigma_2 \\ \sigma_{12} \end{Bmatrix} = (1-D) \begin{bmatrix} \frac{E}{1-\nu^2} & \frac{\nu E}{1-\nu^2} & 0 \\ & \frac{E}{1-\nu^2} & 0 \\ \text{sym} & & G \end{bmatrix} \begin{Bmatrix} \varepsilon_1 \\ \varepsilon_2 \\ \varepsilon_{12} \end{Bmatrix} \quad (3.20)$$

As mentioned above, isotropic quasi brittle damage law, bases on above equations, will be used in its flowing form:

$$\left\{ \begin{array}{ll} D = 0 & , \varepsilon_{eq} \leq \varepsilon_0 \\ D = D_c \varepsilon_{eq}^n & , \varepsilon_0 < \varepsilon_{eq} < \varepsilon_f \\ D = 1 & , \varepsilon_{eq} \geq \varepsilon_f \end{array} \right. \quad (3.21)$$

where ε_f denotes the strain at fracture.

This newly developed coupled approach can be used to simulate femur failure as well as fracture patterns in 3D and 2D FE simulations. It can be also used to investigate the effect of bone property assignment “isotropic and orthotropic” on the predicted fracture pattern.

3.5. Material properties assignment

3.5.1. Anisotropic /orthotropic material properties assignment

Bone material is anisotropic and inhomogeneous due to its varying architecture and composition of its constituents [Yang et al., 1999]. The determination of the elastic constants of trabecular bone by conventional mechanical test procedures is very difficult due to the small size of specimens of human trabecular bone. In general, compressive tests are applied to the trabecular sample leads to inaccuracy of the measurements. Yang et al. [Yang et al.,1999], investigated a data bases consisting of 141 human cancellous bone specimens reported previously by Van Rietbergen et al. [Van Rietbergen et al.,1996] and Kabel et al. [Kabel et al.,1999]. The data analysis method permits the identification of the elastic constants of trabecular bone as a function of volume fraction (BV/TV).

In the current thesis, anisotropic mechanical properties are used for the homogenous model (Model test-II). The properties are estimated as a function of (BV/TV). This arbitrary choice was adopted to preliminary testing the capability of our proposed model to predict the fracture failure as well as fracture patterns. Based on the equations proposed by Yang et al., [Yang et al., 1999], the final result is the solid volume as a function of volume fraction dependent orthotropic Hooke’s law for cancellous bone in the form (with correlation coefficient of 0.934):

$$\begin{aligned} E_1 &= 1240 E_t \left(\frac{BV}{TV} \right)^{1.8} \\ E_2 &= 885 E_t \left(\frac{BV}{TV} \right)^{1.89} \\ E_3 &= 528.8 E_t \left(\frac{BV}{TV} \right)^{1.92} \end{aligned} \quad (3.22)$$

$$\begin{aligned}
G_{12} = G_{21} &= 486.3 E_t \left(\frac{BV}{TV} \right)^{1.98} \\
G_{13} = G_{31} &= 316.65 E_t \left(\frac{BV}{TV} \right)^{1.97} \\
G_{23} = G_{32} &= 266.65 E_t \left(\frac{BV}{TV} \right)^{2.04}
\end{aligned} \tag{3.23}$$

$$\begin{aligned}
\nu_{12} = \nu_{21} &= \frac{1}{2} \left(0.176 \left(\frac{BV}{TV} \right)^{-0.25} + 0.125 \left(\frac{BV}{TV} \right)^{-0.16} \right) \\
\nu_{13} = \nu_{31} &= \frac{1}{2} \left(0.316 \left(\frac{BV}{TV} \right)^{-0.19} + 0.135 \left(\frac{BV}{TV} \right)^{-0.007} \right) \\
\nu_{23} = \nu_{32} &= \frac{1}{2} \left(0.256 \left(\frac{BV}{TV} \right)^{-0.09} + 0.153 \left(\frac{BV}{TV} \right)^{-0.05} \right)
\end{aligned} \tag{3.24}$$

where bone volume fraction $\left(\frac{BV}{TV} \right)$ is assumed to be equal to 30% [Keyak and Falkinstein, 2003], $E_t = 48.17$ MPa [Yang et al., 1999] The anisotropic properties of bone estimated were calculated by using equations 3.22, 3.23 and 3.24 and are provided in Table 3.1.

Table 3.1 Estimated anisotropic Material properties.

	properties	Source
General properties	$\frac{BV}{TV} = 30\%$ $E_t = 48.17$ MPa	[Keyak and Falkinstein, 2003, Yang et al., 1999]
Elastic properties (femur and acetabulum)	$E_1 = 6840$ MPa $E_2 = 4380$ MPa $E_3 = 2524$ MPa $\nu_{12} = 0.19$ $\nu_{23} = 0.27$ $\nu_{31} = 0.22$ $G_{12} = 2159$ MPa $G_{23} = 1423$ MPa $G_{31} = 1101$ MPa	Estimated based on [Keyak and Falkinstein, 2003, Yang et al., 1999]

Material properties for bone used for the orthotropic simulation: model test-II was considered as $E_3 = E_2 = 4380$ MPa. For model B, equations, proposed by Baca et al. [Baca et al., 2008] mentioned in Table 2.1, were applied.

3.5.2. Isotropic material properties assignment

Hook's laws in the form mentioned in equations 3.19 and 3.20 were applied for each element in the heterogeneous Models A and C and for the homogenous Model test-I.

Material properties assigned for these models are shown in Table 3.2.

Table 3. 2 Material properties used for the isotropic simulation: Models A and test I

General parameters	Notation	Femur	Acetubulum	Source
Elastic modulus	E (GPa)	8.0	20.0	[Keyak and Falkinstein, 2003]
Poisson ratio	ν	0.3	0.3	[Keyak and Falkinstein, 2003]

As mentioned above, isotropic quasi brittle damage law is applied in all developed models. The models parameters used for damage are shown in Table 3.3:

Table 3. 3 Damage law parameters used for femur in the isotropic simulation [Hambli et al., 2012].

Damage law parameters	reference		
Damage properties (femur only)	n	2.0	
	D_c^T	0.95	
	D_c^C	0.5	[Arthur Moor and Gibson, 2002, Bayraktar et al.2004, Hambli,2001]
	ϵ_o	0.2 %	
	ϵ_f^T	0.66 %	
	ϵ_f^C	1.2 %	

In the current work, we implemented a practical method into ABAQUS/Standard code (User UMAT Subroutine) to represent fracture by the so-called “kill element” technique [Hambli et al., 2012]. When the damage parameter reaches a critical value (D_c) inside an element, the element mechanical contribution to the stiffness matrix is set to zero leading to the redistribution of the stress state in the crack tip. Once a crack is initiated the propagation direction is simulated by the propagation of the broken elements of the mesh. An overview of this approach is illustrated in Figure 3.3.

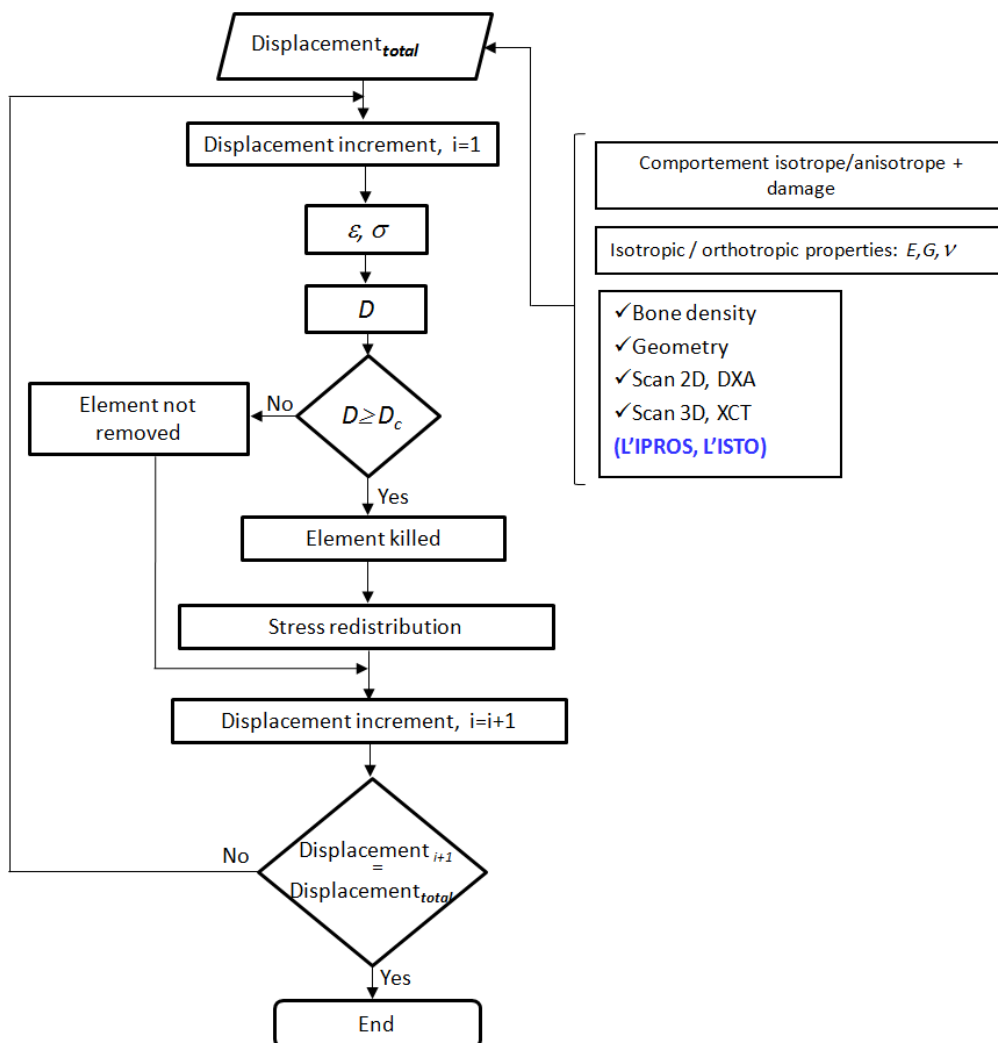


Figure 3.3 Schematic diagram of the proposed simulated crack propagation implemented in UMAT user subroutine based on both isotropic and orthotropic behaviour laws coupled to quasi-brittle damage.

3.5.3. Orthotropic direction assignment

It has been established that trabecular bone exhibits orthotropic behavior with three orthogonal directions [Reilly et al., 1974, Van Rietbergen et al., 1996]. Limited number of studies considered the anisotropic behavior of bone tissue [Fenech and Keaveny, 1999, Hambli, 2010] due mainly to the difficulty to assign the anisotropic material parameters related to the local directional material anisotropy.

From a point of view of CDM, there is no difference between crack initiation and propagation. Both results from the failure of an element with a characteristic dimension (typical size of a crack). Thus, crack initiation and propagation are studied as unified approach [Lemaitre, 1985].

The assignment of local orthotropic directions and orthotropic properties for every FE of the mesh is performed in four steps, Figure 3.4 [Hambli et al., 2012]:

- **Initial conditions:** x_0 and y_0 are the initially assigned reference coordinates (material directions) of every FE (i) of the femur mesh,
- **Orthotropic directions computation:** performed a 2D elastic analysis under a gait cycle with a displacement of 15 mm applied to the acetabulum with an orientation of 20° from the vertical.
- **Assignment of local anisotropic directions:** compute the principal stress directions (x_i and y_i) for every FE (i)) corresponding respectively to the directions of the maximum elongation and its orthogonal direction.

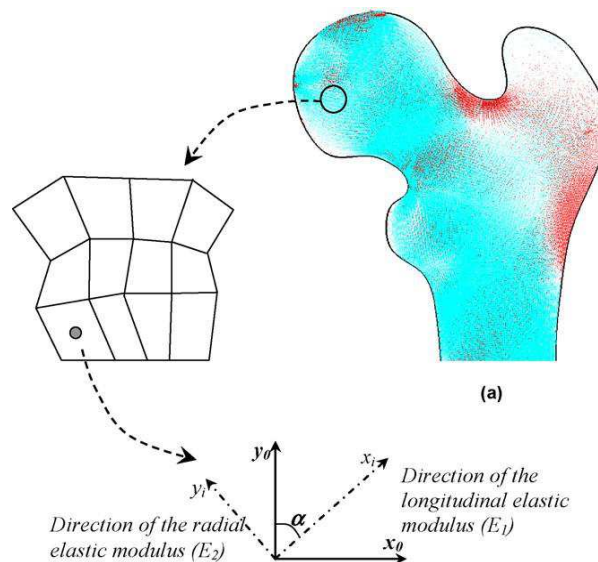


Figure 3. 4 Assignment of orthotropic directions and corresponding material properties [Hambli et al., 2012].

The orientations (x_i , y_i) are stored for every FE in a results file. (x_i) lies along the local predominant trabecular direction, which is locally the stiffest direction (longitudinal direction), the second is orthogonal to the first direction and represent the direction of extrema in stiffness in the local region of the cancellous bone.

- **Orthotropic properties assignment:** the orthotropic bone properties were assigned automatically to each FE (reduced integration) of the femur mesh corresponding to the computed local directions (x_i) and (y_i).

For resuming the using of the proposed coupled approach in the current models, the depicted diagram shown in Figure 3.5 represents the following developed models:

- **Heterogeneous models:**

- 3D FE model (model A): isotropic behavior law coupled to quasi-brittle damage.
- 2D FE model (models B): orthotropic behavior law coupled to quasi-brittle damage.
- 2D FE model (model C): isotropic behavior law coupled to quasi-brittle damage.

These models are used to achieve the objectives of the current thesis.

- **Homogenous models:**

- 2D FE model (model test-I): isotropic behavior law coupled to quasi-brittle damage.
- 2D FE model (models test-II): orthotropic behavior law coupled to quasi-brittle damage.

The purpose of the homogenous models, as we will see in section (3.6), is to preliminary test the fracture failure calculations and fracture patterns.

These models are proposed to simulate the proximal femur fracture under both configurations: single limb stance and sideways fall configurations.

The following section will present the applied boundary conditions and loads used for these two configurations.

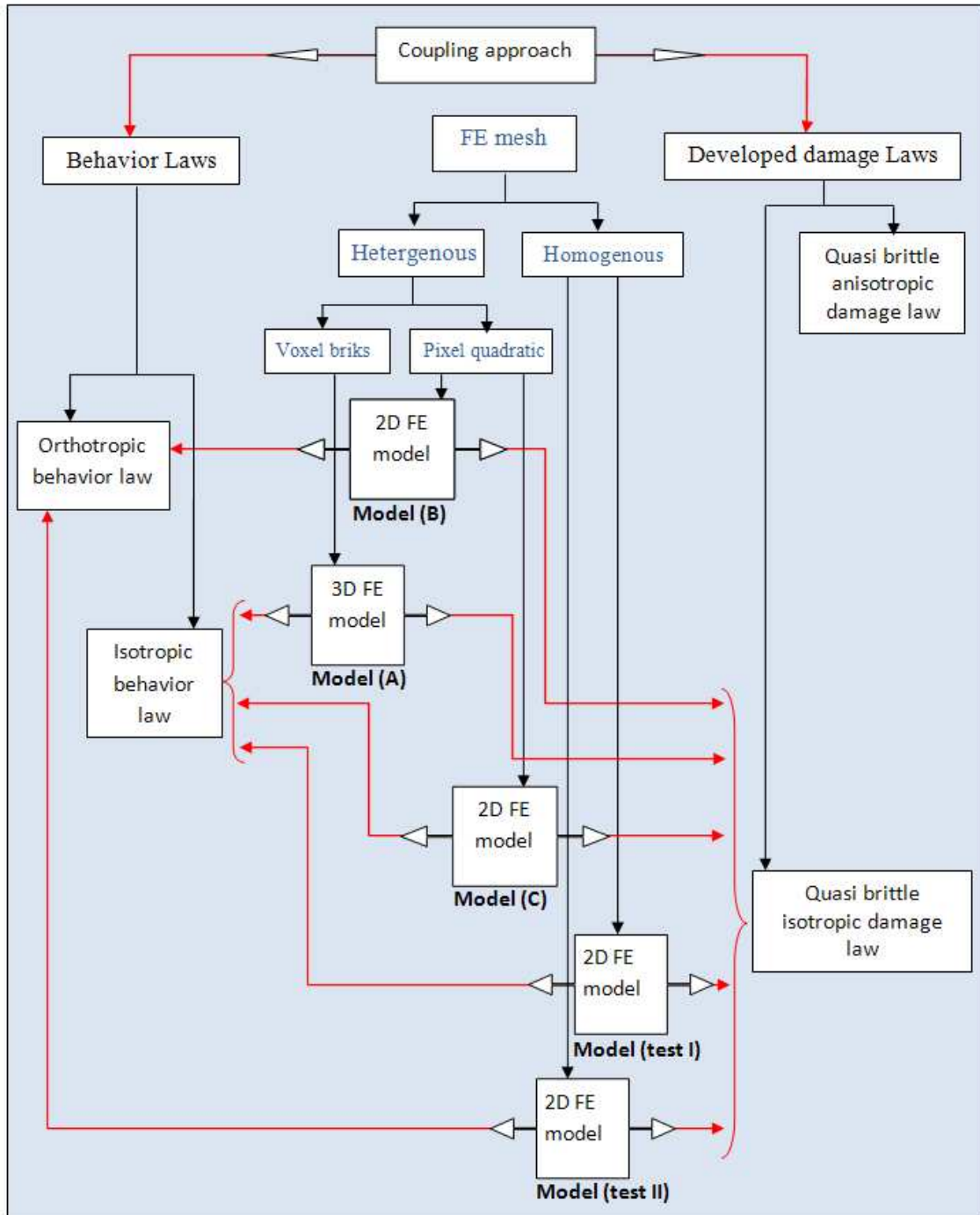


Figure 3. 5 The developed models of the current study.

3.6. Loading and boundary conditions

3.6.1 Loading and boundary conditions of single limb stance simulation in 3D

Boundary conditions were applied to the FE models to represent the conditions of mechanical testing by performing 3D image registration. In each model, the location of the applied displacement was extrapolated from the registration coordinates of the contact points attached to the femoral head which represent in turn the contact between the hip and femur head.

As kinematical boundary conditions, the femur was assumed to be clamped in the distal part, Figure 3.6.

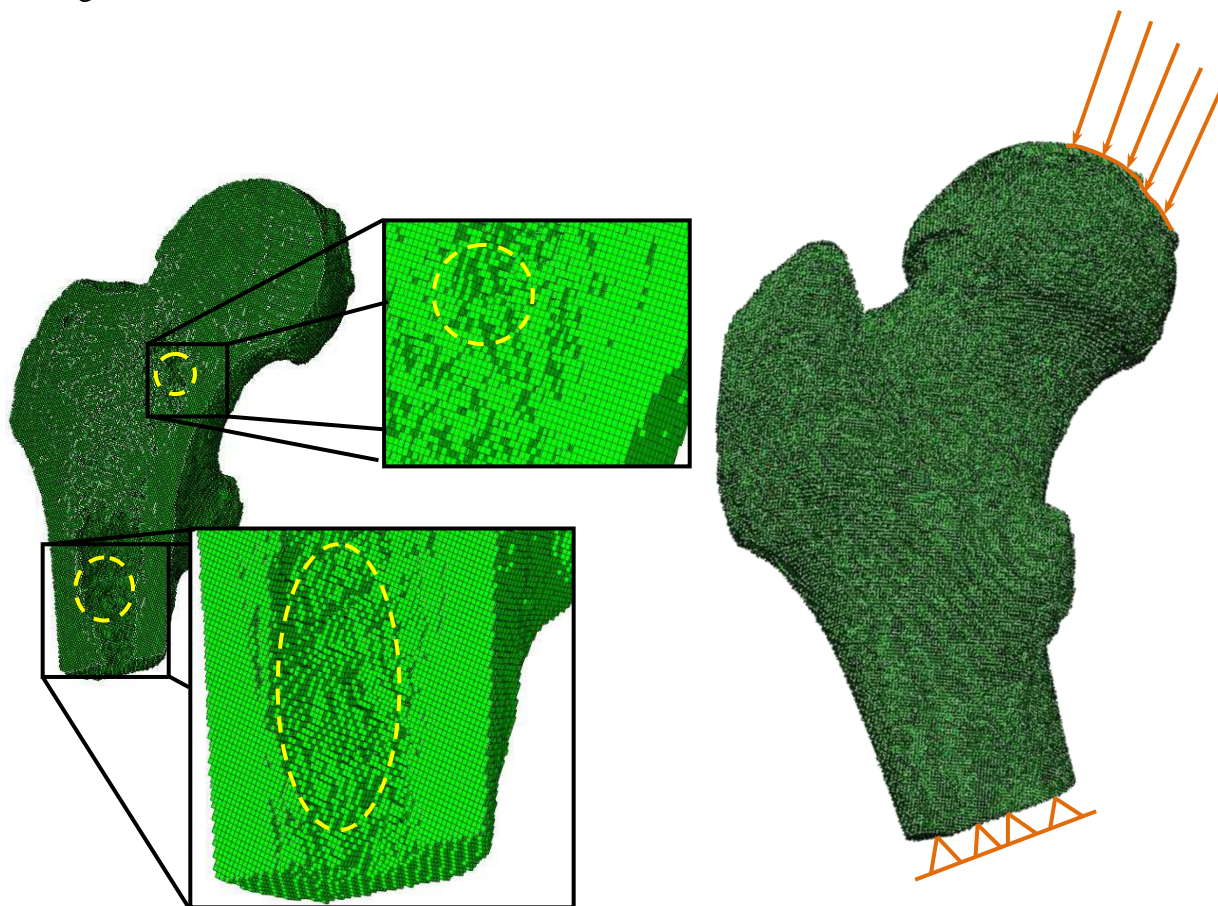


Figure 3. 6 An example of 3D FE loading and boundary conditions applied for human femur.

A displacement of 15 mm was imposed on the assumed contact areas between the centre of the hip joint and femoral head.

3.6.2 Loading and boundary conditions of single limb stance configuration in 2D

A FE model was constructed including the proximal femur articulating freely with a representation of the acetabulum, Figure 3.7. Boundary and loading conditions are chosen according to the experimental study reported in Keyak and Falkinstein, [Keyak and Falkinstein 2003]. The model was loaded by applying displacements incrementally with an orientation of 20° from the vertical to the top surface of the acetabulum. The lower surfaces of the proximal femur were encastred, Figure 3.7. The reaction force applied to the acetabulum was computed considering the femur cracking versus the displacement of femur head.

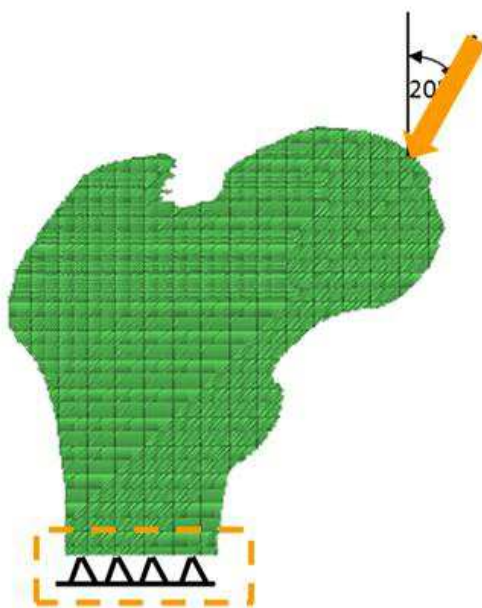


Figure 3. 7 FE model: (a) applied boundary conditions in single limb stance configuration.

The appropriate orientation of the resultant hip force was estimated for all femur specimens. An arbitrary individual hip displacement of 1.5 cm was directed towards the center of contact between the pelvis and the femoral head.

3.6.3 Loading and boundary conditions of sideway falls simulation in 2D

The boundary conditions applied represented a fall onto the greater trochanter based on experimental studies reported earlier [Courtney, 1994,1995], see Figure 3.8. The angle between the femoral shaft and the horizontal was 10° and the femur was internally rotated by 15° .

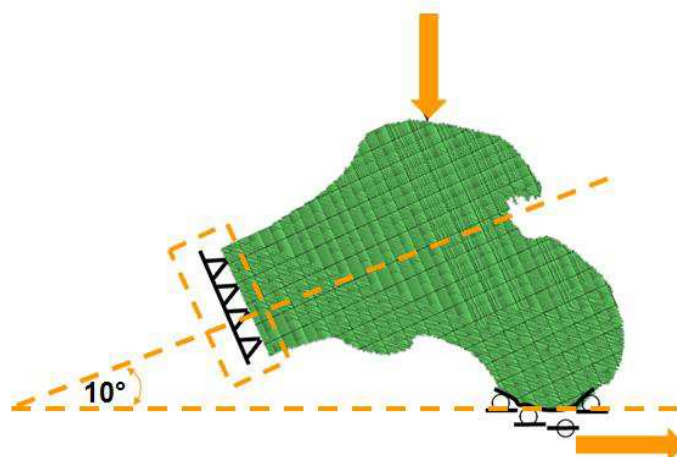


Figure 3.8 Applied boundary conditions in sideways fall configuration [de Bakker et al., 2009, Hambli et al., 2013].

The appropriate orientation of the resultant hip force was estimated for all femur specimens. An arbitrary individual displacement of 1.5 cm was directed towards the greater trochanter. The surface nodes perpendicular to the resultant hip force on the greater trochanter were fixed vertically and allowed to displacement in the horizontal direction to simulate constraints between the femur and a contact surface.

3.7. Validation of the developed quasi brittle damage models

The FE analysis software used in the current study is ABAQUS® 6.7 EF. All laws and relationships discussed above have been implemented in FORTRAN 90 by means of the UMAT (User Material) subroutine. UMAT subroutines can be used to define the mechanical constitutive behavior of a material. They will be called at all material calculation points of elements at all iterations. The current developed programs were subjected to preliminary several tests for 2D models test I and II. The following preliminary tests were performed for:

- Mesh sensitivity test.
- Effect of material property assignments on the fracture pattern.
- Damage nucleation.
- Fracture propagation.

Identical boundary and loading conditions were chosen as imposed in the experimental study of Keyak and Falkinstein [Keyak and Falkinstein 2003].

3.7.1 Preliminary validation of the femur fracture model

To demonstrate the potential of this validation, a left proximal femur of a male (age 61) referred as Model test-I and test-II was loaded until failure under one-leg stance. The model was investigated by keyak and Falkinstein [Keyak and Falkinstein, 2003].

Due to the non-availability of 2D human femur specimens, a validated homogenous model was used. The 2D contour of the femur was digitized based on the geometry of the model investigated by Keyak and Falkinstein, Figure 3.9. A FE model was constructed including the proximal femur and acetabulum. Boundary and loading conditions simulated the experimental setup, reported in keyak and Falkinstein, was applied [Hambli et al., 2012]. The distal portion had a zero displacement condition (Figure 3.9) and a displacement of 15 mm was applied on the proximal femur with an angle of 20° from the vertical. The mechanical properties of bone used for this simulation were compiled in Tables 3.1, 3.2 and 3.3.



Figure 3. 9 FE mesh for the femur and the acetabulum.13150 four-nodes quadratic elements [Hambli et al., 2012]. The arrows represent the direction of the hip displacement.

The main purpose of this test, as mentioned above, was only to examine the applicability of the current developed 2D model for prediction of fracture location.

3.7.2 Evaluation of mesh sensitivity

To investigate the sensitivity of the femur structure responses and fracture pattern on the FE mesh size, sensitivity studies were conducted to quantify the effects of variations in mesh size on the 2D model-predicted reaction force–displacement relationship and proximal femur fracture locations as well as the fracture pattern. Overall, ten different mesh sizes, Table 3.4, defined by a global element size for the edges ranging from 0.25 to 2.5 mm were employed, generating 1000 to 20000 elements.

Table 3. 4 Different mesh sizes used for the evaluation of mesh sensitivity.

Mesh label	m01	m02	m03	m04	m05	m06	M07	m08	M09	M10
Mesh size, mm	0.25	0.5	0.75	1.0	1.25	1.5	1.75	2.0	2.25	2.5

The curves of reaction forces versus the imposed displacements are presented in Figure 3.10.

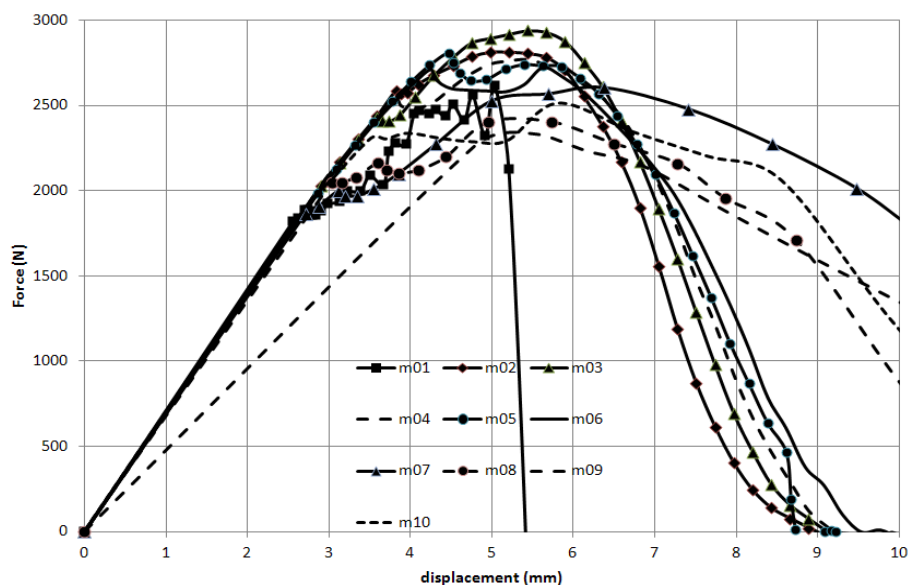


Figure 3.10 Reaction force versus vertical displacement, using ten different FEM meshes: finest mesh is labeled m01, coarsest mesh is labeled m10.

It was found that the models converged at element size in the range of 0.5 to 1.5 mm, on the contrary, at element size of 2.5 mm, the element stiffness presents a significant divergence.

Mesh size	Applied displacement		
	at 1.1 mm	at 4.37 mm	at 5.75 mm
m01			
m05			
m10			

Figure 3.11 Crack propagation (crack profile) in the course of the simulation at different instants for three different mesh sizes.

Figure 3.11 depicts some examples of the obtained crack profiles taken at three different instants: just before crack initiation, at crack initiation and just before complete separation of femur fracture. Only three representatives of ten mesh sizes were presented. The finest element size, 0.25 mm (m01), the middle (m05) and the coarsest one (m10). A distinct variation of the crack propagation and the volume left intact is evident from Figure 3.11.

Examination of the damage under compression loads in single limb stance of human femur head is presented in Figure (3.12). It shows that damage in the tensile zone near the greater trochanter has not suffered from high strains. Only the compressed lower neck side featured a significant damage which is concentrated at the basal zone area. However, elements with $D \geq 0.5$ were deleted. As expected, the coarser the mesh, the more volume is affected by damage as shown in Figure 3.12 and thus, the width of the remaining bone material linking the femoral head to the femur is reduced.

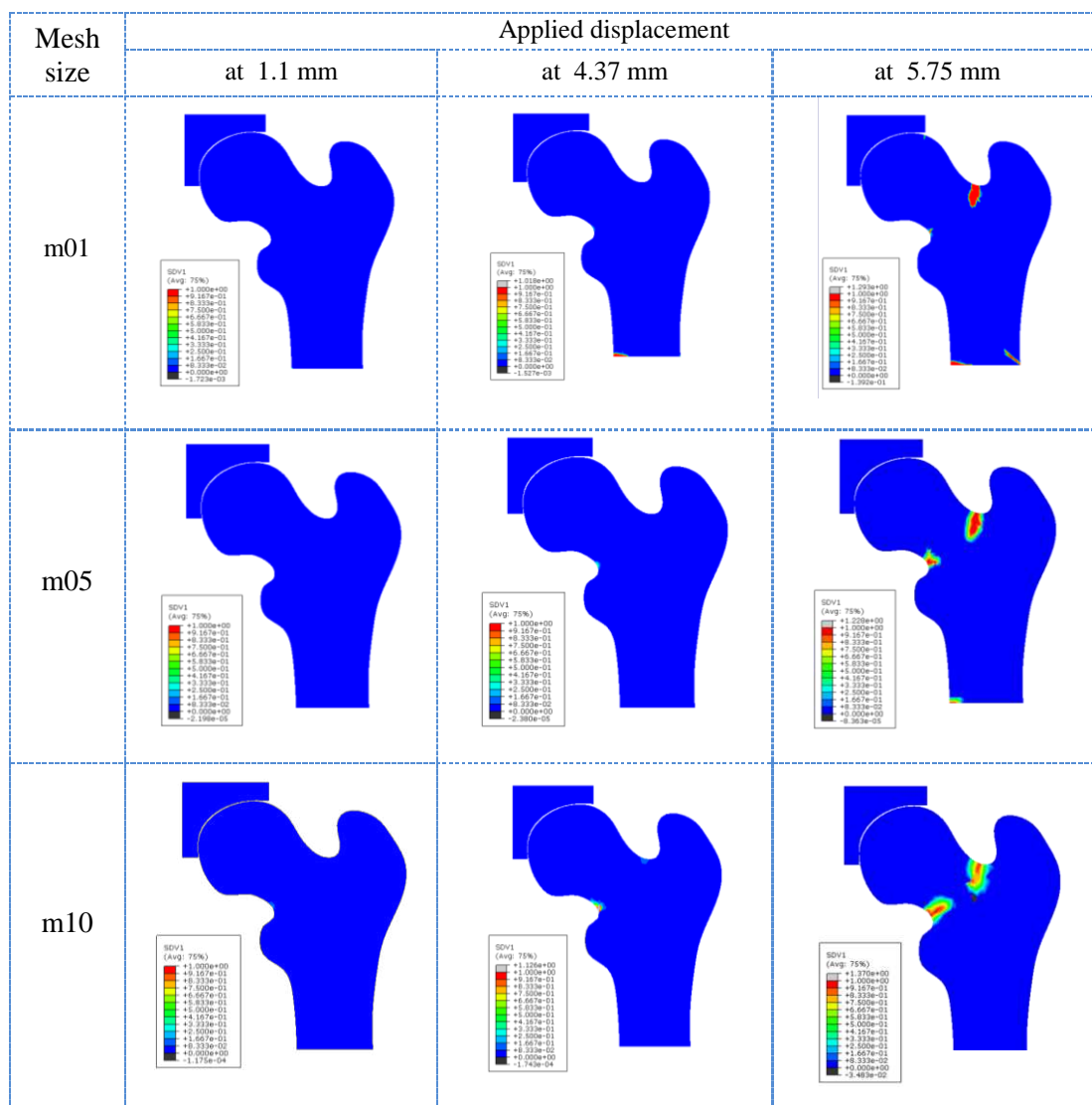


Figure 3. 12 Damage accumulations at different instants for three different mesh sizes.

As shown from Table 3.5, the peak value and the profile of the reaction force is little affected by the mesh size, the failure loads obtained were $2649,3 \pm 194,04$ N (discrepancy of 7.3) at fracture displacement of 5.244 ± 0.624 mm (discrepancy of 11.8%).

Table 3. 5 Resulted maximum failure force at 10 different mesh sizes (m01 to m10) and displacement (at crack initiation and complete fracture).

	No. of elements in femur	Force (N) maximum	Displacement (mm)		
			at end of linear range	at max. force	when force drops abruptly
m01	94148	2613	2,56	5,03	5,03
m02	23128	2812	2,9	5,21	6,13
m03	10380	2940	2,9	5,44	6,13
m04	5840	2767	2,9	5,44	6,59
m05	3712	2809	2,86	4,47	6,54
m06	2541	2708	2,86	4,23	6,31
m07	1938	2600	2,71	6,38	8,44
m08	1432	2400	3,03	4,95	7,28
m09	1223	2333	4,79	5,48	6,86
m10	950	2511	2,71	5,81	8,56

Generally, except for the coarsest mesh size (m10), the current model proved almost insensitive to mesh size. For an optimal balance between computational cost and precision, we chose an element size of 0.25 mm to mesh the homogeneous femur to investigate the effect of isotropic and orthotropic material assignment for the 2D quasi brittle damage model.

3.7.3 Effect of material assignment on two dimensional femur fracture pattern

As shown in Figures 3.13a-d, with isotropic behavior under excessive load deformation, the overall maximum stress started at the inferior cortex of the femoral neck. The evolution of the crack is initiated at the inferior cortex at an imposed displacement value of 1 mm. The crack then expands upwards, following an inclined path towards the upper surface resulting in a complete separation of the proximal femur.

In contrast, with orthotropic behavior, Figures 3.13e-h, the crack is initiated at the lower compression side, Figure 3.13e, and later separately at the tension side, propagates slowly then bifurcated into two directions towards the upper tensile side of the femoral neck.

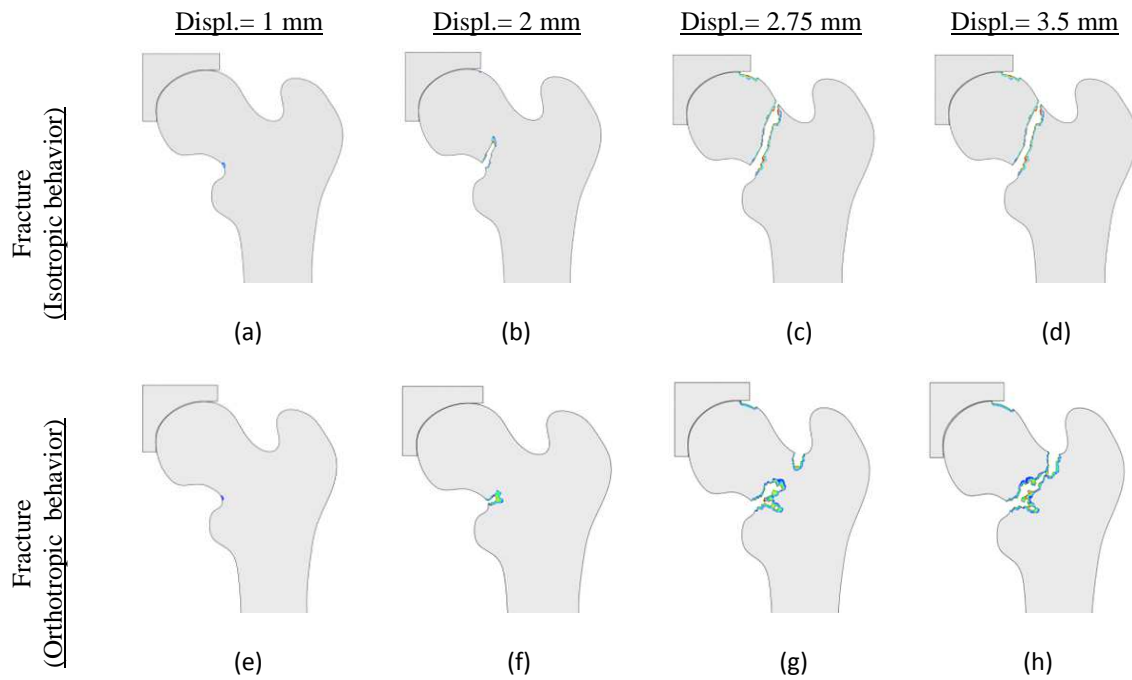


Figure 3. 13 Crack propagation in a homogenous human femur, mesh size (1 mm). Upper row: homogenous isotropic, lower row: homogenous anisotropic [Bettamer et al., 2012a].

At a displacement of 2.75 mm, crack is initiated close to the greater trochanter at the upper tension side, (Figures 3.13f and 3.13g), grows rapidly towards the lower compression side resulting in the complete separation of the proximal femur in the form of basicervical fracture at a displacement of 3.5 mm (Figure 3.13h).

The aim of this point of investigation is to test the ability of the proposed model to predict fracture profile depending on the femur head displacement (Figure 3.13). The results show that our coupled approach can be used to predict the progressive fracture profile through varying the material properties.

3.8. Conclusion

2D and 3D FE simulations models were presented in the current chapter. These models were based on isotropic /orthotropic behavior laws coupled to quasi-brittle damage. The 2D model was preliminary validated by using the right adult human femur model previously investigated by Keyak and Falkinstein and simulated until complete fracture under one-legged stance load. Mesh sensitivity of the current model was evaluated and the concept of coupled damage was introduced. A series of experiments will be presented in the following chapter which will be used to validate the proposed damage models.

Chapter 4

Experimental Work

Abstract

The experimental work will permit to validate the proposed finite element (FE) models. At the first, the current chapter presents the description and the preparation of the femur specimens used in the experimental part. The steps concerning the image segmentation as well as the data extraction from XCT and DXA images to generate finite element meshess will be described. Subsequently, a review of the experimental investigation under limb stance configuration, femur specimen testing will be presented. This configuration has been demonstrated, in previous studies, the ability to reproduce the observed clinical fractures. A totally original validation procedure in the case of femur deformation is developed based on 2D and 3D Digital Image Correlation (DIC) method. Finally the validation of the designed single limb stance assembly will be introduced.

Résumé

L'approche expérimentale permettra de fournir des données afin de valider les résultats obtenus par les modèles numériques. Dans un premier temps, ce chapitre présentera la description et la préparation des échantillons des fémurs utilisés dans la partie expérimentale. Les étapes concernant la segmentation des images ainsi que l'extraction des données à partir des images XCT et DXA pour générer des maillages éléments finis seront décrites. Par la suite, un état de l'art, sur les études expérimentales précédentes, sous la configuration d'appui monopodal et les essais réalisés dans le cadre de cette étude seront présentés. Cette configuration a été choisie car elle a démontré, dans des études précédentes, sa capacité à reproduire les fractures cliniques observées. La méthode de corrélation d'images numériques (en 2D et 3D) totalement nouvelle pour le cas de déformation du fémur sera utilisée. Enfin, une validation du dispositif de l'appui monopodal conçu à l'aide de fémur bovin sera introduite.

4.1. Introduction

Experimental approach comparing with Finite Element (FE) method predicted results, can provide comprehensive predication of mechanical properties and load that leads to failure of neck femoral. For this reason, the objective of the experimental branch in current work is to validate our predicted numerical results.

To introduce the experimental part of the current work, we will start by describing firstly, the steps of specimen preparation, data acquisition from Dual X-ray Absorptiometry (DXA) and X-ray Computed Tomography (XCT) and the steps of meshing the FE models which are used in the current work. Secondly, a review of single limb stance experiments is presented, the current designed experimental device and testing protocol will be introduced. Finally, the mechanical compression testing, loading conditions and assembly validation test will be discussed.

4.2. Femur specimens

In the current work, we used human femur bone to validate the proposed FE models and bovine femurs for validation tests of the designed fixture assembly. Ten human cadaveric femurs were obtained (7 women and 3 men, aged 85.9 ± 10.75 years, range 62–100 years) were purchased from the Institute of Anatomy (University of ParisV, Paris, France). In order to ensure disease-free specimens, for each specimen, a routinely certificate of non-communicable disease was issued by a hospital doctor. Serology for hepatitis C, HIV, HTLV1, HTLV2 was made before the acquisition. Eight specimens will be experimentally tested under axial load compression under single limb stance configuration.

4.2.1 Femur specimens preparation

The length of all human femur received was ranged from 167 mm to 207 mm. Each femur was cut transversely to a maximum length of 120 mm (scanning size limits) beyond the lesser trochanter to the head femoral as shown in Figure 4.1. This dimension has been chosen taking into account the space availability in the different devices that will be used later.



Figure 4. 1 Some samples before testing.

Freshly drawn femurs were wrapped between all processing steps in a cloth soaked in saline (NaCl 0.9%) in order to avoid dehydration. Prior to degreasing, each specimen was marked with a label carrying the date and time of bleaching. Then the femur specimens were immersed in hot water (see Figure 4.2) at a temperature of 85°C by using a thermometer to regulate the temperature. A bleaching agent of 30 ml was poured in the container. Subsequently, the specimens were boiled for two hours and defatted softly, without causing any damage to the bone. This degreasing was done to avoid fat-melting during scan operations which last hours and cause an increase in temperature. This operation was repeated twice for each specimen after cooling between two stages. The specimens were then allowed to cool to room temperature in the container and finally stored in the refrigerator at 4° C.

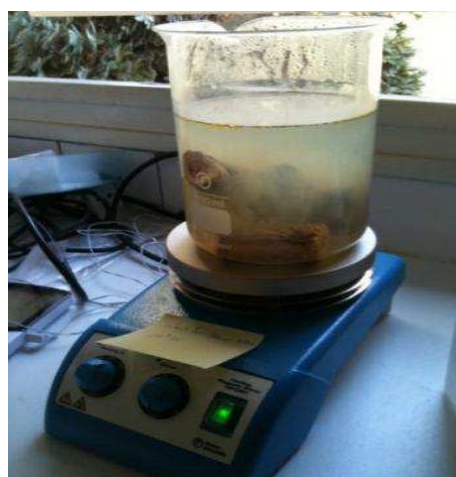


Figure 4. 2 Degreasing process of human femur specimens.

Then, in vitro Dual X-Ray Absorptiometry (DXA) scans of the femurs were obtained with a Hologic QDR 4500 scanner (Hologic Inc., Waltham, USA) using the standard protocol

for the proximal femur. Standard positioning was used across all specimens, and the proximal femoral and neck areal Bone Mineral Density (BMD) was evaluated with the software provided by the manufacturer (Table 4.1).

Table 4.1 Measured total and neck femoral densities for human femur specimens.

Femur ID	Weight	R/L	Age	Sex	BMD Neck, g/cm ²	BMD Total, g/cm ²
A	235.0	Left	62	Male	0,41	0,64
B	244.0	Left	98	Female	0,45	0,72
C	276.0	Right	85	Female	0,50	0,75
D	273.0	Left	85	Female	0,48	0,68
E	378.0	Right	91	Female	0,75	0,83
F	388.0	Left	91	Female	0,79	0,86
G	244.0	Left	98	Female	0,49	0,62
H	271.0	Right	80	Male	0,43	0,53
I	277.0	Left	80	Male	0,44	0,61
J	263.0	Left	87	Female	0,51	0,68

In order to study the effect of femur geometry on failure loads of proximal femur, different geometrical parameters of all femur specimens were taken using ABAQUS measuring commands. As shown in Figure 4.3 the following parameters are measured: femoral neck axis length (AB), femoral head diameter (CD), femoral neck width (EF), cervical-diaphyseal angle (H), trochanteric-diaphyseal diameter (IJ), diaphyseal diameter (KL), and length of femur specimen (L_1) and the diaphyseal length (L_2). These physical measurements are compiled in Table 4.2.

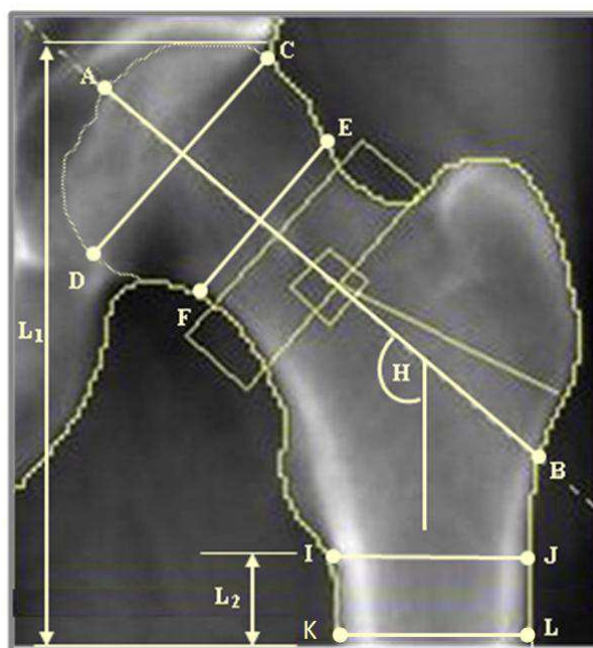


Figure 4.3 Definition of the parameters measured for femur specimens [modified from: Bonnet et al. 2007].

Table 4. 2 Physical dimensions measured for human femurs, mm.

Femur ID	AB	CD	EF	H,deg	IJ	KL	L ₁	L ₂
A	85,12	42,30	30,69	126,00	34,76	27,20	167,00	88,50
B	86,10	42,12	29,83	132,00	31,70	28,15	167,00	86,50
C	90,20	44,25	31,52	129,50	32,60	29,10	187,00	106,70
D	90,02	45,70	31,20	129,00	30,40	29,00	184,00	105,70
E	104,93	50,60	39,89	129,50	34,35	31,10	193,00	94,25
F	104,70	50,10	39,16	132,00	36,10	32,20	184,00	97,50
G	103,44	46,10	32,97	118,00	34,14	30,06	175,00	80,10
H	95,41	43,40	32,56	122,50	33,60	27,40	207,00	108,00
I	107,05	50,30	35,15	117,50	33,90	31,90	193,00	104,10
J	96,68	42,80	31,87	128,50	31,70	28,80	184,00	96,80

4.3. Image acquisition

Image acquisition is the first process concerning the generation of mesh models. This process is performed by using DXA to generate 2D FE model and XCT to generate 3D FE model.

These non-invasive techniques have gained considerably in importance due to continuous improvements in X-ray tubes and XCT devices. These systems are based on the property that X-ray beams satisfy differently in bone and soft tissues as a function of photon energy [Testi et al., 1999]. They can achieve resolutions down to 1 μm . Besides, they enables the generation of accurate FE models for the human femur [Keyak et al., 1998, Cody et al., 1999].

4.3.1 Image Segmentation

Prior to simulating the mechanical properties of the femur, the images are usually segmented for the different phases of the femur to be identified. This process consists of the extraction of outer surface in 3D or outer contours in 2D. The segmentation process consists in partitioning the 3D image voxels into distinct parts based on their grey level values. The segmentation process consists of three main operations: filtering, binarisation and correction [Aufort et al., 2007].

4.3.1.1 Data from DXA

In order to identify our FE models, computer codes were applied by introducing data base form DXA and XCT. These codes were achieved in collaboration with Dr. Rozenbaum's group at the ISTO (Institute des Sciences de la Terre d'Orléans).

First the contour of each image was identified. The images were imported into the MATLAB software. The images were detected after performing several operations like edge dilation the boundary.

The true color image was converted to a grey-scale image (which carries the image intensity information) and used for calculating the density (Figures 4.4a and 4.4b).

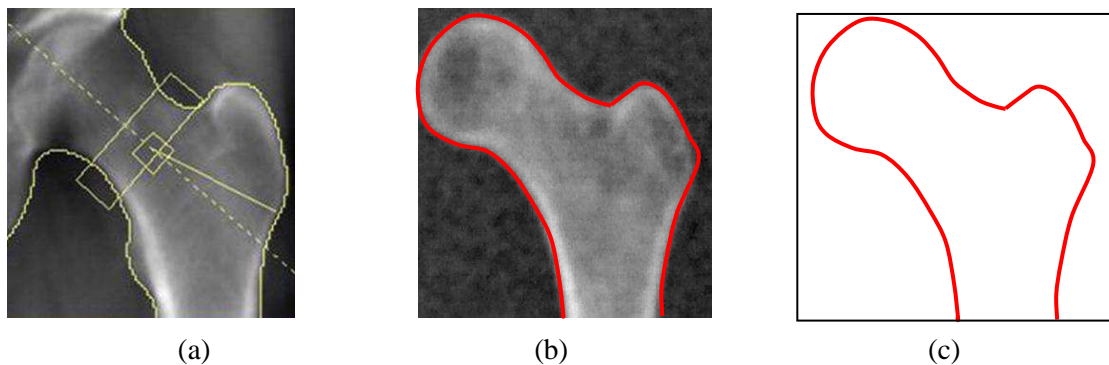


Figure 4. 4 (a) DXA of a proximal femur specimen (b) Grey-scale image obtained from the DXA scan data set of an artificial composite femur (c) contour extraction.

The gray value of each pixel was converted into density of that pixel. A linear correlation was assumed between pixel value and density [Schileo et al., 2008]. As part of the data extraction, Young's modulus was correlated to the density using an exponential correlation, shown in Table 2.1, developed by Keyak and Falkinstein [Keyak and Falkinstein, 2003]. Finally the projected 2D heterogeneous FE model compatible for ABAQUS/Standard code were created.

4.3.1.2 Data extraction from XCT images

In order to localize and determine the volume of interest concerning a selected femur, a segmentation technique was applied. This process has been implemented in collaboration with Dr. Rozenbaum's group at the ISTO laboratory of CNRS-Orléans and Prof. Jenanne's group at the PRISME laboratory of the University of Orléans. Images were obtained using the Skyscan 1072 high-resolution μ CT. The X-ray source was set at 80 kV and 100 μ A, and the magnification was set so as to obtain a pixel size of 50 μ m. A 1024_1024 12-bit digital cooled CCD coupled to a scintillator was used to record the radio-graphic projections. A total of 209 projections were acquired over an angular range of 180° (angular step of 0:9°).

This technique was achieved into three steps: filtering, binarization and correction.

➤ Filtering

The acquired real images are usually noisy, and the noise level highly depends on the quality of the imaging system. In this work, a standard median $3 \times 3 \times 3$ filter was applied in order to reduce possible artifacts such as impulsive noise.

➤ Binarisation

The filtered images were binarized in order to separate bone voxels from pore voxels. A standard binarisation method was applied. In this method, a threshold defined as the local minimum between the two maxima of the histogram of the filtered image was first determined. Then, voxels whose grey levels were below this threshold are considered as pore voxels. The remaining ones were considered as bone voxels.

➤ Correction

After the binarisation step and in order to take into account the anatomical constraints of porous objects, a correction step was applied. Since, all trabeculae of bone tissues are interconnected; the binarised image was verified to ensure the existence of only one connected structure (see Figure 4.5). For this purpose, the Hoshen-Kopelman's clustering algorithm was used [Hoshen and Kopelman, 1976]. Using HK algorithm, each group is assigned a distinct label. The principal (largest) cluster is kept and voxels of the other smaller clusters are considered as pore voxels.

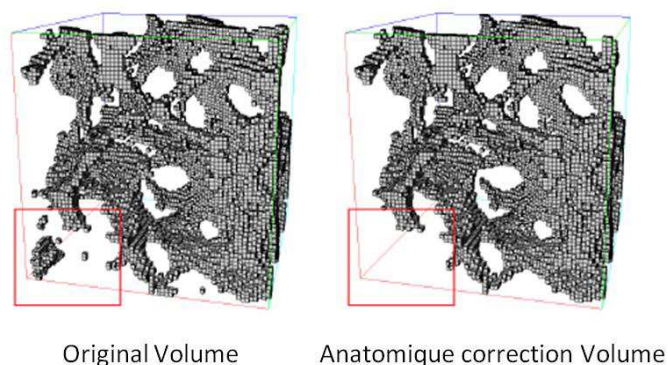


Figure 4. 5 Image segmentation: correction step.

A 3D segmentation software developed at the ISTO was used to automatically identifying cortical and trabecular components of the proximal femur and isolated from the environment in which the bone was scanned (water and air). The values of the voxels are

then converted into two values: '1' for voxels constituting the bone, '0' for the rest (water, air ... etc).

Thus, the segmentation provides a new volume of interest data. The corresponding original grey-level data provides the mechanical properties (section 4.4.1) while the corresponding binary data provides the geometry characterization.

4.4. Femur specimen mesh generation

Various physical properties of the characterized femur specimens were defined using the corresponding meshed FE models. In order to reproduce such models, several image processing methods were applied as indicated in Figure 4.6. All data required for constructing a FE model were extracted from both DXA and XCT images.

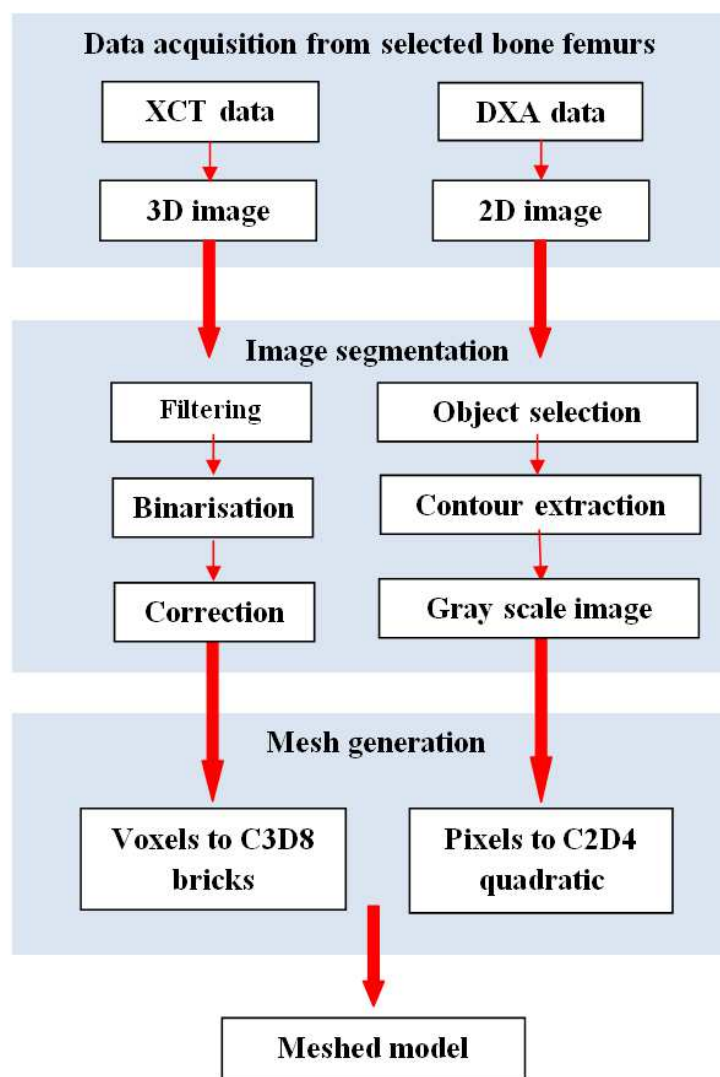


Figure 4. 6 Steps of meshing a FE model from DXA data.

For 3D FE, the entire proximal femurs structures are modeled using ABAQUS/Standard code, element types of C3D8 (8-node quadratic brick). Each voxel of femur structure is converted to a FE. These conversions produce accurate geometrical models and allow modeling the complex porous structures of the trabecular bone.

Table 4.3 compiles the human femurs along with the spatial resolution used in the current 3D simulation.

Table 4.3 Human femur resolution and dimensions used in the current simulations.

Human Femur	Type of Mesh	Dimensions (voxels)	Dimensions (mm)
A	C3D8	168 × 260 × 94	8.40 × 13.000 × 4.700
B	C3D8	180 × 260 × 93	9.00 × 13.000 × 4.650
C	C3D8	230 × 268 × 93	11.50 × 13.400 × 4.650
D	C3D8	190 × 270 × 92	9.50 × 13.500 × 4.600
E	C3D8	180 × 260 × 88	9.90 × 14.300 × 4.840
F	C3D8	180 × 260 × 92	9.90 × 14.300 × 5.060
G	C3D8	200 × 280 × 87	10.00 × 14.000 × 4.350
H	C3D8	190 × 280 × 90	9.50 × 14.000 × 4.500
I	C3D8	200 × 260 × 97	11.00 × 14.300 × 5.335
J	C3D8	190 × 275 × 100	10.45 × 15.125 × 5.500

4.4.1 Relation between grey level and mechanical properties

The porous body formed by a complex network of bone trabeculae has particular mechanical properties, which are determined not only by their porosity, but also by the arrangement of trabeculae in the 3D space. In the current work, each femur specimen, cortical and trabecular bone tissue were identified based on the number of elements in a fixed neighborhood. Each element was assigned a Poisson's ratio of 0.3 and an isotropic Young's modulus that depends on tissue type according to the CT gray value using the empirical equations mentioned above in chapter (2), Table 2.1.

For each voxel, elastic modulus was computed from the ash density of bone (ρ_{ash}) using the following correlations for both trabecular and cortical bone [Keyak and Falkinstein, 2003] :

If $\rho_{ash} \leq 0.27$ then the CT scan voxel element was considered as trabecular bone and its elastic modulus E_{Trab} (in MPa) was calculated by using the following empirical equation:

$$E_{Trab} = 33900 \rho_{ash}^{2.20} \quad (4.1)$$

If $0.27 < \rho_{ash} < 0.6$ then the CT scan voxel element was considered as bone in a transition phase (between trabecular and cortical) and its elastic modulus $E_{Trab/Cort}$ (in MPa) was calculated by using the following equation:

$$E_{Trab/Cort}(\rho_{ash}) = 5307 \rho_{ash} + 469 \quad (4.2)$$

If $\rho_{ash} \geq 0.6$ then the voxel element was considered as cortical bone and its elastic modulus E_{Cort} (in MPa) was calculated by using the following empirical equation:

$$E_{Cort} = 10200 \rho_{ash}^{2.01} \quad (4.3)$$

The ash density (in g/cm^2) for each CT scan voxel was computed from the calibrated CT scan data, [Keyak and Falkinstein, 2003]:

$$\rho_{ash} = 1.2 \rho + 0.0526 \quad (4.4)$$

4.5. Femur specimen testing

In vivo, the femoral neck may undergo different loads. Compressive load through the femoral head acts through a significant moment arm (the length of the femoral neck), which causes large bending loads on the femoral neck [Browner et al., 2009].

In vitro, femur bone has been subjected to all these experimental tests in order to investigate and to assess common daily fractures. However, the most common cause of long bone fractures due to torsion and bending forces occurs, in vivo, in the central third of the shaft [Bramer et al., 1998] which is out of the scope of the current research. We are interested in femoral neck fractures. We believe that the activity and loading on a relatively unprotected hip are the most likely causes of fractures and leads to considerable mortality.

Hence, the main objective in the current work is to assess the femoral neck fracture under one-legged stance loads. This evaluation is necessary to study the incidence of spontaneous fractures [Cristofolini et al., 2007] and the behavior of the hip during daily activities [Juszczak et al., 2011].

4.5.1 Single limb stance test

Some studies have conducted tests with a femoral shaft parallel to the vertical where the proximal femur is mainly subjected to shear [Beck et al., 1990, Esses et al., 1989, Lochmüller

et al., 2002]. Other investigations used angles varying between 7 and 15° [Alho et al., 1988, Bonnaire et al., 2002, Fedida et al., 2005, Kukla et al., 2002, Leichter et al., 1982].

Table 4. 4 Summary of experimental force at fracture values and different force angles under single limb stance configurations.

Force direction	No. of specimens male	female	Force at fracture (N)	Reference
$\theta = 0^\circ$	11	11	1500- 13000	[Beck et al.,1990]
	4	4	200-9550	[Esses et al., 1989]
	34	24	933-7000	[Lochmüller et al., 1998]
	42	63	2740-6100 (male) 1980-3840 (female)	[Lochmüller et al., 2002]
$7^\circ \leq \theta < 15^\circ$	18	18	2750 – 9610	[Alho et al., 1988]
	13	10	4000-12000	[Bonnaire et al., 2002]
	9	1	6319-16040 (male) 7931(female)	[Cristofolini et al., 2007]
	13	7	8430	[Kukla et al., 2002]
	9	9	1599-12753	[Leichter et al., 1982]
	3	0	5916-8041	[Schileo et al., 2008]
$15^\circ \leq \theta \leq 25^\circ$	28	23	6701-13139	[Cody et al., 1999]
	4 (mixed)		7809-12595	[Kaufer et al., 1974]
	8	10	1600-14200	[Keyak et al., 2001]
	13 (mixed)		3500 - 13000	[Lang et al., 1997]
	1	11	3121-8408	[Le bras, 2004]
	22 (mixed)		4937 - 16148	[Smith et al., 1992]
	40 mixed		3579-17711	[Delaere et al., 1989]
5	6	3600-6700	[Bessho et al., 2007]	

During walking and standing, the resultant load vector (F) makes an angle of 16° to the vertical of the femoral neck [Delaere et al., 1989] offset by 3° of the femoral shaft axis from the sagittal plane [Hollister et al., 1993, Sermon et al., 2012]. Therefore, angles ranging from 15° up to 25° were adopted in other researches [Cody et al., 1999, Lang et al., 1997, Le Bras, 2004, Kaufer et al., 1974, Smith et al., 1992, Keyak et al.,1998, 2001, 2005, Tadashi et al.,2007, Van der Steenhoven et al., 2012]. Keyak and Falkinstein, [Keyak and Falkinstein, 2003], made some interesting investigations based on a validated FE models of human

proximal femur under single limb stance loads. They used to apply an angle of 20° in their validated simulations. Picking this arrangement as reference configuration, the same angle was applied in the current thesis. Table 4.4 represents a summary of the reported in vitro destructive tests together with the different directions of the applied force in single limb stance and the obtained failure loads.

4.5.2 Measuring methods used to measure bone deformation

Mechanical in vitro testing of bones is often used on cadaveric human studies in order to evaluate the failure locations. Some parts of the human body have complex geometries such as the proximal femur. The deformation of such geometry when subjected to axial loads requires an accurate measuring tool able to capture the deformation of such complex geometry deformation. The simplest mode of gathering displacement values by the machine LVDT has several essential advantages. The measurement of the actual deformation in the sample is much more intricate, since the measured deformation is not uniquely related to the actual deformation of the specimen.

Strain measurements from bone surfaces can be achieved by using several applications. Although various strain measurement methods such as photoelasticity, holographic interferometry and brittle coating have established, the most common is electric resistance strain gauges [An and Draughn, 2000].

While it is possible to use strain gages, their major disadvantages impose rigorous limitations on the strain value that can be applied to the sample. However, strain gauges measurements of bone deformation are frequently applied in bone mechanics and often used for validation purposes in computer models [Yosibash et al., 2007]. Lotz et al. [Lotz et al., 1991a,b] used the data obtained by strain gauges to validate their simulation model of proximal femur. Composite synthetic models are also tested and strain gauges were applied to assess local deformations [Cristofolini et al., 1996]. When strain gauges are applied, they need to be firmly glued onto the material. It must be assumed to undergo the same deformation as the material without affecting the stiffness. Even if using a large number of strain gages, they do not provide sufficient spatial resolution nor 3D components of strain distributions in zz, xy or xy directions [Yang et al., 2011], thereby risking misinterpretation and large experimental errors [Yosibash et al., 2007].

Besides the restriction to one single spot, several additional constraints can be cited:

- The necessity of a plane and smooth surface to bond the strain gauge.
- Technically, the surface for bonding strain gauges should be free from organic contamination, greases, water proof and sufficiently rough which are almost impossible to reach these cruel conditions.
- The attachment of the strain gauges to the bone surface might stiffen the bone slightly, resulting in an overestimation of stiffness.
- The experiment must be conducted strictly isothermally as temperature effects are the most common cause of error in application of strain gauges.

In order to overcome the above mentioned limitations, optical methods such as Digital Image Correlation (DIC) and Digital Speckle Pattern Interferometry (DSPI) have seen remarkable growth in the recent years. DSPI is also a non-contacting measuring tool like DIC. Even though DSPI was applied to measure 3D bone strain field [Zhang et al., 2001], the surface deformation was not evaluated. Later on, DSPI was applied and local surface contour was evaluated on mouse femora [Yang et al., 2007].

However, due to the relative ease of use and versatility of the methods, the use of 2D-DIC and 3D-DIC becomes widespread in measuring the surface displacements.

2D-DIC was used to study the local distributions of mechanical strain on a section of sheep bone callus- a hard bony tissue that develops around the ends of a fractured bone during healing [Thompson et al., 2007].

3D-DIC has been used earlier for macroscopically strain measurements to determine the local strain in human cortical bone or at microscopic scale to analyze strain distribution around a microcrack around osteocyte lacunae in cortical bone [Nicoletta et al., 2006]. In trabecular bone this technique was used to calculate and visualize the local strains in single trabeculae [Verhulp et al., 2004]. Further studies have applied 3D-DIC method on cartilage [Zhang et al., 2005], and bone fracture callus [Thompson et al., 2007] in order to measure their strains under different loads. Recently, Sztefek et al. [Sztefek et al., 2010] have used sample sections of tissue under conditions directly representative of applied in vivo loading and used 3D-DIC to measure a murine tibia during compressive loading of the knee joint.

Despite the utility of DIC as a tool in the field of experimental solid mechanics [Tiwari et al., 2007], to the best to our knowledge, there are no previous studies have applied it to measure in vitro the 3D surface topology deformation of human cadaver femur.

4.5.3 Single limb stance fixture assembly

Several types of experimental assemblies were suggested to simulate the single-legged stance of human femur in order to measure the experimental mechanical response of proximal femur. The objective is an attempt to recreate the loading conditions of the femur in single limb stance in order to reproduce the several clinical types of fractures.

The proposed assembly for the single limb stance test consists of two main parts: **lower and upper parts** (See Figure 4.7a). The lower part is fixed to the base of machine.

The upper part, in turn, consists of two pieces:

- **Secondary base:** it is designed to be rotatable around the horizontal axis to form an adjustable angle (α) and is shown in Figure 4.7. This option allows testing the femur at various angles. The slot permits to align the head of the femur with the line of applied machine force.
- **Upper sleeve:** this part is attached to the secondary base by means of four screws. The upper sleeve is attached for fastening the femur bottom by means of four fixing screws. The distal part of the tested femur specimens are embedded in this upper sleeve through resin casting.

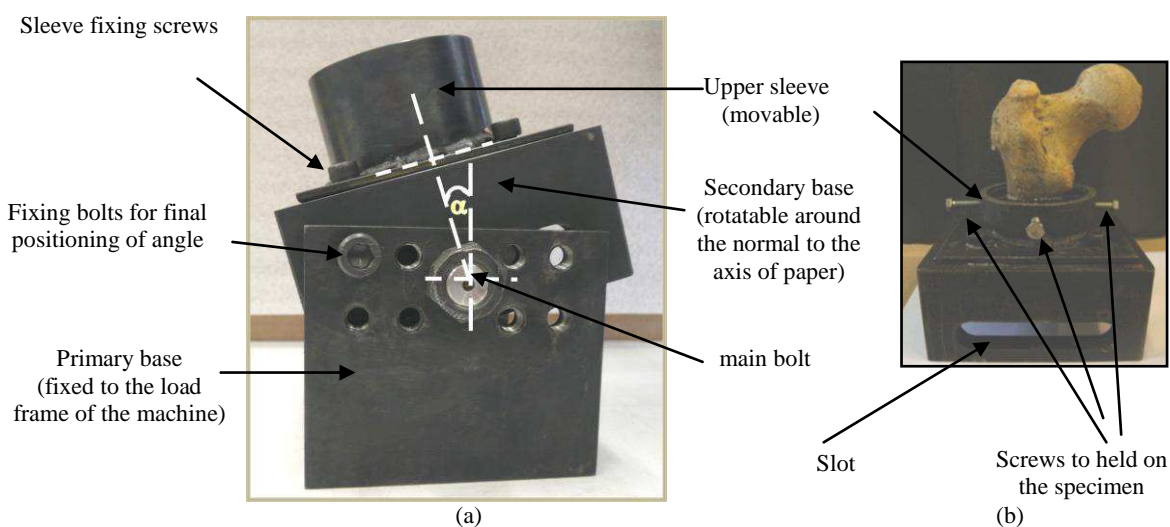


Figure 4.7 Assembly for the single limb test designed in the current research: (a) assembled device, (b) assembly of the secondary base and upper sleeve.

The assembly is designed to safely hold the specimen in place up to a compressive force of 25 kN. This force is greater than that reached in tests reported in the literature (Table 4.4) and gives the opportunity to test other types of femurs.

During testing, four screws held the specimen in a vertical position with respect to the upper part. They also permit to avoid contact between the femur and the walls of the upper part without any pressure being exerted on the specimen surface.

The current fixture assembly provides the following advantages:

- The possibility to make different experiments by applying axial loads at different angles through changing the angle of rotation (α).
- As the upper sleeve is movable, this provides the possibility to fix other sleeves with different diameters. Hence this device can serve over a wide range of different femur types up to the maximum design load.
- The slot in the secondary base part gives the possibility to easily align the head of the femur with the line of interaction of the applied axial compression load of the testing machine.

4.5.4 Mechanical compression test of single limb stance loading configuration of human femur specimens

The compression test was performed in a single limb stance configuration. This position has demonstrated, in previous studies, the ability to reproduce the observed clinical fractures.

The test preparation as well as test conditions are as follows:

- (i) The human cadaver femurs were installed in the single limb assembly presented in Figure 4.7 and maintained in the center of upper sleeve by using the four fixing screws.
- (ii) The distal portion of each femur is fixed by using a casting of epoxy resin (SICOMIN Epoxy Systems, France) which was prepared by mixing 100g of resin (SR 1500) with 33g of hardener (SD2505).
- (iii) The assembly of fixture and femur is left at room temperature so that the resin cures (from 4 to 6 hours).
- (iv) The fixing screws are loosened upon solidification of the resin and the assembly is stored at 4°C until performing the compression test.
- (v) Three hours before use, the assembly is removed from the refrigerator. Noting that the fact to cool and removing the femur from the refrigerator have an effect on his behavior because the bone is a living material. But these necessary steps have been

minimized and standardized as possible so as not to alter too much the behavior of the bone.

- (vi) The assembly is mounted on a universal testing machine Instron, equipped with a load cell of 200 kN (see Figure 4.11) and is oriented within the coronal plane at 20° [Keyak and Falkinstein, 2003, Keyak et al., 2009, Dall'Ara et al., 2013].
- (vii) The compressive load is applied with a crosshead speed of 2 mm/min [Heini et al., 2004].

The displacement of the crosshead is measured with LVDT and is continuously recorded throughout the test along with the applied force. In order to determine displacement and the strains fields of the specimens, optical methods are used. Two optical charge-coupled device cameras (CCD), connected to a computer, were used to continuously record images of the sample surface during the test. The maximum image resolution of this camera is 1380×1024 pixels with a 8-bit digitization for grey levels ($2^8=256$ grey levels). The maximum acquisition frequency used is one image per second. Images are recorded, digitized and stored in a computer as digital images. During the compression tests, a lamp is installed in front of the samples to illuminate them in order to not affect the acquisition by the natural light variations in the room. After that, image processing is performed using the softwares Deftac 3D and 7D-3D [Vacher et al., 1999] based on the Digital Image Correlation (DIC). The outcome are the displacement fields in the three directions on the surface of the specimens.

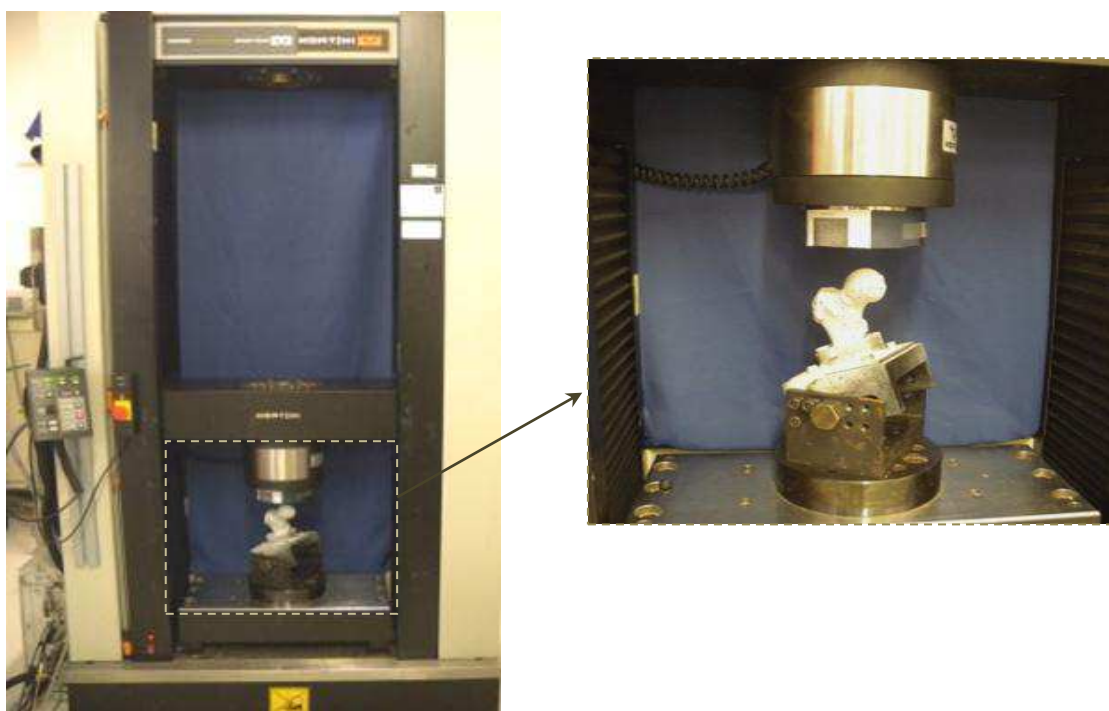


Figure 4. 8 Universal testing machine.

4.5.4.1 Deformation and displacement measurement under compression conditions using DIC method

Displacement and deformation data were measured by using Digital Image Correlation (DIC) method.

The method offers the following advantages [Tyson et al., 2002]:

- Non-contact and Full-Field measurement.
- The possibility to visualize strain gradients and 3D details which are obscured if strain gauges are used,
- The DIC method is particularly suited for use with non-homogenous and anisotropic materials such as bone.

The testing technique is as follows:

Digital image correlation is an optical full-field technique that enables non-contact 2D or 3D deformation measurements on material surfaces. This method has been introduced in the 1980s [Sutton et al., 1983, Peters et al., 1982] and is now widely used in different scientific fields such as biomechanics [Thompson et al., 2007]. The prime advantage of this method is that it makes it possible to measure both local and global variations of the displacement field of a structure under mechanical loads.

The principle of DIC is to assess the displacements fields, and thus strains fields over the surface of a deforming material by comparison of two images acquired at different stages of the deformation (see Figure 4.9). The first image is referred to as the “reference image” or “undeformed image” and the second, acquired after some increment of deformation, as the “deformed image” [Murasawa et al., 2006].

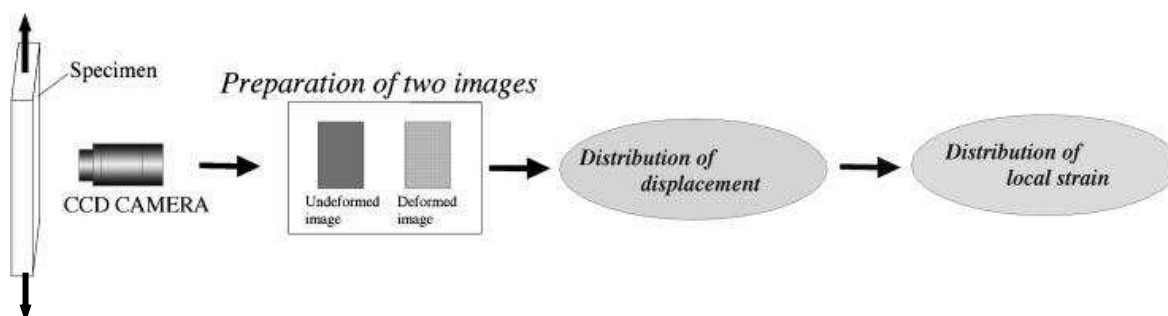


Figure 4. 9 The steps in recording of the displacement distribution and local strain by using Digital Image Correlation. (a) Image acquisition, (b) Digital image correlation and (c) Computation of local strain [Murasawa et al., 2006].

Prior to starting the measuring process, a region of interest (ROI) is manually defined on the initial image and divided into small subsets (squares). Then, a grid of analysis points is

mapped over the reference image and finally, a group of pixels, commonly called a “subset” (see Figure 4.10), is defined about each node of this grid [Bouhas et al., 2008]. Image correlation is performed, for each node, by identifying the most similar subsets in the reference and deformed image based on some statistical measure of correlation of the images within each subset. Once the location of this point in the deformed image is found, the local strain tensor can be determined from the spatial distribution of the displacement field for each image

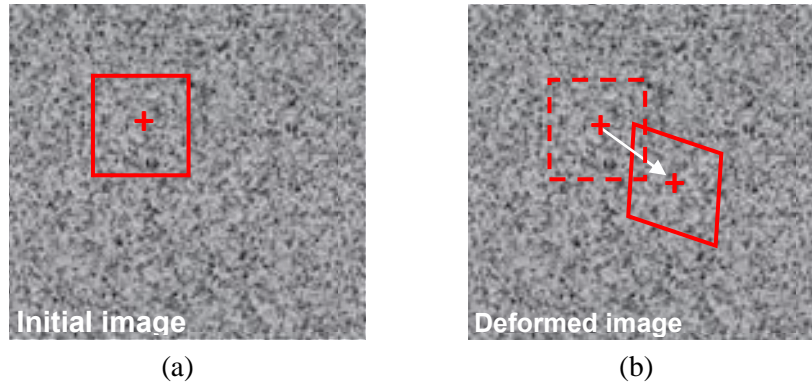


Figure 4.10 Region of interest area on a reference image and a distorted picture, (a) Undeformed image (reference image), (b) Deformed image [Bouhas et al., 2008].

The DIC software used in this work is 7D which was developed at the Université de Savoie [Vacher et al., 1999]. In this software, the statistical measure of correlation used to assess the matching of the subsets is the “zero mean-normalized cross correlation” coefficient (C):

$$C = 1 - \frac{\sum_{i \in D} (f(X_i) - \bar{f}) \times (g(x_i) - \bar{g})}{\sqrt{\sum_{i \in D} (f(X_i) - \bar{f})^2} + \sqrt{\sum_{i \in D} (g(x_i) - \bar{g})^2}} \quad (4.1)$$

where D is the subset over which the correlation coefficient is calculated. The functions f and g are the grey-level values at pixels coordinate X_i and x_i in the reference and deformed images, respectively. The terms \bar{f} and \bar{g} are the mean grey-levels for all the pixels in a subset of the reference and deformed images, respectively.

This mean-normalized formalism implies that the correlation coefficient is almost invariant with any change of lighting conditions between the two images. For each subset, the optimum correlation is given by the transformation that maps X_i onto x_i and minimizes C.

For this technique to work well, a grey scale random pattern is needed on the surface of the specimen. However, it would be extremely difficult to distinguish every single pixel on

the image because the matching point is elusive. Therefore, an area with multiple pixel points is used to perform the matching process. This area, usually called subset, should contain several clear features but it is often a compromise between resolution and accuracy. As a general rule, larger subset sizes will increase the accuracy whereas smaller ones will increase the resolution. In practice, the size of a subset is determined by the quality of the image and speckle pattern.

When dealing with the deformation of non-planar surfaces, a 3D DIC acquisition should be used. For this purpose it is necessary to use two CCD cameras placed at two different locations in front of the sample. These two cameras must be oriented at different angles in order to capture the same area of the tested specimen.

The technique consists in measuring displacement fields by registering interrogation volumes (i.e., whose size defines the spatial resolution) by the help of a binocular stereovision. This technique, demonstrated in Figure 4.11, is able to provide a 3D description of a scene viewed from two different viewpoints.

As shown in Figure 4.11, point $P(X,Y,Z)$ is the 3D point to be measured, points $p_1(u_1,v_1)$ and $p_2(u_2,v_2)$ are its stereo projections in the images, C_1 and C_2 are the optical centers of the two cameras. From a pair of images, it is possible to compute the 3D coordinates of a physical 3D point by firstly matching two images. This can be performed by determining the relative positions of the points p_1 and p_2 and their directions with respect to the position vector of the same physical point P . Secondly, defining the relative position vectors of the two cameras, points C_1 and C_2 .

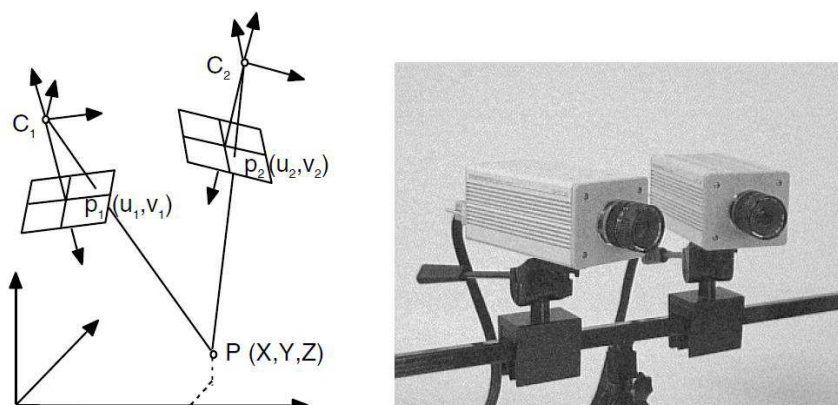


Figure 4.11 Binocular stereovision. The point to be measured $P(X,Y,Z)$, $p_1(u_1,v_1)$ and $p_2(u_2,v_2)$ are its stereo projections in the images, C_1 and C_2 are the optical centers of the two cameras [Garcia and Orteu, 2001].

Once P_1 and P_2 have been matched from a pair of images, it is possible to compute the 3D coordinates of a physical 3D point (P) by triangulation method [Garcia and Orteu, 2001].

To exploit the potential of the measuring process using the DIC technique, enhancing the contrast on the grey scale random pattern is mandatory on the surface of the specimen before testing. In the current study, the specimens are first painted with a white paint before applying a random speckle pattern with spray black paint (see Figure 4.12). The software (7D) is able to capture this pattern on the first image and identify it in an image series. A correlation function is pre-defined to evaluate the similarity between the reference and target subsets.

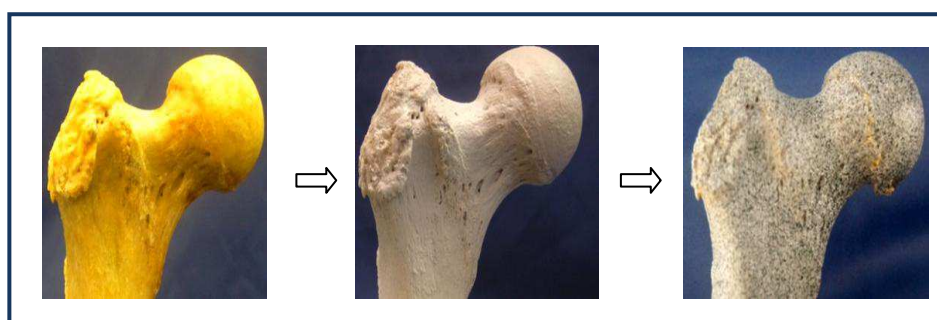


Figure 4. 12 Applying speckle pattern. (a) Femur specimen before applying the speckle pattern, (b) Femur painted with white paint pattern and (c) Femur with spray black paint speckles to enhance the image contrast for Digital Image Correlation processing.

The femurs were painted and scanned with the stereoscopic device. After that, a region of interest (ROI) was selected (see Figure 4.13) and image processing was performed using the software 7D according to the steps detailed below. The 3D DIC was then used and the surface topography in the main 3D directions and the geometry of the 3D external shape were well rebuilt (see Figure 4.13). This confirms that the specimen for preparation protocol and the speckles are well suited.

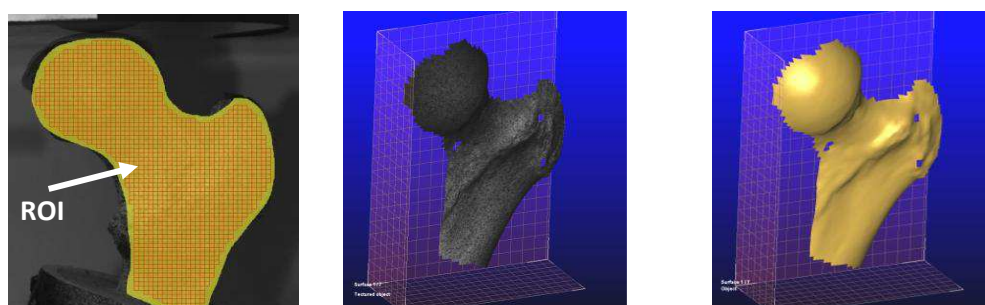


Figure 4. 13 Geometrical reconstruction of the 3D external Shape of the region of interest (ROI) in the reference configuration.

4.5.4.2 Validation of the designed single limb stance assembly and measuring protocol

To validate the designed single limb assembly and the fixture protocol, three fresh bovine femurs were tested (see Figure 4.14). The specimens were cleaned and prepared using the identical testing protocol as used for the human femur. The assembly together with the resin showed good performance during the single limb compression conditions i.e. no cracks in the resin could be observed during load application or its removal of the specimen from the testing machine. Also, no damage was observed at the distal end which comes in contact with the resin.

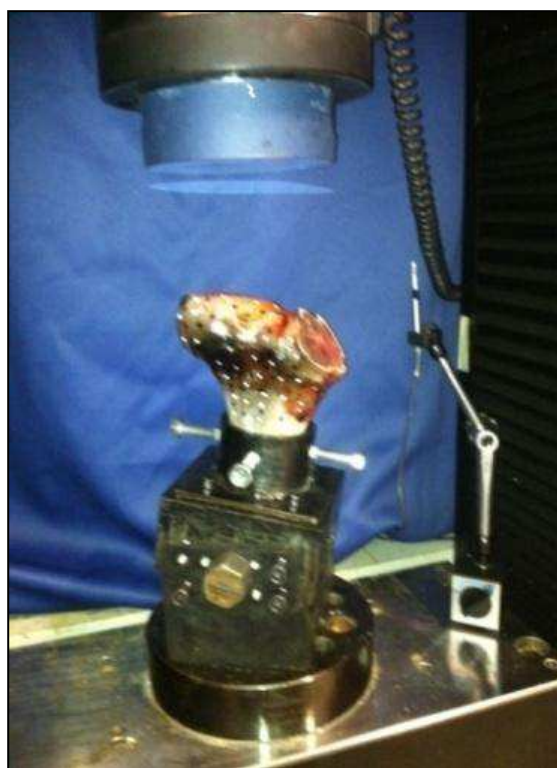


Figure 4. 14 Mechanical test validation on bovine femur in single limb configuration.

An example of the obtained force-displacement curve is presented in Figure 4.15.

Under axial load, the femur of the experimental validation group presented minimal (4.4 mm) subsidence at 2964 N. The ultimate force was defined as the peak of the curve.

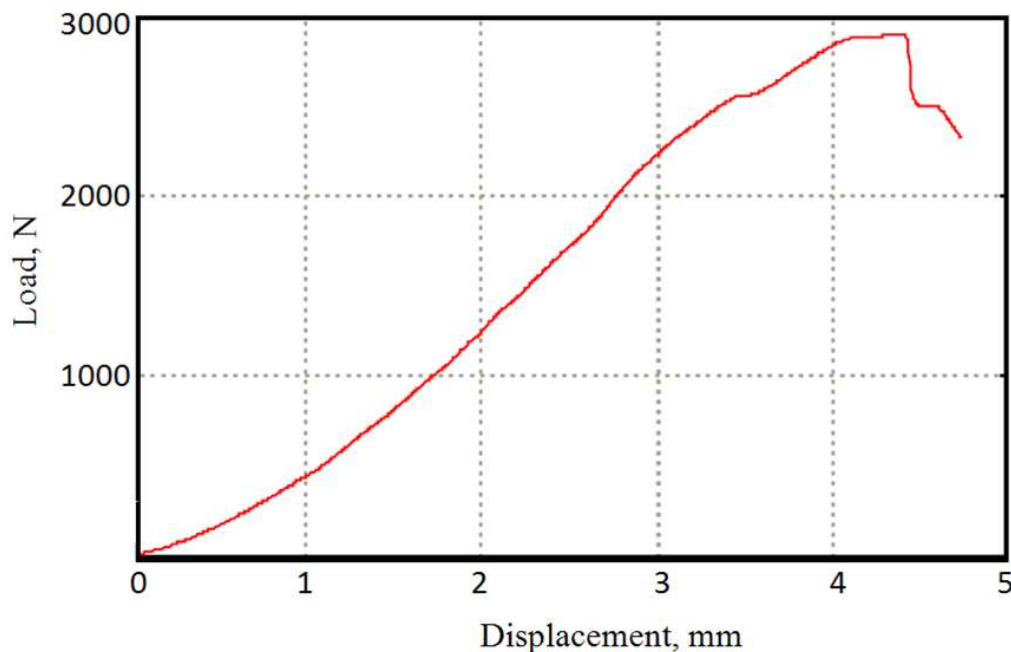
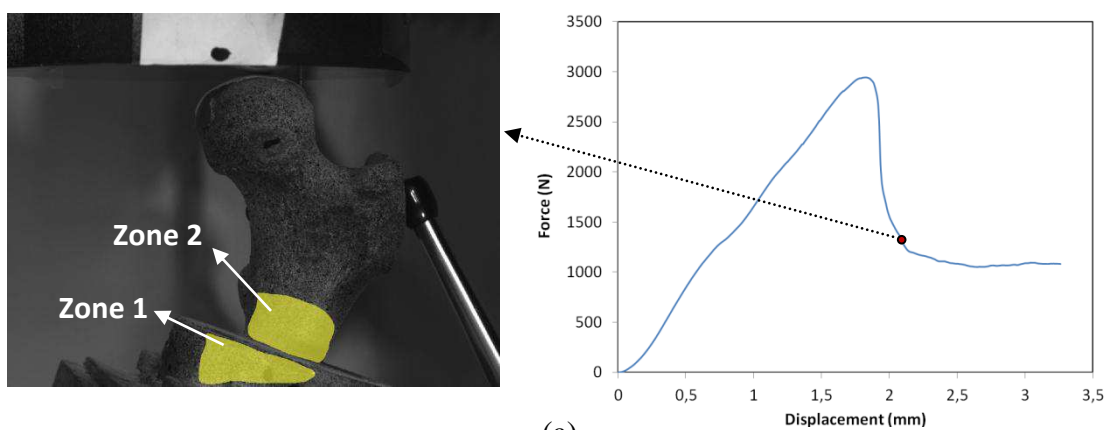


Figure 4. 15 Force-displacement curve of bovine femur under single limb stance configuration.

The failure process can be explained as following: the material deforms reversibly (elastic range). In this step, the material is still structurally coherent but absorbs energy by developing microcracking at the expense of stiffness and residual strength. The fracture mechanics area energy is absorbed adjacent to the final fracture plane. At this point the force displacement curve attains the ultimate force.

Boundary conditions were identical to the ones for the human femur test. The compression fixture assembly integrates with the test system to provide the compression test. The boundary conditions of the assembly were checked, zones 1 and 2 (see Figure 4.16), using the optical measurement.

As evident from Figure 4.16 (b-e), there is almost no significant movement of the fixture system in the different directions for both zones. The maximum local value of displacement of 0.02 mm was found in z-directions which is insignificant value. In x and y directions as well as in the normal direction, no significant values of relative displacements were recorded for both femur distal and fixture. Thus the fixing system is rigid and we can consider that the femur is well embedded with the lower base. These conditions can be used as boundary conditions in the numerical simulations studies.



(a)

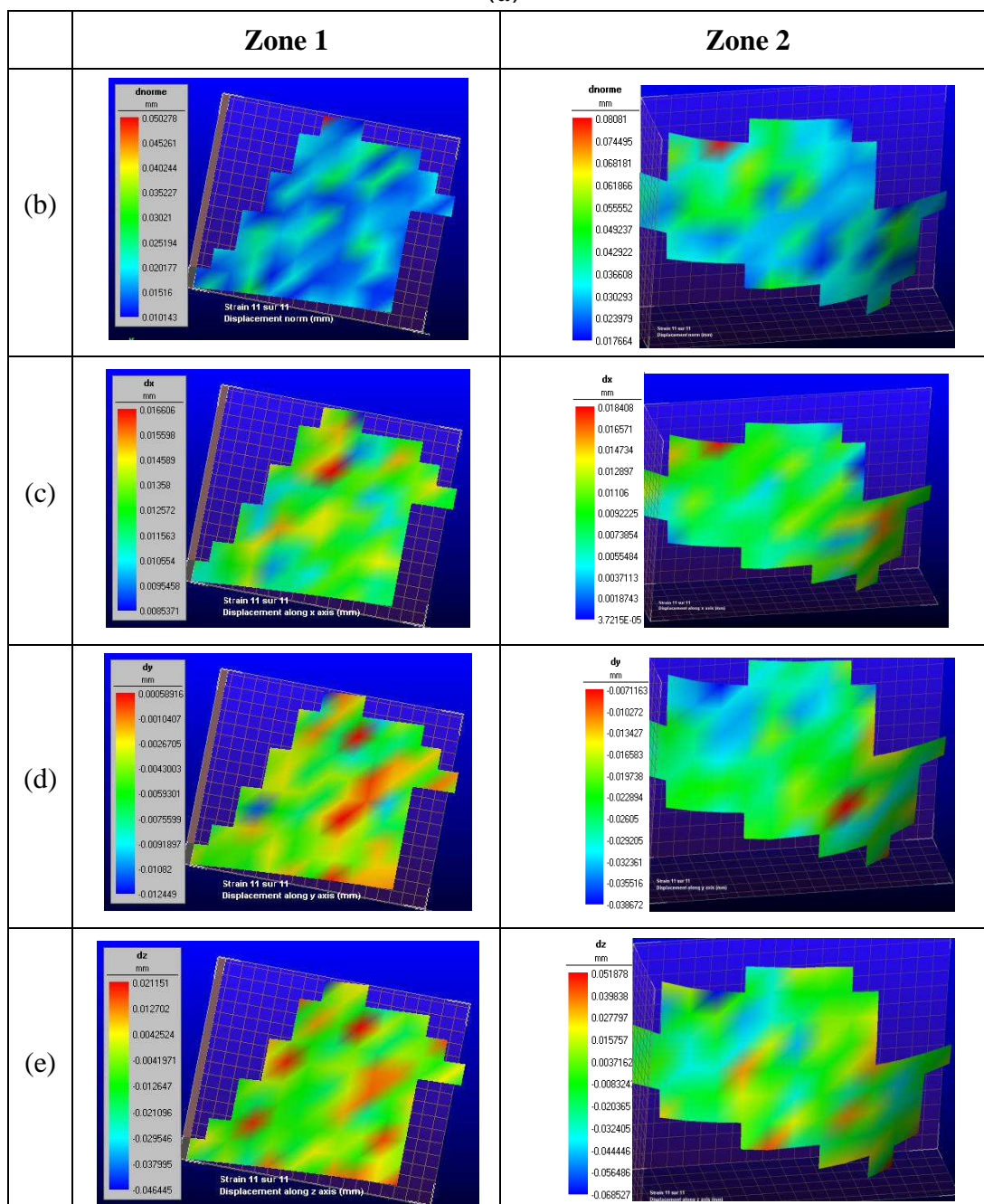


Figure 4. 16 Examination of fixture device assembly under compression loading (a) Region of interest area, (b) measured displacement fields of global displacement (c) measured displacement fields in x-direction, (d) measured displacement fields in y-direction, (e) measured displacement fields in z-direction. Demonstrated fields: specimen (D), post fracture at 1262 N.

4.6. Conclusion

The experimental work will permit to validate the proposed numerical models in chapter (3). An experimental assembly was designed for compressive tests of human femurs in single limb stance configuration. The experimental work comprises the testing of eight specimens of human femur. The novelties of using the 3D optical measurement, advantages of the designed assembly were introduced. The single limb stance device and the experimental protocols were successfully validated.

The next chapter will show how experimental results can be predicted by means of the FE modeling method. The predicted and measured data will be contrasted to each other.

Results and Validation

Abstract

In this chapter, under the assumption of isotropic material properties, we will first validate the proposed 3D heterogeneous model coupled to quasi brittle damage law with our experimental results. The numerical results obtained by the 3D model will be also compared using the experimental results obtained by 3D DIC technique. Its ability of prediction will be evaluated and discussed. In order to provide a practical and rapid prediction tool, we simplified this model to a 2D model which is capable in helping the clinical purposes. This model will be applied into two variants: the first considers damage defined by all strain components (von Mises equivalent strain). The second, damage was defined by shear strain only (equivalent shear strain). After its validation, the 2D model will be applied to study the effect of force direction to represent the consequence of the daily activities on failure load under both limb stance and sideways fall configurations. In order to test the capability of our model to predict the proximal femur failure under sideways fall configuration, the effect of geometry parameters and density on the fracture force will be evaluated and compared with the literature. Finally the 2D model will be evaluated by assigning anisotropic properties for both cortical and trabecular bone for both configurations.

Résumé

Dans ce chapitre, sous l'hypothèse d'un matériau isotrope, le modèle numérique 3D proposé couplé à l'endommagement quasi fragile sera validé par les résultats expérimentaux. Une comparaison des résultats de ce modèle avec les mesures expérimentales obtenus par les mesures de corrélations d'images 3D sera effectuée et discutée afin de mettre en évidence sa capacité de prédiction. Afin de fournir un outil pratique et rapide utilisable pour des fins cliniques, le modèle 3D a été simplifié en 2D. Ce modèle a été appliqué de deux façons différentes: la première considère l'endommagement comme étant défini par toutes les composantes de déformation (déformation équivalente de von Mises). Dans la seconde, l'endommagement a été défini uniquement par la déformation de cisaillement (déformation de cisaillement équivalente). Le modèle 2D de simulation par EF sera utilisé pour étudier l'effet de la direction de chargement mécanique pour représenter la conséquence des activités quotidiennes sur la charge à la rupture sous les deux configurations de chargement: l'appui monopodal et la chute latérale. Afin de tester la capacité de notre modèle à prédire la rupture du col du fémur dans une configuration de chute, l'effet des paramètres géométriques et de la densité sur la force à la rupture sera évalué et comparé avec la littérature. Enfin, le modèle 2D sera évalué en attribuant des propriétés anisotropes pour l'os cortical et l'os trabéculaire pour les deux configurations.

5.1 Introduction

The ability of the proposed FE model to predict hip fracture in human femurs was demonstrated in chapter (4) by the preliminary comparison with the study of Keyak and Falkinstein, 2003. We will first validate the proposed three dimensional Finite Element (FE) model with our experimental results. Secondly, the simplified two dimensional model will be validated. The capability and the predictive power of the two dimensional model will be assessed. A parametric study will be performed on the two dimensional FE models.

5.2 Results and validation of the three dimensional finite element simulation

The objective of the 3D FE analysis is to find the distribution of displacements within the proximal femur and failure forces. As mentioned, the proximal femur model (model A) was divided into finite elements corresponding to voxels. The voxel elements are of type (C3D8) with average dimensions of $9.9 \times 13.9 \times 4.8 \text{ mm}^3$ (Table 4.3). The mechanical properties assigned to each element, as mentioned in chapter (4), are assumed to be isotropic with heterogeneous Young's modulus (Equations from 4.1 to 4.4) and a constant Poisson's ratio of 0.3.

5.2.1 Results and validation of Force-Displacement curve

In Figure 5.1 the force–displacement curves of the tested femurs are shown. All curves show a linear stage followed by a nonlinear post-fracture behavior caused by damage initiation. The occurrence of damage is revealed by a sharp drop in force during failure that was nearly always observed during mechanical testing. The growth of damage can be shorter or longer depending mainly on bone organ geometry, intrinsic properties, specimen preparation (fresh frozen, embalmed), aging (decrease of toughness of bone) and the load testing speed.

The curves presented in Figure 5.1 have been recorded at a very low speed (quasi static load), thus permitting to identify the breaking modes. Schileo et al. [Schileo et al., 2008] loaded proximal femurs in single limb stance at high strain rate. The specimens have failed with a sudden fracture process (sharp decrease of load after reaching the maximum value) without noticeable post-yielding phase, suggesting the presence of generalized yielding

(fracture patterns resembling brittle fracture). A similar failure behavior showing a sudden structural collapse was reported by Link et al. [Link et al., 2003] and Yang et al. [Yang et al., 1996].

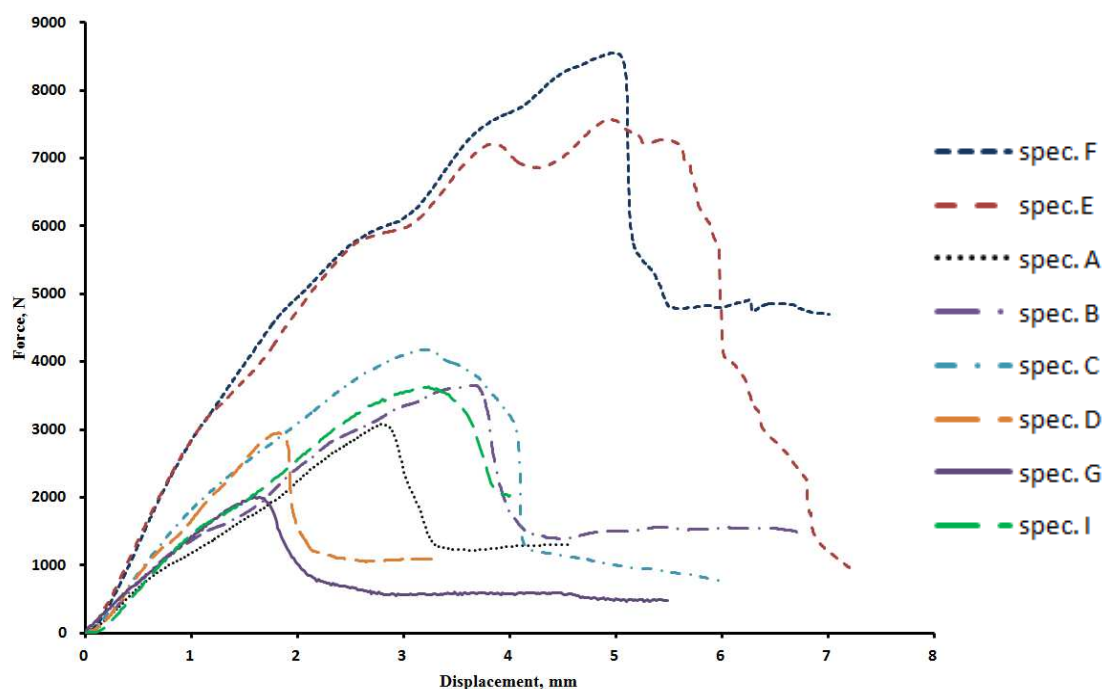


Figure 5. 1 Measured force displacement curves of human femur specimens.

As shown in Figure 5.1, specimens of the same cadavers (A and B, C and D, E and F) have nearly a homogeneous linear behavior. Beyond the elastic limit, the bone material is much less rigid. This is because bone damage accumulation generates microscopic cracks and/or voids which causes a progressive degradation of material continuity of the material [Lemaitre and Chaboche, 1990]. The fluctuations on the curves beyond the peaks are due to the fact that localized contact occurs between the head of the femurs and the piston of the testing machine.

In the current work, the ultimate force fracturing the femoral neck was taken as the peak value for the curve. The average ultimate experimental force was 6210 ± 253 N (range: 2010–8550 N) for single limb stance configurations. These findings are comparable with those reported in the literature. Indeed, prior investigations of uniaxial quasi static compression tests performed on eleven right femora conducted by Bessho et al. [Bessho et al., 2007], loaded at 20° in the coronal plane, gave failure loads in the range of 2800-6100 N. Smith et al., [Smith et al., 1992] reported a range between 4937N and 16148 N, Le bras et al. [Le bras et al., 2006] found under identical conditions a range of 3100 and 7150 N and Duchemin et al., [Duchemin et al., 2006] reported an experimental failure load of 9032 ± 3412 N for four human femur specimens in the frontal plan.

The superposition of the force - displacement curves obtained by mechanical testing and numerical simulation allows a comparative analysis of results and an assessment of the reliability of the numerical model. Some results are depicted in Figure 5.2.

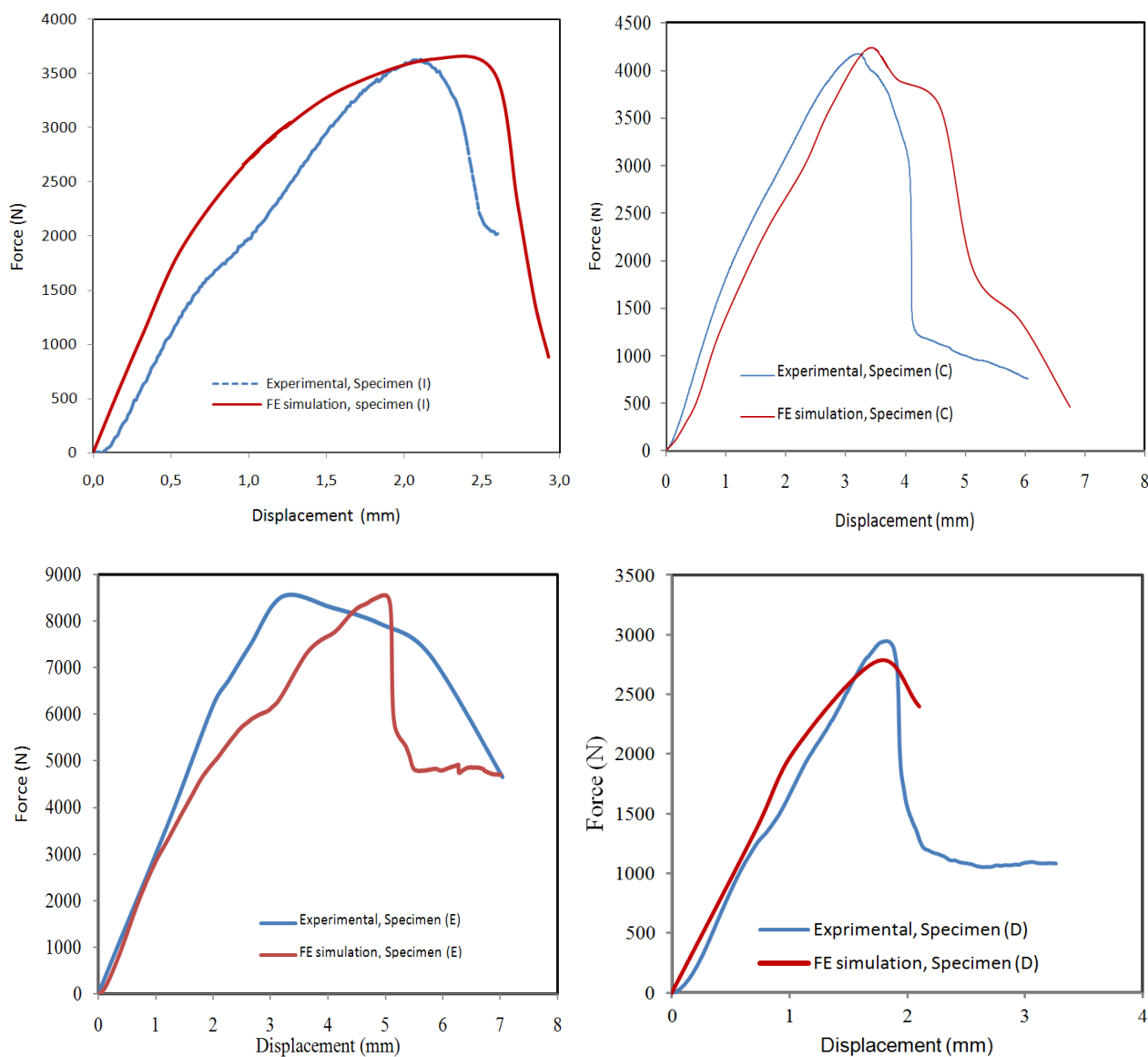


Figure 5. 2 Some examples of the comparison between experimental and 3D FE simulations of force-displacement curves (specimens I, C, E and D).

The predicted force-displacement curves showed the same trend of the curve shape and onset of yielding and fracture as the measured one. The FE-based curves exhibited a linear increase till bone yielding followed by a nonlinear behavior and drop in force during failure that was observed in all simulations. It is evident that the slope of the initial portion of the predicted force-displacement curve is greater than the measured stiffness. This discrepancy

was explained by the strain-softening behavior of the bone [Keyak, 2001] which is not implemented in the FE model.

The current FE proximal femur fracture model provided good agreement between predicted and experimentally measured ultimate force at fracture with a correlation factor for the entire data set $R^2 = 0.833$, Figure 5.3.

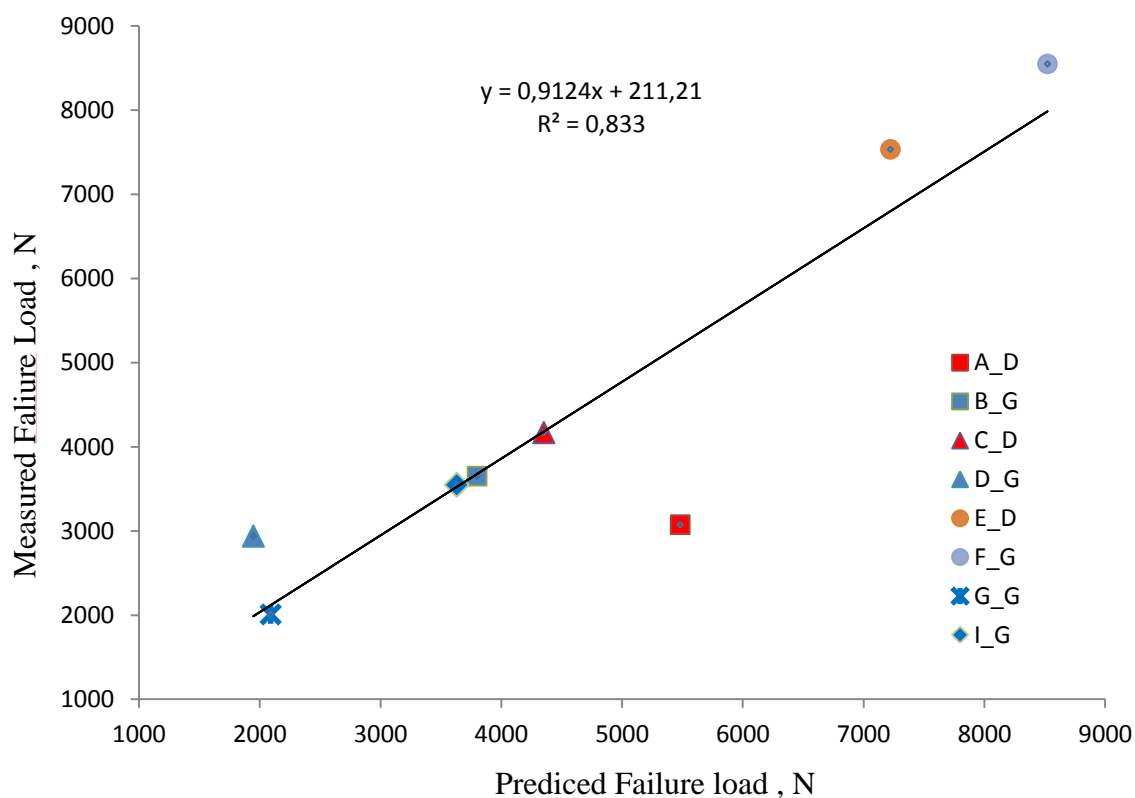


Figure 5. 3 Current predicted and experimental failure load correlation.

Our fit equation for the failure force under single limb stance conditions can be expressed in as $F_{Exp} = 0.912 F_{Num} + 211.2 \text{ N}$, where F_{Exp} is the experimental force and F_{Num} is the predicted value of force. The fit equation from earlier models had less predictive power, for example $F_{Exp} = 0.77 F_{Num} + 1150 \text{ N}$ [Keyak et al., 2001, Keyak et al., 2005]. Prior investigations of uniaxial quasi static compression test of human femur were conducted by Bessho et al. [Bessho et al., 2007]. Using identical conditions under single limb stance of femur loaded at 15° , Besso et al. found $F_{Exp} = 0.809F_{Num} + 1592 \text{ N}$ [Besso et al., 2007]. Le Bras et al. [Le Bras et al., 2006] performed the tests under the same conditions and have given the results of failure forces similar to ours (3000 N and 8000 N) with a correlation between experimental and numerical data of 0.84, see Figure 5.4.

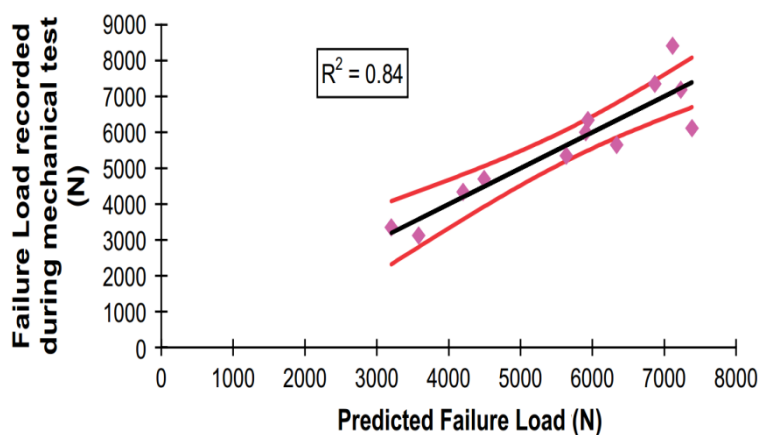


Figure 5. 4 Predicted and experimental failure load correlation [Le Bras et al., 2006].

Even though, their models arrived at reliable fracture forces, they were unable to predict the fracture profile as well as the complete force displacement curves. Furthermore, damage accumulation was not evaluated.

5.2.2 Results and validation of three dimensional fracture pattern

Nonlinear continuum-level voxel models have been used before to study the mechanical behaviour of the proximal femur beyond the yield point [Cody et al., 1999, Keyak et al., 2001] up to and beyond maximum fracture stress values. Using the current damage based model, damage is expected to start in the vicinity of the femur neck. This may be explained by the thin cortical shell at the neck of the femur (see Figure 5.5a) that diminishes the strength of the femoral neck [Zysset et al., 1999]. Besides, in this zone trabecular bone is dominant as shown by the qualitative comparison in Figures 5.5a and 5.5b. The discontinuity due to damage in the trabecular bone and the smallest section area may lead to stress concentration and causes finally the failure in the vicinity of the femoral neck (see Figures 5.5 and 5.6).

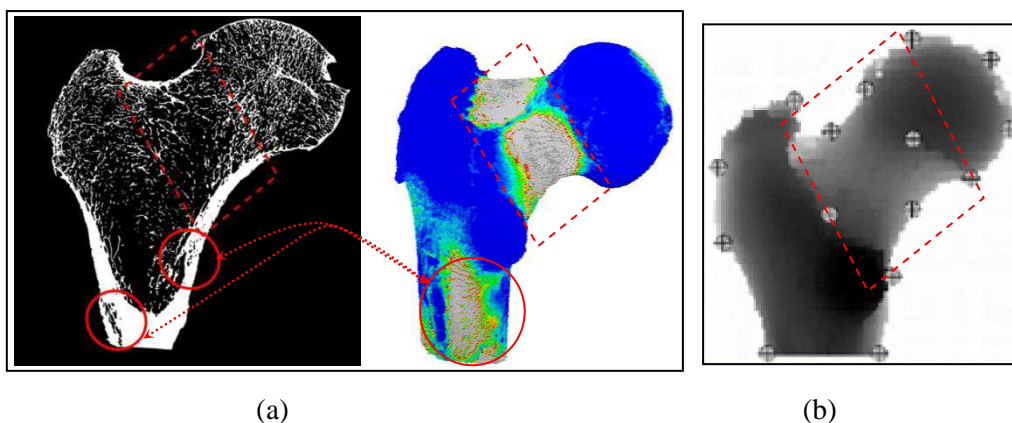


Figure 5. 5 Weak areas in femur bone. (a) cross section from CT scanner showing the regions of trabecular bone (left) with FE simulation of the accumulated damage (second left) for a tested sample (specimen I) (b) BMD image taken from [Langton et al., 2009]. Dashed rectangle refers to neck zone and the solid circles refer to the lack (or cracks) of bone material at the femur shaft.

Microdamage in general refers to discrete microcracks, cross-hatched and diffuse damage. In vivo, microdamage is found in both cortical and trabecular bone. In addition, microdamage accumulation has been shown to underlie the development of stress fractures and plays a role in the increased bone fragility associated with aging and osteoporosis. Many trabeculae in osteoporotic bone are disconnected and whole regions without bone can exist in the femoral neck zone producing the different types of neck fractures [Thomas et al., 2004]. The single limb stance configuration was able to reproduce the several typical femoral neck fractures.

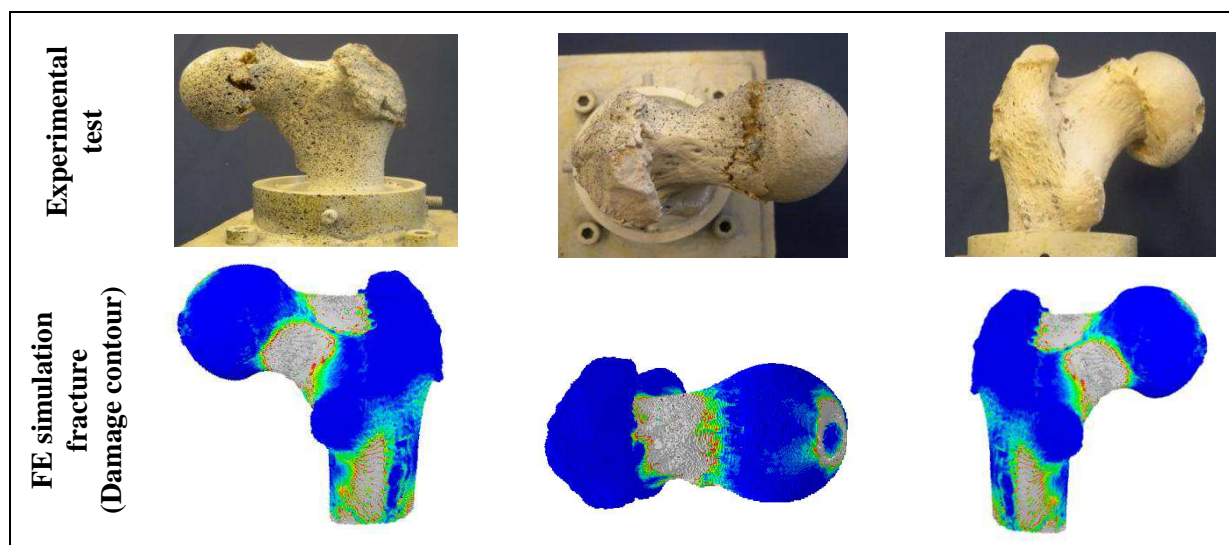


Figure 5. 6 Fracture sites (upper row) and 3D damage pattern (lower row) for sample (G).

In our sample size, different typical fractures were obtained: 13% cervical, 50% subcapital, 25% subcapital-cervical and 12% typical fracture in the femoral head. Figure 5.7 depicts some of the obtained fracture patterns.



Figure 5. 7 Different obtained fracture patterns of proximal femurs under single limb stance configuration. (Upper row: specimens F, B and I, Lower row: specimens C, E and A).

Not only the correlation between numerical and experimental values was similar to previous studies, also the fracture location site and patterns were alike.

Few investigations have compared the predicted fracture location with that obtained experimentally and have visibly shown conformity between them. Ota et al. [Ota et al., 1999] reported on the accuracy of fracture site prediction, but only for one case. Some other studies compared the experimental fracture site on radiographs with a non-linear model under limb stance load at 20° [Keyak et al., 2001]. They reported that their models succeeded to determine the fracture sites for 13 out of 18 specimens under single limb stance configuration. Recently, Dall'Ara et al. [Dall'Ara et al., 2013] performed a nonlinear CT-based FE model validation study of human femur loaded in single limb stance and sideways fall configuration. They tested 36 pairs (17 males, 19 females) with age (76±12) years, range (46–96). In their single limb stance test, the load was applied also at 20°. They found typical femoral fractures in most cases (subcapital: 24%, neck: 54%, trochanteric: 13%, atypical in the femoral head: 3%, not clear: 6%). However, Dall'Ara et al.'s model succeeded to qualitatively predict in 66% of all cases the failure location and the motion of the femoral head.

A representative example of the experimentally and numerically obtained fracture pattern is shown in Figure 5.8 for one femur.

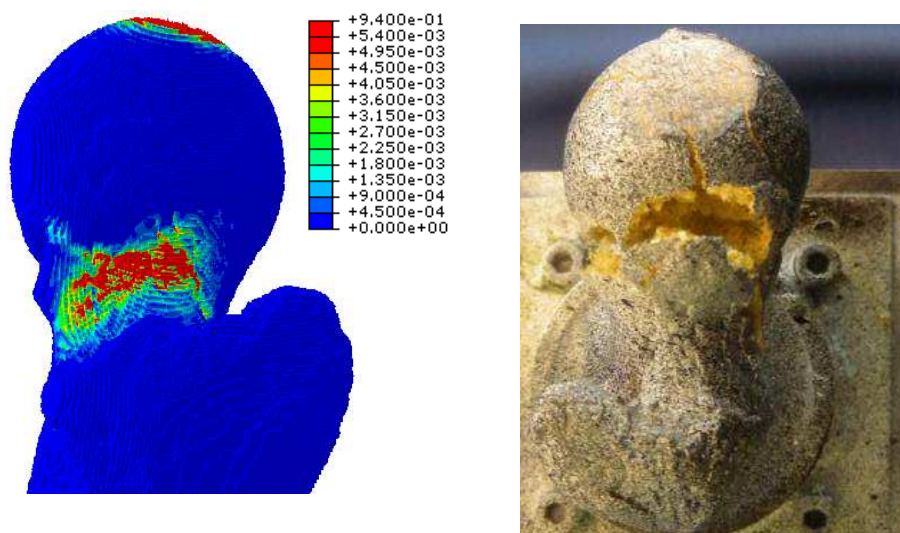


Figure 5. 8 Simulated 3D damage contour (left) and fracture sites (right) for a tested specimen (I).

Our results predict slightly different fracture profiles and locations compared to the experimental results. Such differences may reside in the voxel mesh used for the current models, the applied boundary conditions and the assigned material properties.

5.2.3 Results and validation of three dimensional model using digital image correlation technique

To compare the results of the 3D model to those obtained experimentally using the DIC method, spatial contour plots of the displacement fields corresponding to different states of loading were plotted for each femur.

As the surface of the femur is three-dimensional and neither uniform nor plane, the measurement of the deformation components of the femur surface was not possible. Hence, our comparison will be based only on the displacement fields gathered from DIC. To achieve this, the constitutive behavior was divided into three phases: elastic, just before failure and after failure. For each of these regions, we define different states of loading where we carry out the comparison of experimental and numerical displacement fields.

These states are identified by the crosshead displacement. The example presented in Table 5.1 is the specimen B.

Table 5. 1 Post processing treatments on a representative sample (B).

Displacement, mm	Load, N	Remarks
-0.001	0.00	
0.643	991.87	State 1 (elastic region)
1.295	1614.47	
1.945	2429.39	
2.666	3067.29	State 2 (just before failure)
3.333	3560.93	Maximum strength
3.999	1793.86	State 3 (just after failure)
4.666	1436.86	

All surface displacement components were recorded. Figure 5.9 shows perspective plots of the instantaneous displacement taken for the specimen (B), as an example, for the states 1, 2 and 3 defined in Table 5.1.

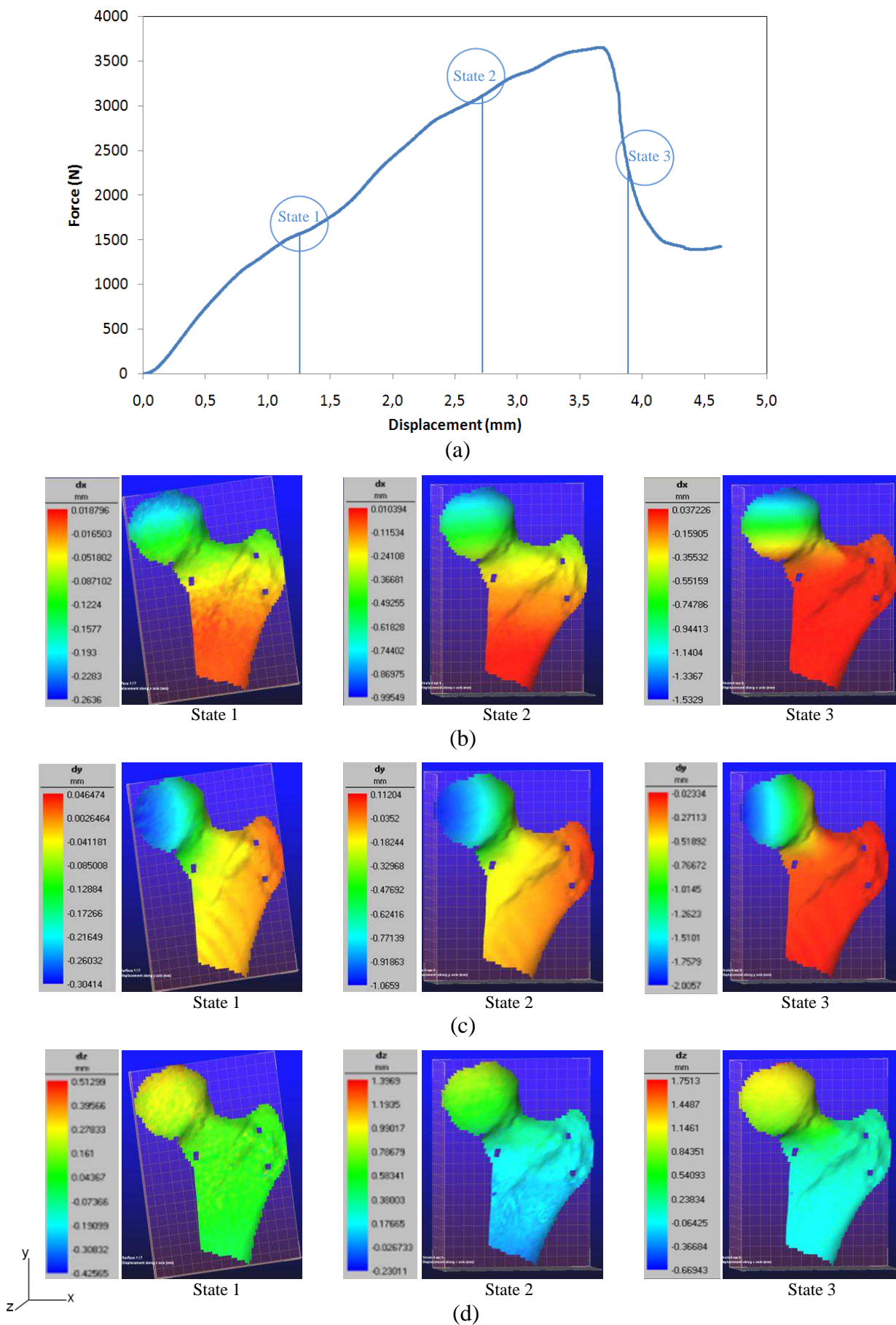


Figure 5.9 Measured displacement fields in the temporal matching of the compression experiment of a representative specimen (B). (a) the chosen three states on the force displacements curve, (b) displacement values in y-direction, (c) displacement values in x-direction and (d) displacement values in z-direction.

Figure 5.9 shows the obtained displacement fields distribution for the states defined in Table 5.1.

The vertical displacement component (dy) corresponding to the line of action of the compressive force is the most relevant one. As shown in Figure 5.9a corresponding to state 3, the experimental value of the vertical displacement is about 4 mm. DIC measures a maximum value of 2.7 mm. Thus, there is a discrepancy of 50%. This deviation is mainly due to the following reasons:

- The crumbling and ensuing damage of the femoral head caused by the head plate. This translates into a loss of local stiffness which can be easily identified on the curve (such as between 1.3 and 1.8 mm on the curve, Figure 5.9a).
- The maximum experimental displacement of 4 mm is the one of the head plate and represents the displacement of the contact point of that plate with the femur tip. The selection of the ROI for DIC was dictated by the need to observe identical zones throughout the entire test. Hence, areas directly in contact with the head plate were not tracked.
- Throughout a compression (or tension) test, the local deformation varies within the volume. Heterogeneity causes displacement and deformation to deviate more from the values at the head plate the greater the distance from that point.

The displacements dx and dz are not zero as shown on Figure 5.9c and 5.9d. Those components are measured when the femoral head is damaged and bent or broken.

The resultant displacement vectors comparisons are presented in Figures 5.10a, 5.10b and 5.10c. The displacement is characterized by a gradual variation from the point of load application (red arrows) about 1.6 mm (Fig 5.10b) to the lowest values about in the trochanter region (blue values). The spatial variation of displacement comparison shows a remarkable consistency between the numerical and experimental recordings.

The results presented in Figures 5.9 and 5.10 show that the higher part of the proximal femur, i.e. the head and subcapital zone in Figure 5.9b (stat 3) were displaced by a value ranging from 1.01 mm to 2.01 mm. The lower part of the proximal femur, i.e. the neck and trochanter, were displaced by 0.02 mm to 0.27 mm. Similarly, at the femoral neck, if we take

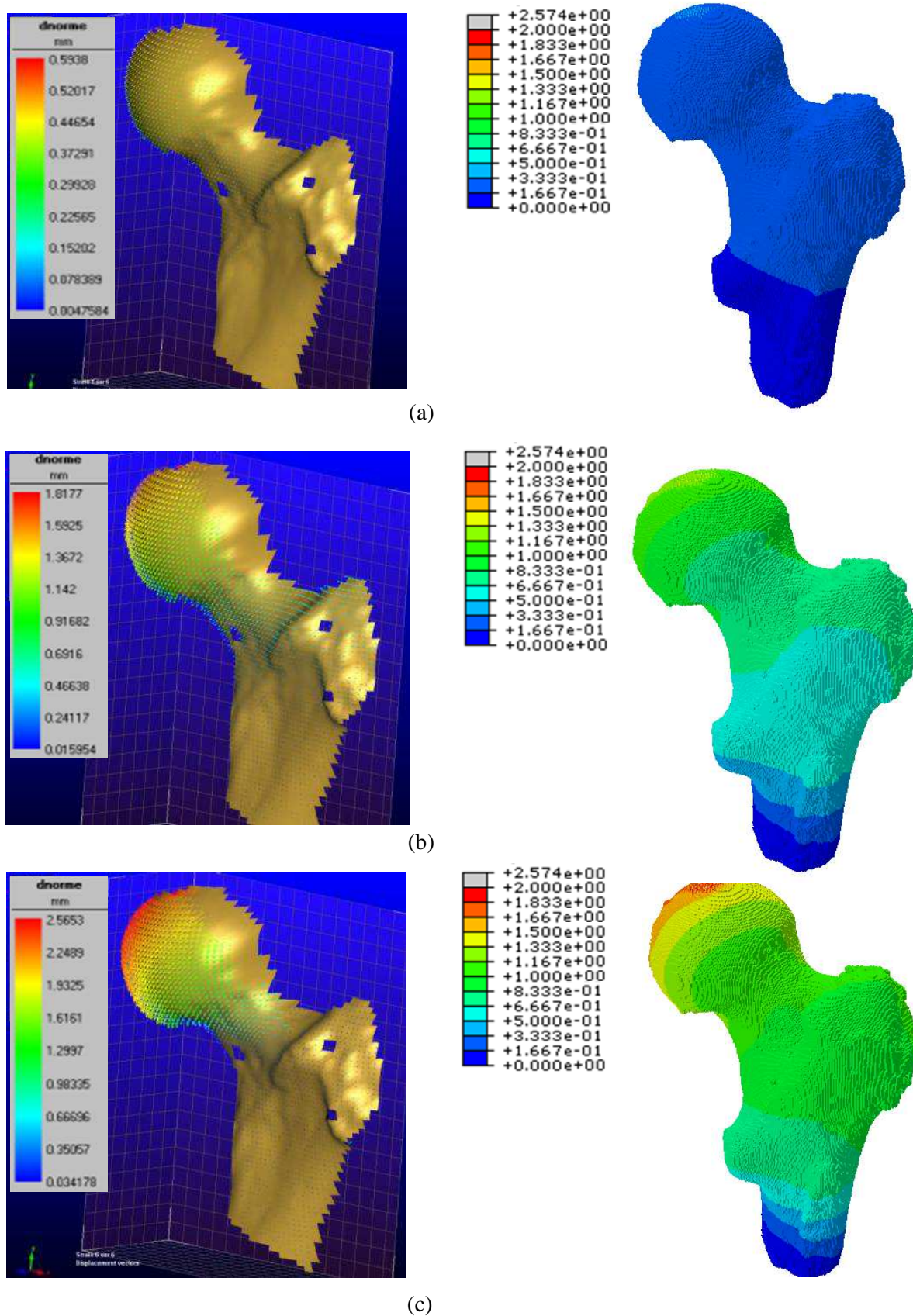


Figure 5.10 Comparison between the predicted displacements (right), mm and measured displacement fields, mm by DIC method (left) for specimen B. (a) elastic region at 991.87 N, (b) just before failure at 3067.29 N and (c) just after failure at 1793.86 N.

average differences between the upper and lower parts of the proximal femur are 0.47 mm and 0.18 mm respectively. With such a relatively high interface variation of the response, it can be suggested that the failure may take place by shearing at the neck zone.

It is obvious that the measurement of the displacement with the DIC method is more suitable than the strain gauges. As they permit to acquire only local point measurements while the DIC method gives the local and global fields distribution.

5.3 Results and validation of the two dimensional finite element model

The clinical implementation of 3D CT/FE methods is still limited due to the requirement of expensive computer hardware to achieve solutions of 3D FE models within a clinically acceptable time, as well as, the need for robust 3D segmentation and meshing techniques [Aspray et al., 2009]. Segmentation, meshing and FE analysis of a 2D geometry can be accomplished fast and is potentially more robust than 3D CT/FE [Langton et al., 2009]. DXA scanners are becoming more widely available and they play an increasingly important role in clinical practice [Testi et al., 1999]. It is currently the clinical standard for assessing osteoporotic fracture risk but is not a reliable predictor of fracture [Aspray et al., 2009]. In several studies, the status of the proximal femur has been examined in vivo by DXA.

In order to provide a practical and rapid tool, we simplified our 3D model to a 2D model which is capable in helping the clinical purposes. This 2D model, preliminarily validated in chapter (3), models test-I and test-II, will be validated using the 2D-DIC measuring technique and finally its capability will be evaluated and discussed in the following subsections.

5.3.1 Results and validation of single limb stance model

In a 3D-DIC technique, color-coded displacement values represent at high spatial resolution the topography of the moving surface when subjecting the femur to a load. Notwithstanding the fact that the femur surfaces are not flat, the 2D-DIC visualization technique is capable of representing an appropriate and realistic mapping of the fracture pattern.

Contrary to the 2D-DIC technique, the spatial resolution of the 3D-DIC technique does not allow locating the precise spot of fracture initiation. Hence, though the comparison is only qualitative in nature, but not quantitative, the reliability of the 2D-DIC technique can be

corroborated and additionally lend support to the hypothesis that the out-of-plane deformation component is less relevant for the deformation process and fracture profiles.

The local displacement and strain fields at the femur surface were evaluated by utilizing 7D software in 2D based on DIC technique. In the 2D-DIC procedure, images were taken at each time increment. During image acquisition, the corresponding displacement and the applied load were also recorded. Figure 5.11a presents the force-displacement response for a representative specimen along with DIC data presented in Figure 5.11b. The fields of the maximum shear, maximum/minimum principal strains are presented for three chosen states: elastic loading (state 1), before failure (state 2) and post failure (state 3). The results indicate distinctly different patterns of strain development for single limb stance configuration. The maximum shear was found at the proximal femur with a distinct anterior concentration of both maximum shear and minimum principal strains. This may be explained by the particular density distribution at neck region subcapital zone. This result was also observed by other investigations. Cristofolini et al. [Cristofolini et al., 2007] investigated, in vitro, the occurrence of spontaneous fractures of proximal human femur. Surface strains were recorded by using strain gauges. They found that the most common fracture initiation site was the subcapital region (80% of their 10 cadaveric femur specimens). This is not surprising since the boundary condition is essentially a constant axial displacement across the longitudinal y-component where the shear takes the place. The reduced bone mass at the femur neck due to the concentration of trabecular bone (as presented in Figure 5.5) and a high bone loss at this site [Chevelley et al., 1991] suggest the initiation of fracture in this area. This lack of strength was also elucidated in the current work as 75% occurred in the neck femur fracture of subcapital and subcapital-cervical zone, as shown in Figure 5.7. The plots are more sensitive to subtle differences of maximum shear distributions at trochanter and diaphyseal regions which are also characterized by general homogenization of maximum and minimum strains (Figure 5.11b, state 3) produced by the applied load.

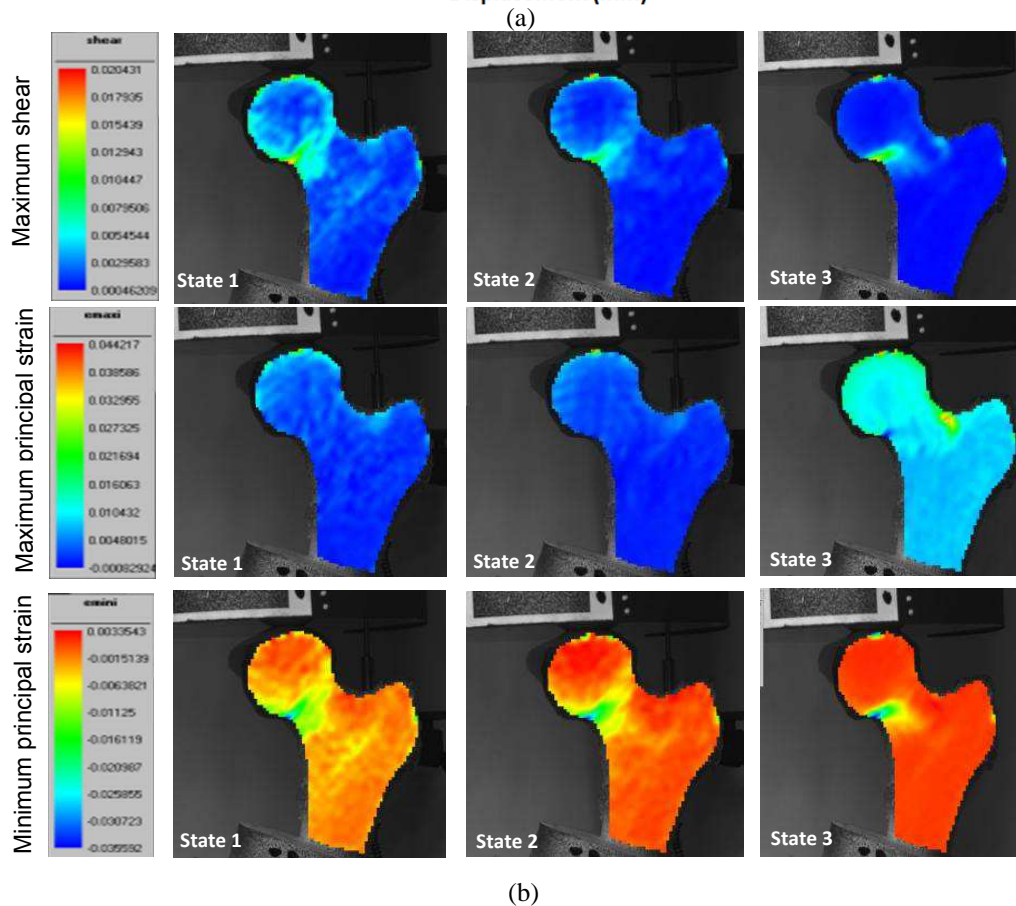
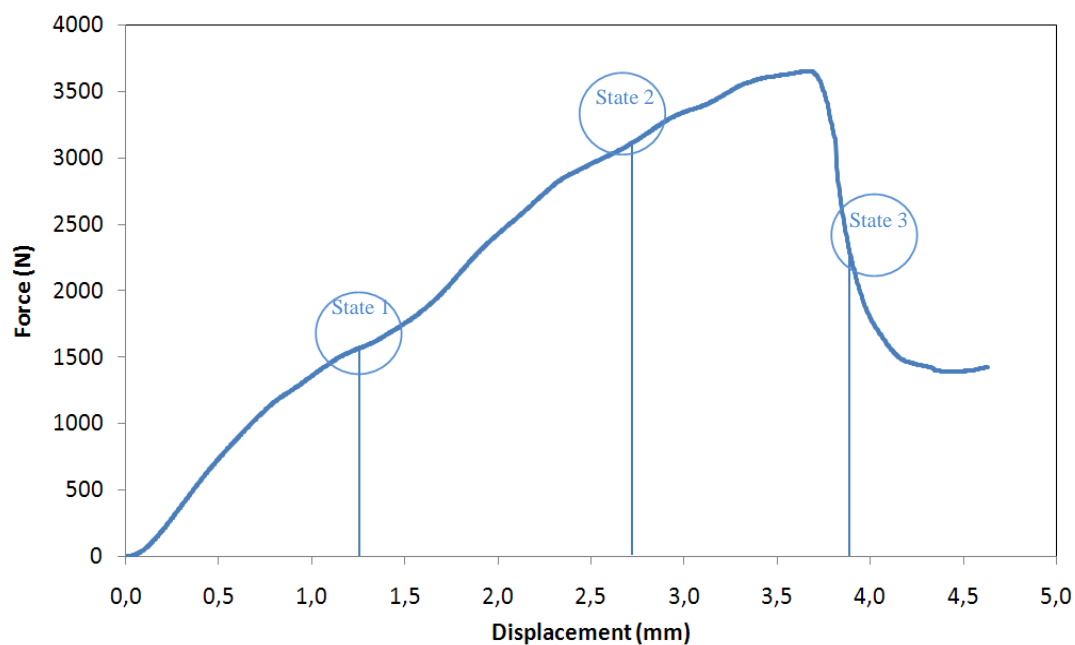


Figure 5. 11 Shear and principal strain distribution for the two dimensional measurement areas of a proximal femur (specimen B). (a) the chosen three states on the force displacements curve (b) corresponding shear and principal strain distributions (maximum and minimum) contours.

The measured strain values were ranged from 0.35% to 0.56%. In many other investigations, when surface strains of femur are of interest, a larger number of strain gauges were bonded on the femur surface [Cristofolini et al., 2007, Taddei et al., 2006, Viceconti et

al., 1998, Yosibash et al., 2007]. In these works, the local strains were reported as 0.33% (see Figure 5.12) [Viceconti et al., 1998], between 0.1% to 1.0 % [Taddei et al., 2006] and 0.12% to 0.16% [Taddei et al., 2007].

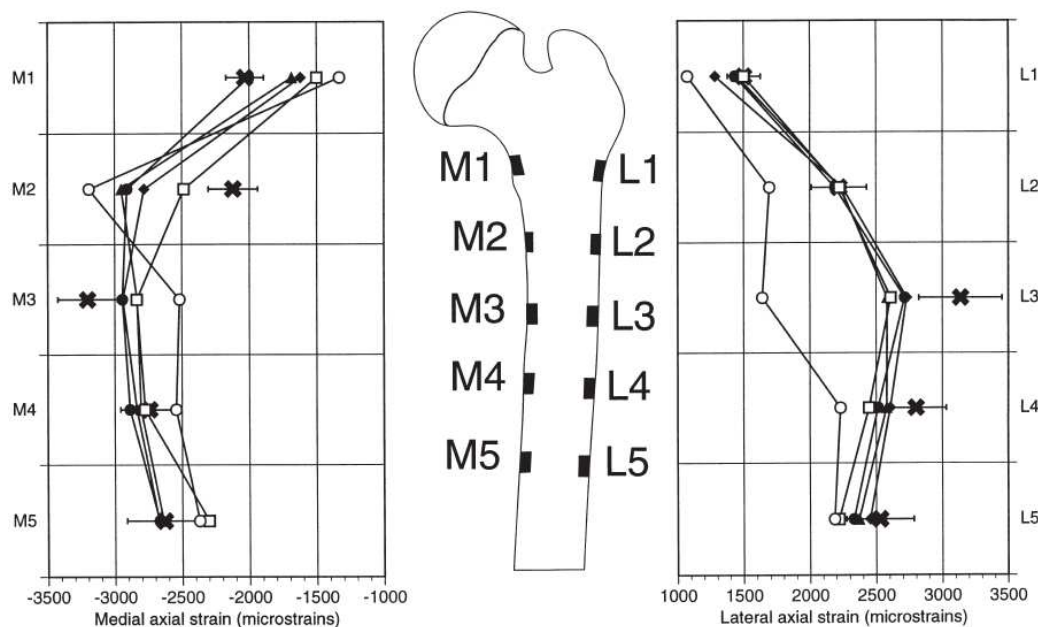


Figure 5. 12 Axial strains measured in vitro using strain gauges along the femoral shaft. Experimental data points are denoted by 'x' [Viceconti et al., 1998].

The distribution of deformations along the femur shaft for a representative femur specimen is presented in Figure 5.13. The vertical deformation (ϵ_{yy}) and horizontal deformation (ϵ_{xx}) are presented for two states: at maximum strength and just after failure. In terms of values, the measured deformations corresponding to these two states are between -0.55% and +0.33%. The extrema of these values occur in both compression and tension sides.

By comparing these findings with those using strain gauges along the femoral shaft mentioned in the experimental work of Viceconti et al. [Viceconti et al., 1998]. A values of -33% and +0.32% were found corresponding to the compression and tension sides.

Our goal in the current work is to use the DIC measurements for a qualitative comparison. The comparison between our deformation measurements obtained with the DIC with those reported in the literature [Taddei et al., 2006, Viceconti et al., 1998, Taddei et al., 2007] suggest that our DIC measurements can be used for quantitative validation.

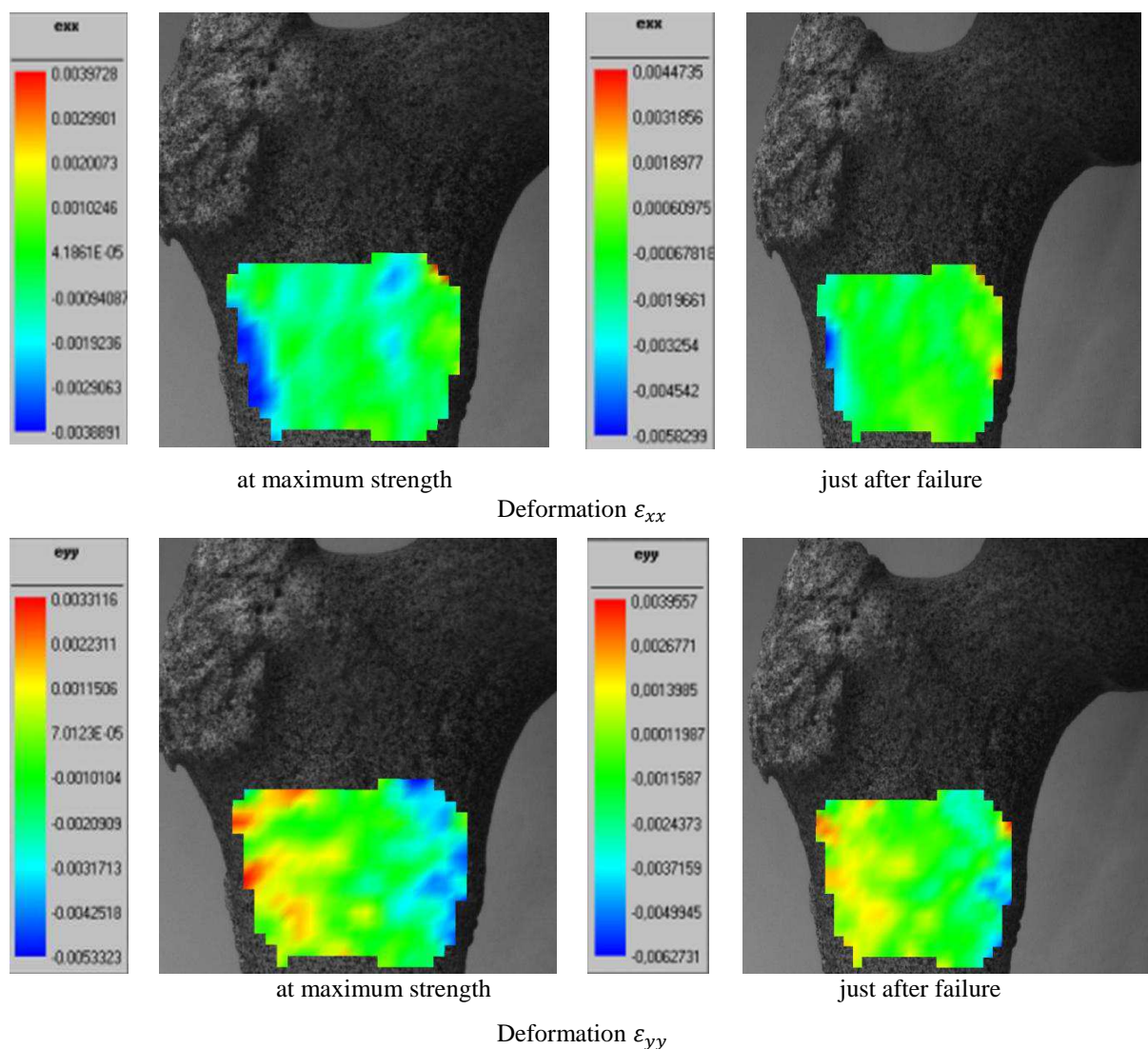


Figure 5. 13 Axial strains measured *in vitro* using DIC technique along the femoral shaft (specimen B).

5.3.1.1 Results and validation of two dimensional fracture pattern

Damage in bone could be caused by shear failure of the organic matrix [Kotha and Guzelsu, 2003]. The single limb stance configuration has been shown in previous studies to produce maximum shear stresses in the femoral neck region in a manner consistent with clinical subcapital fractures [Smith et al., 1992, Cotton et al., 1994] similar to the predicted ones.

Stress-strain criteria are the most widely applied criteria for strength evaluation of materials. Quasi brittle behavior could be accepted to behave linearly elastic before reaching its proper threshold level of stress. In the elastic range, the stress criterion is equivalent to the strain criterion. The strain equivalent criterion is based on a limiting energy of distortion, i.e. energy associated with shear strains. This criterion has succeeded to give good validated

results and is widely used for estimating the proximal femoral fracture load and assessing hip fracture risk [Ford et al., 1996, Keyak et al., 1998, Lotz et al., 1991a].

Trabeculae in the subcapital region collapsed under the applied load. The damage distribution sequences of the presented specimens F and A given in Figure 5.14 (two left columns) indicate that damage accumulation occurred during the loading which ultimately formed a high strain concentration region in the form of shear band. In the current study, the 2D models were applied into two variants:

- The first considers damage defined by all strain components (von Mises equivalent strain) and for which results are presented in the first column of Figure 5.14.
- The second, damage was defined by shear strain only (equivalent shear strain) and for which results are shown in the second column of Figure 5.14.

The fracture patterns obtained with the 2D models were compared with the maximal shear strain, measured using 2D digital image correlation, just before the femur specimens failure and the experimentally obtained fracture patterns in the two right columns of Figure 5.14.

It is well known that bone resistance to shear is weaker than in tension and compression. The analysis revealed that equivalent strain was concentrated in the inferior cortex of the subcapital region. Microcracks have been observed in cortical [Morgan et al., 2005] and trabecular [Wachtel and Keaveny, 1997] tissue following compressive overloads and have been suggested to result from local shear stresses.

The simulation presented in Figure 5.14 (second column) was applied with considering only the effect of shear strain components under axial compression. The results show that the damage computation incorporates exclusively the shear strain components. This can be explained by behavior of bone under excessive mechanical load which is characterized by diffuse microcracking and localizes in relatively narrow zone, referred to fracture process zone [Vashishth et al., 2000].

This zone was the origin of a major crack that resulted in a catastrophic failure. In normal gait, the greatest stresses occur in the subcapital and mid-femoral neck regions. Within these regions, maximum compressive and shear stresses occur inferiorly and tensile stresses of small magnitude occur superiorly [Lotz et al., 1995].

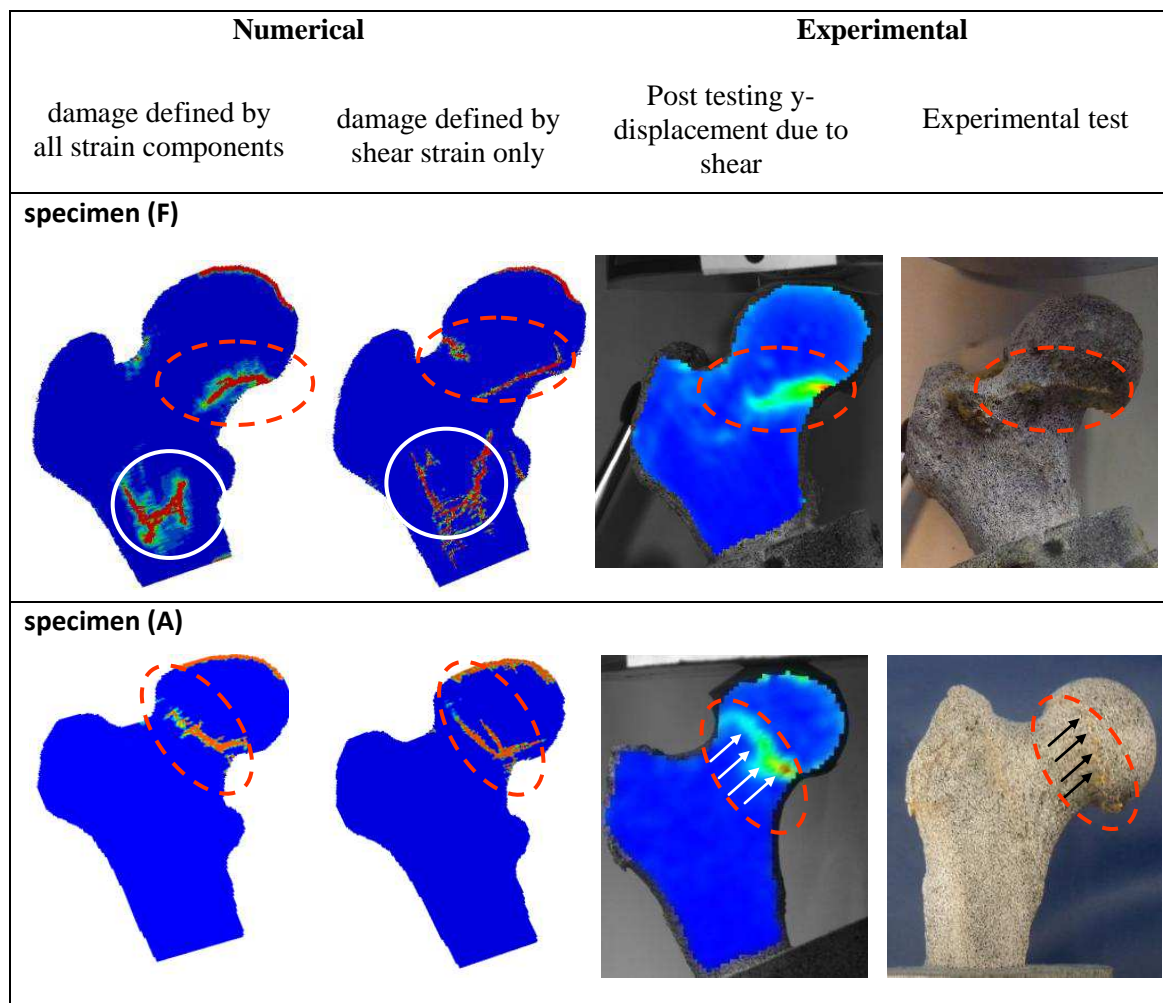


Figure 5. 14 Prediction of failure location. Damage defined by all equivalent strain components (first column). Damage defined by shear strain only (second column). Dashed circles highlight the failure location from the experiments and are reported in solid on the models. The arrows indicate the fracture site. Solid circles at the diaphysis of the presented specimen (F) refers to a damaged zone that may be explained by a lack of mass density in this specimen.

The failure due to equivalent shear strain was studied in the current work under single limb stance configuration by using 2D FE models. The obtained damage contours are compared with experimental failure due to shear. Figure 5.15 present some examples of this comparison.

The predicted and actual fracture locations were consistent for all femora. The current FE proximal femur fracture model provided excellent agreement between predicted and experimentally (DIC) displacement values and distribution.

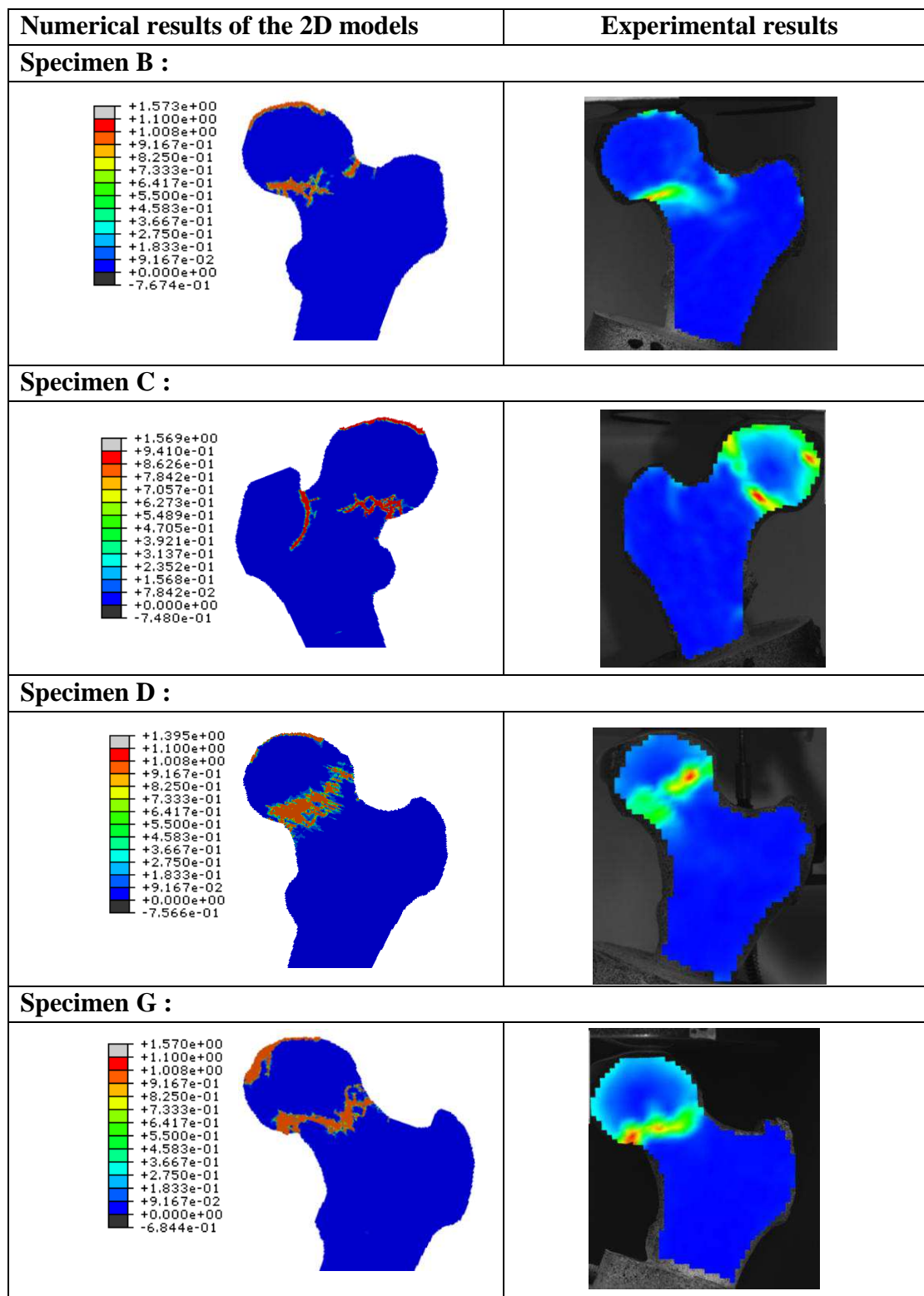


Figure 5. 15 FE and experimental Fracture patterns under single limb stance configuration.

As shown in the comparisons presented in Figure 5.16, the subcapital fracture resulted under limb configuration. The region of the greatest principal displacement of the femur head (1.47 mm to 2.3 mm) is the predicted fracture site at subcapital zone.

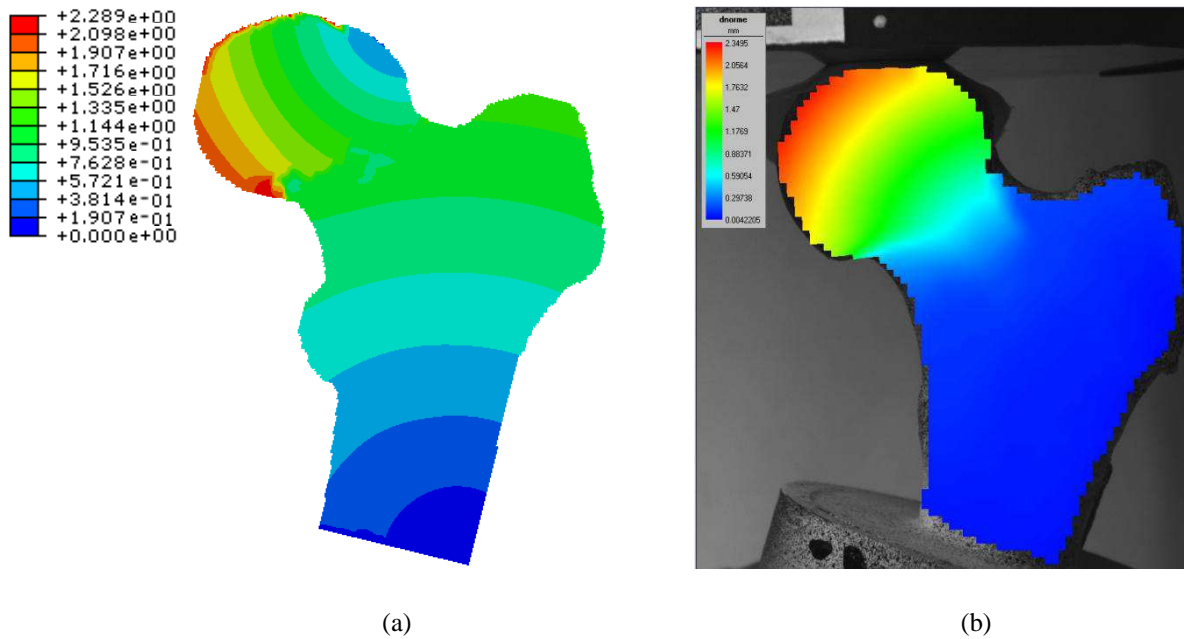


Figure 5. 16 Displacement fields (mm) just before failure for specimen (B) measured by:
 (a) 2D-FE model (b) 2D-DIC method.

The formation of a shear band which ultimately causes the subcapital fracture is the consequence of local material response. It depends mainly on the local apparent trabecular bone density [Ford and Keaveny, 1996]. At the elastic deformation phase (prior to yielding), the external load causes local homogeneous strains within the femur neck. After damage initiation, strain gradient instability occurs due to the difference of resistance of the trabecular bone and generates the shear band.

Our findings suggest that when damage taken into consideration, the predicted fracture sites are more precised. Furthermore, the predicted fracture forces were less when defining damage only by shear components suggesting that shear failure plays a large role in trabecular bone fracture [Ford and Keaveny, 1996]. The proposed damage law defined by the von Mises equivalent strain suggests that yielding and cracking begins when the elastic energy of distortion (also known as the shear energy) reaches a critical values of applied strains [Hill, 1950]. The suggested equivalent strain in the FE damage model can be considered as an adequate variable to capture the damaging process within bone since the equivalent strain is expressed in function of the deviatoric strain tensor which captures the shearing component of the applied strain.

5.3.1.2 Comparison between the predicted two dimensional model and experimental force displacement curves for single limb stance

Results from 2D FE analyses have been previously validated with those obtained with a 3D FE analysis of CT data. Testi et al. [Testi et al., 1999] found good agreement between the results of a 2D FE model with a DXA image to 3D FE model, and also validated the results in-vitro. Based on 2D structural geometry derived from DXA, Mourtada et al. [Mourtada et al., 1996] used the BMD data to propose a 3D model from a 2D DXA data. Recently, Buijs and Dragomir-Daescu [Buijs and Dragomir-Daescu, 2011] used a 2D FE model derived from CT scans of human femur. The strain distributions were identified from recorded high speed video of the fracture procedure and were validated against the FE results.

While an acceptable agreement was found, our current approach proposes a 2D FE based DXA projection from the BMD data. This model takes in consideration the material properties for both cortical and trabecular tissues with significant accuracy. See Figure 5.17.

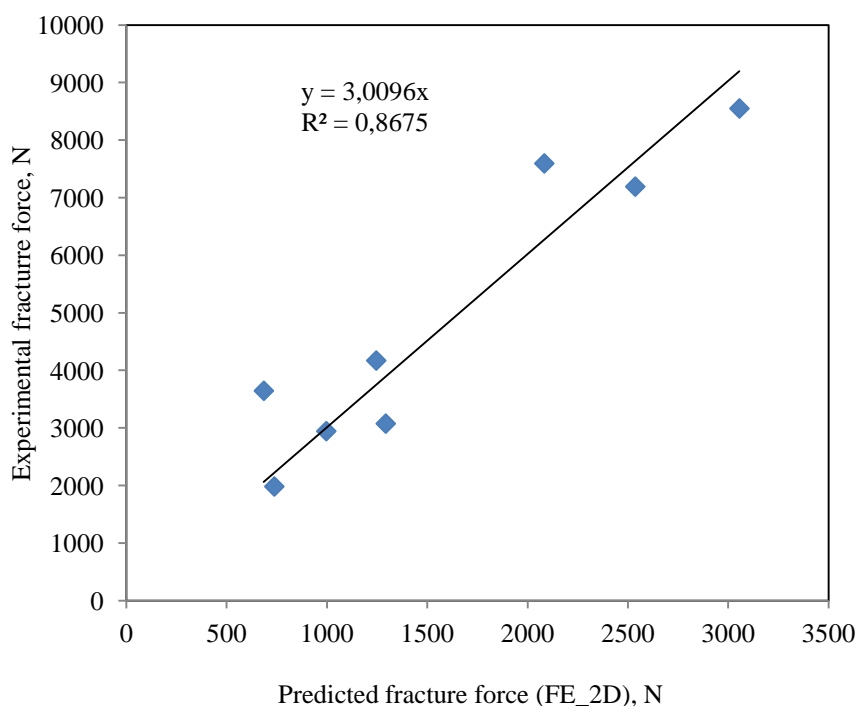


Figure 5. 17 Correlation between experimental and predicted proximal femur fracture under single limb stance configuration.

As shown in Figure 5.17 there is a significant linear correlation between the predicted fracture load FE analysis and the measured values ($r^2 = 0.867$). By applying the calibration coefficient of 3, reasonable accuracy was obtained as shown in Figure 5.18.

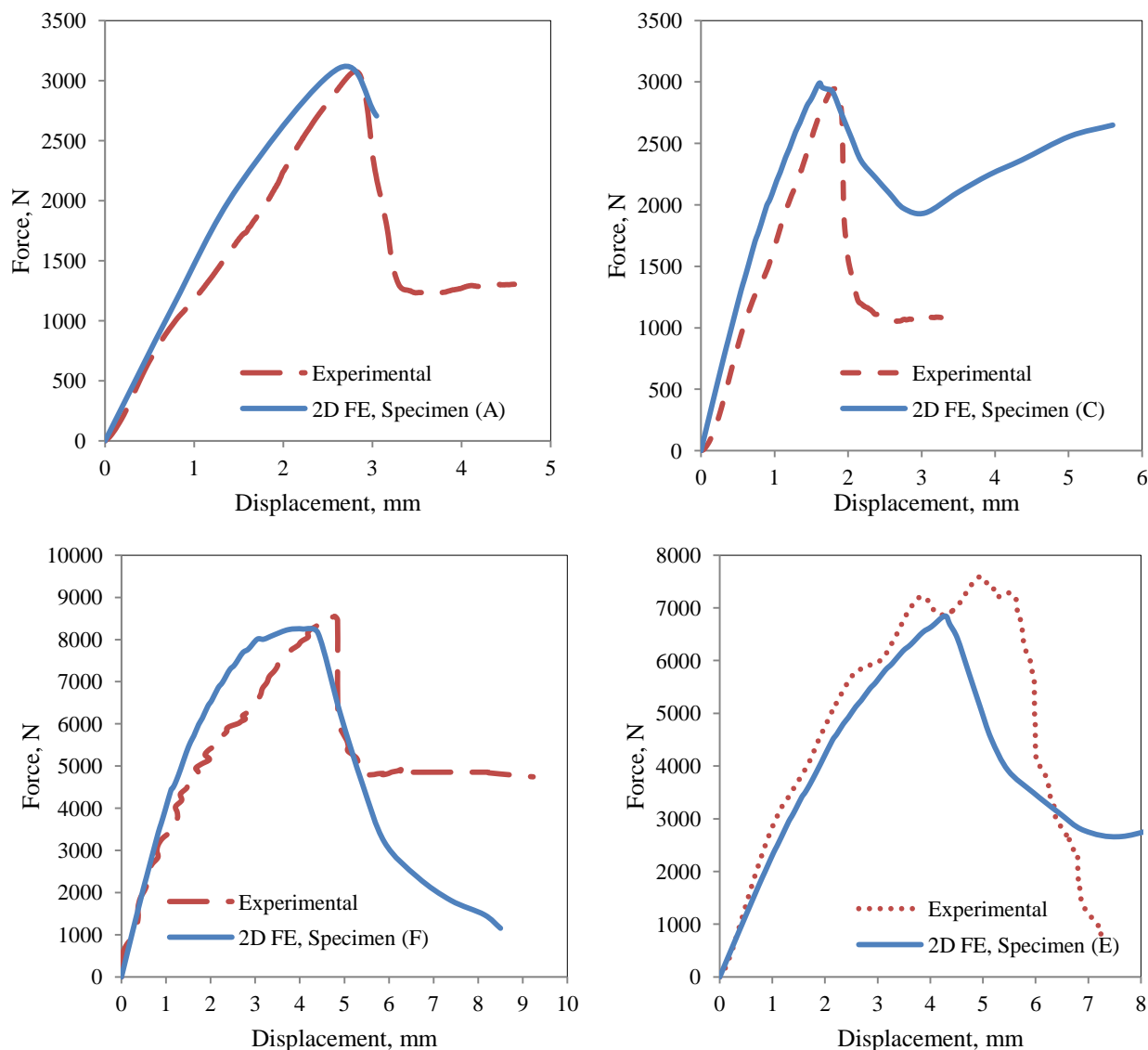


Figure 5. 18 Experimental and equivalent 2D force displacement curves.

The results showed that our proposed coupled approach results in a good correlation between 2D FE force displacement and measured curves. Even though the isotropic scalar damage variable which is implemented in the proposed model achieves a good agreement with the experimental obtained, the assumption of anisotropic damage may give more close results.

5.3.1.3 Effect of force direction on femoral fracture load in single limb stance

The head of the femur is attached to the femoral shaft by the femoral neck, which varies in length depending on human body anatomy. The cervical-diaphyseal angle varies around

$125 \pm 5^\circ$ in the normal adult. During the daily activities, the hip transmits a resultant contact force (F) through the acetabulum to the head of femur [Bergmann et al., 2001].

According to this anatomy the angle exerted by hip on the head femur varies. In addition, other normal activities, such as: slow walking, normal walking, fast walking, upstairs, downstairs, standing up, sitting down, standing on 2-1-2 legs and bending of the knee can vary the inclination of the resultant hip force on the head of the femur (see Figure 5.19).

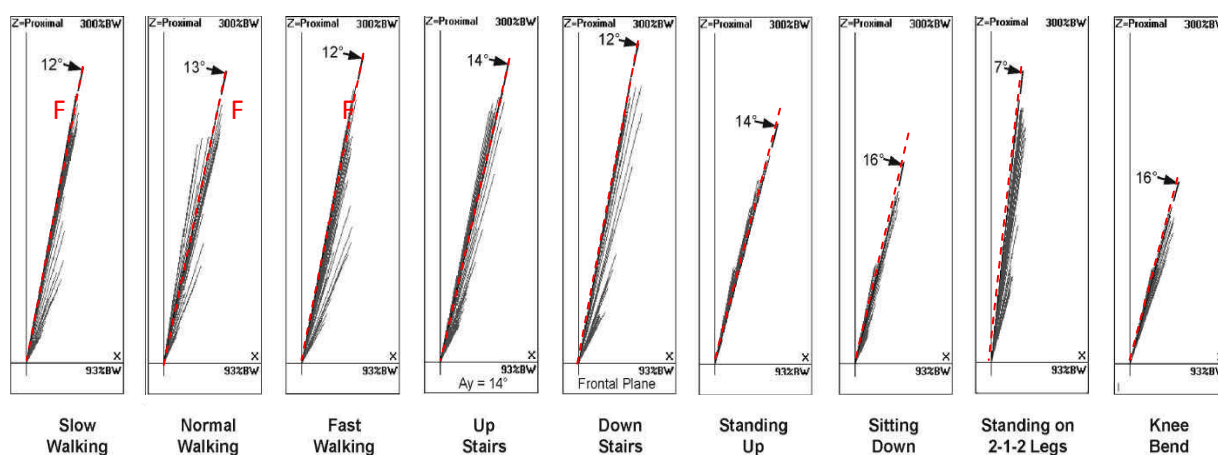


Figure 5. 19 Contact force vector F (Frontal plan) during nine activities [Bergmann et al., 2001].

If we consider the 3° offset of the femoral shaft axis from the frontal plane [Hollister et al., 1993 Sermon et al., 2012], the inclination of the contact force from the frontal plane varies from 10° to 25° depending on the type of activity (see Table 5.2). These angles correspond to daily activities and are based on the study performed by Bergmann et al. [Bergmann et al., 2001].

Table 5. 2 Hip force angles versus the daily activities.

Hip loading angle	Daily activities
$\alpha \leq 10^\circ$	Standing on 2-1-2 legs
$10^\circ < \alpha \leq 15^\circ$	Downstairs, fast walking, slow walking
$15^\circ < \alpha \leq 25^\circ$	Normal walking, upstairs, Sitting down, standing up, knee bend

In the current work, model (C) was developed to study the effect of force direction to represent the consequence of the daily activities on failure load under limb stance configuration, Figure 5.20. Five angles ($\alpha = 5^\circ, 10^\circ, 15^\circ, 20^\circ$ and 25°) of the load vectors on proximal femur represent the various activities.

Force directions were referenced to the 2D plane. To evaluate the effect of the various loading conditions on the head femur fracture, the applied force in each loading condition is compared with the load at 20° that is considered as reference.

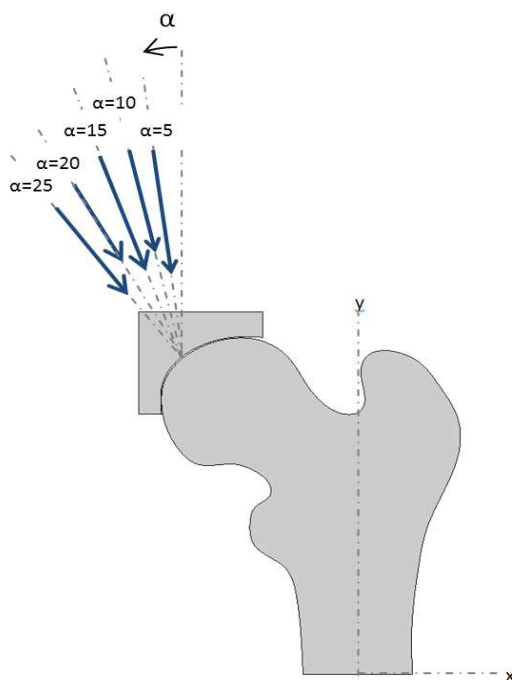


Figure 5. 20 Force directions for single limb stance loading condition (Frontal plane).

The force displacement curves are superposed to determine the force directions achieving the lowest fracture load under single limb stance, Figure 5.21.

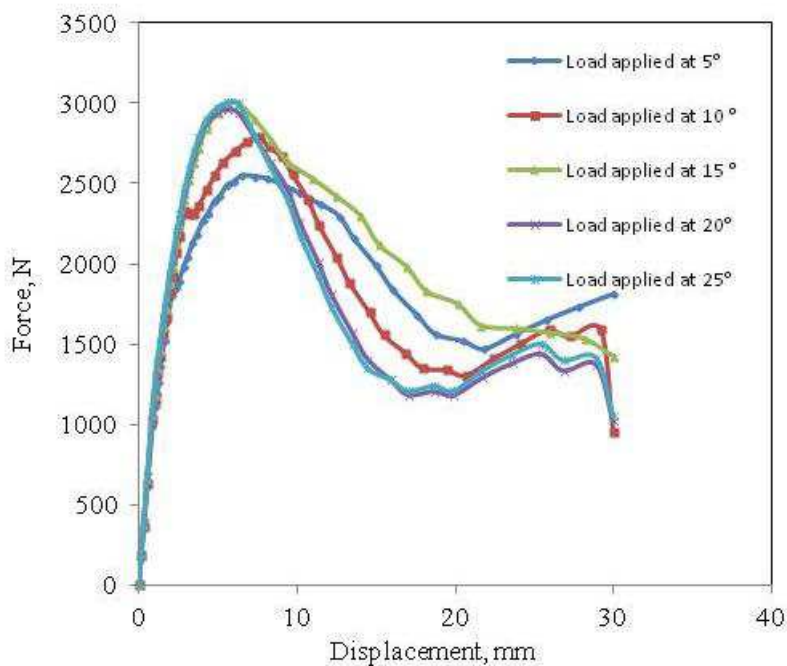


Figure 5. 21 Force displacement curves at different load angles: 5°, 10°, 15°, 20°, 25° (specimen I).

It is evident that the highest fracture forces occur at angles between 15° and 25° corresponding to normal walking, sitting and walking upstairs. So the femurs are more intensely resistant in these conditions (angles of 15° to 25°). The force acting on the femoral

head can be split into two different actions. The first one is the vertical component, generating a bending moment on the head whereas the second (horizontal) component exerts a compressive force on the head. When the angle increases, the vertical component will decrease and the moment value on the proximal head will decrease.

Bergmann et al. [Bergmann et al., 2001] perform an investigation about the hip joint loads during the nine daily activities. The objective of their study was to provide a database of the measurements of hip contact forces of human proximal femur during the most frequent activities of daily life. In their analysis, it was found that the measured axial component of the 3D resultant force, F_z , was close to the total resultant force as shown in Figure 5.22. This suggests that this component has the major effect of proximal femur failure. In the current study the vertical component, F_z , as well as the horizontal component, F_x , were taken into consideration for calculating the failure forces of proximal femur.

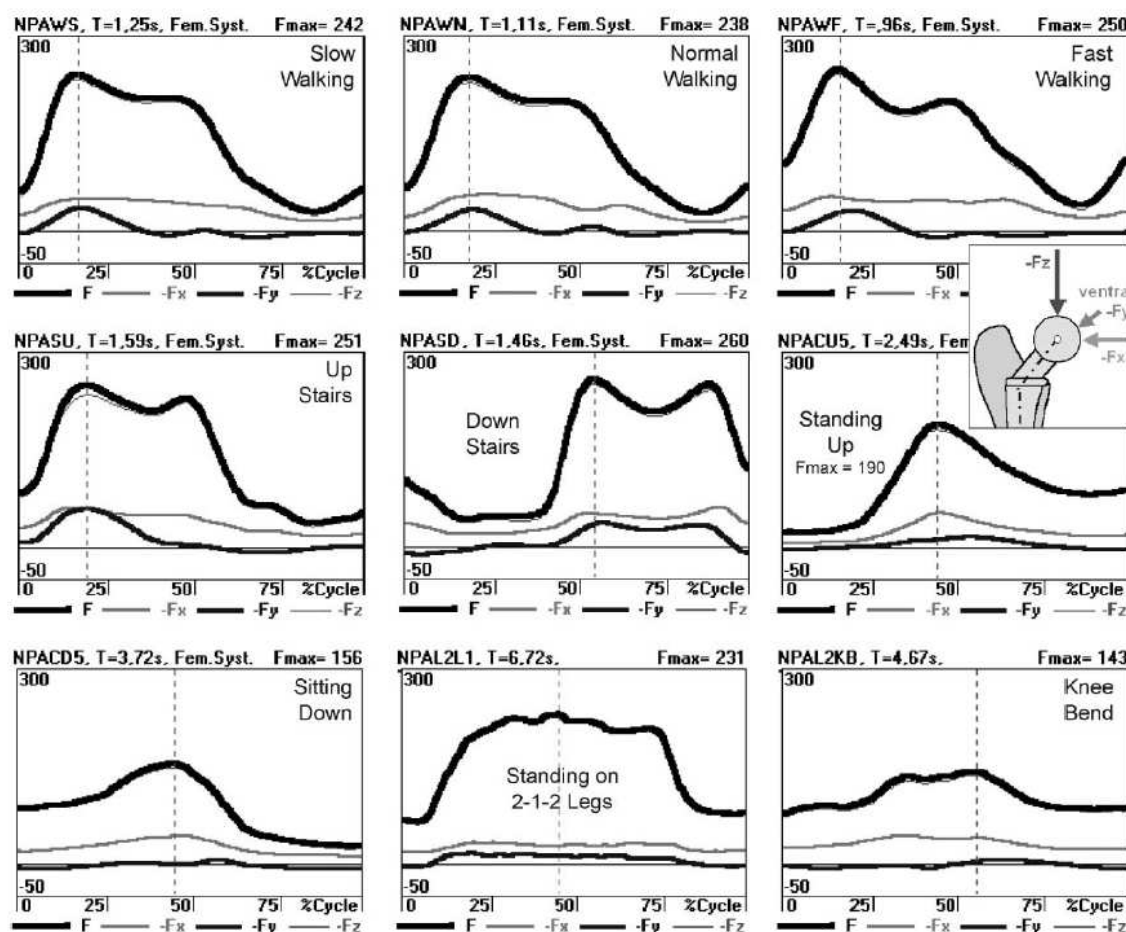


Figure 5.22 Contact force F during nine activities [Bergmann et al., 2001].

The current investigation provides information on the forces applied by hip on the head femur by the frequent daily activities angle.

However, the obtained results did not convey a significant influence of the angle on the predicted fracture pattern, Figure 5.23. As a rule, the most of the resulted fracture types remains subcapital fracture. Subcapital fractures are the most common types of spontaneous fractures [Cotton et al., 1994].

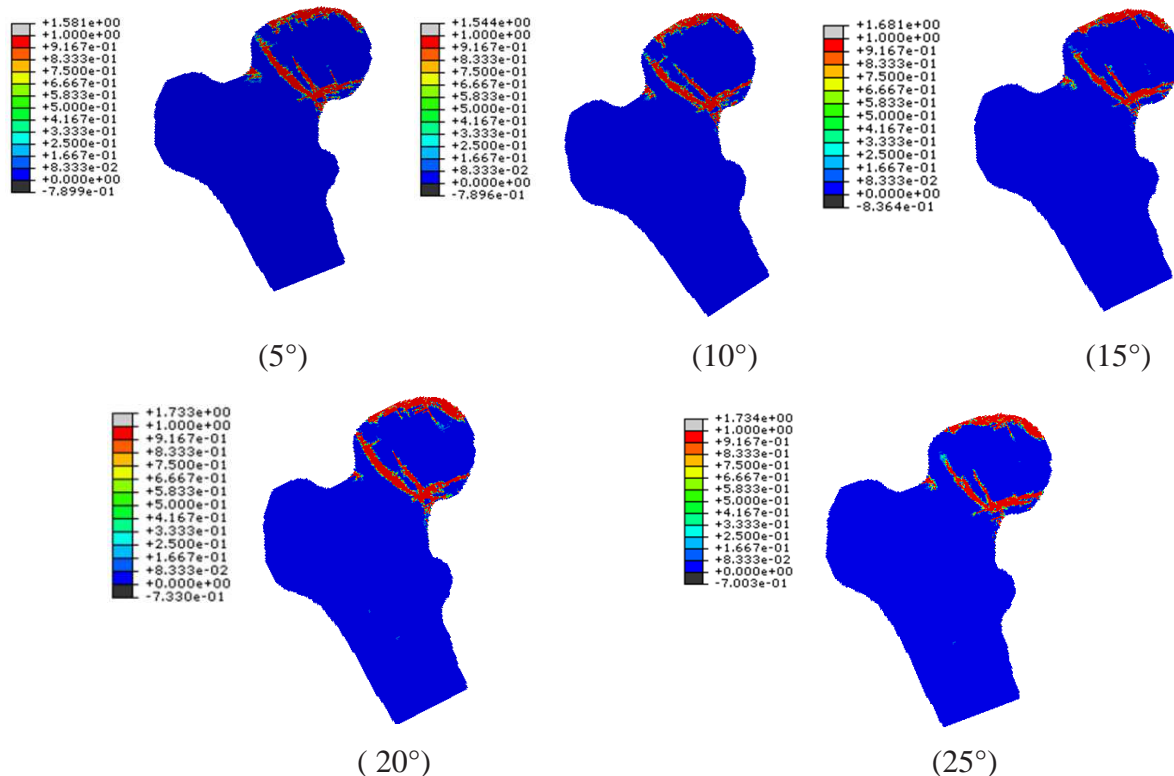


Figure 5.23 Fracture pattern during different applied load directions under single limb stance configuration (specimen A).

In all specimens used by Bessho et al. [Bessho et al., 2007] under identical conditions (limb stance, 20°), fractures occurs at the subcapital region. This was explained by the collapse of trabeculae in the subcapital region. In their FE analysis it was found that the solid and shell elements subjected to compressive failure were at the subcapital region. This contributed to confirming the accuracy of the current simulation model.

5.3.2 Sideways fall configuration results

5.3.2.1 Resulted two dimensional fracture patterns under sideways fall configuration.

In order to evaluate the risk of fracture as well as its type, if the tested femur is exposed to a sideways fall instead of single limb stance load, the 2D FE models were loaded until fracture under sideways fall configuration. The applied loads and boundary conditions were mentioned in chapter 3.

The resulting damage patterns and fracture types of some specimens are presented in Figure 5.24.

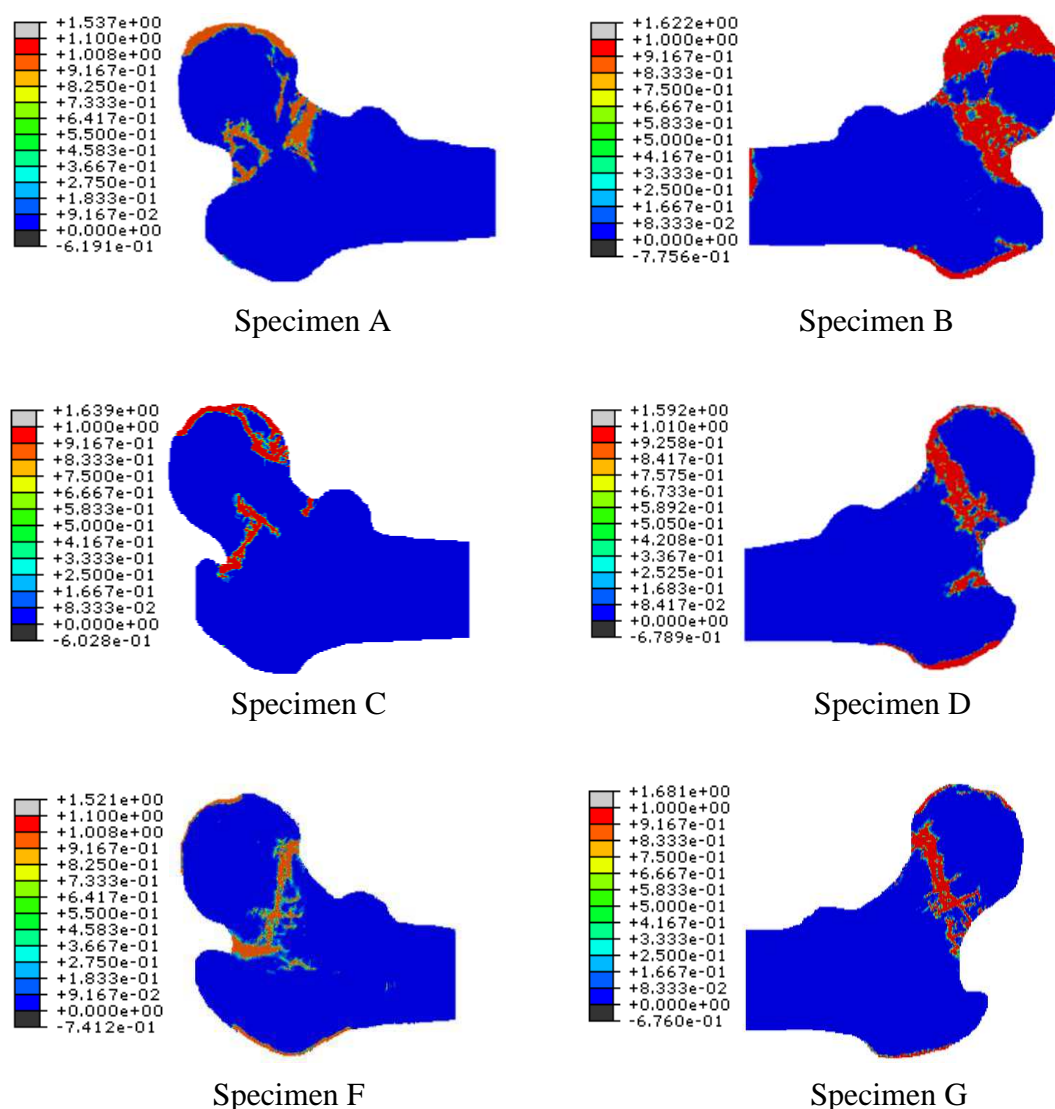


Figure 5.24 Fracture location and fracture pattern for side way fall configuration.

As shown in Figure 5.24, fracture starts at the same area (the weakest zone). The predicted fracture types appear to be in the basiservical zone in sideways falls as shown in Figure 5.24 for specimens A, B, C, D, F and G. In the specimens A and B, the highest damage accumulation due to a fall occurs in the cortex of the femoral neck and large compressive stresses develop in the superior region (Figure 5.24). Mayhew et al. [Mayhew et al., 2005] reported that human proximal femurs have thinner superior than inferior cortices at the mid femoral neck region. As shown in our results in specimens A and C, it was remarked that the damage appears in the inferior cortex. This is evident as during the sideways fall on the greater trochanter, the maximal compressive strain occurs at the superior femoral neck

[Lotz et al., 1995, Pinilla et al., 1996] with maximal tensile strain in the inferior cortex [de Bakker et al., 2009].

Under axial compression load testing under sideways fall configuration, femurs commonly fractured at the thin superior cortex [de Bakker et al., 2009]. In the current work, the predicted fractures were found mainly at the femoral neck as the basicervical type in specimens A, B and C or subcapital fracture in D, F and G. Very recently, the trabecular bone micro architecture of the femoral neck was studied in elderly women both with and without a hip fracture. The fractured cases had lower bone volume fraction, lower connectivity density and higher trabecular separation. Particularly, the superolateral region of the neck displayed substantial trabecular microarchitectural weakness in the elderly women who had sustained a femoral neck fracture [Milovanovic et al., 2012].

5.3.2.2 Effect of load direction angle on the damage of human neck femoral under sideways fall configuration

Two-dimensional FE model (model C) of cadaveric femurs was developed to study the effect of load direction on the damage of femoral neck. For the fall configuration, the force was applied to the femoral head at an angle (α) with the y-direction, Figure 5.25. The surface of the greater trochanter opposite the load was restrained in the direction of the applied load, but is free to slide horizontally. The angle (α) represents the angle between the shaft and the ground.

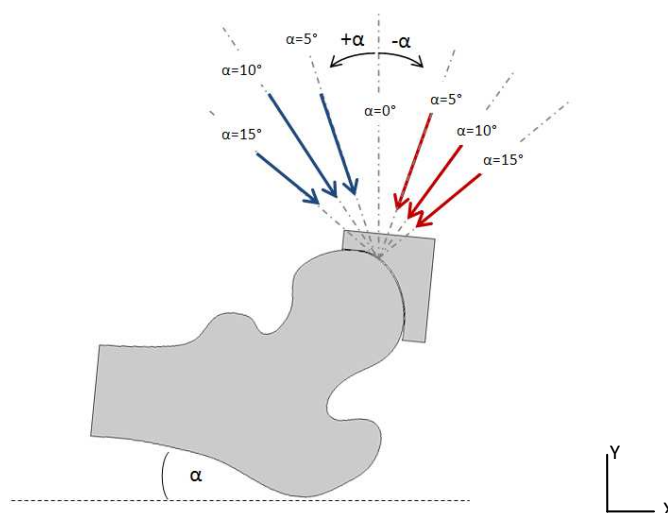


Figure 5. 25 Force directions for the sideways fall configuration.

In most sideways fall configurations investigations, a 10° angle (α) with the horizontal was adopted. The angle ($\alpha=10^\circ$) represents the load at 0° is the reference case [Bouxsein et al.,1995] which is used in most sideways fall configuration experimental tests.

In this investigation, under sideways fall configurations, the femurs were subjected to different load directions through changing the shaft angle with the horizontal from 0 to 15°. This range of angles was taken in cw (clock wise) and ccw (counter clock wise) direction (see Figure 5.26) in order to investigate the effect of load direction on proximal failure load. If successfully validated, such methods could be clinically applied to predict patient bone strength using simpler and less costly radiographs.

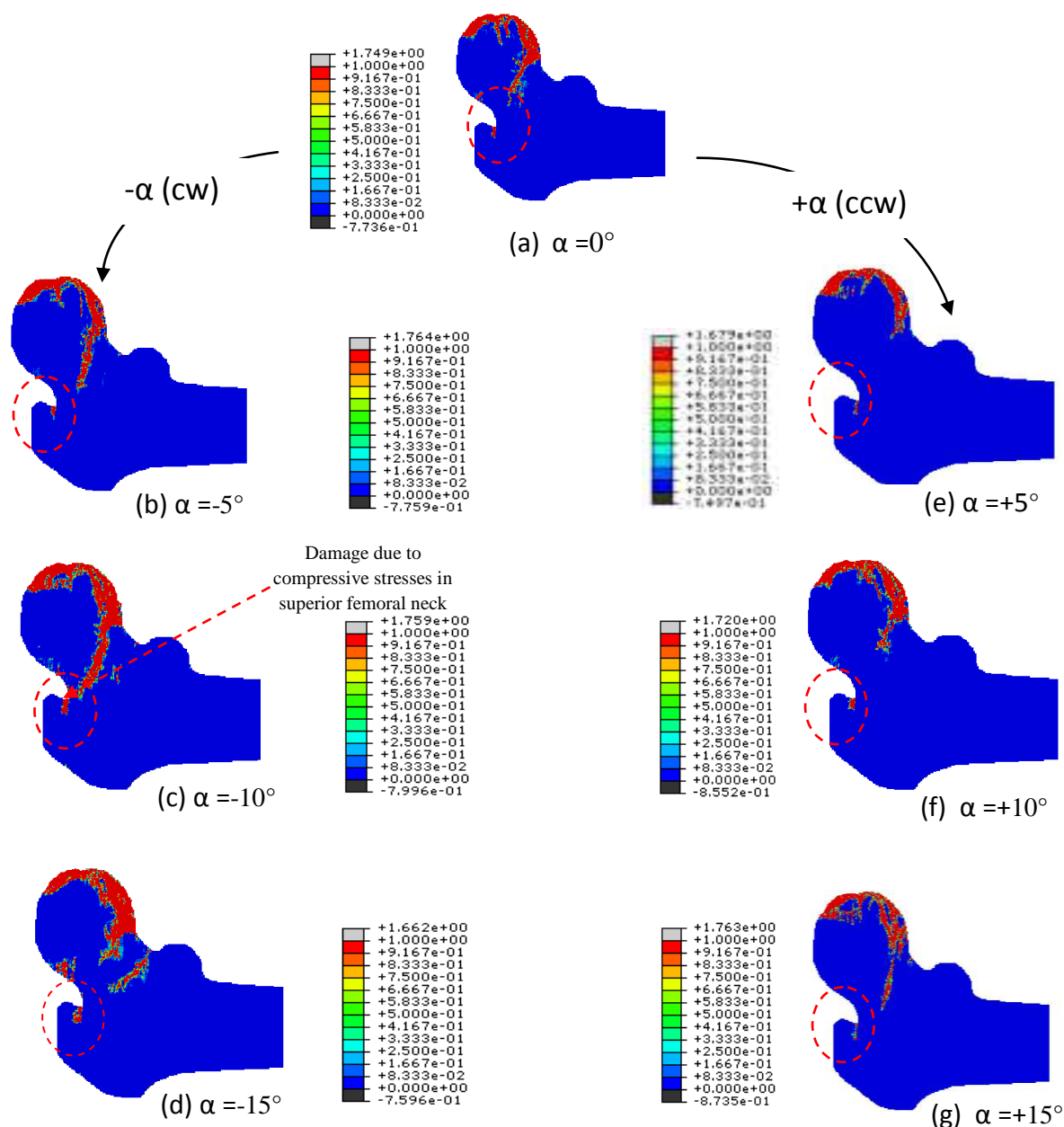


Figure 5.26 An example of the predicted different damage patterns at different load directions (at the same increment state), specimen C.

At the same displacement, during a sideways fall on the greater trochanter, the greatest compressive stresses occur in the superior femoral neck while the smaller tensile stresses occur in the inferior region [de Baker et al., 2004].

Clearly, a strong correlation between fracture load and load direction was found ($R^2 = 0.815$). The most critical cases are 'c' and 'g' which correspond to $\alpha = -10^\circ$ and $\alpha = -15^\circ$ respectively as shown in a representative sample (Figures 5.27a and 5.27b).

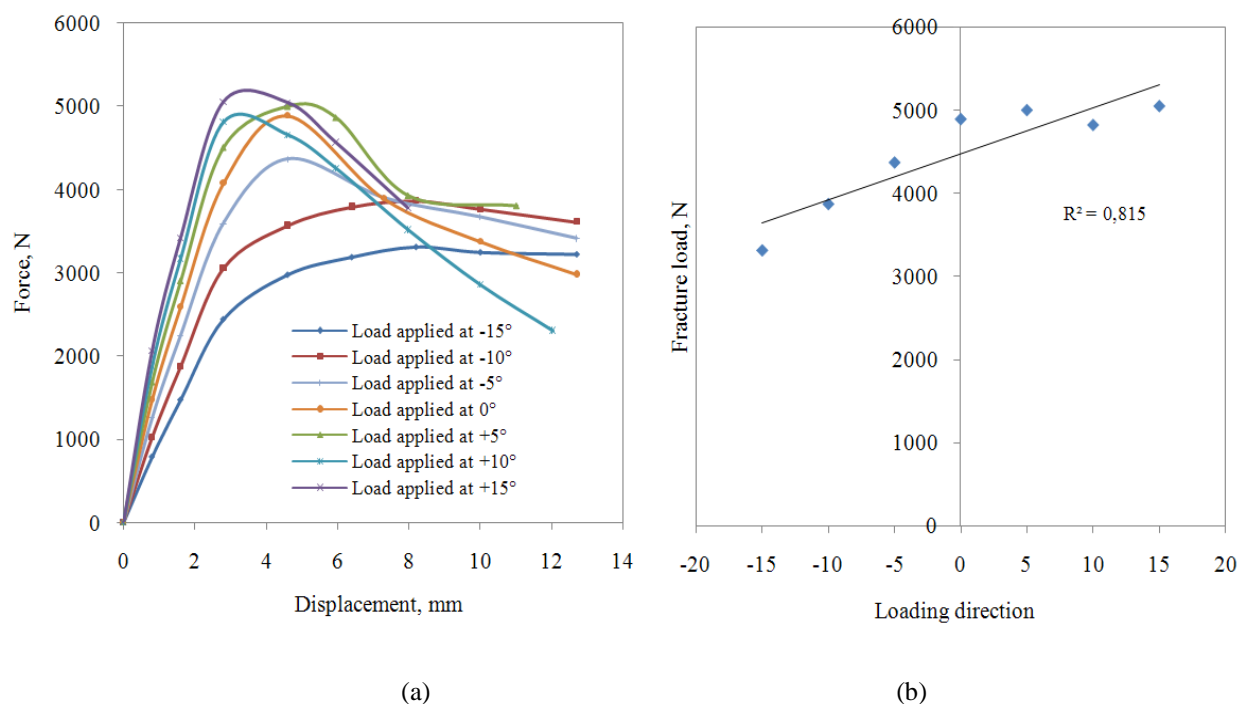


Figure 5.27 Effect of loading direction on predicted fracture load under sideways fall conditions (specimen 'D', age =91, Male, left femur). (a) Equivalent 2D Force-displacement curves at different loading angles
(b) impact of loading direction on fracture load.

It can be seen from Figure 5.26 that the amount of damage accumulation is also affected by the loading angle. As these damage patterns resulted from stress fracture, they can represent thus the resulted type of fracture pattern [Voo et al., 2004]. The obtained damage profiles represent typical fractures types: cervical fracture propagating parallel to the neck in the cases 'b', 'c' and 'g', showing two crack initiation sites laterally, which indicate the fracture risk area and initiation of subcapital cracks in cases 'c' and 'g'. Finally a cervical fracture, propagating also parallel to the neck, but including a secondary subcapital crack on the medial side results in case 'd'.

However, it is hardly feasible to determine all parameters which influence femur fracture. Other factors than scrutinized here might also affect the structural capacity of the femur, and many studies on bone strength of the proximal femur have been reported. For example, the study of Lotz and Hayes [Lotz et al., 1990] investigate the correlation between fracture load of human femur and its density. They reported the loads and energies needed to cause a proximal femur fracture. Courtney et al. [Courtney et al., 1995] studied the effect of age and loading rate on the femur failure. They compared the loads at fracture of the proximal femur from the cadavers of older and younger individuals. They reported a 20% increase in

failure load due to the high displacement rate [Courtney et al., 1994]. Keyak et al. [Keyak et al., 2001] investigated the influence of loading direction on the fracture load of the elderly proximal femur. Ford et al. [Ford et al., 1996] also reported the structural capacity of the proximal femur in four loading configurations that represent a range of possible falls on the greater trochanter. Pinilla et al. [Pinilla et al., 1996] studied the influence of changes in loading angle, under sideways fall position, on the failure load of the proximal femur ex vivo and on the fracture pattern. They assigned in their investigation three distinct loading angles 0°, 15° and 30° to simulate three fall positions: fall on the hip rolled slightly forward (0° position), to side (15°) or rolling slightly backwards (30°). The 15° loading configuration was identical to that used by Courtney et al. [Courtney et al., 1995]. The angle of the femoral shaft with respect to the horizontal (defined as femoral shaft angle) was 10°. Their results showed that a slight variation in the fall-related loading angle significantly reduces the failure load of the proximal femur. The femurs tested at 30° failed at a 24% lower load than the ones tested at 0° i.e. from 4000N at 0° to 3000N at 30°.

However, all these studies have highlighted that the loading direction influences the generation of a proximal femur fracture. The limitation of these studies is that they used subjects affected by osteoporosis. Furthermore, damage was not evaluated. In the current thesis, both were taken into consideration through using the damage as a coupling approach and the heterogeneous mesh.

The fracture patterns revealed by our model in sideways fall configuration were not significantly dissimilar suggesting that the load direction has not a significant effect on the fracture pattern at the used range of load directions ($\alpha=0^\circ \pm 15^\circ$). Our conclusion is confirmed by Pinilla et al. [Pinilla et al., 1996] who discussed also whether the fracture location is affected by loading direction. They found no significant difference in fracture patterns among the three groups.

The damaged zone due to the accumulation of equivalent strain was qualitatively compared with the an elastic equivalent strain field obtained with the 2D FEA model of representative proximal femur image obtained from high speed video recordings using digital image correlation from [Buijs and Dragomir-Daescu, 2011]. This qualitative example is presented in Figure 5.28.

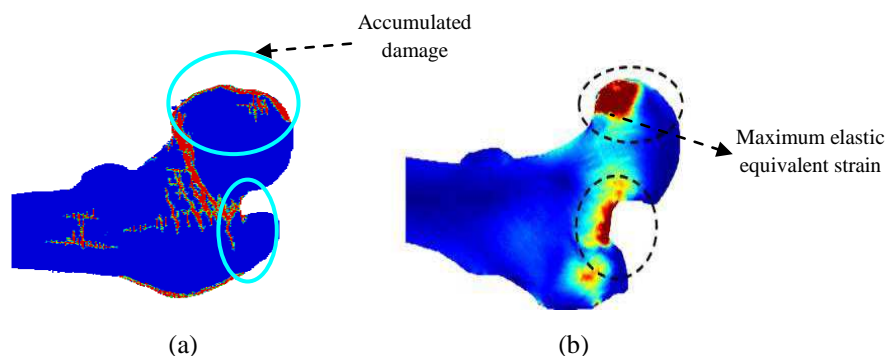


Figure 5.28 A Qualitative comparison of damaged areas in sideways fall configuration (a) 2D damage accumulation (current FE model) (b) Elastic equivalent strain distributions in a validated 2D-FE model of proximal femur [Buijs and Dragomir-Daescu, 2011].

Our results suggest that the damage occurs in areas which experience maximum strains. Previous investigations have concluded that neck femur fractures are typically initiated by a failure in the superior side of the femoral neck, followed by a failure in the inferior aspect of the femoral neck [de Baker et al., 2009, Lotz et al., 1995]. This can be explained by several factors:

- The femurs with a longer moment arm are exposed to higher forces applied to the hip [Wang et al., 2009].
- A fall onto the greater trochanter may also generate an axial force along the femoral neck, resulting in fracture due to the impact force.
- The lower extremity rotates externally during a fall on the femoral neck which impinges against the posterior acetabular rim. The acetabular rim then acts like a fulcrum to concentrate the stress experienced by that region upon impact [Koval & Zuckerman, 1994].

5.3.2.1 Effect of geometric parameters and density on the fracture force of human proximal femur under sideways fall configuration

There is indisputable evidence that BMD as measured by DXA, particularly at the proximal femur, is a strong predictor of hip fracture [Cummings et al., 1993]. However, considerable overlap exists in BMD values between subjects with and without hip fractures, suggesting that the geometry the proximal femur may contribute to femoral neck strength [Bergot et al., 2002].

In this study of proximal fracture risk evaluation from hip DXA scans, our objective was to test the potential of our proposed coupled damage approach to predict the proximal femur under sideways fall configuration. Using the heterogeneous isotropic model, model C, the effect of femoral neck width, femoral neck axis, cervical diaphyseal angle and density on the strength of the proximal femur will be evaluated and compared with those obtained in literature.

Figure 5.29 compiles the predicted femoral fracture load under sideways fall configuration correlated with femur geometry and density. The effect of femoral neck width (Figure 5.29a) and the femoral neck axis length (Figure 5.29b) support the results previously reported in hip fracture patients [Alonso et al., 2000, Gnudi et al., 1999, Karlsson et al., 1996].

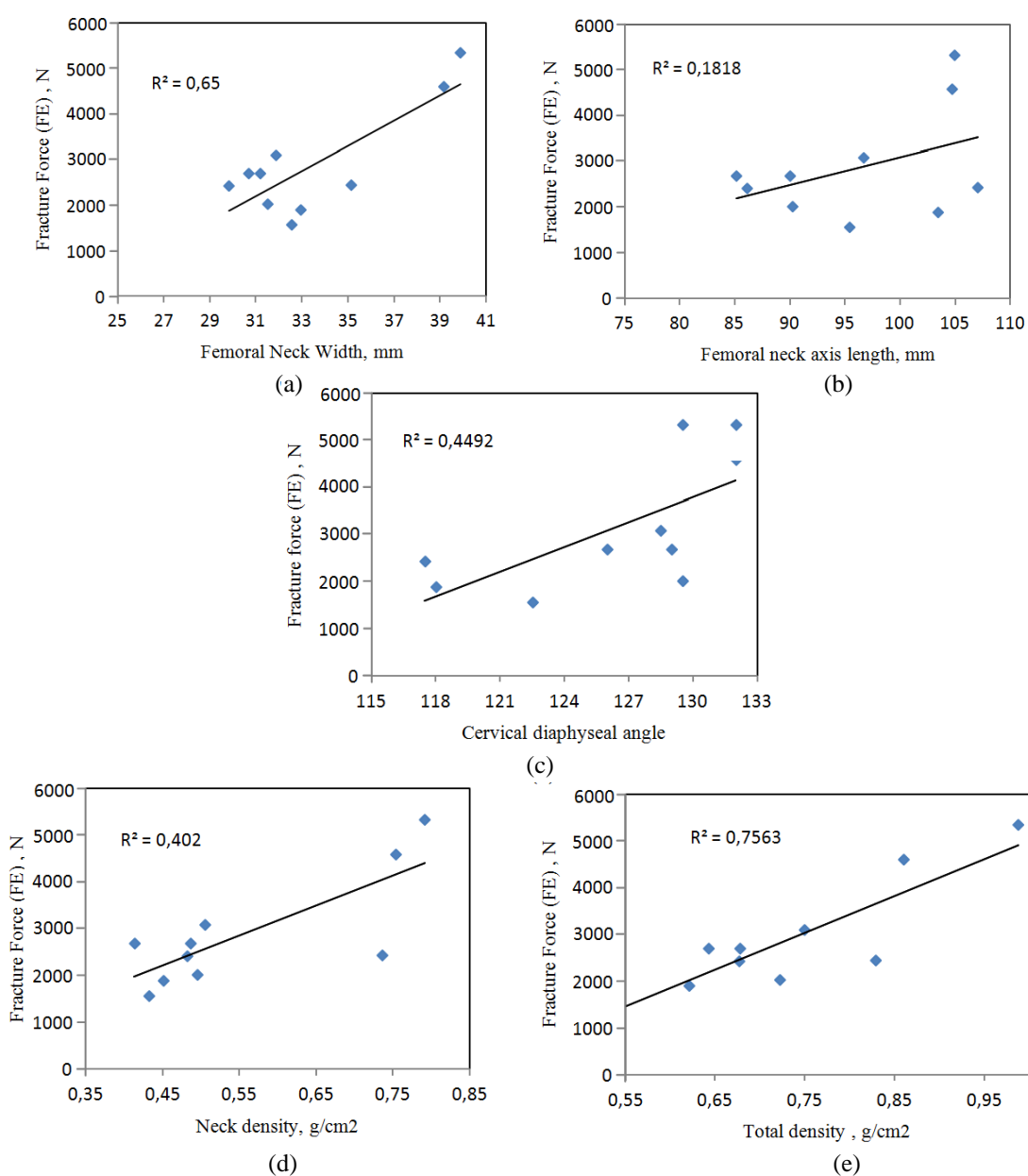


Figure 5. 29 Effect of femur geometry and density on the femur fracture load under sideways fall configuration.

Hip axis length (Figure 5.29b) and neck shaft angle (Figure 5.29c) both contribute to the moment arm of the hip and both have been independently shown to influence hip fracture [Leslie et al., 2009, Patron et al., 2006].

However, this effect cannot be considered as universally valid in the current investigation due to the small sample size and the absence of experimental validation tests. Alternatively, some specimens have less resistance even though they are characterized by higher neck density.

The results assembled in Figures (5.29d and 5.29e) imply the fact that the failure load is proportional to the femoral neck density. Hence, it can be inferred that the model using the isotropic behavior coupled to damage can give reasonable results.

5.4 Anisotropic finite element modeling results for single limb stance and sideways fall configurations

In the current work, 2D heterogeneous models coupled to quasi brittle isotropic damage law were evaluated by assigning anisotropic properties for both cortical and trabecular bone (Model B). The fracture of the femoral head and stiffness in both single limb stance and sideways fall configurations were evaluated.

Under single limb stance configuration, the correlation between the predicted failure load and the predicted stiffness was moderate ($R^2=0.51$), Figure 5.30a. In contrast, fair agreement ($R^2=0.75$) was obtained for the correlation between the predicted stiffness and BMD of the femoral neck, Figure 5.30b.

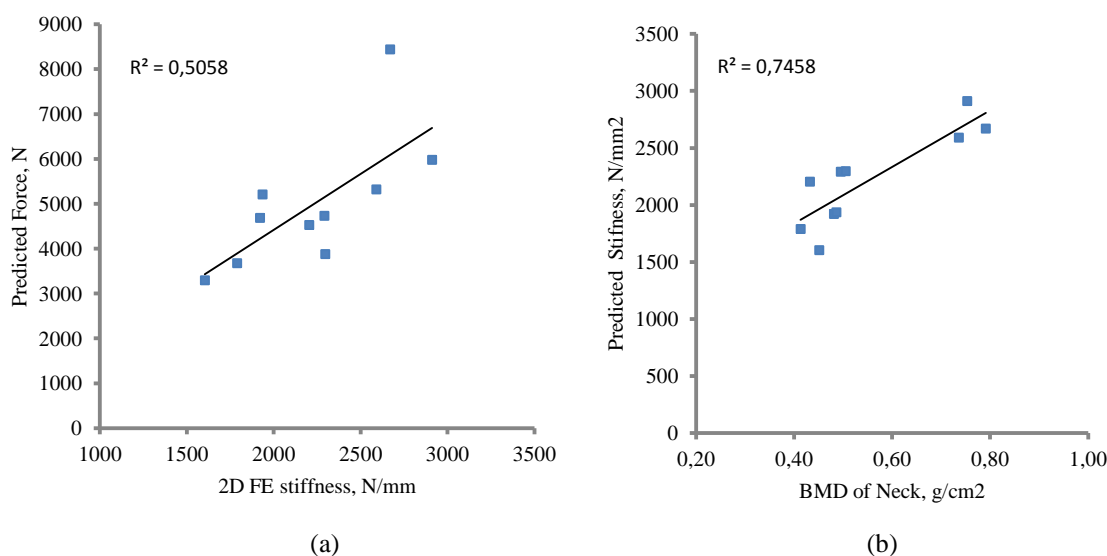


Figure 5. 30 Correlations under single limb stance configuration. (a) between 2D FE stiffness and predicted failure loads (b) between femoral neck density and predicted 2D FE stiffness.

Although most studies adopted the isotropic assignment in their simulations, bone was occasionally interpreted as being orthotropic [Peng et al., 2006, Taylor et al., 2002, Wirtz et al., 2003]. So far, the impact of using a model with orthotropic material property assignment compared to an isotropic model is still a matter of dispute [Peng et al., 2006].

For sideways fall configuration, the correlation between the predicted stiffness and predicted force was relatively strong ($R^2 = 0.86$) for our sample size specimens. The findings were compared with a recently validated 2D model [Buijs and Dragomir-Daescu, 2011], see Figures 5.31a and 5.31b.

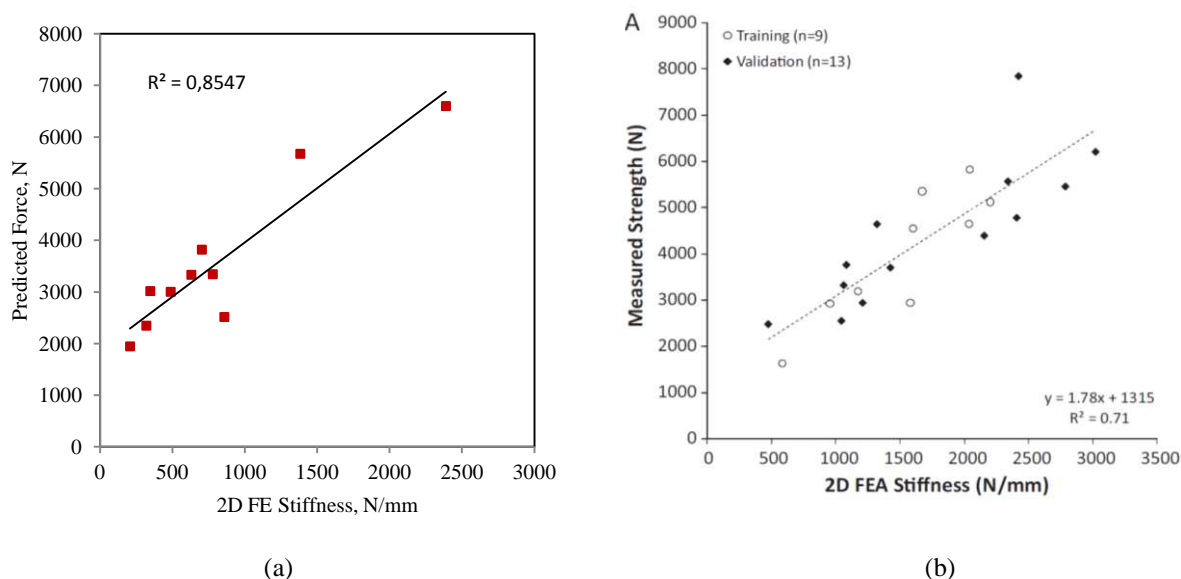


Figure 5.31 Correlation between stiffness and failure loads under sideways fall configuration. (a) predicted fracture load versus predicted stiffness obtained by current FE model, (b) Measured failure load versus predicted FE stiffness obtained by 2D FE model proposed by Buijs and Dragomir-Daescu, [Buijs and Dragomir-Daescu, 2011].

Our results show that the 2D FE models yield substantially accurate predictions of the femoral stiffness and ultimate proximal femur strength. The predicted stiffness is correlated with the neck femoral density by a not very significant correlation was found ($R^2=0.53$), see Figure 5.32a.

In the current study, we have investigated the relationships occurring between BMD of the femoral neck, 2D bone structure parameters calculated from DXA images and predicted bone 2D stiffness. It was reported that BMD can be used as a predictor of bone strength in cortical bone, i.e., in the femoral shaft.

However, when trabecular bone is present in the specimen (as in the femoral neck), BMD is of limited value in predicting bone strength, showing only a weak correlation with stiffness. This has earlier been stressed by Buijs and Dragomir-Daescu, Figure 5.32. Their data set shows a weak correlation ($R^2 = 0.48$).

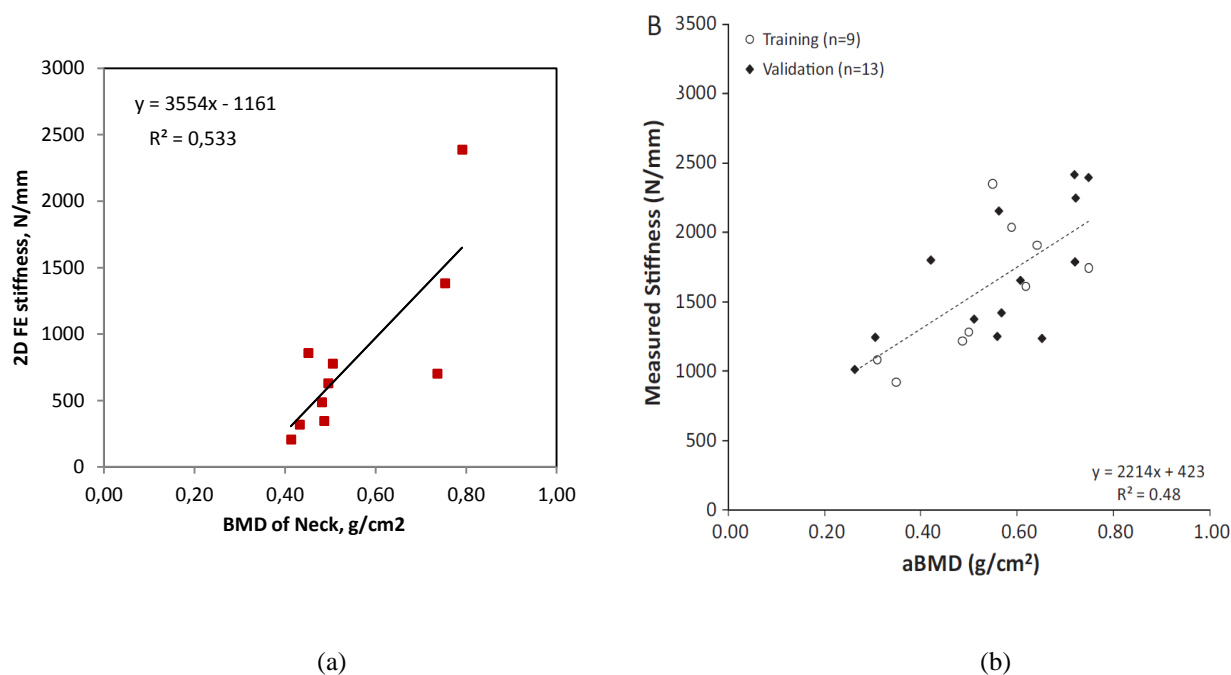


Figure 5.32 Correlation between femur neck density and femur stiffness under sideways fall configuration. (a) Current 2D FE model (b) Experimentally obtained stiffness versus BMD [Buijs and Dragomir-Daescu, 2011].

5.5 Conclusion

Our aim in this chapter was to validate the developed 3D FE models as well as the simplified 2D models using eight experimentally tested femurs. In this chapter we validated the proposed 2D and 3D FE models describing the progressive proximal femur fracture under single stance load and sideways fall configurations in the quasi-static regime.

The adopted equivalent shear strain in the FE damage model can be considered as a reliable variable able to simulate the fracture process till complete fracture.

The local and global surface deformation measurements of the proximal femur head was carried out by DIC method.

Our 3D results succeeded to predict the complete force displacement curves as well as the location of the fracture initiation. The total fracture patterns were slightly different from those obtained experimentally suggesting that the used voxel mesh method may not lead to a better prediction of the 3D fracture shape. Although CT based 3D FE analysis can give reliable predictive information on the complex proximal femur, a 2D FE model from DXA images may be sufficient for clinical purposes. The proposed simplified 2D model was preliminarily validated by another previously published model under identical boundary conditions. The obtained 2D force displacement curves were qualitatively compared with results from experiments and from the literature. Our model achieves a qualitatively good

match. Contrary to the proposed 3D model, the 2D model succeeded to predict the fracture location as well as total fracture profile by using voxel method.

The Femoral neck axis length, neck width, and neck-shaft angle were measured on radiographs of ten proximal femora. Bone mineral density (BMD) was measured using dual energy X-ray absorptiometry (DXA) for the region of interest. The strength of the femur was determined by a mechanical test simulating a single limb stance and the fracture type (subcapital, cervical or trochanteric) was subsequently determined and discussed. Among our samples, 13% cervical, 50% subcapital, 25% subcapital-cervical and 12% atypical fracture in the femoral head were observed. Under sideways fall configuration, DXA total density was more strongly correlated with femoral strength ($R^2 = 0.76$). A significant correlation was observed between femoral strength and neck width ($R^2 = 0.65$). Weak correlations were observed between fracture force and femoral neck axis length ($R^2 = 0.18$). Using anisotropic material, the predicted 2D failure load was strongly correlated to the 2D stiffness ($R^2 = 0.85$) under sideways fall configuration. In contrast, a fair correlation was found between the predicted 2D FE stiffness and DXA BMD of femoral neck ($R^2 = 0.53$).

Some limitations could be pointed out. It is evident that the number of samples in the current study was limited due to poor availability of human femurs. As a consequence, we were not able to validate our numerical results in the sideways fall configuration. Besides, it should be noted that the reason of using the 2D-DIC on the non-planar surfaces was to perform a qualitative comparison as the objective was qualitative rather than quantitative.

GENERAL CONCLUSION

The literature review conducted has confirmed the potential of the FE modeling technique to simulate the human femur fracture, and highlighted the relevance of appropriate geometric and mechanical representation of individual behavior, thereby increasing the discriminating power of models for risk fracture prediction. The first part of the current work has identified the widespread relevance of proper geometric and mechanical representation of individual specimens. Furthermore, this part is also focusing on determining the mechanical properties of bone and their dependence on bone density in terms of damage limit.

In the second part, the validation of the proposed models is achieved by engineering experimental setups for in vitro testing of the proximal femur and exerting loads causing fracture profiles similar to the ones observed in the clinical practice.

After evaluating the literature, the main objectives have been formulated as follows:

- Develop a 2D dual X-ray absorption and 3D quantitative computer tomography FE models based on the CDM approach in order to predict the human hip progressive fracture. The models take into account the geometry and mechanical properties of each bone specimen. The behavior law retained to describe the bone material is coupled to a quasi-brittle damage law to describe the progressive damaging process leading to the crack initiation and propagation. The propagation of the cracks were simulated by the the element deletion technique which consists in deleting the local fractured element of the mesh when it the damage reach its critical value of failure [[Hambli et al., 2012](#), [Hambli, 2013](#)].
- Development of an experimental validation technique based on three metrics: (i) the force-displacement curve, (ii) the fracture pattern and (iii) the distribution of the full-strain contour during the fracturing tests based on a powerful optical resolution techniques. This validation procedure of femur deformation is developed based on 2D and 3D Digital Image Correlation (DIC) method. In addition to the advantage of a noncontact process, the DIC method measures and quantifies the full-strain contour at all recorded instants using visual strain gradients and is able to catch details absent in single point measurement such as strain gauges. This technique permits to measure the global and spatially resolved

deformation at each instant throughout the experiment up to complete fracture. Although the determination of surface topology deformation and strains of proximal femur has its limitations, this optical approach can provide detailed data that cannot be obtained by traditional methods such as strain gages. This additional information is of great importance for a better understanding of mechanically induced femur neck fracture and should find more widespread use in bone fracture studies.

The results generated by previously published 3D FE models, which are also more complex and computationally expensive, deviate more from measured data, for example $F_{\text{exp}} = 0.77 F_{\text{num}} + 1150 \text{ N}$ [Keyak et al., 2001, Keyak et al., 2005]. Using identical conditions under single limb stance of femur loaded at 15° , Besso et al. found $F_{\text{exp}} = 0.809F_{\text{num}} + 1592 \text{ N}$ [Besso et al., 2007].

The FE models introduced here are capable of predicting more accurate values of the failure force of a proximal femur under single limb stance conditions. The correlation of experimental and numerical data is given by $F_{\text{exp}} = 0.912 F_{\text{Num}} + 211.2 \text{ N}$, suggesting that the applied innovative coupled approach is highly appropriate to address bone fracture.

The simulation results obtained with our model indicate the major role of damage and its impact on the behavior of the neck femur fracture. A combination of densitometric and geometric variables measured by 3D CT-scan explained 76% of the variability in the failure force in single limb stance configuration and 69% with the DXA model [Bousson et al., 2006]. Dall'Ara et al's model [Dall'Ara et al., 2013] succeeded to predict only 66% of cases. The contribution of the current model based on the experimental samples succeeded to predict more than 80 % of cases. These findings emphasize the need for continued refining of the model by introducing anisotropic damage. These findings encourage further studies that focus on the use of 3D data provided by CT-scan and analyze separately the role of anisotropic damage.

Once validated, this 3D FE model can be considered as a sophisticated tool for the clinician to predict failure forces and fracture type though its main disadvantage is the excessive consumption of computing time (up to 3 weeks). Therefore, the clinical implementation of 3D CT/FE methods is still limited, in part due to the requirement of expensive computer hardware to achieve solutions of 3D FE models within a clinically acceptable time, as well as the need for robust 3D segmentation and meshing techniques.

DXA is currently the clinical standard for assessing the risk of osteoporotic fracture but is not a reliable predictor of fracture.

The measuring technique (DIC) applied on in vitro experiments has enabled us to identify our FE modeling tool as a viable research technique as fracture forces of a considerable number of specimens in the two configurations could be reliably predicted.

In contrast to all previously developed models, the simplified 2D FE model coupled to quasi-brittle damage law succeeded to describe the initiation and progressive propagation of multiple cracks.

Our model can be applied also to simulate sideways fall configurations. In order to test its predictive power under this condition, a geometric study was performed. The effect of different geometrical parameters on the strength of the proximal femur was evaluated. These investigations have highlighted the role of the neck-shaft angle ($r = 0.67$), the radius of the femoral neck ($r = 0.8$), neck axis length ($r = 0.43$), and above all, the interaction of these three parameters and their combined effect on the risk of fracture. However, the analysis of the femur loaded in the configuration of lateral support calls for further research and should ultimately achieve distinction between cervical fractures and trochanteric fractures, as suggested by some clinical studies.

Finally, it should be mentioned that the proposed coupled quasi brittle damage can be applied at both mesoscale i.e. cortical bone [Bettamer et al., 2012b] as well as at nanoscale level [Barkaoui et al., 2011]. It gives reasonable results when compared with in vitro tests and other models from the literature.

Using the proposed 2D and 3D isotropic damage models could also be extended to include other parameters of anisotropic damage by analyzing, for example, the impact of a change in bone mineral density, either global or local, loading environment for femur and muscle forces in some cases.

However, some limitations of the present study must be noted. First, the small size of the samples constitutes the main limitation of our study. The small sample size conceals any direct experimental information about the sensitivity of the load at femoral fracture on the direction of loading in the sideways fall configuration. Furthermore, the present FE simulations of sideways fall simulated only one type of fall, i.e., the fall on the greater

trochanter, the applied quasi static load did not replicate the rates of loading (impact velocities) of actual falls.

Second, as the bone tissue consists of highly structured sheets of proteins, calcium phosphate, water, and cells (lamellae), it is highly unlikely that this tissue material is homogeneous and isotropic. Strictly speaking, though good results were obtained, this invalidates the assumption of homogeneity in the 2D model and of isotropy in the 3D model. In vitro, more extensive validation is still necessary for the current simplified model particularly for the simplified 2D model. First, other specimens should be tested in sideways fall configuration, from both fractured and unfractured ones. If encouraging results are achieved, this tool, which takes into account the geometric and densitometric characteristics of each specimen, should enable the clinicians to refine the diagnosis of the fracture risk and thus guide their decisions.

CONCLUSION GÉNÉRALE

L'étude bibliographique effectuée a mis en évidence le potentiel de la technique de modélisation par éléments finis pour simuler la fracture de fémurs humains. Les principaux objectifs ont été formulés comme suit:

- *Développer un modèle EF en 2D à partir de DEXA et un modèle EF en 3D à partir de la tomodensitométrie XCT (X-ray Computed Tomography), basé sur le concept de la mécanique d'endommagement (CDM) afin de prédire la fracturation progressive du col du fémur humain. Une loi de comportement couplée à l'endommagement quasi-fragile a été développée et implémentée au code de calcul Abaqus/Standard à l'aide de la routine UMAT. Ceci a permis de décrire le processus d'endommagement progressive conduisant à l'initiation et à la propagation des fissures. La propagation des fissures ont été simulées par la technique de suppression des éléments, qui consiste à supprimer l'élément fracturé du maillage quand le dommage atteindra sa valeur critique de rupture [Hambli et al., 2012, Hambli, 2013].*
- *Développement d'une technique expérimentale de validation sur la base de trois critères: (i) la courbe force-déplacement, (ii) le type de fracture, et (iii) la distribution du contour complet au cours des essais de fracturation basé sur une puissante technique de résolution optique. Cette procédure innovante de validation de la déformation du fémur est développée sur la base de corrélation d'images (DIC). Cette méthode a l'avantage d'être une technique de mesure sans contact et permet de quantifier les contours complets de déplacements et déformations à différentes séquences des essais jusqu'à la fracture totale du fémur. Bien que la détermination de la déformation surfacique du fémur a ses limites, cette approche optique peut fournir des données détaillées qui ne peuvent être obtenus par des méthodes traditionnelles telles que les jauges de déformation. Cette information supplémentaire est d'une grande importance pour une meilleure compréhension sur les mécanismes de fracturation du col du fémur et doit trouver une utilisation plus répandue dans les études sur les fractures des os.*

Les résultats générés par les modèles EF 3D publiés dans la littérature, présentent des corrélations correctes. $F_{exp} = 0.77 F_{num} + 1150 \text{ N}$ par [Keyak et al., 2001, Keyak et al., 2005]. $F_{exp} = 0.809F_{num} + 1592 \text{ N}$ par [Besso et al., 2007].

Les modèles EF 3D aboutie à une équation plus précise donnée par $F_{exp} = 0.912 F_{Num} + 211.2 \text{ N}$, ce qui suggère que l'approche proposée est plus fiable pour prédire la fracture osseuse.

Les résultats de simulation obtenus avec notre modèle indiquent le rôle majeur de l'endommagement et de son impact sur le comportement de la fracture du col du fémur.

Une combinaison de variables densitométriques et géométriques mesurés par CT-scan a expliqué 76% de la variabilité dans la force à la rupture dans la configuration monopodal et 69% avec le modèle DEXA [Bousson et al., 2006]. Le modèle de dall'Ara et al [dall'Ara et al., 2013] a réussi à prédire que 66% des cas. La contribution du modèle actuel sur la base des échantillons expérimentaux a réussi à prévoir plus de 80% des cas. Ces résultats soulignent la nécessité de poursuivre le raffinement du modèle en introduisant dommages anisotrope. Ces résultats encouragent d'autres études qui mettent l'accent sur l'utilisation des données 3D fournies par CT-scan et d'analyser séparément le rôle de dommages anisotrope.

Une fois validé, ce modèle 3D EF peut être considéré comme un outil fiable destiné aux cliniciens pour prédire les forces à la rupture et le type de fracture. Cependant, il nécessite une mise en œuvre complexe pour imager les fémurs in vivo et générer les maillages EF pour les prédictions et un temps de calcul très long. Par conséquent, la mise en œuvre clinique de méthodes 3D CT/EF reste limitée. Actuellement, la DEXA est la norme clinique pour évaluer le risque de fracture ostéoporotique mais n'est pas un indicateur fiable de fracture. En effet, dans l'optique d'une application clinique de la prédiction par EF de la fracture osseuse, une modèle EF 2D simplifié basé sur l'imagerie DEXA a été développé et validé par les essais.

Afin de tester son pouvoir de prédiction en configuration de chute latérale, une étude paramétrique a été effectuée. L'effet des différents paramètres géométriques sur la résistance de la partie proximale du fémur a été évalué. Ces recherches ont mis en évidence le rôle de l'angle cervico-diaphysaire ($r = 0,67$), le rayon du col du fémur ($r = 0,8$), la longueur du col de l'axe ($r = 0,43$). La conclusion de cette étude appelle à poursuivre les travaux en mode chute latérale et devrait à terme aboutir à la prédiction des fractures cervicales et fractures trochantériennes, comme suggéré par certaines études cliniques.

Cependant, certaines limites de la présente étude doivent être notées. Tout d'abord, la faible taille des échantillons constitue la principale limite de notre étude incapable de fournir une étude statistique robuste et effectuer des essais en mode chute latérale. Cependant, des simulations de chutes. Un seul type de chute ont été effectuée basée sur la validation faite en mode monopodale.

Deuxièmement, le tissu osseux est constitué d'une structure multiéchelle hiérarchique (fibres, ostéons, lamelles, travées, etc...). Par conséquent, il possède un comportement anisotrope et des propriétés hétérogènes. Une simulation considérant un endommagement et une fracturation anisotrope devra être menée pour améliorer la prédiction des faciès de fracture.

In vitro, une validation plus approfondie est encore nécessaire pour le modèle simplifié actuel en particulier pour le modèle 2D simplifié. Premièrement, d'autres échantillons doivent être testés dans la configuration de chute latérale. Si des résultats encourageants sont obtenus, cet outil, qui prend en compte les caractéristiques géométriques et densitométriques de chaque spécimen, devrait permettre aux cliniciens d'affiner le diagnostic du risque de fracture et ainsi orienter leurs décisions.

References

- Alho A., Husby T., Hoiseth A. (1988) Bone mineral content and mechanical strength. An ex vivo study on human femora at autopsy. *Clinical Orthopaedics and Related Research*, (227):292-297.
- Alonso C., Curiel M. et al. (2000) Femoral bone mineral density, neck-shaft angle and mean femoral neck width as predictors of hip fracture in men and women. Multicenter Project for Research in Osteoporosis. *Osteoporosis International*, (8):714-20.
- An Y., Draughn R. (2000) Mechanical testing of bone and the bone-implant interface. CRC, USA.
- Arthur Moore T., Gibson L. (2002) Microdamage accumulation in bovine trabecular bone in uniaxial compression. *Journal of Biomedical Materials Research*, (124):63-71.
- Ashman R., Rho J. (1988) Elastic modulus of trabecular bone material. *Journal of Biomechanics*, (21):177.
- Aspray T., Prentice A. et al. (2009) Low bone mineral content is common but osteoporotic fractures are rare in elderly rural Gambian women. *Journal of Bone and Mineral Research*, (11):1019-1025.
- Aufort G., Jennane R., Harba R., Benhamou C. (2007) Shape classification techniques for discrete 3D porous media. Application to trabecular bone., in: *IEEE International conference on engineering in medicine and biology society*. Lyon, France.
- Baca V., Horak Z., Mikulenska P., Dzupa V. (2008) Comparison of an inhomogeneous orthotropic and isotropic material models used for FE analyses. *Journal of Medical Engineering and Physics*, (30):924-930.
- Basso T., Klaksvik J., Syversen U., Foss O. (2012) Biomechanical femoral neck fracture experiments: A narrative review. *Injury*, (43):1633-1639.
- Baste S., El Guerjouma R., Gérard A. (1989) Mesure de l'endommagement anisotrope d'un composite céramique par une méthode ultrasonore. *Revue Physics*, (24):721-731.
- Bayraktar H., Morgan E. (2004) Comparison of the elastic and yield properties of human femoral cortical and trabecular bone tissue. *Journal of Biomechanics*, (37): 27-35.
- Beck T., Ruff C. et al. (1990) Predicting femoral neck strength from bone mineral data. A structural approach. *Investigative Radiology*, 25(1): 6-18.
- Bergmann G., Deuretzbacher G. et al. (2001) Hip contact forces and gait patterns from routine activities. *Journal of Biomechanics*, (34):859-871.
- Bergot C., Bousson V. et al. (2002) Hip fracture risk and proximal femur geometry from DXA scans. *Osteoporosis International*, (13):542-550.
- Bessho M., Ohnishi I. et al. (2007) Prediction of strength and strain of the proximal femur by a CT-based finite element method. *Journal of Biomechanics*, (40):1745-1753.
- Bettamer A., Hambli R., Allaoui S. (2011) Finite element prediction of proximal femur fracture profile based on anisotropic behaviour law coupled to damage, ASBMR2011 Annual Meeting, September, San Diego, California, USA, September 16-20,2011.

- Bettamer A., Hambli R., Allaoui S., Barkaoui A. (2012a) Proximal human femur fracture assessment using isotropic and orthotropic materials: a comparative FE-study using a quasi brittle damage models. 6th European Congress on Computational Methods in Applied Sciences and Engineering-ECCOMAS, Vienna, Austria, September 10-14, 2012.
- Bettamer A., Hambli R., Allaoui S., Barkaoui A. (2012b) A quasi brittle damage assessment simulation model of cortical bone specimens under compression load, 6th European Congress on Computational Methods in Applied Sciences and Engineering - ECCOMAS, Vienna, Austria, September 10-14, 2012.
- Black D., Bouxsein M. et al. (2008) Proximal femoral structure and the prediction of hip fracture in men: A large prospective study using QCT. *Journal of Bone and Mineral Research*, (23):1326-1333.
- Blain H., Chavassieux P. et al. (2008) Cortical and trabecular bone distribution in the femoral neck in osteoporosis and osteoarthritis. *Bone*, (43): 862–868.
- Bonfield W., Grynpas M. (1977) Anisotropy of Young's modulus of bone. *Nature*, (270) : 453-454.
- Bonnaire F., Buitrago-Tellez C. et al. (2002) Correlation of bone density and geometric parameters to the mechanical strength of the femoral neck. *Osteoporosis International*, (11): 765-771.
- Bonnet N., Gadois C. et al. (2007) Protective effect of β blockers in postmenopausal women: Influence on fractures, bone density, micro and macroarchitecture. *Bone*, (40):1209–1216.
- Bouhas F., Millien A., Pop O., Petit C. (2008) Apport de la corrélation d'images à l'étude du comportement des enrobes bitumineux en fatigue par cisaillement. XXVI^e Rencontres Universitaires de Génie Civil. 4-6 June 2008, France.
- Bousson V., Le Bras A. et al. (2006) Volumetric quantitative computed tomography of the proximal femur: relationships linking geometric and densitometric variables to bone strength. Role for compact bone. *Osteoporosis International*, (17):855–864
- Bouxsein M., Courtney L., Hayes A. (1995) Ultrasound and densitometry of the calcaneus correlate with the failure loads of cadaveric femurs. *Calcified Tissue International*, (56): 99–103.
- Bouxsein M., Karasik D. (2006) Bone geometry and skeletal fragility. *Current Osteoporosis Reports*, (4):49-56.
- Bramer J., Barentsen R. et al. (1998) Representative assessment of long bone shaft biomechanical properties: an optimized testing method. *Journal of Biomechanics*, (31): 741-745.
- Brown J., Prince R. et al. (2009) Comparison of the effect of denosumab and alendronate on bmd and biochemical markers of bone turnover in postmenopausal women with low bone mass. *Journal of Bone and Mineral Research*, (24) :153-161.
- Buijs J., Dragomir-Daescu D. (2011) Validated finite element models of the proximal femur using two-dimensional projected geometry and bone density. *Computer Methods and Programs in Biomedicine*, (104):168-174
- Bumrerraj S., Katz J. (2001) Scanning acoustic microscopy study of human cortical and trabecular bone. *Annals of Biomedical Engineering*, (12):1034-1042.
- Burr D., Martin R., Schaffler M., Radin E. (1985) Bone remodelling in response to in vivo fatigue microdamage. *Journal of Biomechanics*, (18):189–200.

- Burr D., Stafford T. (1990) Validity of the bulk-staining technique to separate artifactual from in vivo bone microdamage. *Clinical Orthopaedics and Related Research*, (260):305–308.
- Burr D., Forwood M., Fyhrie D., Martin R., Schaffler M., Turner C. (1997) Bone microdamage and skeletal fragility in osteoporotic and stress fractures. *Journal of Bone and Mineral Research*, (12):6–15.
- Burr D., Turner C. et al. (1998) Does microdamage accumulation affect the mechanical properties of bone? *Journal of Biomechanics*, (31): 337-345.
- Burstein A., Reilly D., Martens M. (1976) Aging of bone tissue: mechanical properties. *Journal of Bone Joint Surgery*, (58): 82-6.
- Cann C. (1988). Quantitative CT for determination of bone mineral density: a review. *Radiology*, (166): 509-521.
- Canton B., Gilchrist M. (2010) Automated hexahedral mesh generation of complex biological objects. *Strength, Fracture and Complexity*, (6): 51–68.
- Carter D., Hayes W. (1976) Bone compressive strength: the influence of density and strain rate. *Science*, (194):1174-1 176.
- Choi K., Fyhrie D., Schaffler M. (1994) Failure mechanisms of compact bone in bending: a microstructural analysis. *Transactions of the Annual Meeting 40th. Orthopaedic Research Society*, 425.
- Cody D., Gross G. et al. (1999) Femoral strength is better predicted by finite element models than QCT and DXA. *Journal of Biomechanical Engineering*, (32): 1013–1020.
- Cotton D., Whitehead C. et al. (1994) Are hip fractures caused by falling and breaking or breaking and falling? Photoelastic stress analysis. *Forensic Science International*, (65):105–112.
- Courtney A., Wachtel E., Myers E., Hayes W. (1994) Effects of loading rate on strength of the proximal femur. *Calcified Tissue International*, (55):53–8.
- Courtney A., Wachtel E., Myers E., Hayes W. (1995) Age-related reductions in the strength of the femur tested in a fall loading configuration. *The Journal of Bone and Joint Surgery*, (3):387– 395.
- Cowin S. (2001) *Bone mechanics handbook*, CRC Press. Boca Raton, FL.
- Cristofolini L., Juszczak M. et al. (2007) In vitro replication of spontaneous fractures of the proximal human femur. *Journal of Biomechanics*, (40):2837–2845
- Cummings S., Kelsey J., Nevitt M., O'Dowd K. (1985) Epidemiology of osteoporosis and osteoporotic fractures. *Epidemiologic Reviews*, (7):178-208.
- Cummings S., Rubin S., Black D. (1990) The future of hip fractures in the United States. *Clinical Orthopaedics Related Research*, (252):163-166.
- Cummings S., Black D. et al. (1993). Bone density at various sites for prediction of hip fractures. *The Lancet*, (341): 72-75.
- Currey J. (2002) *Bones: Structure and Mechanics*. Princeton University Press, Princeton.
- Currey J. (2010) Mechanical properties and adaptations of some less familiar bony tissues. *Journal of the Mechanical Behavior of Biomedical Materials*, (3):357-372.

- Dall'Ara E., Luisier B. et al. (2013) A nonlinear QCT based finite element model validation study for the human femur tested in two configurations in vitro. *Bone*, (52):27-38.
- de Bakker P., Manske S. et al. (2009) During sideways falls proximal femur fractures initiate in the superolateral cortex: Evidence from high-speed video of simulated fractures. *Journal of Biomechanics*, (12): 1917-25
- Delaere O., Dhem A., Bourgois R. (1989) Cancellous bone and mechanical strength of the femoral neck. *Archives of Orthopaedic and Trauma Surgery*, (108):72-75.
- Diab T., Condon K., Burr D., Vashishth D. (2006) Age-related change in the damage morphology of human cortical bone and its role in bone fragility. *Bone*, (38): 427–431.
- Dong X., Guo X. (2004) The dependence of transversely isotropic elasticity of human femoral cortical bone on porosity. *Journal of Biomechanics*, (37):1281–1287.
- Dragomir-Daescu D., Op Den Buijs J. et al. (2011) Robust QCT/FEA models of proximal femur stiffness and fracture load during a sideways fall on the hip. *Annals of Biomedical Engineering*, (2):742–755.
- Duchemin L. (2006) Prédiction du risque fracturaire de l'extrémité supérieure du fémur à partir d'une modélisation par éléments finis personnalisée. Thèse de l'Ecole Nationale Supérieure d'Arts et Métiers, France.
- Ebacher V., Tang C. et al. (2007) Strain redistribution and cracking behavior of human bone during bending. *Bone*, (40): 1265–1275.
- Ebacher V., Guy P., Oxland T., Wang R. (2012) Sub-lamellar microcracking and roles of canaliculi in human cortical bone. *Acta Biomaterialia*, (8):1093-1100.
- Fazzalari N., Forwood M. et al. (1998) Assessment of cancellous bone quality in severe osteoarthritis: bone mineral density, mechanics, and microdamage. *Bone*, (22): 381-388.
- Fedida R., Yosibash Z., Milgrom C., Joskowicz L. (2005) Femur mechanical simulation using high-order fe analysis with continuous mechanical properties. 2nd International Conference on Computational Bioengineering . Lisbon, Portugal, September 14-16.
- Fenech C., Keaveny T. (1999) A cellular solid criterion for predicting the axial-shear failure properties of bovine trabecular bone. *Journal of Biomechanics*, (121):414–22.
- Fondrk M., Bahniuk E., Davy D., Michaels C. (1988). Some viscoplastic characteristics of bovine and human cortical bone. *Journal of Biomechanics*, (8): 623–630.
- Fondrk M., Bahniuk E., Davy D. (1999) A damage model for nonlinear tensile behavior of cortical bone. *Journal of Biomechanical Engineering*, (121):533–41.
- Ford C., Keaveny T. (1996) The dependence of shear failure properties of trabecular bone on apparent density and trabecular orientation. *Journal of Biomechanics*, (29):1309–1317.
- Ford C., Keaveny T., Hayes C. (1996) The effect of impact direction on the structural capacity of the proximal femur during falls. *Journal of Bone and Mineral Research*, (3):377–83.
- Frost H. (1960) Presence of microscopic cracks in vivo in bone. *Henry Ford Hospital Medical Bulletin*, (8):25–35.

- Fyhrie D., Schaffler M.(1994) Failure mechanisms in human vertebral cancellous bone. *Bone*, (1): 105–109.
- Garcia D., Orteu J. (2001) 3D deformation measurement using stereocorrelation applied to experimental mechanics. The 10th FIG International Symposium on Deformation Measurements, 19-22 March, California, USA.
- Garcia D., Zysset P., Charlebois M., Curnier A. (2009) A Three-dimensional elastic plastic damage constitutive law for bone tissue. *Biomechanics and Modeling in Mechanobiology*,(8):149–165.
- Garrison J., Gargac J., Niebur G. (2011) Shear strength and toughness of trabecular bone are more sensitive to density than damage. *Journal of Biomechanics*,(16):2747-54.
- Gnudi S., Ripamonti C., Gualtieri G., Malavolta N. (1999) Geometry of proximal femur in the prediction of hip fracture in osteoporotic women. *The British Journal of Radiology*, (72):729–33.
- Goldstein S. (1987) The mechanical properties of trabecular bone: Dependence on anatomic location and function. *Journal of Biomechanics*, (20):1055-1061.
- Graves E. (1992) Detailed diagnoses and procedures, national hospital discharge survey, 1990. Vital and Health Statistics, Series 13, no. 113. U.S. Dept. of Health and Human Services.
- Guo X. (1994) Finite element modeling of damage accumulation in trabecular bone under cyclic loading. *Journal of Biomechanics*, (27):145–155.
- Hambli R. (2010) Application of neural networks and finite element computation for multiscale simulation of bone remodeling. *Journal of Biomechanical Engineering*, (11):114502.
- Hambli R. (2011) Multiscale prediction of crack density and crack length accumulation in trabecular bone based on neural networks and finite element simulation. *International Journal for Numerical Methods in Biomedical*, (4):461–75.
- Hambli R. (2012) A quasi-brittle continuum damage finite element model of the human proximal femur based on element deletion. *Medical and Biological Engineering and Computing*. DOI 10.1007/s11517-012-0986-5.
- Hambli R., Bettamer A., Allaoui S. (2012) Finite element prediction of proximal femur fracture pattern based on orthotropic behaviour law coupled to quasi-brittle damage. *Medical Engineering and Physics*, (34):202-210.
- Hambli R., Lespessailles E., Benhamou C. (2013) Integrated remodeling-to-fracture finite element model of human proximal femur behavior. *Journal of the Mechanical Behavior of Biomedical Materials*, (17):89–106.
- Hammer A. (1989) The structure of the femoral neck: a physical dissection with emphasis on the internal trabecular system. *Annals of Anatomy*, (192):168–177.
- Heini P., Franz T., Fankhauser C., Gasser B., Ganz R. (2004) Femoroplasty-augmentation of mechanical properties in the osteoporotic proximal femur: a biomechanical investigation of PMMA reinforcement in cadaver bones. *Clinical Biomechanics*,(19):506–512.
- Hill R. (1950) *The mathematical theory of plasticity*. Oxford, Clarendon Press.
- Hoffmeister B., Smith S., Handley S., Rho J. (2000) Anisotropy of Young's modulus of human tibial cortical bone. *Medical & Biological Engineering & Computing*, (3):333-338.

- Hollister A., Jatana S. et al. (1993) The axes of rotation of the Knee. *Clinical Orthopaedics and Related Research*, (290):259-268.
- Hoshaw S., Cody D., Saad A., Fyhrie D. (1997) Decrease in canine proximal femoral ultimate strength and stiffness due to fatigue damage. *Journal of Biomechanics*, (30): 323–329.
- Hoshen J., Kopelman R. (1976) Percolation and cluster distribution. *Physical Review B*, (14): 3438-3445.
- Jepsen K., Davy D. (1997) Comparison of damage accumulation measures in human cortical bone. *Journal of Biomechanics*, (30):891-894.
- Johnell O., Kanis J. et al. (2005) Predictive value of BMD for hip and other fractures. *Journal of Bone and Mineral Research*, (7):1185-94.
- Johnson T., Socrate S., Boyce M. (2010) A viscoelastic, viscoplastic model of cortical bone valid at low and high strain rates. *Acta Biomaterialia*, (6):4073-4080.
- Juszczyk M., Cristofolini L., Viceconti M. (2011) The human proximal femur behaves linearly elastic up to failure under physiological loading conditions. *Journal of Biomechanics*, (44):2259–2266.
- Kabel J., Van Rietbergen B. et al. (1999) The role of an effective isotropic tissue modulus in the elastic properties of cancellous bone. *Journal of Biomechanics*, (32): 673–80.
- Kaneko T., Pejčić M., Tehranzadeh J., Keyak J. (2003) Relationships between material properties and CT scan data of cortical bone with and without metastatic lesions. *Medical Engineering & Physics*, (6):445–54.
- Kanis J., Johnell O. (2005) Requirements for DXA for the management of osteoporosis in Europe. *Osteoporosis International*, (3):229-38.
- Karlsson K., Sernbo I. et al. (1996) Femoral neck geometry and radiographic signs of osteoporosis as predictors of hip fracture. *Bone*, (18):327–30.
- Kaufner H., Matthews L., Sonstegard D. (1974) Stable fixation of intertrochanteric fractures. *Journal of Bone Joint Surgery*, (5): 899-907.
- Keaveny T., Wachtel E., Guo X., Hayes W. (1994) Mechanical behavior of damaged trabecular bone. *Journal of Biomechanics*, (11):1309–1318.
- Keaveny T., Wachtel E., Zadesky S., Arramon Y. (1999) Application of the Tsai–Wu quadratic multiaxial failure criterion to bovine trabecular bone. *Journal of Biomechanical Engineering*, (1):99–107.
- Keaveny T., Morgan E., Niebur G., Yeh O. (2001) Biomechanics of trabecular bone. *Annual Review of Biomedical Engineering*, 3(1):307–333.
- Kefalas V., Eftaxiopoulos D. (2012) Experimental study of cancellous bone under large strains and a constitutive probabilistic model. *Journal of the Mechanical Behavior of Biomedical Materials*, (6):41-52.
- Kelsey J., Hoffman S. (1987) Risk factors for hip fracture. *New England Journal of Medicine*, (316):404-406.

- Keyak J., Rossi S. (1983) Prediction of femoral fracture load using finite elements models: an examination of stress- and strain-based failure theories. *Journal of Biomechanics*, (33):209–14.
- Keyak J., Rossi S., Jones K., Skinner H. (1998) Prediction of femoral fracture load using automated finite elements modeling. *Journal of Biomechanics*, (31):125–33.
- Keyak J., Rossi S. (2000) Prediction of femoral fracture load using finite element models. *Journal of Biomechanics*, (33):209–14
- Keyak J. (2001) Improved prediction of proximal femoral fracture load using nonlinear finite element models. *Medical Engineering and Physics*, (23):165–73.
- Keyak J., Rossi S., Jones K. (2001) Les CM, Skinner HB. Prediction of fracture location in the proximal femur using finite element models. *Medical Engineering and Physics*, (9):657–64.
- Keyak J., Falkinstein Y. (2003) Comparison of in situ and in vitro CT scan-based finite element model predictions of proximal femoral fracture load. *Medical Engineering and Physics*, (25):781–787.
- Keyak J., Kaneko T., Tehranzadeh J., Skinner H. (2005) Predicting proximal femoral strength using structural engineering models. *Clinical Orthopedics and Related Research*, (437):219-228.
- Keyak J., Koyama A. et al. (2009) Reduction in proximal femoral strength due to long duration spaceflight. *Bone*, (44):449–453.
- Khanoki S., Damiano P. (2013) Fatigue design of a mechanically biocompatible lattice for a proof-of-concept femoral stem. *Journal of the Mechanical Behavior of Biomedical Materials*, (22):65-83.
- Kotha S., Guzelsu N. (2003) Tensile damage and its effects on cortical bone. *Journal of Biomechanics*, (36): 1683-1689.
- Koval K., Zuckerman J. (1994) Hip fractures: overview and evaluation and treatment of femoral neck fractures. *Journal of the American Academy of Orthopaedic Surgery*, (2):141-149.
- Krajcinovic D., Fonseka G. (1981) The continuum damage theory of brittle materials. Part 1: general theory. *Journal of Applied Mechanics*, (48): 809-815.
- Kruzic J., Ritchie R. (2008) Fatigue of mineralized tissues: Cortical bone and dentin. *Journal of the Mechanical Behavior of Biomedical Materials*, (1):3-17.
- Kukla C., Gaebler C. et al. (2002) Predictive geometric factors in a standardized model of femoral neck fracture. Experimental study of cadaveric human femurs. *Injury*, (5): 427-433.
- Kulin R., Jiang F., Vecchio K. (2011) Effects of age and loading rate on equine cortical bone failure. *Journal of the Mechanical Behavior of Biomedical Materials*, (4): 57-75.
- La Borderie C., Berthaud Y., Pijaudier-Cabot G. (1990) Crack closure effects in continuum damage mechanics. Numerical implementation. Proceedings of the 2nd International Conference on Computer Aided.
- Ladd A., Kinney J., Goldstein D. (1998) Finite-element modeling of trabecular bone: comparison with mechanical testing and determination of tissue modulus. *Journal of Orthopaedic Research*, (16): 622-628.

- Laporte S., Skalli W. et al. (2003) A biplanar reconstruction method based on 2D and 3D contours: application to the distal femur. *Computer Methods in Biomechanics and Biomedical Engineering*, (1):1-6.
- Lang T., Keyak J. et al. (1997) Volumetric quantitative computed tomography of the proximal femur: precision and relation to bone strength. *Bone*, (1): 101-108.
- Langton C., Pisharody S., Keyak J. (2009) Comparison of 3D finite element analysis derived stiffness and BMD to determine the failure load of the excised proximal femur. *Medical Engineering & Physics*, (6):668-672.
- Le Bras A., Laporte S. et al. (2003) Three-dimensional (3D) detailed reconstruction of human vertebrae from low-dose digital stereoradiography. *The European Journal of Orthopaedic Surgery & Traumatology*, (13):57-62.
- Le Bras A. (2004) Exploration des potentialités du système EOSTM pour la caractérisation mécanique de structures osseuses: application à l'extrémité supérieure du fémur. Thèse de l'Ecole Nationale Supérieure d'Arts et Métiers, France.
- Le Bras A., Kolta S. et al. (2006) Assessment of femoral neck strength by 3-Dimensional X-ray absorptiometry. *Journal of Clinical Densitometry*, (9): 425-430.
- Lee T., Myers E., Hayes W. (1998) Fluorescence-aided detection of microdamage in compact bone. *Journal of Anatomy*, (193):179-184.
- Lee T., Arthur T., Gibson L., Hayes W. (2000) Sequential labelling of microdamage in bone using chelating agents. *Journal of Orthopaedic Research*, (18):322-325.
- Lee T., Mohsin S. et al. (2003) Detecting microdamage in bone. *Journal of Anatomy*, (203):161-172.
- Lee W., Kim T., Cho M., Lee S. (2005) Content adaptive finite element mesh generation of 3-D complex MR volumes for bioelectromagnetics problems, proceedings of the IEEE, Engineering in Medicine and biology 27th annual conference, 4373-4376.
- Leichter I., Margulies J. et al. (1982) The relationship between bone density, mineral content, and mechanical strength in the femoral neck. *Clinical Orthopaedics and Related Research*, (163): 272-281.
- Lemaitre J. (1985) Continuous damage mechanics model for ductile fracture. *Journal of Engineering Materials and Technology*, (107):83-9.
- Lemaitre J., Chaboche J. (1990) *Mechanics of solid materials*. Cambridge University Press. UK.
- Lemaitre J. (1996) *A Course on damage mechanics*. Berlin.
- Lenaerts L., Lenthe G. (2009) Multi-level patient-specific modelling of the proximal femur. A promising tool to quantify the effect of osteoporosis treatment *Philosophical Transaction A*, (367):2079-2093
- Leslie W., Pahlavan P., Tsang J., Lix L. (2009) Prediction of hip and other osteoporotic fractures from hip geometry in a large clinical cohort. *Osteoporosis International*, (10): 1767-1774.
- Link T., Vieth V. et al. (2003) Structure analysis of high resolution magnetic resonance imaging of the proximal femur: in vitro correlation with biomechanical strength and BMD. *Calcified Tissue International*, (2): 156-165.

- Lochmüller E., Zeller J. et al. (1998) Correlation of femoral and lumbar DXA and calcaneal ultrasound, measured in situ with intact soft tissues, with the in vitro failure loads of the proximal femur. *Osteoporosis International*, (8): 591–598.
- Lochmüller E., Groll O. et al. (2002) Mechanical strength of the proximal femur as predicted from geometric and densitometric bone properties at the lower limb versus the distal radius. *Bone*, (30): 207–216.
- Lotz J., Hayes W. (1990) The use of quantitative computed tomography to estimate risk of fracture of the hip from falls. *The Journal of Bone and Joint Surgery*, (72): 689–700.
- Lotz J., Cheal E., Hayes W. (1991a) Fracture prediction for the proximal femur using finite element models: Part I—Linear analysis. *Journal of Biomechanical Engineering*, (60):113:353.
- Lotz J., Cheal E., Hayes W. (1991b) Fracture prediction for the proximal femur using finite element models: Part II--Nonlinear analysis. *Journal of Biomechanical Engineering*, (4):361-365.
- Lotz J., Cheal E., Hayes W. (1995) Stress distributions within the proximal femur during gait and falls: implications for osteoporotic fracture. *Osteoporosis International*, (5):252–261
- Malik L., Stover M., Martin B., Gibeling C. (2003) Equine cortical bone exhibits rising R-curve fracture mechanics. *Journal of Biomechanics*, (36):191–8.
- Mammone J., Hudson S. (1993) Micromechanics of bone strength and fracture. *Journal of Biomechanics*, (26):439–446.
- Mayhew P., Thomas C. (2005) Relation between age, femoral neck cortical stability, and hip fracture risk. *The Lancet*, (366):129-135.
- Mazars J., Pijaudier-Cabot G. (1989) Continuum damage theory. Application to concrete. *ASCE Journal of Engineering Mechanics*, (2):345-365.
- Mercer C., He M., Wang R., Evans A. (2006) Mechanisms governing the inelastic deformation of cortical bone and application to trabecular bone. *Acta Biomaterialia*, (2):59–68.
- Merz B., Niederer P., Muller R., Rueggsegger P. (1996) Automated finite element analysis of excised human femora based on precision -QCT. *Journal of Biomechanical Engineering*, (3): 387-390.
- Milovanovic P., Djonic D. (2012) Micro-structural basis for particular vulnerability of the superolateral neck trabecular bone in the postmenopausal women with hip fractures. *Bone*, (50): 63-68.
- Mirzaei M., Samiezadeh S., Khodadadi A., Ghazavi M. (2012) Finite element prediction and experimental verification of the failure pattern of proximal femur using quantitative computed tomography images. *World Academy of Science, Engineering and Technology*, (66):111-117.
- Morgan E., Lee J., Keaveny T. (2005) Sensitivity of multiple damage parameters to compressive overload in cortical bone. *Journal of Biomechanical Engineering*, (4):557-62.
- Mori S., Harruff R., Ambrosius W., Burr D. (1997) Trabecular bone volume and microdamage accumulation in the femoral heads of women with and without femoral neck fractures. *Bone*, (21):521-526.
- Mourtada F., Beck T. et al. (2005) Curved beam model of the proximal femur for estimating stress using dual-energy X-ray absorptiometry derived structural geometry. *Journal of Orthopaedic Research*, (3):483–492.

- Murasawa G., Yoneyama S., Sakuma T., Takashi M. (2006) Influence of cyclic loading on inhomogeneous deformation behavior arising in NiTi shape memory alloy plate. *Materials Transactions*, (47): 780-786.
- Nagaraja S., Couse T., Guldberg R. (2005) Trabecular bone microdamage and microstructural stresses under uniaxial compression. *Journal of Biomechanics*, (38):707-716.
- Nalla R., Kinney J., Ritchie R. (2003) Mechanistic fracture criteria for the failure of human cortical bone. *Nature Materials*, (2):164-8.
- Nalla K., Kruzic J., Kinney H., Ritchie O. (2005) Mechanistic aspects of fracture and R-curve behavior in human cortical bone. *Biomaterials*, (26):217-31.
- Nicolella D., Moravits D. et al. (2006) Osteocyte lacunae tissue strain in cortical bone. *Journal of Biomechanics*, (9):1735-1743.
- Norman T., Wang Z. (1997) Microdamage of human cortical bone: incidence and morphology in long bones, *Bone*, (20): 375-379.
- O'Brien F., Taylor D., Dickson G., Lee T. (2000) Visualisation of three-dimensional microcracks in compact bone. *Journal of Anatomy*, (197):413-420.
- O'Neal J., Diab T. et al. (2010) One year of alendronate treatment lowers microstructural stresses associated with trabecular microdamage initiation. *Bone*, (47):241-247.
- Orwoll E., Marshall L. et al. (2009) Finite element analysis of the proximal femur and hip fracture risk in older men. *Journal of Bone and Mineral Research*, (24):475-483.
- Ota T., Yamamoto I., Morita R. (1999) Fracture simulation of femoral bone using finite-element method: How a fracture initiates and proceeds. *Bone and Mineral Metabolism*, (175):108-112.
- Parker M., Dynan Y. (1998) Is Pauwels classification still valid?. *Injury*, (7):521-523.
- Patron M., Duthie R., Sutherland A. (2006) Proximal femoral geometry and hip fractures. *Acta Orthopaedica Belgium*, (1): 51-5.
- Pattin C., Caler W., Carter D. (1996) Cyclic mechanical property degradation during fatigue loading on cortical bone. *Journal of Biomechanics*, (29):69-79.
- Peng L., Bai J., Zeng X., Zhou Y. (2006) Comparison of isotropic and orthotropic material property assignments on femoral finite element models under two loading conditions. *Medical Engineering & Physics*, (28):227-233.
- Perilli E., Baleani M. et al. (2008) Dependence of mechanical compressive strength on local variations in microarchitecture in cancellous bone of proximal human femur. *Journal of Biomechanics*, (2):438-46.
- Peters W., Ranson W. (1982) Digital imaging techniques in experimental stress analysis. *Optical Engineering*, (3):427-31.
- Pidaparti R., Burr D. (1992) Collagen fiber orientation and geometry effects on the mechanical properties of secondary osteons. *Journal of Biomechanics*, (8):869-80.

- Pietruszczak S., Inglis D., Pande G. (1999) A Fabric-dependent fracture criterion for bone. *Journal of Biomechanics*, (32):1071–1079.
- Pietruszczak S., Gdela K., Webber C., Inglis D. (2007) On the assessment of brittle–elastic cortical bone fracture in the distal radius. *Engineering Fracture Mechanics*, (74):1917-1927.
- Pinilla T., Boardman K. et al. (1996) Impact direction from a fall influences the failure load of the proximal femur as much as age-related bone loss. *Calcified Tissue International*, (58):231–235
- Pothuaud L., Rietbergen B. et al. (2004) A new computational efficient approach for trabecular bone analysis using beam models generated with skeletonized graph technique. *Computer Methods in Biomechanics and Biomedical Engineering*, (7): 205-213.
- Reginster J., Gillet P. et al. (1999) Direct costs of hip fractures in patients over 60 years of age in Belgium. *Pharmaco Economics*, (15):507-514.
- Reilly D., Burstein A. (1975) The elastic and ultimate properties of compact bone tissue. *Journal of Biomechanics*, (8): 393-405.
- Rho J., Kuhn-Spearing L., Zioupos P. (1998) Mechanical properties and the hierarchical structure of bone. *Medical Engineering & Physics*, (20):92–102.
- Rubin M., Jasiuk I. (2005) The TEM characterization of the lamellar structure of osteoporotic human trabecular bone. *Micron*, (7-8):653-664.
- Rudman K., Aspden R., Meakin J. (2006) Compression or tension? The stress distribution in the proximal femur. *Biomedical Engineering Online*, (5):12.
- Schaffler M., Pitchford W., Choi K., Riddle J. (1994) Examination of compact bone microdamage using back-scattered electron microscopy. *Bone*, (15): 483–488.
- Schaffler M., Choi K., Milgrom C. (1995) Aging and matrix microdamage accumulation in human compact bone. *Bone*, (17): 521-25.
- Schileo E., Taddei F. et al. (2007) Subject-specific finite element models can accurately predict strain levels in long bones. *Journal of Biomechanics*, (13):2982-9.
- Schileo E., Taddei F., Cristofolini L., Viceconti M. (2008) Subject- specific finite element models implementing a maximum principal strain criterion are able to estimate failure risk and fracture in human femurs tested in vitro. *Journal of Biomechanics*, (41):356–367.
- Sermon A., Boner K. et al. (2012) Biomechanical evaluation of bone-cement augmented Proximal femoral nail antirotation blades in a polyurethane foam model with low density. *Clinical Biomechanics*, (27):71–76.
- Shane E., Burr D., Ebeling P. et al. (2010) Atypical subtrochanteric and diaphyseal femoral fractures: Report of a task force of the American Society for Bone and Mineral Research. *Journal of Bone Mineral Research*, (25): 2267–2294.
- Smith M., Cody D. et al. (1992) Proximal femoral bone density and its correlation to fracture load and hip-screw penetration load. *Clinical Orthopaedics and Related Research*, (283):244–251.
- Sobelman O., Gibeling J. et al. (2004) Do microcracks decrease or increase fatigue resistance in cortical bone? *Journal of Biomechanics*, (37):1295–1303.

- Sutton M., Wolters W. et al. (1983) Determination of displacements using an improved digital correlation method. *Image & Vision Computing*, (1): 133-139.
- Sztefek P., Vanleene M. et al. (2010) Using digital image correlation to determine bone surface strains during loading and after adaptation of the mouse tibia. *Journal of Biomechanics*, (43):599–605.
- Tadashi S., Skinner H., Keyak J. (2007) Feasibility of a percutaneous technique for repairing proximal femora with simulated metastatic lesions. *Medical Engineering & Physics*, (29):594–601.
- Taddei F., Cristofolini L. et al. (2006) Subject-specific finite element models of long bones: an in vitro evaluation of the overall accuracy. *Journal of Biomechanics*, (39):2457–2467.
- Taddei F., Schileo E. et al. (2007). The material mapping strategy influences the accuracy of CT-based finite element models of bones: an evaluation against experimental measurements. *Medical Engineering and Physics*, (9):973–979.
- Tanck E., Van Aken J. (2009) Pathological fracture prediction in patients with metastatic lesions can be improved with quantitative computed tomography based computer models. *Bone*, (45):777–783.
- Taylor W., Roland E. et al. (2002) Determination of orthotropic bone elastic constants using FEA and modal analysis. *Journal of Biomechanics*, (35):767–773.
- Testi D., Viceconti M., Baruffaldi F., Cappello A. (1999) Risk of fracture in elderly patients: a new predictive index based on bone mineral density and finite element analysis. *Computer Methods and Programs in Biomedicine*, (1):23-33.
- Testi D., Cappello A. et al. (2004) A new software for prediction of femoral neck fractures. *Computer Methods and Programs in Biomedicine*, (2):141-145.
- Thomas C., Mayhew P. et al. (2004) Femoral neck trabecular bone: loss with aging and role in preventing fracture. *Journal of Bone Mineral Research*, (11):1808-1818.
- Thompson M., Schell H., Lienau J., Duda G. (2007) Digital image correlation: a technique for determining local mechanical conditions within early bone callus. *Medical Engineering and Physics*, (7):820-823.
- Turner P., Wyss P. et al. (2006) Time-lapsed investigation of three-dimensional failure and damage accumulation in trabecular bone using synchrotron light. *Bone*, (39):289–99.
- Turner P., Erickson B. et al. (2007) High-speed photography of compressed human trabecular bone correlates whitening to microscopic damage. *Engineering Fracture Mechanics*, (4):1928–1941.
- Tiwari V., Sutton M., McNeill S. (2007) Assessment of high speed imaging systems for 2D and 3D deformation measurements: methodology development and validation. *Experimental Mechanics*, (47):561–579.
- Trabelsi N., Yosibash Z. (2011) Patient-specific finite-element analyses of the proximal femur with orthotropic material properties validated by experiments. *Journal of Biomechanical Engineering*, (133): 1-11.
- Turner C., Rho J. et al. (1999) The elastic properties of trabecular and cortical bone tissues are similar: results from two microscopic measurement techniques. *Journal of Biomechanics*, (32): 437-441.
- Turner C. (2006) Bone strength: current concepts. *Annals of the New York Academy of Science*, (1068):429-446.

- Tsai S., Wu E. (1971) A general theory of strength for anisotropic materials. *Journal of Composite Materials*, (5):58–80.
- Tyson J., Schmidt T., Galanulis K. (2002) Biomechanics deformation and strain measurements with 3d image correlation photogrammetry. *Experimental Techniques*, (26): 39–42.
- Ulrich D., Rietbergen B., Weinans H., Ruegsegger P. (1998) Finite element analysis of trabecular bone structure: a comparison of image-based meshing techniques. *Journal of Biomechanics*, (31): 1187-1192.
- Ural A., Vashishth D. (2006) Cohesive finite element modeling of age-related toughness loss in human cortical bone. *Journal of Biomechanics*, (39): 2974–2982.
- Ural A., Vashishth D. (2007) Effects of intracortical porosity on fracture toughness in aging human bone: A microCT-based cohesive finite element study. *Journal of Biomechanical Engineering*, (129): 625–631.
- Vacher P., Dumoulin S., Morestin F., Mguil-Touchal S. (1999) Bidimensional strain measurement using digital images. *Proceedings of the Institution of Mechanical Engineers*, (213): 811-817.
- Van Buskirk W., Ashman R. (1981) The elastic moduli of bone. *The Joint ASME-ASCE Conference*, (45): 131–143.
- Van der Linden J., Birkenhager-Frenkel D., Weinans J. (2001) Trabecular bone's mechanical properties are affected by its non-uniform mineral distribution. *Journal of Biomechanics*, (34): 1573-1580.
- Van der Steenhoven T., Schaasberg W. et al. (2012) Cyclic loading of fractured cadaveric femurs after elastomer femoroplasty: An in vitro biomechanical study. *Clinical Biomechanics*, (27):819-823.
- Van Rietbergen B., Odgaard A., Kabel J., Huiskes R. (1996) Direct mechanical assessment of elastic symmetries and properties of trabecular bone architecture. *Journal of Biomechanics*, (29):1653–1657.
- Van Rietbergen B., Müller R. et al. (1999) Tissue stresses and strain in trabeculae of a canine proximal femur can be quantified from computer reconstructions. *Journal of Biomechanics*, (32):165-173.
- Vashishth D., Behiri J., Bonfield W. (1997) Crack growth resistance in cortical bone: Concept of microcrack toughening. *Journal of Biomechanics*, (8):763–769.
- Vashishth D., Koontz J. et al. (2000) In vivo diffuse damage in human vertebral trabecular bone. *Bone*, (26):147-152.
- Vashishth D., Gibson G. et al. (2001) Influence of nonenzymatic glycation on biomechanical properties of cortical bone. *Bone*, (28):195-201
- Vashishth D., Tanner E., Bonfield W. (2003) Experimental validation of a microcracking-based toughening mechanism for cortical bone. *Journal of Biomechanics*, (36):121–4.
- Vellas S., Gillette-Guyonnet S. et al. (2000) Chute, fragilité et ostéoporose chez la personne âgée : Un problème de santé publique. *La Revue de Médecine Interne*, (21):608–613.
- Verhulp E., Van Rietbergen B., Huiskes R. (2004) A three-dimensional digital image correlation technique for strain measurements in microstructures. *Journal of Biomechanics*, (9):1313-1320.

- Viceconti M., Bellingeri L., Cristofolini L., Toni A. (1998) A comparative study on different methods of automatic mesh generation of human femurs. *Medical Engineering & Physics*, (1): 1-10.
- Viceconti M., Davinelli M., Taddei F., Cappello A. (2004) Automatic generation of accurate subject specific bone finite element models to be used in clinical studies. *Journal of Biomechanics*, (37):1597–605.
- Voo L., Armand M., Kleinberger M. (2004) Stress fracture risk analysis of the human femur based on computational biomechanics. *Technical Digest*, (25):223-230.
- Wachtel E., Keaveny T. (1997) Dependence of trabecular damage on mechanical strain. *Journal of Orthopaedic Research*, (5):781–787.
- Wang Z., Teo J. et al. (2005) Computational biochemical modeling of the lumbar spine using marching-cubes surfaces smoothed finite element voxel meshing. *Computer methods and Programs in Biomedicine*, (80):25-35.
- Wang X., Niebur G. (2006) Microdamage propagation in trabecular bone due to changes in loading mode. *Journal of Biomechanics*, (39):781–790.
- Wang Q., Teo J., Ghasem-Zadeh A., Seeman E. (2009) Women and men with hip fractures have a longer femoral neck moment arm and greater impact load in a sideways fall. *Osteoporosis International*, (20): 1151-1156.
- Wirtz D., Pandorf T. et al. (2003) Concept and development of an orthotropic FE model of the proximal femur. *Journal of Biomechanics*, (36):289–293.
- Wolfram U., Wilke H., Zysset P. (2011) Damage accumulation in vertebral trabecular bone depends on loading mode and direction. *Journal of Biomechanics*, (44):1164-1169.
- Yang H., Shen L. et al. (1996) The relationship between loading conditions and fracture patterns of the proximal femur. *Journal of Biomechanical Engineering*, (118):575–578.
- Yang G., Kabel J. et al. (1999) The anisotropic Hooke's law for cancellous bone and wood. *Journal of Elasticity*, (53): 125–146.
- Yang Q., Cox B., Nalla R., Ritchie R. (2006) Re-evaluating the toughness of human cortical bone. *Bone*, (38):878–887.
- Yang L., Zhang P. et al. (2007) Measurement of strain distributions in mouse femora with 3D-Digital speckle pattern interferometry. *Optics Lasers in Engineering*, (8):843-851.
- Yang P., Brüggemann G., Rittweger J. (2011) What do we currently know from in vivo bone strain measurements in humans? *Journal of Musculoskeletal and Neuronal Interactions*, (1):8-20.
- Yoon H., Katz J. (1976) Ultrasonic wave propagation in human cortical bone. II Measurements of elastic properties and microhardness. *Journal of Biomechanics*, (9): 459-464
- Yosibash Z., Trabelsi N., Milgrom C. (2007) Reliable simulations of the human proximal femur by high-order finite element analysis validated by experimental observations. *Journal of Biomechanics*, (40):3688–3699.
- Zhang D., Arola D., Rouland J. (2001) Evaluating the elastic modulus of bone using electronic speckle pattern interferometry. *Experimental Technique*, (25):32–34.

Zhang G., Qin L., Shi Y., Leung K. (2005) A comparative study between axial compression and lateral fall configuration tested in a rat proximal femur model. *Clinical Biomechanics*, (20): 729–735.

Zhang J., Michalenko M., Kuhl E., Ovaert T. (2010) Characterization of indentation response and stiffness reduction of bone using a continuum damage model. *Journal of the Mechanical Behavior of Biomedical Materials*, (3):189-202.

Ziopoulos P., Currey J. (1994) Extent of microcracking and morphology of microcracks in damaged bone. *Journal of Material Science*, (4):978-986.

Ziopoulos P. (2001) Accumulation of in-vivo fatigue microdamage and its relation to biomechanical properties in ageing human cortical bone. *Journal of Microscopy*, (201):270-278.

Ziylan T., Murshid K. (2002) An analysis of anatolian human femur anthropometry. *Turkish Journal of Medical Science*, (32): 231-235.

Zysset P. (1994) A constitutive law for trabecular bone. Ph.D. thesis, Ecole Polytechnique Federale de Lausanne.

Zysset P., Curnier A. (1996) A 3d damage model for trabecular bone based on fabric tensors. *Journal of Biomechanics*, (29):1549–1558.

Awad BETTAMER

**PREDICTION DE LA FRACTURE OSSEUSE DU COL DU FEMUR : MODELISATION PAR
ELEMENTS FINIS BASEE SUR LA MECANIQUE D'ENDOMMAGEMENT
ET VALIDATION EXPERIMENTALE**

Résumé:

Les fractures causées par l'ostéoporose de l'extrémité supérieure du fémur sont devenues un problème majeur de santé publique. Par conséquent, ce sujet devient un axe de recherche de plus en plus important pour les cliniciens et les chercheurs biomédicaux. Le but de cette étude est de développer une nouvelle approche pour prédire la fracture du col du fémur. Cette étude propose de développer et valider des modèles par Eléments Finis (EF) en 2D et 3D, basés sur le concept de l'endommagement mécanique des milieux continus, permettant de simuler la fracture de la partie proximale du fémur en tenant compte de l'initiation progressive de fissures et leur progression. Deux configurations ont été utilisées: appui monopodal et chute.

L'ensemble des lois de comportements quasi fragile couplées à une loi d'endommagement sont implémentées en langage FORTRAN dans ABAQUS/Standard (sous-programme de type UMAT). La densité minérale osseuse (BMD) a été mesurée par l'absorptiométrie à rayon X en double énergie DXA pour la région d'intérêt. Les modèles ont été développés dans deux variantes (l'une isotrope et l'autre orthotrope) puis validés avec des résultats expérimentaux obtenus sur des essais en appui monopodale réalisés sur des fémurs humains. Durant ces essais, des mesures optiques basées sur la méthode de corrélation d'images numériques (DIC) ont été réalisées afin d'acquérir les différents champs de déplacement et de déformation.

Le modèle numérique 3D a réussi à prédire l'ensemble de la courbe force-déplacement ainsi que l'emplacement et l'amorce de la rupture des fémurs. Par ailleurs, Malgré sa robustesse, la variante 3D du modèle numérique reste difficilement exploitable dans l'état pour réaliser un diagnostic préventif dans des délais acceptables pour des cliniciens, car très consommatrice en temps de calcul. Pour pallier à cela, le modèle simplifié en 2D a été préliminairement validé sous les mêmes conditions aux limites et les résultats ont montré une bonne corrélation avec l'expérience. Ces travaux ont souligné le potentiel de la modélisation par éléments finis basée sur l'endommagement quasi-fragile à devenir un outil complémentaire de prédiction du risque de la fracture osseuse.

Mots clés : Fémur, Eléments finis, Expérimentation, Endommagement, Fracture, Validation.

**PREDICTION OF PROXIMAL FEMUR FRACTURE: FINITE ELEMENT MODELING
BASED ON MECHANICAL DAMAGE AND EXPERIMENTAL VALIDATION**

Summary:

Femoral fractures caused by the osteoporosis become major problem of public health, and therefore, this subject becomes an increasingly important goal for both clinicians and biomedical researchers. The purpose of this study is to develop a new coupled approach to predict the fracture of neck femoral. The current study proposes a validated 2D and 3D Finite Element (FE) models based on continuum damage mechanics in order to simulate human proximal femur fracture considering the progressive cracks initiation and propagation. These models are applied and validated under single limb stance and sideways fall configuration.

Quasi brittle behavior laws coupled to damage are implemented in FORTRAN and fed into ABAQUS/Standard codes to describe the constitutive behavior (subroutine UMAT). Bone mineral density (BMD) is measured using dual energy X-ray absorptiometry (DXA) for the region of interest. The models have been developed within two variants (one isotropic, the other anisotropic) and validated with experimental results of tests performed on human femur samples under single limb stance configuration. During these tests, optical measurements based on the method of digital image correlation (DIC) were conducted to acquire the various fields of displacement and deformation. To calculate the fracture risk of the femoral head, it is necessary to assign correctly the bone material properties.

The 3D FE models were able to predict the overall force-displacement curve, location and initiation of femur fractures. Moreover, despite its robustness, this 3D FE model is still limited to be used, within clinically acceptable time, for diagnostic purposes. To overcome this, the model was simplified into 2D model which has been preliminarily validated under identical boundary conditions and the results showed a good correlation with experiments. These studies have highlighted the potential of the finite element model based on quasi-brittle damage to become a complementary tool for predicting the risk of bone fracture.

Keywords : Femur, Finite element, Experiment, Damage, Fracture, Validation.



**Laboratoire PRISME
8 rue Léonard de Vinci
45072 Orléans cedex 2**

